

*SPITZER'S* CONTRIBUTION TO THE AGN POPULATION

by

Jennifer Lynn Donley

---

A Dissertation Submitted to the Faculty of the  
DEPARTMENT OF ASTRONOMY  
In Partial Fulfillment of the Requirements  
For the Degree of  
DOCTOR OF PHILOSOPHY  
In the Graduate College  
THE UNIVERSITY OF ARIZONA

2009

THE UNIVERSITY OF ARIZONA  
GRADUATE COLLEGE

As members of the Dissertation Committee, we certify that we have read the dissertation prepared by Jennifer Lynn Donley entitled "*Spitzer's* Contribution to the AGN Population" and recommend that it be accepted as fulfilling the dissertation requirement for the Degree of Doctor of Philosophy.

\_\_\_\_\_ Date: 12 Dec 2008  
George Rieke

\_\_\_\_\_ Date: 12 Dec 2008  
Yancy Shirley

\_\_\_\_\_ Date: 12 Dec 2008  
Mark Dickinson

\_\_\_\_\_ Date: 12 Dec 2008  
Chris Impey

\_\_\_\_\_ Date: 12 Dec 2008  
Richard Green

Final approval and acceptance of this dissertation is contingent upon the candidate's submission of the final copies of the dissertation to the Graduate College.

I hereby certify that I have read this dissertation prepared under my direction and recommend that it be accepted as fulfilling the dissertation requirement.

\_\_\_\_\_ Date: 12 Dec 2008  
Dissertation Director: George Rieke

## STATEMENT BY AUTHOR

This dissertation has been submitted in partial fulfillment of requirements for an advanced degree at The University of Arizona and is deposited in the University Library to be made available to borrowers under rules of the Library.

Brief quotations from this dissertation are allowable without special permission, provided that accurate acknowledgment of source is made. Requests for permission for extended quotation from or reproduction of this manuscript in whole or in part may be granted by the head of the major department or the Dean of the Graduate College when in his or her judgment the proposed use of the material is in the interests of scholarship. In all other instances, however, permission must be obtained from the author.

SIGNED: Jennifer Lynn Donley

## ACKNOWLEDGMENTS

As with most things in life, this thesis could not have been completed without the help and guidance of others. I would first like to thank my advisor, George Rieke, for his input, advice, and support. I am constantly amazed by his ability to mentor students working on such a wide range of topics (and to do it incredibly well) while also building the next generation of infrared instrumentation, teaching, pursuing his own research, and even writing the occasional book. And I thought there were only 24 hours in a day...

Second, I'd like to thank my main collaborators: Pablo Pérez-González, Jane Rigby, and Almudena Alonso Herrero, as well as the many people who have enabled, improved, or assisted with my work over the years: Dave Alexander, Dave Ballantyne, Niel Brandt, Thomas Boller, Richard Cool, Mark Dickinson, Mike Eracleous, Kris Eriksen, Xiaohui Fan, Fabrizio Fiore, Trish Henning, Baerbel Koribalski, Renee Kraan-Korteweg, Mark Lacy, Emeric Le Floch, Casey Papovich, Mari Polletta, Anja Schroeder, Lister Staveley-Smith, Henrique Schmitt, Richard Wade, my journal referees, and my thesis committee. A special thanks also goes to Don McCarthy, whose dedication towards public outreach and education is truly inspiring, and from whom I have learned a lot over the past 5 years.

Third, many thanks are in order to the fellow grad students who helped to keep me sane, especially Richard Cool, Kris Eriksen, Kristian Finlator, Chris Groppi, Karen Knierman, Wilson Liu, Andy Marble, Jackie Monkiewicz, Moire Prescott, Mandy Proctor, Jane Rigby, Wayne Schlingman, Amy Stutz, Krystal Tyler, and Patrick Young. The same can also be said for a number of people in the "real world" including Sandy Cohen, Renee and James Dennison, Allison Ewing, Matt Hughes, Ana Lucero-Liu, Jonathan Mandell, Heather Phillips, Maggie Sullivan, and the Tucson Tri Girls.

Of course, none of this would have been possible had I decided not to pursue astronomy in the first place. For that, I thank Dwight Anderson, whose enthusiasm for and dedication towards astronomy is contagious. I also thank the Penn State Astronomy Department, especially Niel Brandt, Jane Charlton, Don Schneider, and Richard Wade, for providing me with the theoretical and research background necessary to succeed in graduate school.

Finally, I want to thank my family (and especially Kris) for their support and encouragement and for reminding me from time to time that there is far more to life than astronomy.

I acknowledge support from an NSF Graduate Research Fellowship, as well as from NASA through contracts 960785 and 1255094 issued by JPL/California Institute of Technology.

## DEDICATION

To Mr. Anderson, who first inspired me to study the stars  
To my family, who have supported me throughout this long journey  
And to Kris, the light at the end of my tunnel

## TABLE OF CONTENTS

LIST OF FIGURES . . . . .	9
LIST OF TABLES . . . . .	11
ABSTRACT . . . . .	12
CHAPTER 1 INTRODUCTION . . . . .	14
CHAPTER 2 UNVEILING A POPULATION OF X-RAY NON-DETECTED AGN	20
2.1 Introduction . . . . .	20
2.2 Observations and Data Reduction . . . . .	22
2.3 The X-ray Faint AGN Population . . . . .	24
2.3.1 Sample Selection . . . . .	24
2.3.2 Potential Sources of Contamination . . . . .	29
2.3.3 Sample Completeness . . . . .	30
2.4 Redshifts . . . . .	31
2.5 X-ray Detection and Coaddition . . . . .	34
2.5.1 X-ray Detection . . . . .	34
2.5.2 X-ray Coaddition . . . . .	36
2.5.3 X-ray Upper Limits . . . . .	39
2.5.4 Column Densities . . . . .	40
2.5.5 Compton-thick AGN . . . . .	41
2.6 Interpretation . . . . .	43
2.6.1 Radio Extent and Spectral Shape . . . . .	43
2.6.2 Radio, 24 $\mu\text{m}$ , and X-ray Luminosities . . . . .	44
2.6.3 Observed X-ray vs. Radio Emission . . . . .	46
2.6.4 Intrinsic X-ray vs. Radio Emission . . . . .	52
2.6.5 X-ray vs. Optical Emission . . . . .	55
2.7 Conclusions . . . . .	57
CHAPTER 3 POWER-LAW AGN CANDIDATES IN THE <i>Chandra</i> DEEP FIELD-NORTH . . . . .	60
3.1 Introduction . . . . .	61
3.2 Observations and Data Reduction . . . . .	63
3.3 Sample selection . . . . .	64
3.4 Redshifts . . . . .	70
3.5 Multiwavelength Properties . . . . .	75
3.5.1 X-ray Emission . . . . .	75
3.5.2 24 $\mu\text{m}$ Emission . . . . .	86
3.5.3 Radio Loudness . . . . .	90
3.5.4 Optical Morphology and Detection Fraction . . . . .	92

TABLE OF CONTENTS — <i>Continued</i>	
3.5.5	Optical–MIR SEDs . . . . . 93
3.6	Comparison with other MIR selection techniques . . . . . 94
3.6.1	Optical vs 24 $\mu$ m Emission . . . . . 95
3.6.2	<i>Spitzer</i> Color-Color Selection . . . . . 96
3.7	Obscuration . . . . . 111
3.7.1	Column Densities . . . . . 112
3.7.2	Space Densities of Obscured AGN . . . . . 118
3.7.3	Effect of Reddening on Obscured AGN . . . . . 119
3.8	Conclusions . . . . . 121
CHAPTER 4 <i>Spitzer's</i> CONTRIBUTION TO THE AGN POPULATION . . . . . 126	
4.1	Introduction . . . . . 127
4.2	Sample Selection . . . . . 129
4.2.1	Multi-wavelength Data . . . . . 129
4.2.2	Power-law, color-selected, and IR-normal samples . . . . . 131
4.2.3	IR-Excess Galaxies . . . . . 133
4.3	Redshifts . . . . . 135
4.4	X-ray Properties . . . . . 139
4.5	IRAC color-color selection . . . . . 142
4.5.1	Comparison of the IRAC color-color selection criteria . . . . . 142
4.5.2	Star-forming Templates . . . . . 144
4.5.3	Redshift-dependent color selection . . . . . 146
4.5.4	Properties of Color-selected AGN candidates . . . . . 147
4.5.5	Flux dependency of color selection . . . . . 153
4.5.6	Comparison with previous work . . . . . 155
4.6	IRAC Power-law selection . . . . . 158
4.7	IR-Excess Selection . . . . . 164
4.7.1	Daddi et al. (2007) Compton-thick AGN candidates . . . . . 166
4.7.2	Fiore et al. (2008) Compton-thick AGN candidates . . . . . 175
4.8	Implications for IR Selection of AGN . . . . . 179
4.8.1	Infrared power-law and color-selected AGN . . . . . 180
4.8.2	Radio/Infrared-selected AGN . . . . . 181
4.8.3	IR-excess Galaxies . . . . . 182
4.9	AGN Fraction of the MIR Sample . . . . . 184
4.10	Summary . . . . . 187
CHAPTER 5 CONCLUSIONS AND FUTURE DIRECTIONS . . . . . 189	
5.1	Radio-excess AGN . . . . . 189
5.2	Infrared power-law AGN . . . . . 191
5.3	The Combined Contribution from <i>Spitzer</i> -selected AGN . . . . . 193
5.4	The Role of Obscured AGN in Galaxy Formation and Evolution . . 194

TABLE OF CONTENTS — *Continued*

APPENDIX A	STAR-FORMING TEMPLATES . . . . .	197
APPENDIX B	PHOTOMETRIC REDSHIFT TECHNIQUE . . . . .	201
APPENDIX C	REDSHIFT-DEPENDENT COLOR SELECTION . . . . .	206
REFERENCES	. . . . .	211



## LIST OF FIGURES

2.1	Radio-excess selection technique . . . . .	25
2.2	SEDs of radio-excess AGN . . . . .	33
2.3	Example of a weak X-ray detection . . . . .	38
2.4	X-ray column density distribution . . . . .	42
2.5	Radio power distribution . . . . .	45
2.6	Observed X-ray luminosities . . . . .	48
2.7	Ratio of radio to X-ray power, $q'$ . . . . .	50
2.8	Relationship between $q'$ and the radio compactness . . . . .	53
2.9	Distribution of absorption- and K-corrected $q'$ . . . . .	54
2.10	X-ray to optical flux ratios . . . . .	56
3.1	SEDs of the power-law galaxies . . . . .	67
3.2	X-ray to optical flux ratios . . . . .	71
3.3	Comparison between spectroscopic and photometric redshifts . . . . .	73
3.4	Redshift distribution . . . . .	74
3.5	X-ray detection fraction . . . . .	83
3.6	X-ray luminosity distribution . . . . .	84
3.7	Median SEDs of X-ray-selected AGN, as a function of $L_x$ . . . . .	85
3.8	X-ray luminosity vs. redshift . . . . .	87
3.9	24 $\mu\text{m}$ detection fraction as a function of $L_x$ . . . . .	89
3.10	Median optical-MIR SEDs of the power-law galaxies . . . . .	94
3.11	Optical/MIR color-color diagram of Yan et al. (2004) . . . . .	98
3.12	IRAC color-color diagram of Lacy et al. (2004) . . . . .	100
3.13	IRAC color-color diagram of Stern et al. (2005) . . . . .	102
3.14	Redshift dependence of IRAC colors . . . . .	104
3.15	X-ray luminosity dependence of IRAC colors . . . . .	105
3.16	Survey detection limits in L(TIR) . . . . .	109
3.17	X-ray to optical flux ratios of color-selected sources . . . . .	110
3.18	X-ray column density distribution . . . . .	113
3.19	Obscured AGN fractions . . . . .	115
4.1	Comparison between spectroscopic and photometric redshifts . . . . .	136
4.2	Redshift distribution . . . . .	138
4.3	Position in IRAC color-space . . . . .	143
4.4	Star-forming tracks in IRAC color-space . . . . .	145
4.5	Redshift-dependent colors in Lacy et al. IRAC color space . . . . .	148
4.6	Redshift-dependent colors in Stern et al. IRAC color space . . . . .	149
4.7	Lacy et al. colors of galaxies with varying power-law slopes . . . . .	159
4.8	Stern et al. colors of galaxies with varying power-law slopes . . . . .	160
4.9	24 $\mu\text{m}$ to 3.6 $\mu\text{m}$ colors of the power-law galaxies . . . . .	162

LIST OF FIGURES — *Continued*

4.10	Position in IRAC color-space of the IR-excess sources . . . . .	165
4.11	2-10 keV luminosity vs. 25 $\mu\text{m}$ power . . . . .	169
4.12	Median SEDs of the Daddi et al. IR-normal and IR-excess samples .	173
4.13	Star-forming ULIRG tracks in Fiore et al. color space . . . . .	178
4.14	AGN fraction as a function of 24 $\mu\text{m}$ flux density . . . . .	185
A.1	SED templates . . . . .	200

## LIST OF TABLES

2.1	Radio, 24 $\mu\text{m}$ , and X-ray Properties . . . . .	26
2.1	Radio, 24 $\mu\text{m}$ , and X-ray Properties . . . . .	28
2.2	X-ray Properties of X-ray Weakly-Detected AGN . . . . .	37
2.3	Limits on the X-ray flux of 5 X-ray Non-Detected AGN . . . . .	39
2.4	X-ray Properties of X-ray Detected AGN . . . . .	47
3.1	Power-law Galaxy Sample . . . . .	77
3.1	Power-law Galaxy Sample . . . . .	78
3.1	Power-law Galaxy Sample . . . . .	80
3.2	X-ray Properties of X-ray Weakly-Detected Power-law Galaxies . .	81
3.3	X-ray Properties of X-ray-Detected Power-law AGN . . . . .	97
4.1	Photometric Redshifts . . . . .	137
4.2	X-ray Detection Statistics . . . . .	141
4.3	Fraction of sources that lie outside the star-forming contours . . . .	150
4.4	X-ray detection fraction (and total number) of sources that lie outside the star-forming contours . . . . .	152
4.5	Percent of secure color-selected galaxies vs. 24 $\mu\text{m}$ flux . . . . .	156
A1	Input Data for Templates . . . . .	198
A2	Templates . . . . .	199
B1	Photometric Redshift Templates . . . . .	202
B1	Photometric Redshift Templates . . . . .	203

## ABSTRACT

Using large multiwavelength datasets, we study obscured AGN in the distant universe that have been missed via traditional selection techniques (e.g. UV/optical/X-ray). To do so, we take particular advantage of the mid-IR, which is minimally affected by obscuration. We first select as AGN candidates those objects whose radio emission is significantly brighter, relative to the mid-IR, than would be predicted by the well known radio/infrared correlation, indicating that the radio emission originates in the central engine. We find that of the 27 such sources identified in the CDF-N, 60% lack solid X-ray detections and 25% lack even  $2\sigma$  X-ray emission. The absorbing columns of the faint X-ray-detected objects indicate that they are obscured but unlikely to be Compton thick, whereas the radio-excess AGN which are X-ray non-detected are Compton-thick candidates.

We similarly use the infrared emission to select IRAC (3.6-8.0  $\mu\text{m}$ ) power-law AGN. In these luminous AGN, the hot dust emission from the AGN fills in the gap in a galaxy's SED between the 1.6  $\mu\text{m}$  stellar bump and the long-wavelength dust emission feature. While sources selected in this way are more luminous than the radio-excess AGN, we find a similar X-ray detection fraction. Of the 62 power-law galaxies in the CDF-N, only 55% are detected in the X-ray, and 15% lack evidence for even weak  $2\sigma$  X-ray emission. A study of their X-ray properties indicates that  $\sim 75\%$  are obscured.

Finally, we test IRAC color-color and infrared-excess selection criteria. We find that while these selection techniques identify a number of obscured AGN, they may also select a significant number of star-forming galaxies. By combining only the secure AGN candidates selected via all methods discussed above, we

estimate that the addition of Spitzer-selected AGN candidates to the deepest X-ray selected AGN samples directly increases the number of known AGN by 54-77%, and implies a total increase to the number of AGN of 71-94%.

## CHAPTER 1

## INTRODUCTION

One of the most exciting astronomical breakthroughs of the past decade was the discovery that supermassive black holes (SMBHs) reside at the center of nearly all massive galaxies. Even more surprising, however, was the resulting discovery that the masses of these SMBHs are tightly correlated to the velocity dispersions of their host galaxy's bulges, via the so-called  $M_{\text{BH}} - \sigma$  relationship (Ferrarese & Merritt 2000; Gebhardt et al. 2000). Such a correlation was previously considered unlikely because of the factor of  $10^3$  offset in scale between the black hole's radius of influence and the size of the host galaxy's bulge. It had therefore been assumed that SMBH growth via accretion in an active galactic nucleus (AGN) proceeded independently of the large-scale properties of its host galaxy. It is now clear, however, that AGN activity and feedback are intimately linked to the formation and evolution of the galaxies in which they reside. If we are to understand how galaxies form and evolve, we must therefore first constrain the accretion history of the universe.

An accurate measurement of accretion activity across cosmic time, however, requires a complete and unbiased sample of AGN and creating such a sample has been remarkably challenging due to the differing luminosities, accretion rates, orientations, and intrinsic obscurations of AGN. As an illustration of these differences, take as an example the prototypical quasar 3C 273, the first quasar (or "quasi-stellar radio object") identified by Maarten Schmidt in 1963. A Type 1 AGN, 3C 273 is a bright optical source with broad emission lines, and was one of the first extragalactic X-ray sources to be identified. The majority of AGN, however, do not share 3C 273's properties. For instance, only 15% emit the strong

nuclear radio emission seen in 3C 273, and are thus referred to as “radio-loud” (Kellermann et al. 1989). Furthermore, narrow-line Type 2 AGN in the local universe outnumber broad-line Type 1 AGN like 3C 273 by a factor of 4:1 (Maiolino & Rieke 1995), and more than half of Seyfert 2 nuclei are Compton-thick with X-ray column densities of  $N_{\text{H}} > 10^{24} \text{ cm}^{-2}$ . Finally, while all luminous AGN are believed to be intrinsically bright in the X-ray, not all AGN are detectable in the X-ray, even in the deepest X-ray surveys.

Many of the apparent differences between various classes of AGN can be explained by the unified model. Under this model, Type 1 and Type 2 AGN have intrinsically identical central engines, but are viewed at different angles with respect to an orientation-dependent obscuring medium (often visualized as a torus). When this parsec-sized torus is viewed face-on, as in Type 1 AGN, the central engine is relatively unobscured by dust and gas and both the broad-line region and narrow-line region are visible. Alternatively, when viewed edge-on, the torus blocks the broad-line region from view, resulting in a spectrum dominated by narrow emission lines and a Type 2 classification. This intrinsic obscuration affects not only the optical/UV continuum and line emission, biasing UV and optical surveys towards unobscured AGN, but the X-ray emission as well. If the intrinsic X-ray column density is sufficiently high ( $N_{\text{H}} \geq 10^{23} \text{ cm}^{-2}$ ), even hard (2-10 keV) X-rays are absorbed. Furthermore, in the case of moderate to strong Compton-thick obscuration where the opacity to Thomson scattering is  $\tau \gg 1$ , the majority of X-ray photons at all energies are down-scattered and eventually absorbed.

Because nearly all bright X-ray sources are AGN, and because nearly all AGN are intrinsically X-ray bright, hard X-ray surveys have long been considered the most efficient and complete way to select AGN. Due to the intrinsic absorption

discussed above, however, even hard X-ray surveys can be substantially incomplete to obscured Type 2 AGN. This is true even for the deepest X-ray observations taken to date, the 2 Ms *Chandra* Deep Fields North and South. In fact, one need only move local Compton-thick AGN such as NGC 1068, Circinus, and NGC 4051 out to  $z \gtrsim 0.2 - 1$  for them to drop below the deep-field detection limits (e.g., Brandt & Hasinger 2005). Therefore, if heavily obscured AGN are as common at high redshift as they are in the local universe, even the deepest X-ray surveys will be substantially incomplete.

Direct evidence for a large population of distant obscured AGN comes from the cosmic X-ray background (CXRB), whose broad  $\sim 1 - 200$  keV emission peaks at  $\sim 30$  keV. While the CXRB was once thought to be diffuse like the cosmic microwave background (CMB), deep X-ray surveys with *Chandra* and *XMM-Newton* have now resolved 70-90% of the CXRB at 2-8 keV into discrete sources (Muschotzky et al. 2000; Giacconi et al. 2002; Alexander et al. 2003; Bauer et al. 2004; Worsley et al. 2004, 2005). This resolved fraction, however, drops to 60% at 6-8 keV and to 50% at  $\geq 8$  keV (Worsley et al. 2004, 2005), indicating that we have not yet individually detected the bulk of the sources collectively responsible for the hard X-ray background.

Population synthesis models of the CXRB all agree that the missing sources are heavily obscured AGN, but they differ in their predictions of the numbers and properties of this missing population. For instance, while Ballantyne et al. (2006) estimate that deep X-ray surveys miss  $\sim 50\%$  of obscured AGN with  $\log L_x > 10^{44}$  ergs s $^{-1}$  and that most of the missing objects are Compton-thick, Worsley et al. (2005) find that the unresolved sources are likely to lie at  $z = 0.5 - 1.5$ , have column densities of  $N_H > 10^{23}$  cm $^{-2}$  (obscured yet Compton-thin) and have fainter X-ray luminosities of  $< 5 \times 10^{43}$  ergs s $^{-1}$ . Most recently, the joint analysis



of the CXRB and the soft and hard X-ray luminosity functions and number counts by Gilli et al. (2007) finds that a population of Compton-thick AGN as large as that of moderately obscured AGN is required to fit the 30 keV peak in the CXRB spectrum. In this model, the majority of obscured and Compton-thick AGN lie at relatively low X-ray luminosities ( $L_x \leq 10^{44}$  ergs s<sup>-1</sup>), a trend that has also been noted in recent observational studies (Ueda et al. 2003; Hasinger 2004; La Franca et al. 2005; Georgakakis et al. 2006).

Some of the discrepancies in the studies discussed above can be attributed not to the models, but to uncertainties in the intensity of the CXRB itself. The CXRB was first measured by the HEAO-1 X-ray observatory in the late 1970's. Later observations at  $E < 10$  keV, however, indicate that the HEAO-1 measurements may be systematically low by  $\sim 25 - 40\%$ , leading some authors to renormalize the CXRB spectrum at high energies. Doing so, however, has a large effect on the inferred population of Compton-thick AGN, increasing their numbers by a factor of 2-3 (e.g. Gilli et al. 2007). The most recent results from the high-energy Integral telescope indicate that a renormalization of the HEAO-1 observations is necessary, but only by 10% (Churazov et al. 2007).

While population synthesis models of the X-ray background therefore point to a significant population of distant obscured AGN not yet detected in the deepest X-ray fields observed to date, the uncertainties in the normalization of the CXRB and the discrepancies between various theoretical models limit the insights we can gain from the CXRB alone. If we hope to determine the numbers and nature of this elusive population of missing AGN, and thus create a far more complete sample of AGN than is possible via X-ray selection alone, a way must be found to detect them directly.

In order to select obscured AGN, one must focus on emission from wavebands

minimally affected by obscuring dust and gas: the radio and infrared. While deep radio observations of AGN have long been possible, only limited infrared capabilities existed prior to the launch of *Spitzer* in 2003. *Spitzer* samples the mid-infrared in the following bands: 3.6-8.0  $\mu\text{m}$  (IRAC), 24  $\mu\text{m}$ , 70  $\mu\text{m}$ , and 160  $\mu\text{m}$  (MIPS), and 5-38  $\mu\text{m}$  (IRS). The shorter of these bands (IRAC and MIPS 24  $\mu\text{m}$ ) probe the hot dust emission from AGN, and thus provide a promising new means of selecting AGN independently of their optical and X-ray emission. Identifying the AGN in large infrared samples, however, is not a simple task. Unlike the X-ray, where nearly all bright sources are AGN, both AGN and star-forming galaxies produce bright infrared emission, with the AGN fraction dropping rapidly as a function of decreasing mid-IR flux. The challenge in selecting AGN on the basis of their IR emission therefore lies in successfully distinguishing between AGN and star-formation-dominated sources.

Despite this challenge, a number of IR-based AGN selection methods have been developed over the past 6 years. Some make use of infrared data alone, whereas others combine infrared data with other multiwavelength indicators. In this thesis, I take advantage of deep multiwavelength coverage in the *Chandra* Deep Fields North and South to develop and test two IR-based AGN selection methods: radio-excess selection and IRAC power-law selection. The first of these methods, discussed in Chapter 2, takes advantage of the well-known radio/infrared correlation for star-forming galaxies, and selects as AGN those sources whose radio emission significantly exceeds that predicted from the infrared. The second method, discussed in Chapter 3, selects as AGN sources in which hot dust emission from the central engine fills in the dip in a galaxy's SED between the 1.6  $\mu\text{m}$  stellar bump and the long-wavelength dust emission feature. Finally, in Chapter 4, I critically review a number of additional infrared-selection

criteria including IRAC color-color selection (Lacy et al. 2004; Stern et al. 2005) as well as infrared-excess selection (Daddi et al. 2007; Fiore et al. 2008, Dey et al. 2008, Polletta et al. 2008). I then combine the reliable AGN candidates selected via all methods described above to estimate *Spitzer's* total contribution to the AGN population. Chapter 5 summarizes the results of this thesis, and explores possible avenues for future work.

## CHAPTER 2

## UNVEILING A POPULATION OF X-RAY NON-DETECTED AGN

We define a sample of 27 radio-excess AGN in the *Chandra* Deep Field North by selecting galaxies that do not obey the radio/infrared correlation for radio-quiet AGN and star-forming galaxies. Approximately 60% of these radio-excess AGN are X-ray undetected in the 2 Ms *Chandra* catalog, even at exposures of  $\geq 1$  Ms; 25% lack even  $2\sigma$  X-ray detections. The absorbing columns to the faint X-ray-detected objects are  $10^{22} \text{ cm}^{-2} < N_H < 10^{24} \text{ cm}^{-2}$ , i.e., they are obscured but unlikely to be Compton thick. Using a local sample of radio-selected AGN, we show that a low ratio of X-ray to radio emission, as seen in the X-ray weakly- and non-detected samples, is correlated with the viewing angle of the central engine, and therefore with obscuration. Our technique can explore the proportion of obscured AGN in the distant Universe; the results reported here for radio-excess objects are consistent with but at the low end of the overall theoretical predictions for Compton-thick objects.

## 2.1 Introduction

Hard X-ray surveys are an efficient means to define AGN samples, as hard X-ray emission is able to penetrate the dust and gas capable of obscuring an AGN's optical, UV, and soft X-ray emission. However, AGN with high columns of absorbing gas can be missed even in the hard (2-10 keV) X-ray. Many local AGN have very high absorbing column; Seyfert 2's are about four times more numerous than Seyfert 1s (Maiolino & Rieke 1995), and more than half of Seyfert 2 nuclei are Compton thick with  $N_H > 10^{24} \text{ cm}^{-2}$  (Maiolino et al. 1998; Risalti et al. 1999). X-ray background population synthesis models predict that AGN

are similarly obscured out to high ( $z = 2 - 3$ ) redshift;  $\sim 60\%$  of high-redshift AGN are predicted to have obscuring columns greater than  $N_H = 10^{23} \text{ cm}^{-2}$  (e.g., Comastri et al. 2001, Gilli 2004). If distant AGN are indeed this obscured, the deep hard X-ray *Chandra* surveys will be moderately incomplete for obscured AGN ( $N_H > 10^{22} \text{ cm}^{-2}$ ); Treister et al. (2004) estimate 25% incompleteness at  $N_H = 3 \times 10^{23} \text{ cm}^{-2}$ . Such surveys will also miss nearly all of the Compton-thick AGN, a large population of which are expected both locally and in the high-redshift Universe (c.f. Ueda et al. 2003).

Quantifying the fraction of AGN missed by current surveys is necessary if we are to understand the accretion history of the Universe. In addition, the identification of heavily obscured AGN is in itself interesting, as such sources are poorly understood in the distant Universe.

The availability of deep mid-infrared (MIR) and radio images of the *Chandra* Deep Field North (CDFN) provides a new way to search for heavily obscured AGN, as extinction in the MIR and radio is small. Radio-excess AGN are significantly brighter in the radio relative to the infrared than are star-forming galaxies, which fit the well-defined radio/infrared correlation (Helou et al. 1985; Appleton et al. 2004). With the deep MIR data, we have separated the radio-excess AGN population from star-forming galaxies by comparing their radio and MIR flux densities. Because this radio/infrared method of classification is independent of the optical, UV, and X-ray characteristics of the deep radio sample, we detect via this selection approach AGN that are missed at other wavelengths, thereby testing the completeness of current AGN samples. We find that a significant number of radio-excess AGN do not appear even in the deepest available X-ray surveys.

This paper is organized as follows. In §2 we discuss the radio and infrared observations and data reduction. The X-ray faint AGN population is introduced

in §3, followed by a discussion of redshifts in §4. We focus in §5 on lower-significance X-ray detections, along with the X-ray coaddition of undetected AGN. The discussion follows in §6, and we summarize the conclusions of the paper in §7.

## 2.2 Observations and Data Reduction

Our initial sample consists of 371 radio sources detected at 1.4 GHz by the Richards et al. (2000) VLA survey of the CDFN; this survey has a detection limit of  $40 \mu\text{Jy}$ , rms noise of  $\sim 7.5 \mu\text{Jy}$ , and is 95% complete to  $80 \mu\text{Jy}$ <sup>1</sup>. We later restrict this initial sample to those sources with X-ray exposures  $> 1$  Ms; this reduces the radio sample size to 162, and the effective area of the survey to  $\sim 230 \text{ arcmin}^2$  (Alexander et al. 2003).

The  $24 \mu\text{m}$  properties of the radio sources are determined from a  $\sim 1400\text{s}$  Spitzer MIPS observation of the CDFN. The MIPS  $24 \mu\text{m}$  image was processed with the MIPS GTO data analysis tool (Gordon et al. 2004a). The measured count rates are corrected for dark current, cosmic-rays, and flux nonlinearities, and are then divided by flat-fields for each MIPS scan-mirror position. Images are then interpolated to half pixels, corrected for geometric distortion, and mosaicked. The final mosaic has a pixel scale of  $1''.25 \text{ pix}^{-1}$ , with a point-spread function full-width at half maximum (FWHM) of  $\approx 6''$ . Source extraction at  $24 \mu\text{m}$  was performed using the task *allstar* in the DAOPHOT package of IRAF<sup>2</sup> (see Pérez-González et al. 2005). We detect 1868  $24 \mu\text{m}$  sources in the  $> 1$  Ms field, 1167 of

<sup>1</sup>A rereduction of the radio data by G. Morrison shows flux density differences from the original reduction that are generally no more than  $\sim 10\%$ , with the notable exception of source VLA J123659+621832, where there is a discrepancy by a factor of ten (private communication, F. Bauer and G. Morrison). Adopting the new value for this source would push it further into the AGN regime in our selection method but would have no effect on the conclusions of this paper.

<sup>2</sup>IRAF is distributed by the National Optical Astronomy Observatories, which is operated by the Association of Universities for Research in Astronomy, Inc. (AURA) under cooperative agreement with the National Science Foundation

which have flux densities higher than the 80% completeness limit of the MIPS 24  $\mu\text{m}$  image processed in this manner, 80  $\mu\text{Jy}$  (Papovich et al. 2004). Systematic photometric errors in the MIPS photometry are small ( $\sim 1\%$ ), so the measurement accuracy is determined by statistical errors (about 15  $\mu\text{Jy}$  rms) and confusion noise (about 11  $\mu\text{Jy}$  rms).

The 1.4 GHz and 24  $\mu\text{m}$  sources were matched using a 2'' search radius, after adjusting the 24  $\mu\text{m}$  positions to remove any systematic positional offset between the radio and infrared images. We exclude from our final radio-excess AGN sample one radio source whose nearest 24  $\mu\text{m}$  counterpart lies between 2'' and 3'' of the radio position, as the reliability of counterparts in this region is ambiguous. If a source was not detected because it is blended with a brighter 24  $\mu\text{m}$  source, we use the flux density of the blended source as a conservative upper limit. Sources that were not detected at 24  $\mu\text{m}$  were assigned the  $\sim 5\sigma$  limit of 80  $\mu\text{Jy}$ . At the detection limits, there are  $\sim 0.7$  radio sources and  $\sim 5$  infrared sources per square arcmin. Consequently, one expects  $\sim 3$  false coincidences of radio and 24  $\mu\text{m}$  sources in the entire sample. Since we identify AGN by their relatively faint 24  $\mu\text{m}$  flux densities, the false detections will tend to remove some AGN from our sample but will not bias our results otherwise.

We also use a 500 s IRAC observation of the CDFN. The IRAC observations were divided into 4 dithers of 125 s each; the  $5\sigma$  point source sensitivity limits for the IRAC 3.0, 4.5, 5.8, and 8.0  $\mu\text{m}$  bands are 1.4, 2.8, 18.4, and 22.7  $\mu\text{Jy}$  respectively (Fazio et al. 2004). The IRAC data analysis is described in Huang et al. (2004). Source extraction in the IRAC bands was conducted using SExtractor (Bertin & Arnouts 1996).

Optical and near-infrared (NIR) photometry are measured from datasets published for the CDFN by the GOODS team (*bviz*, Giavalisco et al. 2004) and by Ca-

pak et al. (2004) (*UBVRIZHK*). When there is a single optical counterpart within  $2''$  of the radio source, the optical and NIR magnitudes are aperture-matched for consistency as described in Pérez-González et al. (2005). For radio sources with more than 1 optical or NIR counterpart within a  $2''$  radius of the radio position, we choose the counterpart that is nearest the radio position and use its individual SExtractor magnitude, measured within an elliptical aperture corresponding to 2.5 times the Kron radius (Kron 1980). The magnitudes measured in the GOODS dataset in this way are identical to those given by Giavalisco et al. (2004). When multiple GOODS counterparts are available, we choose the nearest source and do not use the ground-based optical data, which is likely to be blended.

### 2.3 The X-ray Faint AGN Population

We use the 1.4 GHz and  $24\ \mu\text{m}$  flux densities of our sample, along with the well-known radio/infrared relation of star-forming galaxies and radio-quiet AGN, to select a sample of radio-excess AGN independently of their X-ray properties. Appleton et al. (2004) define  $q = \log (f_{24\ \mu\text{m}}/f_{1.4\ \text{GHz}})$ . They show for star-forming galaxies that  $q$  is tightly constrained out to  $z \sim 1$ :  $q = 0.94 \pm 0.23$  after K-correction. Galaxies with values of  $q$  well below this range (strong radio with respect to  $24\ \mu\text{m}$  emission) are unlikely to be dominated by star formation and instead are radio-emitting AGN (Drake et al. 2003).

#### 2.3.1 Sample Selection

Figure 1 illustrates the selection criteria. We set a selection threshold of  $q < 0$  to classify a galaxy as probably having an AGN and require a *Chandra* exposure of  $> 1\ \text{Ms}$  to provide high X-ray sensitivity. This selection identifies 27 radio-excess AGN in the CDFN, as listed in Table 1. Of these, 16 (60%) have no X-ray counterpart in the Alexander et al. (2003) catalog.



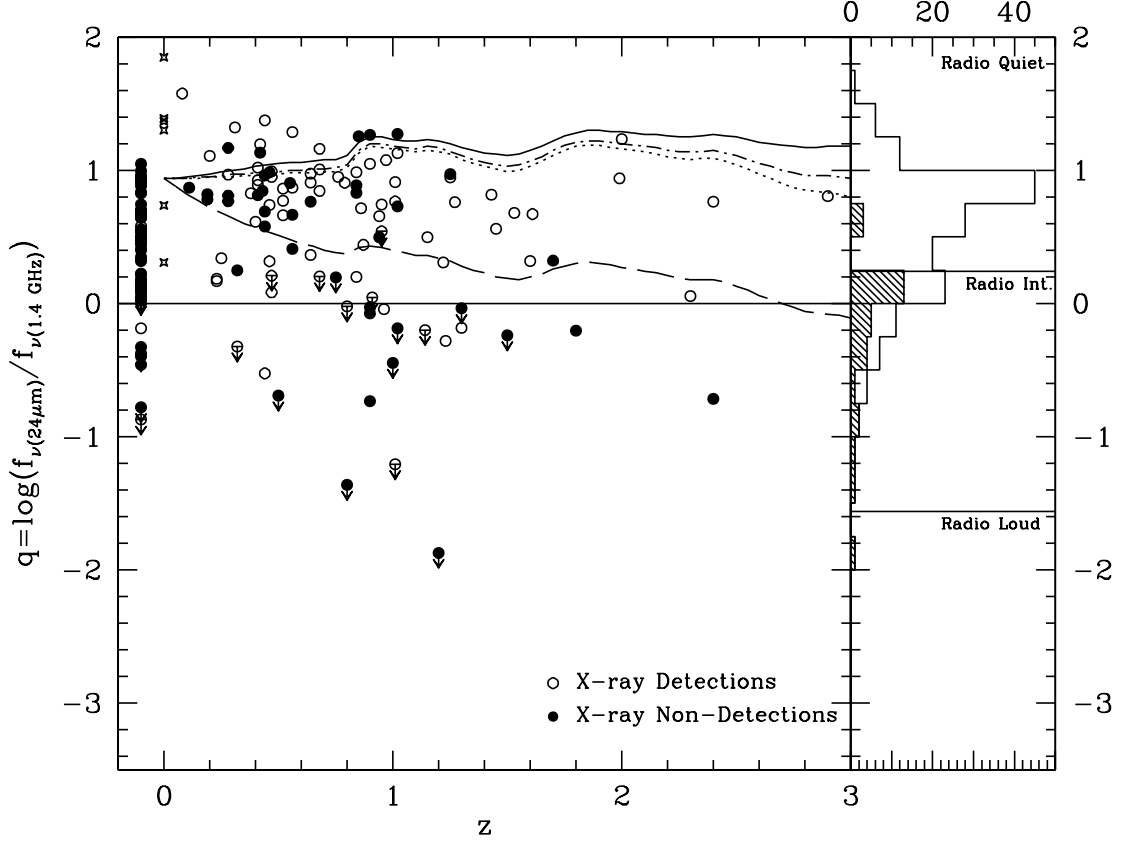


Figure 2.1 Relationship between  $q$  and redshift. All sources without known redshifts have been assigned  $z = -0.1$ . Circles represent all radio sources with X-ray exposures in excess of 1 Ms. Crosses represent the 6 lowest-metallicity galaxies from the Engelbracht et al. (2005) sample. The lines represent the change in the observed  $q$  with redshift for SEDs with LINER (solid), Seyfert 2 (dot-dashed), spiral galaxy (dotted), or ULIRG (dashed) templates, normalized to the best-fit local value of  $q$  as determined by Appleton et al. (2004). The histogram shows the distributions of  $q$  in the radio-quiet, radio-intermediate, and radio-loud regimes, where the shaded histogram represents sources for which we have only upper limits on  $q$ , and the clear histogram gives the distribution of  $q$  for all sources. We define as our radio-excess AGN sample all galaxies with  $q < 0$ .

Table 1. Radio, 24  $\mu\text{m}$ , and X-ray Properties

$\alpha_{2000}$	$\delta_{2000}$	$z$	1.4 GHz flux ( $\mu\text{Jy}$ )	log 1.4 GHz Power ( $\text{erg s}^{-1}$ )	24 $\mu\text{m}$ flux ( $\mu\text{Jy}$ )	log 24 $\mu\text{m}$ Power ( $\text{erg s}^{-1}$ )	X-ray <sup>a</sup> flux ( $\text{erg cm}^2 \text{ s}^{-1}$ )	log X-ray Luminosity ( $\text{erg s}^{-1}$ )	$q$	$q'$	$\alpha$	$\theta$ ( $''$ )	$z$ Ref.
X-ray Weakly-Detected and Non-Detected AGN													
12 35 47.96	62 15 29.2	...	118	...	40.8	...	$<2.28 \times 10^{-16}$	...	-0.46	$>7.1$	...	$<2.1$	...
12 36 10.57	62 16 51.6	1.5	139	40.4	$<80$	$<44.1$	$<1.57 \times 10^{-16}$	$<42.3$	$<-0.24$	$>7.3$	...	2.7	7
12 36 17.57	62 15 40.7	...	200	...	$<80$	...	$1.33 \times 10^{-16}$	...	$<-0.40$	7.5	$>0.55$	$<2.0$	...
12 36 20.28	62 08 44.1	1.02	123	40.0	$<80$	$<43.7$	$2.56 \times 10^{-16}$	42.1	$<-0.19$	7.0	$0.01 \pm 0.07$	$<2.1$	1,2
12 36 23.54	62 16 42.7	...	481	...	$<80$	...	$9.64 \times 10^{-17}$	...	$<-0.78$	8.0	$0.63 \pm 0.07$	$<1.9$	...
12 36 40.15	62 20 37.4	0.8	1840	40.9	$<80$	$<43.5$	$<3.02 \times 10^{-16}$	$<41.9$	$<-1.36$	$>8.1$	...	$<1.9$	7
12 36 40.74	62 10 10.6	1.3	86.8	40.1	$<80$	$<44.0$	$<1.38 \times 10^{-16}$	$<42.1$	$<-0.04$	$>7.1$	$0.44 \pm 0.15$	3.7	7
12 36 46.34	62 16 29.6	0.50	393	39.7	$<80$	$<43.0$	$<1.10 \times 10^{-16}$	$<41.0$	$<-0.69$	$>7.9$	$>1.62$	2.7	1,2
12 37 00.26	62 09 9.8	1.8	324	41.0	203	44.7	$<1.57 \times 10^{-16}$	$<42.5$	-0.20	$>7.7$	$0.89 \pm 0.12$	$<2.0$	7
12 37 08.78	62 22 01.9	...	170	...	$<80$	...	$<6.97 \times 10^{-16}$	...	$<-0.33$	$>6.7$	...	$<2.1$	...
12 37 14.96	62 08 23.5	0.9	1380	40.9	255	44.1	$5.97 \times 10^{-16}$	42.4	-0.73	7.7	$0.15 \pm 0.08$	$<1.9$	7
12 37 17.53	62 08 27.7	0.9	126	39.9	106	43.7	$<3.00 \times 10^{-16}$	$<42.1$	-0.08	$>7.0$	$>0.77$	2.1	7
12 37 25.73	62 11 28.5	1.2	5960	41.8	$<80$	$<43.9$	$1.50 \times 10^{-16}$	42.1	$<-1.87$	9.0	$1.35 \pm 0.06$	5.5	7
12 37 45.73	62 14 56.3	0.9	63.6	39.6	59.4	43.5	$<2.64 \times 10^{-16}$	$<42.0$	-0.03	$>6.7$	...	...	7
12 37 46.60	62 17 38.4	2.4	998	41.8	192	45.0	$<4.22 \times 10^{-16}$	$<43.3$	-0.72	$>7.7$	...	$<1.9$	7
12 37 51.21	62 19 19.1	1.0	223	40.2	$<80$	$<43.7$	$<6.25 \times 10^{-16}$	$<42.5$	$<-0.45$	$>6.9$	...	$<2.0$	7
X-Ray Detected AGN													
12 35 56.05	62 15 55.6	0.44	89.7	38.9	26.8	42.3	$1.31 \times 10^{-14}$	42.9	-0.52	5.2	...	2.5	3
12 36 40.6	62 18 33	1.14	324	40.5	$<205$	$<44.2$	$2.13 \times 10^{-16}$	42.2	$<-0.20$	7.5	$>0.8$	$<2.0$	1
12 36 42.09	62 13 31.4	...	467	...	197	...	$2.76 \times 10^{-16}$	...	-0.37	7.6	$0.94 \pm 0.06$	2.2	4,5
12 36 44.39	62 11 33.1	1.01	1290	41.0	$<80$	$<43.7$	$2.44 \times 10^{-16}$	42.1	$<-1.21$	8.1	$0.3 \pm 0.05$	12	1,2
12 36 46.34	62 14 4.7	0.96	179	40.1	162	44.0	$2.46 \times 10^{-14}$	44.0	-0.04	5.2	$-0.04 \pm 0.06$	$<2.0$	1,2
12 36 52.92	62 14 44.0	0.32	168	38.9	$<80$	$<42.5$	$4.63 \times 10^{-16}$	41.2	$<-0.32$	6.9	$-0.12 \pm 0.07$	2.5	1,2
12 36 59.15	62 18 32.8	...	506	...	329	...	$8.76 \times 10^{-16}$	...	-0.19	7.1	$0.26 \pm 0.07$	$<2.0$	...
12 37 1.10	62 21 9.6	0.8	304	$<40.1$	$<289$	$<44.0$	$3.22 \times 10^{-16}$	42.0	$<-0.02$	7.3	...	$<2.0$	1,2
12 37 9.94	62 22 58.9	1.23	708	40.9	370	44.6	$5.21 \times 10^{-15}$	43.6	-0.28	6.5	...	$<1.9$	6
12 37 13.87	62 18 26.5	...	595	...	$<80$	...	$1.69 \times 10^{-15}$	...	$<-0.87$	6.9	$>0.92$	$<1.9$	...
12 37 21.25	62 11 30.0	1.3	382	40.7	250	44.5	$5.09 \times 10^{-16}$	42.7	-0.18	7.2	$-0.28 \pm 0.06$	0.9	7

Because of the lack of spectral information, we have chosen not to K-correct our radio and infrared flux densities and instead illustrate in Figure 1 the redshift evolution of  $q$  for galaxies with LINER, Seyfert 2, spiral galaxy, and ultra-luminous infrared galaxy (ULIRG) templates, normalized to the best-fit value of Appleton et al. (2004). Templates were taken from Devriendt et al. (1999). A spectral index of  $\alpha = 0.7$  ( $S_\nu \propto \nu^{-\alpha}$ ) was assumed for the radio continuum. For the LINER, Seyfert 2, and spiral templates, the observed  $q$  is slightly larger than the intrinsic value out to redshifts of  $z \geq 2.7$ . Redshifting a ULIRG SED causes the observed  $q$  to drop below the intrinsic value as  $z$  increases.

Because we have not K-corrected our flux densities, we use the slightly higher non K-corrected dispersion,  $\sigma = 0.28$ , from Appleton et al. to calculate the significance of our selection threshold at  $z = 0$ . Our selection threshold of  $q < 0$  is 3.4 standard deviations below the average value of  $q$  at  $z = 0$ , and therefore our sample should not be significantly contaminated with normal star-forming galaxies. The significance of our selection at  $z > 0$  depends on each object's individual SED, and will increase slightly for LINERS, Seyfert 2's and spirals, but decrease for ULIRGS. We estimate the maximum error on the measured values of  $q$  by assuming both a radio and infrared flux density of  $80 \mu\text{Jy}$ , the approximate limits of our survey. This corresponds to a  $5\sigma$   $24 \mu\text{m}$  detection and a  $10\sigma$  radio detection and gives an error of 0.1 on  $q$ ; we therefore do not expect our sample to be strongly affected by errors in the flux determination. The crowded nature of several of the fields implies that some of our sources may have blended  $24 \mu\text{m}$  emission. This will cause  $q$  to increase, however, and will therefore remove sources from our radio excess sample instead of introducing contaminants.

Yun et al. (2001) define radio-excess objects as those with radio emission exceeding the radio/FIR correlation prediction by a factor of  $\geq 5$  (a behavior here-

Table 1—Continued

$\alpha_{2000}$	$\delta_{2000}$	z	1.4 GHz flux ( $\mu\text{Jy}$ )	log 1.4 GHz Power ( $\text{erg s}^{-1}$ )	24 $\mu\text{m}$ flux ( $\mu\text{Jy}$ )	log 24 $\mu\text{m}$ Power ( $\text{erg s}^{-1}$ )	X-ray <sup>a</sup> flux ( $\text{erg cm}^2 \text{ s}^{-1}$ )	log X-ray Luminosity ( $\text{erg s}^{-1}$ )	$q$	$q'$	$\alpha$	$\theta$ ( $''$ )	z Ref.
-----------------	-----------------	---	---------------------------------------	---	--	--	--	--	-----	------	----------	----------------------	--------

<sup>a</sup>5 $\sigma$  upper limits are given for all AGN that were not weakly-detected in the X-ray (see §5.3)

References. — (1) Cowie et al. 2004 (Hawaii); (2) Wirth et al. 2004 (TKRS); (3) Barger et al. 2002; (4) Waddington et al. 1999; (5) Barger et al. 2000; (6) Barger et al. 2003 (photometric); (7) our photometric estimate

after described as a radio excess by a factor of 5). From the measurement of this correlation by Appleton et al. (2004), the corresponding threshold would be  $q < 0.24$  at  $z = 0$ . At  $z = 1$ , the radio-excess threshold ranges from  $q = 0.46$  to  $q = 0.53$  for LINER, Seyfert 2, or spiral galaxy templates. For all these cases, our selection criterion of  $q < 0$  (which corresponds to a radio excess of 8.7) isolates radio-excess AGN. For a ULIRG template, the radio-excess threshold is  $-0.30$  at  $z = 1$ ; a  $q$  of 0 for such a template at  $z = 1$  corresponds to a radio excess of 2.5, half the AGN threshold suggested by Yun et al. (2001). As will be discussed in §4, however, a small fraction of the sources in our sample have ULIRG SEDS, and all are likely to be AGN.

Following Drake et al. (2003), radio-loud objects would have  $q < -1.6$  at  $z = 0$ ; since few sources fall in this range, the AGN sample consists almost entirely of radio-intermediate sources, as illustrated in the histogram inset in Figure 1.

### 2.3.2 Potential Sources of Contamination

At high redshift, the  $24\ \mu\text{m}$  emission of normal star-forming galaxies is dominated by PAH features, which are absent at low metallicity (e.g., Houck et al. 2004, Engelbracht et al. 2005). As Figure 1 demonstrates, however, low metallicity star-forming galaxies also tend to have  $q > 0$  and therefore they should not contaminate our radio-excess AGN sample.

Nearly all star-forming galaxies in the field fit the radio/infrared correlation. Even within dense galaxy clusters, where environmental effects might boost the radio emission, the relation holds well with only a tiny minority of galaxies having radio excesses as large as a factor of five (Miller & Owen 2001). Bressan et al. (2002) show that a radio excess is expected in post-starburst galaxies due to the slower fading time of the radio emission with respect to the FIR; their models predict a maximum radio enhancement of  $\sim 5$  above the radio/FIR correlation.

As mentioned above, our selection criterion selects AGN whose radio enhancements exceed a factor of  $\sim 9$  in LINER, Seyfert 2, and spiral galaxy templates. We therefore expect minimal contamination from post-starburst galaxies.

The strong silicate absorption feature seen in a handful of ULIRGS is another potential source of sample contamination. This feature is centered at  $9.7 \mu\text{m}$  and would therefore be redshifted into our  $24 \mu\text{m}$  band at redshifts of  $z \sim 1.2 - 1.5$ , where it could suppress the observed infrared flux density. Four of the X-ray non-detected radio-excess sample have redshifts in this range.

It is unlikely, however, that a large fraction of AGN are affected in this way. The  $12 \mu\text{m}$  flux of AGN provides the best estimate of their bolometric luminosity, allowing for effective infrared selection (Spinoglio & Malkan 1989). The silicate absorption feature is within the IRAS  $12 \mu\text{m}$  passband, and evidently has only a secondary effect on the luminosity estimate. In fact,  $\sim 50\%$  of high-luminosity AGN have silicate *emission* features (Hao et al. 2005). In such cases, the  $q$  of true AGN will be shifted towards the star-forming range, resulting in incompleteness in our sample, but not contamination.

### 2.3.3 Sample Completeness

Because the 95% completeness limit of the radio sample is equal to the upper limit we can place on the flux densities of non-detected  $24 \mu\text{m}$  sources,  $80 \mu\text{Jy}$ , restricting the radio flux densities to  $S_\nu > 80 \mu\text{Jy}$  would provide a 95% complete radio-excess ( $q < 0$ ) sample (subject to the cautions mentioned above). While we do not apply a radio flux-density cut for the sample discussed in this paper, only one AGN in our sample, an X-ray non-detected source, has a radio flux density that falls below this limit. In addition, the counterpart uncertainties and  $24 \mu\text{m}$  blending discussed in §2 only led to the removal of one source that could fall into such a complete sample. Therefore, if we were to define a complete sample by

requiring that  $S_\nu > 80 \mu\text{Jy}$ , our sample would essentially remain the same. Also, in §2 we estimated that up to 3 radio-excess AGN would be removed from our sample due to chance coincidences with  $24\mu\text{m}$  sources; this process will reduce the sample size but have no other effect. Thus, we can say that for a sample of 27 radio-excess objects in the CDFN (with X-ray exposures in excess of 1 Ms) that is sufficiently complete to be largely unbiased for this class of AGN, 16 (60%) sources are previously uncataloged as AGN. The remainder of this paper probes the characteristics of these objects in more detail.

## 2.4 Redshifts

Spectroscopic redshifts for 8 AGN, and photometric redshifts for an additional 2, were taken from the literature (Barger et al. 2002, Cowie et al. 2004, Wirth et al. 2004 (TKRS)). The redshifts are tabulated in Table 1 and Figure 1. All but one of the AGN for which Team Keck Redshift Survey (TKRS) spectra are available appear to be early-type galaxies with no obvious signs of nuclear activity in the optical/UV. The remaining source, VLA 123646+621404, is X-ray detected and has weak narrow emission lines.

For most of the remaining AGN in our sample, we estimated redshifts photometrically by fitting the Devriendt et al. (1999) templates to the galaxy optical through MIR spectral energy distributions (SEDs). SED fitting was conducted both by an automated fitting routine and by eye; the two methods give results consistent to within the errors quoted below. The SEDs of all radio-excess AGN in our sample are shown in Figure 2. Pérez-González et al. (2005) provide further details on use of Spitzer and other data to obtain photometric redshifts. The redshifted SED fits are in good agreement with spectroscopic redshifts in all cases where spectroscopic data are available. We are able to find or estimate

redshifts for 12 of the 16 X-ray non-detected AGN and for 8 of the 11 X-ray detected AGN. The typical errors in our photometric redshift determinations are  $\Delta(z)/(1+z) < 0.1$  (see Pérez-González et al. 2005). The mean redshifts of the X-ray non-detected and X-ray detected AGN samples are  $z = 1.2$  and  $z = 0.9$ , with dispersions of 0.5 and 0.4, respectively.

Source VLA J123642+621331 has a published redshift of  $z = 4.42$ , based on a single emission line believed to be  $\text{Ly}\alpha$  (Waddington et al. 1999). The validity of this measurement has been questioned by Barger et al. (2000). In addition, none of the Devriendt et al. templates are able to fit the global SED, so we do not assign a redshift to this source.

The Devriendt et al. templates used to obtain photometric redshifts are comprised of spirals, LINERS, Seyfert 2's, starbursts, and ULIRGS. Of the X-ray non-detected AGN, 9 are best-fit by LINER or Seyfert 2 templates, 2 have ULIRG templates, and 1 appears to be a spiral galaxy. Six of the X-ray detected AGN are best-fit by LINER or Seyfert 2 templates; the remaining 2 are ULIRGS.

With redshifts and fitted SED templates for most of the sample, we can test the robustness of our original  $q < 0$  selection. Using the best-fit Devriendt et al. SED templates and the radio spectral slopes from Richards et al. (2000), we estimate the K-corrected radio excesses for the 20 sources with estimated redshifts. All but 1 of the X-ray non-detected AGN (with known redshifts) have radio excesses well above both the Yun et al. “radio-excess” definition of 5 and our  $q < 0$  selection, which is equivalent to a radio excess of  $\sim 9$ . The remaining source has a radio excess of 4 and thus should also be dominated by AGN radio emission. Similarly, 6 of the 8 X-ray detected AGN with known redshifts have radio excesses greater than 10; an additional source has a radio excess of 4, and therefore is likely to be AGN-dominated. The remaining source has a radio excess of only



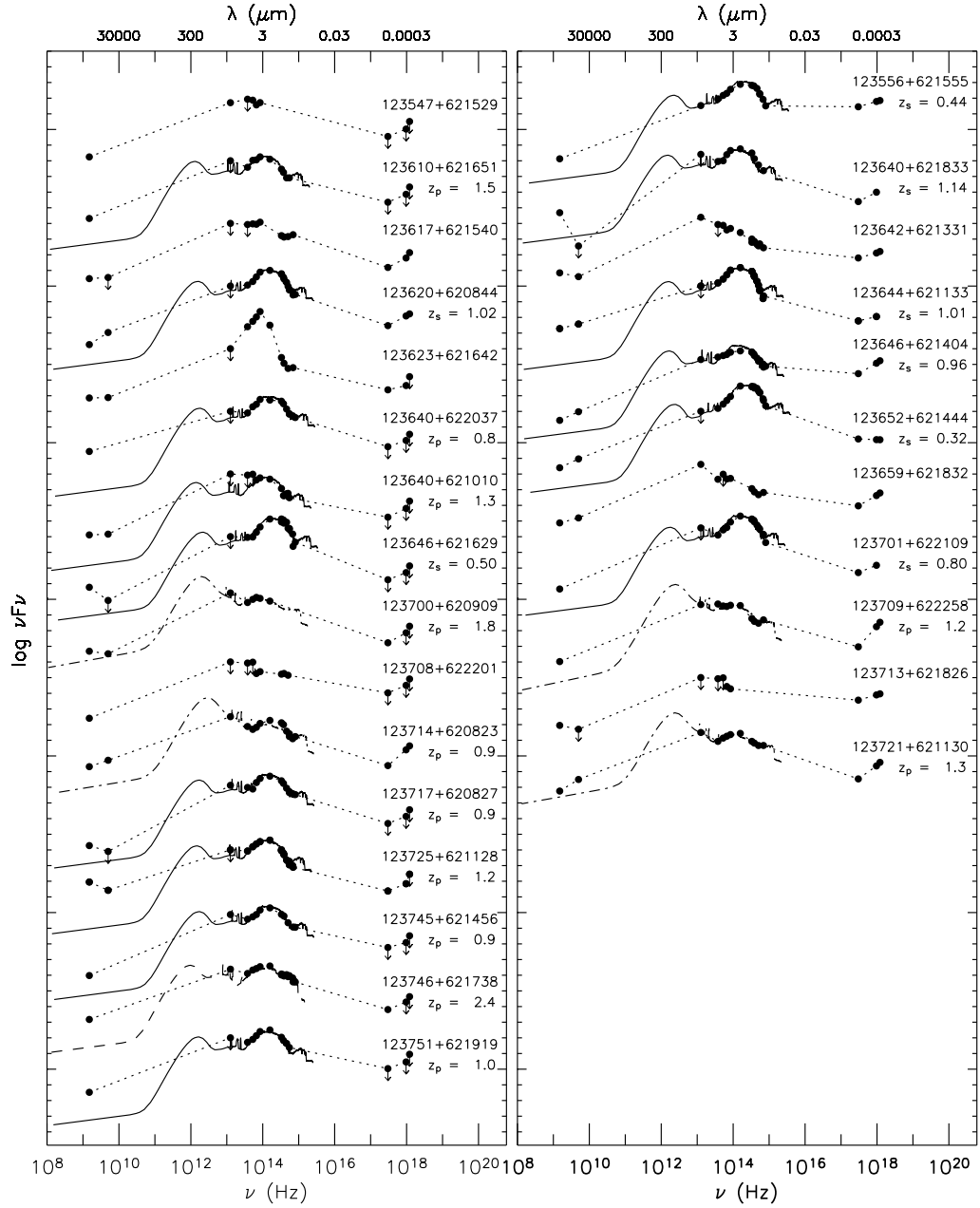


Figure 2.2 Observed-frame SEDs of the radio-excess AGN. Sources with weak or non-detected X-rays are plotted in the left panel, and sources with high-significance X-ray detections are plotted in the right panel. We list VLA source IDs and photometric ( $z_p$ ) or spectroscopic ( $z_s$ ) redshifts. Templates were taken from Devriendt et al. (1999). Seyfert 2 and LINER templates are given by solid lines. Dot-dashed lines represent ULIRG templates, and dashed lines represent spiral templates. Large ticks along the y-axis represent a interval of 10 in  $\log \nu F_\nu$ .

1.3. This source, VLA 123721+621130, is best-fit by a ULIRG template, has an inverted radio spectrum,  $\alpha = -0.28$ , a very hard X-ray photon index,  $\Gamma = 0.28$ , and an absorbed X-ray luminosity of  $\log L_{0.5-8 \text{ keV}} = 42.7$ , all of which indicate the presence of an AGN. We therefore do not remove it from our sample.

## 2.5 X-ray Detection and Coaddition

Although the X-ray non-detected AGN all fall below the Alexander et al. (2003) *Chandra* detection limit, detection to lower significance is possible now that source positions are known *a priori*. We test for X-ray emission by comparing the X-ray counts measured at the positions of our radio sources to the local X-ray background distributions. Four of the X-ray non-detected AGN were excluded from this analysis, as they are separated from known X-ray sources by less than 2 times their 95% encircled energy radii (EER), and are therefore likely to be contaminated. We find signals for 7 of the 12 remaining X-ray “non-detected” AGN at significance levels of 2.5 to 5.2  $\sigma$ . For the remaining 5 sources, we use a stacking analysis to constrain the average flux. We give details of these measurements below.

### 2.5.1 X-ray Detection

To search for X-ray signal from each of the X-ray non-detected AGN, we first extract the total number of X-ray counts within the 60%, 70%, and 80% EER centered on the radio position, using the CDFN 2 Ms image provided by Alexander et al. (2003). The average source exposure time is similarly extracted from the X-ray exposure maps. The EER for the full (0.5-8 keV), hard (2-8 keV), and soft (0.5-2 keV) X-ray bands were calculated using the MKPSF task in CIAO<sup>3</sup>, from which we created an exposure-weighted average PSF for each source, taking into account the

---

<sup>3</sup>*Chandra* Interactive Analysis of Observations (CIAO), <http://cxc.harvard.edu/ciao/>

sources' positions on the ACIS-I detector during each of the 20 CDFN observations<sup>4</sup>. We assume a photon index of  $\Gamma = 1.4$  when calculating the EER, though we have verified that changing this to  $\Gamma = 1.0$  negligibly affects the results.

We use a Monte-Carlo simulation similar to that of Brandt et al. (2001) to estimate the local sky background in the 3 X-ray bands and 3 apertures. For each source, we first choose a random position that (1) lies within  $1'$  of the radio source, (2) does not overlap with the source aperture, (3) is a minimum distance of 2 times the source's 95% EER from any cataloged X-ray source, and (4) has an exposure time that differs from the source exposure time by less than 50%. The final condition is set to minimize the effect of large gradients in exposure on our local sky background distributions. To determine the sky background distributions, we measure the sky counts at this random position using the 3 source apertures. We repeat 10,000 times.

Before fitting the sky distributions for each band and EER, we normalize the counts to the source exposure time. We then fit a Poisson distribution to the resulting distributions of normalized background counts, from which we measure the mean sky background. The dispersion of the sky background determines the likelihood of measuring by chance the observed number of counts in an aperture centered on the radio source. We define as "weakly-detected" all sources at  $> 2\sigma$  above the background in at least 1 of the 3 *Chandra* energy bands, and in at least 1 of the 3 apertures. Although we require only a  $> 2\sigma$  detection, all 7 of the weakly-detected sources are at  $> 2.5\sigma$  in at least one of the 3 bands, and 2 are detected to  $\geq 5\sigma$ . In Table 2, we give the X-ray properties of all X-ray weakly-detected AGN. For each source and energy band, we list the results for the aperture (60%

---

<sup>4</sup>At intermediate to large off-axis angles, the CXC PSF libraries crop a small fraction (5-10%) of the X-ray flux, affecting the determination of the EER. We do not attempt to correct for this effect, as the PSFs of the weakly-detected sources are undersampled.

EER, 70% EER, or 80% EER) with the highest detection significance. To illustrate our detection method, we show in Figure 3 the X-ray background distribution for VLA J123617+621450, along with the source signal, which corresponds to a  $3\sigma$  detection.

To calculate the X-ray flux from the aperture-corrected count rate, we first need to know the X-ray photon index,  $\Gamma$ . If a given source is detected to  $\geq 2\sigma$  in both the hard and soft X-ray bands, the photon index is estimated from the ratio of the hard to soft count rates,  $H/S$ . If a source is not detected to  $\geq 2\sigma$  in both the hard and soft bands, we assume that  $\Gamma = 1.4$ . Although  $\Gamma$  spans a fairly wide range of values for the sources where it can be estimated, the derived fluxes should only be weakly dependent on the value adopted. For consistency, we use the *Chandra* 2 MS Catalog  $H/S$  to  $\Gamma$  and X-ray count rate to X-ray flux conversions (Alexander et al. 2003). For comparison with the cataloged fluxes, we do not correct the X-ray fluxes for Galactic absorption. The quoted X-ray flux ratios, however, have been corrected for Galactic absorption of column density  $N_{\text{H}} = 1.6 \times 10^{20} \text{ cm}^{-2}$  (Stark et al. 1992).

If a weakly-detected AGN does not have a  $\geq 2\sigma$  detection in one or more of the 3 X-ray bands, we quote in Table 2 conservative  $2\sigma$  upper limits on the count rate and flux. Upper limits were calculated by adding any positive net source counts to 2 times the sky dispersion.

### 2.5.2 X-ray Coaddition

For the five sources that are undetected and also a minimum distance of 2 times their 95% EER from the nearest cataloged X-ray source, we determine limits on the X-ray flux by coaddition. Individual source counts are measured as described above, and are then summed to provide the total number of counts from our stacked source. We similarly construct the coadded sky background distribution

Table 2. X-ray Properties of X-ray Weakly-Detected AGN

Source	$z$	Nearest X-ray Source <sup>a</sup>	Band	EER (%)	Detection $\sigma$	Aperture Corrected Count Rate ( $\text{s}^{-1}$ )	$H/S$	$\Gamma$	Flux ( $\text{erg s}^{-1} \text{cm}^{-2}$ )	Hard/Soft Flux Ratio	$N_{\text{H}}$ ( $\text{cm}^{-2}$ )	Abs. Corrected $\log L_{0.5-8 \text{ keV}}$ ( $\text{erg s}^{-1}$ )	$q'_{\text{corr}}$
VLA J123617+621540	...	20.4(4.3)	Full	70	3.1	$7.06 \times 10^{-06}$	1.5	0.47	$1.33 \times 10^{-16}$	8.6	$(5.0 \times 10^{22} - 5.6 \times 10^{23})$	(41.4-43.2)	7.2-7.0
			Hard	80	2.5	$6.14 \times 10^{-06}$			$1.76 \times 10^{-16}$			(41.3-43.1)	
			Soft	60	3.9	$4.15 \times 10^{-06}$			$1.99 \times 10^{-17}$			(41.3-43.1)	
VLA J123620+620844	1.02	29.5(5.6)	Full	60	3.6	$1.60 \times 10^{-05}$	1.0	0.80	$2.56 \times 10^{-16}$	5.4	$6.8 \times 10^{22}$	42.4	6.5
			Hard	60	2.1	$8.02 \times 10^{-06}$			$2.12 \times 10^{-16}$			42.1	
			Soft	60	3.5	$7.79 \times 10^{-06}$			$3.78 \times 10^{-17}$			42.1	
VLA J123623+621642	...	14.3(3.1)	Full	60	3.6	$8.27 \times 10^{-06}$	<0.7	>1.09	$9.64 \times 10^{-17}$	<3.3	$(<1.8 \times 10^{22} - <1.8 \times 10^{23})$	(<41.2-<42.9)	>7.9->7.7
			Hard	70	0.9	$<4.56 \times 10^{-06}$			$<1.05 \times 10^{-16}$			(<41.0-<42.8)	
			Soft	60	5.2	$6.12 \times 10^{-06}$			$3.07 \times 10^{-17}$			(<41.0-<42.8)	
VLA J123700+620909	1.8	31.2(5.9)	Full	60	0.7	$<5.36 \times 10^{-06}$	<1.3	>0.60	$<6.25 \times 10^{-17}$	<5.7	$<1.9 \times 10^{23}$	<42.4	>7.8
			Hard	80	-0.7	$<5.57 \times 10^{-06}$			$<1.28 \times 10^{-16}$			<42.5	
			Soft	70	2.5	$4.33 \times 10^{-06}$			$2.17 \times 10^{-17}$			<42.5	
VLA J123714+620823	0.9	27.2(3.7)	Full	60	5.0	$2.46 \times 10^{-05}$	2.7	-0.06	$5.97 \times 10^{-16}$	17.7	$1.6 \times 10^{23}$	42.8	7.1
			Hard	60	4.2	$1.82 \times 10^{-05}$			$5.91 \times 10^{-16}$			42.5	
			Soft	60	2.8	$6.83 \times 10^{-06}$			$3.26 \times 10^{-17}$			42.5	
VLA J123725+621128	1.2	31.1(5.4)	Full	80	2.9	$1.29 \times 10^{-05}$	<1.4	>0.53	$1.50 \times 10^{-16}$	<6.1	$<1.0 \times 10^{23}$	<42.4	>8.8
			Hard	70	1.5	$<8.52 \times 10^{-06}$			$<1.96 \times 10^{-16}$			<42.2	
			Soft	80	2.8	$6.15 \times 10^{-06}$			$3.08 \times 10^{-17}$			<42.2	
VLA J123746+621738	2.4	44.1(5.2)	Full	60	1.8	$<1.69 \times 10^{-05}$	<0.7	>1.12	$<1.97 \times 10^{-16}$	<3.2	$<1.6 \times 10^{23}$	<43.2	>7.7
			Hard	80	0.0	$<1.18 \times 10^{-05}$			$<2.72 \times 10^{-16}$			<43.1	
			Soft	70	4.1	$1.65 \times 10^{-05}$			$8.27 \times 10^{-17}$			<43.1	

<sup>a</sup>Nearest X-ray source in arcseconds and ratio of this distance to the hard-band 95% encircled energy aperture radius

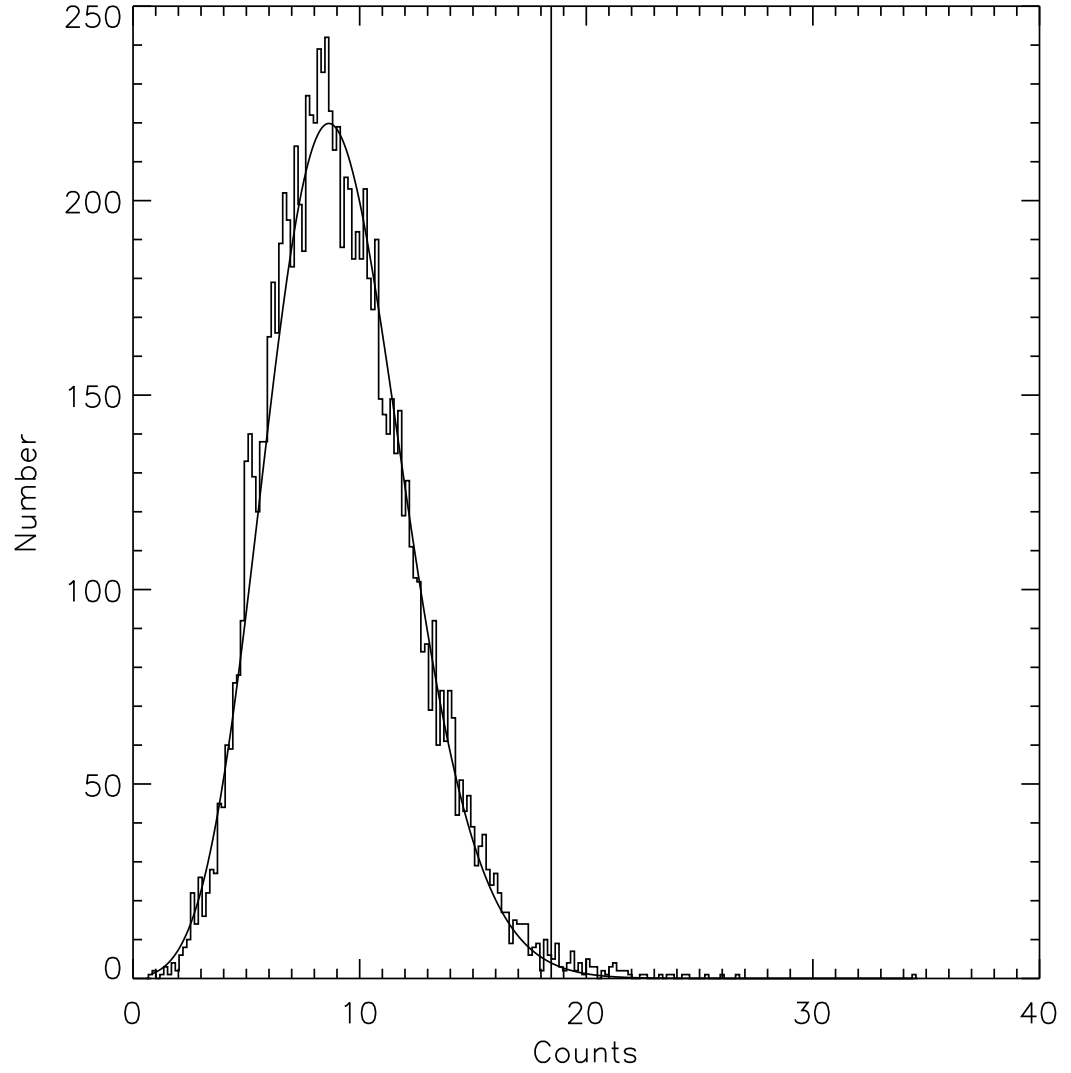


Figure 2.3 X-ray background distribution for source VLA J123617+621540 in the full X-ray band (0.5-8 keV). The counts have been normalized to the source exposure time. The Poisson fit to the background distribution is shown. The vertical line indicates the total number of counts obtained at the source position, and corresponds to a  $3\sigma$  detection.

Table 3. Limits on the X-ray flux of 5 X-ray Non-Detected AGN

Band	$2\sigma$	$5\sigma$	$2\sigma$ Individ.	$5\sigma$ Individ.
	Flux Limit	Flux Limit	Flux Limit	Flux Limit
	(erg s <sup>-1</sup> cm <sup>-2</sup> )	(erg s <sup>-1</sup> cm <sup>-2</sup> )	(erg s <sup>-1</sup> cm <sup>-2</sup> )	(erg s <sup>-1</sup> cm <sup>-2</sup> )
Full	$<4.11 \times 10^{-16}$	$<8.42 \times 10^{-16}$	$<8.23 \times 10^{-17}$	$<1.68 \times 10^{-16}$
Hard	$<6.50 \times 10^{-16}$	$<1.41 \times 10^{-15}$	$<1.30 \times 10^{-16}$	$<2.81 \times 10^{-16}$
Soft	$<8.32 \times 10^{-17}$	$<1.79 \times 10^{-16}$	$<1.66 \times 10^{-17}$	$<3.59 \times 10^{-17}$

by adding the individual sky backgrounds from each of the 10,000 trials.

We list in Table 3 the X-ray properties of the coadded source. Because the detection significance for all 3 X-ray bands is  $< 1\sigma$ , we list conservative  $2\sigma$  and  $5\sigma$  upper limits on the count rates and fluxes, calculated as described above. We also list  $2\sigma$  and  $5\sigma$  upper limits on the flux for a “typical” one of these five sources by assuming that an equal amount of flux is coming from each of the sources that contributed to the coaddition.

### 2.5.3 X-ray Upper Limits

For all AGN that are not X-ray detected at full band to greater than  $2\sigma$ , including those that are close to a known X-ray source, we set conservative  $5\sigma$  upper limits on the X-ray flux by adding any positive source flux to a  $5\sigma$  limit on the local X-ray background, computed as described above. We use an aperture equal to the 70% EER to measure both the source and background counts. These  $5\sigma$  X-ray upper limits are used throughout the rest of the paper.

#### 2.5.4 Column Densities

The column densities to the X-ray detected AGN are given in Table 4. To estimate the column density, we assume that AGN have an intrinsic non-absorbed photon index of  $\Gamma = 2$  (e.g., George et al. 2000). We do not include a Compton reflection component in our intrinsic spectral model because of possible dependencies of its strength on luminosity, radio-loudness, and optical Seyfert type (e.g., Lawson & Turner 1997, Reeves & Turner 2000, Zdziarski et al. 1995, Zdziarski et al. 2000). These reflection components have been shown to be important in fitting the peak of the X-ray background (XRB; see Ueda et al. 2003). If a Compton reflection component is added via the ‘pexrav’ model in XSPEC (Magdziarz & Zdziarski 1995), assuming a solid angle of  $2\pi$ , a cutoff energy of  $E_c = 500$  keV, an inclination angle of  $\cos i = 0.5$ , and solar abundance, the computed column densities decrease by an average of 20%.

Excluding upper limits, the column densities of the X-ray-detected AGN range from  $N_H = 1.0 \times 10^{22} \text{ cm}^{-2}$  to  $N_H = 3.7 \times 10^{23} \text{ cm}^{-2}$ , and are therefore consistent with our definition of obscured AGN. One additional AGN for which we were unable to estimate  $N_H$  (due to an observed photon index,  $\Gamma = 2.1$ , that is softer than our assumed photon index) is likely to be relatively unobscured. All of the columns fall below the Compton-thick limit ( $N_H > 10^{24} \text{ cm}^{-2}$ ). If we correct for the Compton-reflection component, 2 of the 11 X-ray detected AGN (20%) are likely to be unobscured.

We list in Table 2 intrinsic column densities for all weakly-detected AGN. For the two X-ray weakly-detected AGN with known flux ratios and redshifts, we calculate column densities of  $N_H = 6.8 \times 10^{22} \text{ cm}^{-2}$  and  $N_H = 1.6 \times 10^{23} \text{ cm}^{-2}$ . We place upper limits on the X-ray column densities of the remaining X-ray weakly-detected AGN. If we have no redshift estimate for a given source, we calculate



the column density at redshifts of  $z = 0.5$  and  $z = 2.5$ , the approximate upper and lower redshift bounds of the sources in our sample. All of the column densities fall below the Compton-thick limit.

In Figure 4, we compare the column density distributions of the X-ray detected and weakly-detected AGN. The column densities for AGN with known redshifts *and* flux ratios are given by cross-hatched histograms. Clear histograms give the column densities for all AGN with known redshifts, including those with upper limits on the flux ratio, and therefore on the column density. There is significant overlap between the 2 samples. The X-ray non-detected AGN are likely to have higher column densities than the weakly-detected sample; if so, there would be a stronger offset between the X-ray detected and X-ray weakly- and non-detected samples.

### 2.5.5 Compton-thick AGN

Approximately 50% of Seyfert 2 galaxies in the local Universe are Compton-thick (Risaliti et al. 1999); if we assume a Seyfert 2 to Seyfert 1 ratio of 4:1, the Compton-thick fraction of all local Seyferts is  $\sim 40\%$ . In the more distant Universe, XRB population synthesis models predict that  $\sim 30\%$  of AGN with  $N_H < 10^{25} \text{ cm}^{-2}$  have column densities of  $N_H = 10^{24} - 10^{25} \text{ cm}^{-2}$  (Comastri et al. 2001). Ueda et al. (2003) similarly find that current measurements of the XRB are consistent with roughly equal numbers of Compton-thick AGN with  $N_H = 10^{24} - 10^{25} \text{ cm}^{-2}$  and obscured AGN with  $N_H = 10^{23} - 10^{24} \text{ cm}^{-2}$ . This ratio is slightly lower than that in local Universe, where there are 1.6 times as many Seyfert 2's with  $N_H > 10^{24} \text{ cm}^{-2}$  as Seyferts 2's with  $N_H = 10^{23} - 10^{24} \text{ cm}^{-2}$  (Risaliti et al. 1999).

We therefore expect that as many as  $\sim 25 - 40\%$  of the AGN in our radio-selected sample could be Compton-thick. Of the 27 radio-excess AGN, we have placed constraints on the column densities of 13, and have estimated constraints

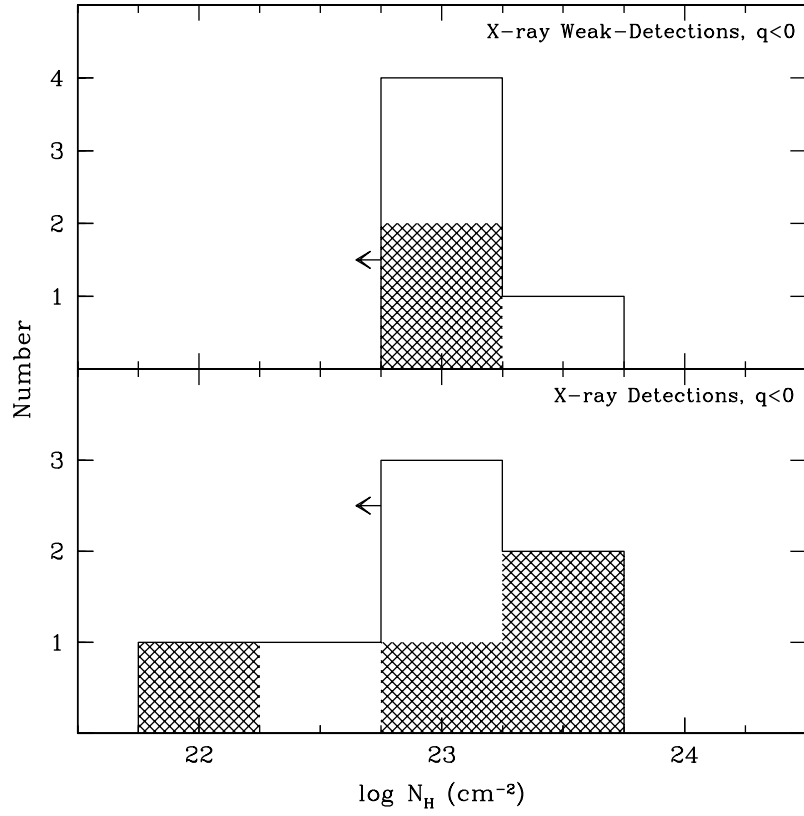


Figure 2.4 Rest-frame column densities measured using the X-ray flux ratios and redshifts of the X-ray weakly-detected and X-ray detected radio-excess AGN samples. The clear histograms represent all sources, including those for which we have only upper limits on  $N_H$ . The cross-hatched histograms represent only those sources with known  $N_H$ .

for a further 5 for which no redshift is available. All sources have column densities that fall below the Compton-thick limit. Of the remaining sources in the sample, 5 are X-ray non-detected, and 4 are too close to a known X-ray source to test for low-significance emission. If we assume that (like the sources for which we could test for X-ray emission)  $3/4$  of the latter would be X-ray detected, 6 sources in our sample of 27 (22%) could be Compton-thick. This estimate will improve as we increase our sample by extending the current study to additional fields.

## 2.6 Interpretation

There is direct evidence, from the determination of X-ray column densities discussed above, that at least several of the X-ray weakly-detected AGN are highly obscured. It appears, however, that many of the X-ray detected AGN also have high column densities. To better understand these two samples, and their relation to one another, we discuss below their radio properties, their X-ray, radio, and infrared luminosity distributions, and the ratios of their X-ray to radio and X-ray to optical emission.

### 2.6.1 Radio Extent and Spectral Shape

We give in Table 1 the spatial extent of the radio emission,  $\theta$ , as determined by Richards et al. (2000). Of the 27 sample members, 1 has no listed extent, 16 are unresolved, and 10 are resolved. There is no significant difference with X-ray flux in the degree of resolution, at least in this small sample. The most highly resolved sources, VLA J123644+621133 and J123725+621128, also have high 1.4 GHz luminosities and very low values of  $q$ . It is likely that the large radio spatial extent of these sources is due to powerful radio jets oriented approximately in the plane of the sky. If this is the case, the AGN torus would be oriented edge-on, a con-

dition that would lead to high X-ray obscuration. Nonetheless, the absorption levels of  $N_{\text{H}} < 2.0 \times 10^{22} \text{ cm}^{-2}$  and  $N_{\text{H}} < 2.0 \times 10^{23} \text{ cm}^{-2}$ , respectively, are not exceptionally large. It follows that if the unresolved X-ray weakly- or non-detected AGN are also viewed close to edge-on, as we would expect, they must not have strong extended radio jets. This is not surprising, however, as all but 1 of these AGN (the exception being VLA J123725+621128) have  $q$  values that fall short of the radio-loud definition of Yun et al. (2001).

We also list in Table 1 radio spectral slopes for the 17 radio-excess AGN observed at 8.5 GHz by Richards et al. (1998). Following Richards et al. (2000), we define flat spectrum sources as those with  $\alpha < 0.5$  and steep spectrum sources as those with  $\alpha > 0.5$ . Flat spectral slopes are expected for AGN in which synchrotron self-absorption is important. Steep-spectrum emission with a slope of  $\alpha = 0.7$  is generally associated with optically thin synchrotron radiation. Of the X-ray weakly- or non-detected AGN, 3 are flat spectrum and 6 are steep spectrum. Five of the X-ray detected AGN are flat spectrum; 3 are steep spectrum. No obvious trend is seen, although the X-ray detected AGN may generally have flatter spectral slopes ( $-0.28 < \alpha < 0.94$ ) than the X-ray non-detected AGN ( $0.01 < \alpha < 1.62$ ). This is consistent with a picture in which our viewing angle to the X-ray detected AGN is aligned closer to the jet axis, resulting in more core-dominated, and therefore flatter, radio emission.

## 2.6.2 Radio, 24 $\mu\text{m}$ , and X-ray Luminosities

The 1.4 GHz radio powers,  $P_{1.4 \text{ GHz}} = \nu F_{\nu}$ , of the radio-excess sample are shown in Figure 5. Because radio emission is not affected by obscuration, the radio power is a measure of the intrinsic power of the sample. The X-ray weakly- or non-detected and X-ray detected AGN span similar ranges of  $P_{1.4 \text{ GHz}}$ , although the 2 most radio-luminous AGN have been missed in the X-ray. We do not have

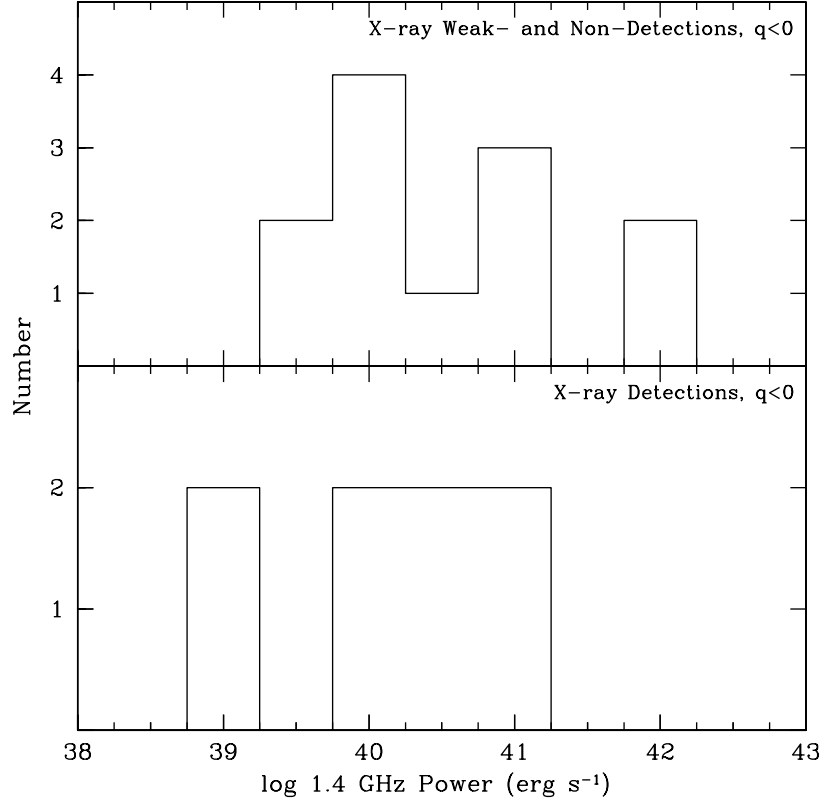


Figure 2.5 1.4 GHz radio powers of the radio-excess AGN sample.

redshift estimates for 4 of the X-ray weakly- or non-detected AGN and 3 of the X-ray detected AGN; the true power distributions are therefore likely to differ slightly from those presented here.

Within the limitations of the small number of 24 $\mu$ m detections, the X-ray weakly- or non-detected and X-ray detected AGN also span similar ranges of 24  $\mu$ m power. Using the best-fit SEDs from our redshift determinations, we can estimate  $L_{\text{IR}}$ , the infrared luminosity from 8 – 1000  $\mu$ m. We caution that these values are only approximate, as the SEDs in the FIR are not well-constrained by our data. We find that of the X-ray non- and weakly-detected AGN (with redshift estimates), 1 is a ULIRG ( $L_{\text{IR}} > 10^{12} L_{\odot}$ ), 2 are LIRGS ( $10^{11} L_{\odot} < L_{\text{IR}} < 10^{12} L_{\odot}$ ),

8 have luminosities of  $10^{10} L_{\odot} < L_{\text{IR}} < 10^{11} L_{\odot}$ , and 1 has a luminosity that falls below  $10^{10} L_{\odot}$ . Two of the X-ray detected AGN are ULIRGS, 1 is a LIRG, 3 have luminosities of  $10^{10} L_{\odot} < L_{\text{IR}} < 10^{11} L_{\odot}$ , and 2 have a luminosity that falls below  $10^{11} L_{\odot}$ .

The 0.5-8 keV X-ray luminosities of our radio-excess sample are shown in Figure 6. For all sources with column density estimates, we calculate absorption-corrected X-ray luminosities, assuming an intrinsic photon index of  $\Gamma = 2$ . The results are listed in Tables 2 and 4. They are subject to relatively large errors, given the uncertainties in the measurements of  $\Gamma$  at low signal to noise as well as possible intrinsic variations in the photon index. They are nonetheless useful as rough estimates. Because there is no X-ray K-correction for a spectrum with  $\Gamma = 2$ , rest-frame 0.5-8 keV luminosities are equivalent to observed-frame, absorption-corrected 0.5-8 keV luminosities. We overplot on Figure 6, as solid lines, the rest-frame 0.5-8 keV X-ray luminosities of all sources with known redshifts and column density estimates. We see that of the AGN for which we can estimate intrinsic luminosities, those with the highest luminosities were detected in the X-ray. Low-luminosity AGN (LLAGN), however, were also detected in the X-ray; one such source, VLA J123652+621444, has an X-ray luminosity of  $L_{0.5-8 \text{ keV}} = 1.6 \times 10^{41} \text{ erg s}^{-1}$  and an optical through MIR SED that is well fit by a LINER template.

### 2.6.3 Observed X-ray vs. Radio Emission

The ratio of X-ray to radio emission provides another probe of the nature of sources in our sample. We define  $q' = \log (f_{1.4 \text{ GHz}}/f_{4 \text{ keV}})$  and compute the X-ray flux densities at an energy of 4 keV (assuming a photon index of  $\Gamma = 1.7$ , equivalent to a spectral index of  $\alpha = 0.7$ , for a bandpass correction). Since a typical radio spectrum has a slope of  $\alpha = 0.7$  ( $S_{\nu} \propto \nu^{-\alpha}$ ), we do not apply any K-corrections

Table 4. X-ray Properties of X-ray Detected AGN

Source	$z$	X-ray Band	$\Gamma^a$	Flux ( $\text{erg s}^{-1} \text{cm}^{-2}$ )	Hard/Soft Flux Ratio	$N_H$ ( $\text{cm}^{-2}$ )	Abs. Corrected log $L_x$ ( $\text{erg s}^{-1}$ )	$q'_{\text{corr}}$
VLA J123556+621555	0.44	Full	1.37	$1.31 \times 10^{-14}$	2.4	$1.0 \times 10^{22}$	43.1	5.0
		Hard		$9.10 \times 10^{-15}$			42.8	
		Soft		$3.62 \times 10^{-15}$			42.8	
VLA J123640+621833	1.14	Full	$\geq 0.26$	$2.13 \times 10^{-16}$	$< 8.3$	$1.3 \times 10^{23}$	$< 42.5$	$> 7.2$
		Hard		$< 2.76 \times 10^{-16}$			$< 42.4$	
		Soft		$3.20 \times 10^{-17}$			$< 42.4$	
VLA J123642+621331	...	Full	1.35	$2.76 \times 10^{-16}$	2.5	$(1.2 \times 10^{22} - 1.1 \times 10^{23})$	(41.6-43.3)	7.5-7.4
		Hard		$2.08 \times 10^{-16}$			(41.3-43.0)	
		Soft		$8.03 \times 10^{-17}$			(41.3-43.0)	
VLA J123644+621133	1.01	Full	$\geq 1.43$	$2.44 \times 10^{-16}$	$< 2.2$	$< 2.0 \times 10^{22}$	$< 42.3$	$> 7.8$
		Hard		$< 1.80 \times 10^{-16}$			$< 42.0$	
		Soft		$7.74 \times 10^{-17}$			$< 42.0$	
VLA J123646+621404	0.96	Full	0.67	$2.46 \times 10^{-14}$	6.4	$7.6 \times 10^{22}$	44.3	4.7
		Hard		$2.17 \times 10^{-14}$			44.1	
		Soft		$3.26 \times 10^{-15}$			44.0	
VLA J123652+621444	0.32	Full	2.10	$4.63 \times 10^{-16}$	0.9	...	41.2	6.8
		Hard		$2.19 \times 10^{-16}$			40.8	
		Soft		$2.44 \times 10^{-16}$			40.9	
VLA J123659+621832	...	Full	0.67	$8.76 \times 10^{-16}$	6.5	$(3.9 \times 10^{22} - 4.3 \times 10^{23})$	(42.2-44.0)	6.8-6.4
		Hard		$7.86 \times 10^{-16}$			(41.9-43.7)	
		Soft		$1.18 \times 10^{-16}$			(41.9-43.7)	
VLA J123701+622109	0.8	Full	$\geq 0.40$	$3.22 \times 10^{-16}$	$< 7.1$	$< 6.8 \times 10^{22}$	$< 42.3$	$> 7.0$
		Hard		$< 4.83 \times 10^{-16}$			$< 42.2$	
		Soft		$6.56 \times 10^{-17}$			$< 42.2$	
VLA J123709+622258	1.23	Full	-0.58	$5.21 \times 10^{-15}$	36.2	$3.7 \times 10^{23}$	44.1	6.0
		Hard		$4.99 \times 10^{-15}$			43.8	
		Soft		$1.35 \times 10^{-16}$			43.8	
VLA J123713+621826	...	Full	1.37	$1.69 \times 10^{-15}$	2.4	$(1.1 \times 10^{22} - 1.1 \times 10^{23})$	(42.4-44.1)	6.8-6.8
		Hard		$1.19 \times 10^{-15}$			(42.1-43.8)	
		Soft		$4.71 \times 10^{-16}$			(42.1-43.8)	
VLA J123721+621130	1.3	Full	0.28	$5.09 \times 10^{-16}$	10.8	$1.9 \times 10^{23}$	43.1	6.5
		Hard		$5.07 \times 10^{-16}$			42.8	
		Soft		$4.45 \times 10^{-17}$			42.8	

<sup>a</sup>Alexander et al. assume a  $\Gamma$  of 1.4 for sources not detected in the hard band. For those AGN with hard band upper limits, however, we give the limit on  $\Gamma$  as calculated from the hard to soft band count rate ratio,  $H/S$ .

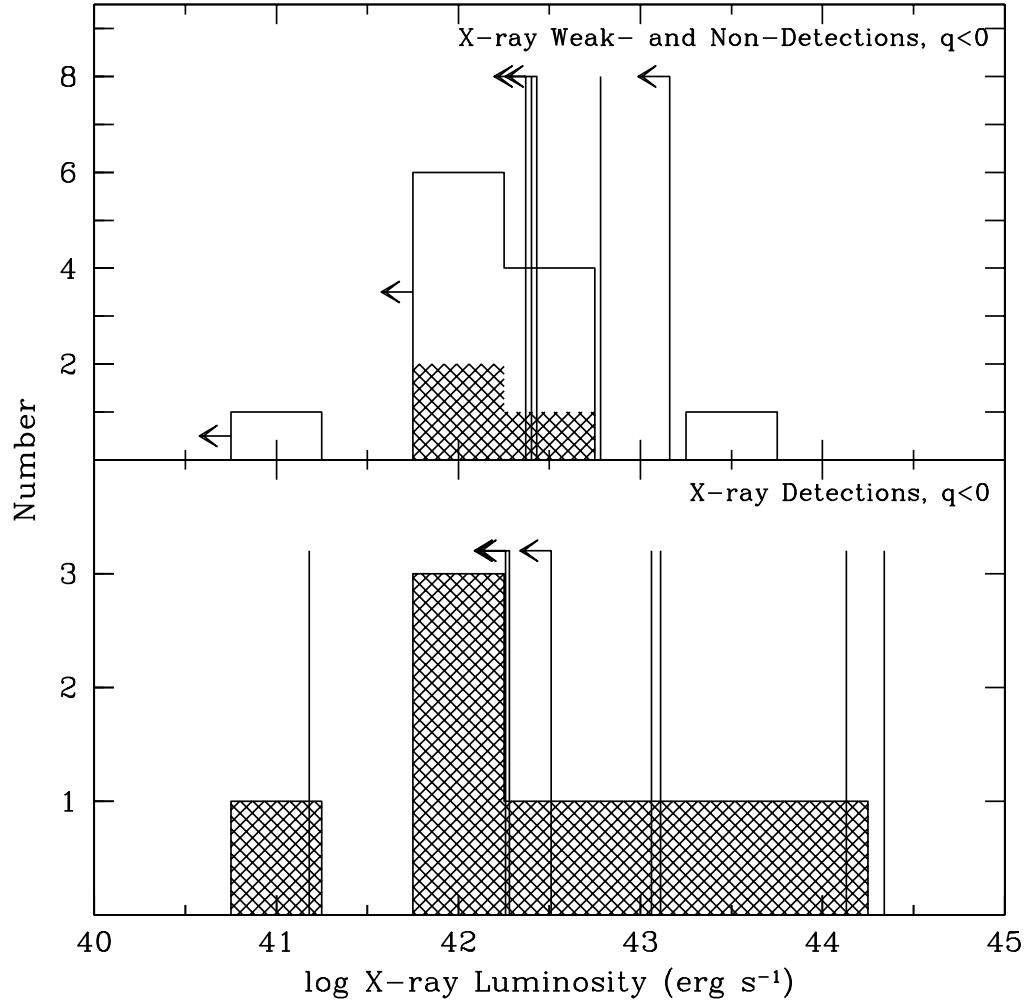


Figure 2.6 Observed X-ray luminosity distributions of the radio-excess AGN sample. The clear histograms represent all sources, including those for which we have only upper limits on  $L_{0.5-8 \text{ keV}}$ . The cross-hatched histograms represent only those sources with known  $L_{0.5-8 \text{ keV}}$ . For those AGN for which we can estimate  $N_{\text{H}}$ , we overplot as solid lines the intrinsic 0.5-8 keV absorption-corrected X-ray luminosities.



to the ratio of radio to X-ray flux density. Thus, the values we use are as close as possible to the observed radio vs. the observed X-ray flux densities. Figure 7 shows the distribution of  $q'$  for our X-ray detected and non-detected AGN samples, along with all X-ray detections that meet our exposure cut.

To compare with a control sample, we have also plotted  $q'$  for the X-ray detected (with *ASCA*) radio sample of Sambruna et al. (1999). This study is of representative sources, not of a complete well-defined sample, and contains 28 objects with sufficient data to be plotted (of 38; the omitted sources are 3C99, 3C 275, 3C 295, 3C 330, 3C 368, 3C 411, 4C +41.17, 4C +55.16, 4C +74.26, PKS 0625-53, and NGC 6251). All but four of the plotted sources are at  $z \sim 0.3$  or less. All the objects for which IRAS 25  $\mu\text{m}$  data are available have  $q < 0$  and are therefore AGN by the same criterion used in this paper. Of the 28 sources, 16 are radio-intermediate ( $q > -1.6$ ) and four more are only slightly more radio luminous ( $-1.6 > q > -2$ ). They therefore are reasonable to compare with our predominantly radio-intermediate sources.

We have also included sources from Gambill et al. (2003). This study uses *Chandra* data for bright quasars over a large range of redshift. The sample is mostly useful to augment the statistics for radio quasars, which are not well represented in the Sambruna et al. work.

Figure 7 shows that the overall behavior of  $q'$  is as one might expect from selection biases: a sample of AGN selected in the X-ray tends to be relatively brighter in X-rays compared with the radio than does a sample of AGN selected in the radio (i.e. the control sample). Because our use of  $q'$  normalizes both samples to radio flux density, this behavior reflects an intrinsic difference in radio-to-X-ray spectral energy distributions, and is not simply an effect of low-luminosity radio sources without X-ray counterparts. *If the local radio-detected sample has analogs at*

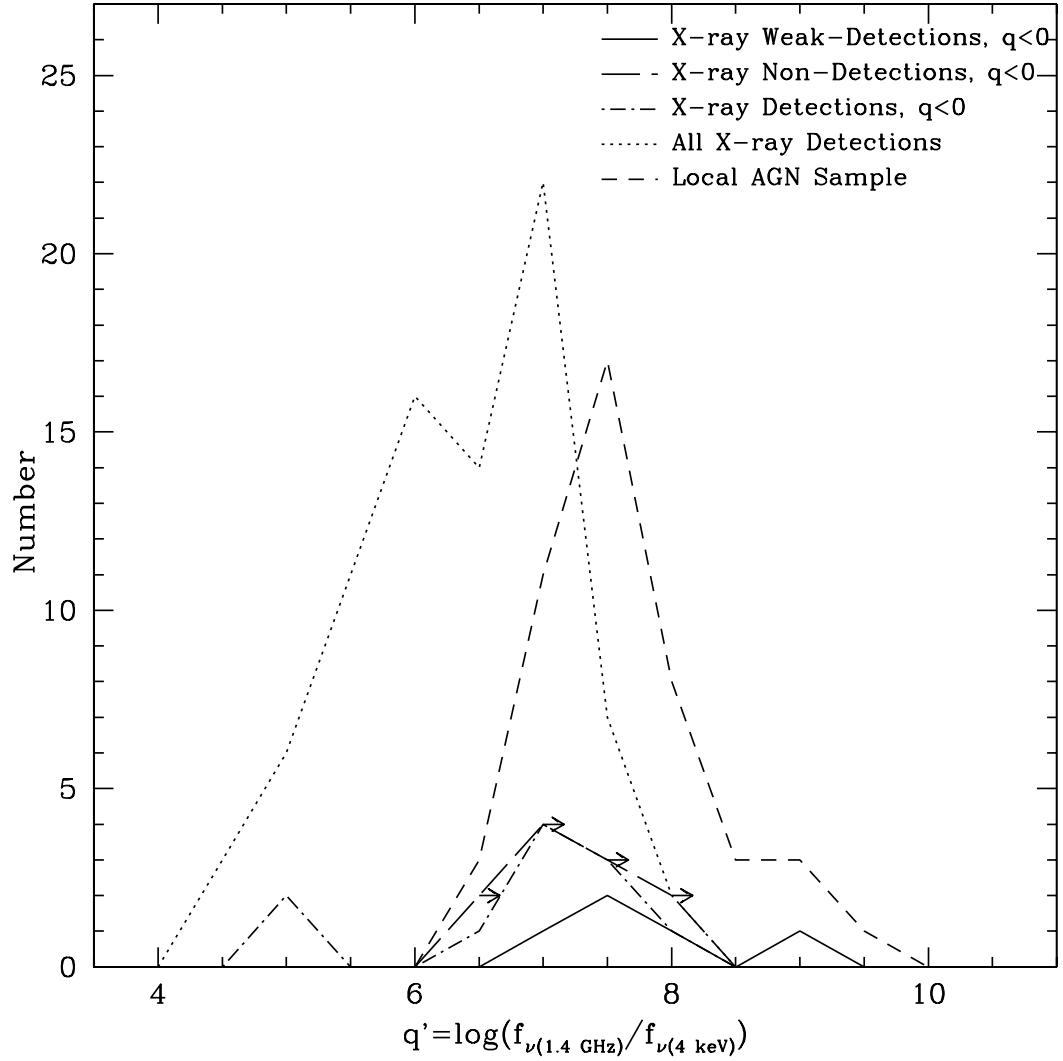


Figure 2.7 Histogram of  $q'$ . X-ray detections, weak detections, and non-detections are samples as defined in this paper. The "local" sample is from Sambruna et al. (1999), augmented by Gambill et al. (2003). The sample labeled "all X-ray detections" represents the X-ray sources in the CDFN that have radio counterparts in the catalog of Richards (2000). For viewing clarity, we do not plot the full histograms, but instead connect their values at the bin centers.

*higher redshift, as expected, they would fall below the current Chandra detection limit, yielding incomplete samples in the X-ray.*

The  $q'$  distribution of the 5 X-ray weakly-detected sources is clearly more consistent with that of the control sample than the full *Chandra*-detected sample. The  $q'$  distributions also suggest that some fraction of our X-ray non-detected AGN are more similar in nature to these local AGN than they are to the full *Chandra*-detected sample. In contrast, the radio-excess X-ray detected AGN sample is more consistent with the overall *Chandra*-detected sample than with the local AGN sample. A two-sided Kolmogorov-Smirnov (KS) test gives a probability of 4% that the full *Chandra*-detected and radio-excess X-ray detected AGN are drawn from the same sample. The corresponding probability for the *Chandra*-detected and radio-excess X-ray weakly-detected AGN sample is 0.2%.

The large values of  $q'$  for the control sample and the X-ray weakly- or non-detected sample could be due to intrinsically lower X-ray to radio luminosity, to heavy obscuration, or to some combination of the two. We test the obscuration hypothesis by comparing  $R$ , the ratio of compact to total radio emission, to  $q'$  for the control sample. The compactness,  $\log R$ , is often used as an indication of the orientation of the radio source relative to the observer. If the source is viewed down the jet axis,  $\log R = 0$ , and the flux is dominated by beamed emission. As the viewing angle moves away from the jet axis,  $\log R$  becomes more negative.

Figure 8 compares  $\log R$  to  $q'$  for all of the control sample except 3C28. We have excluded this object because the X-ray emission from its position appears to be strongly dominated by emission by its galaxy cluster, not the AGN (Hardcastle & Worrall 1999). There is a strong correlation in the sense that the more negative  $\log R$ , the larger  $q'$ . That is, the more the radio jets are aligned away from the observer, the weaker the X-rays are relative to the radio. This behavior

is consistent with a standard unification model where the circumnuclear torus plays an increasing role in absorbing the X-rays as the viewing angle of the central accretion disk approaches edge-on. The parameter  $q'$  therefore appears to be correlated with viewing angle, and consequently with obscuration, in local samples. We note that the 2 highly radio-resolved sources discussed in §6.1 also have the highest values of  $q'$ , a result that is consistent with the above interpretation. The relatively high limits on  $q'$  for the X-ray non-detected AGN therefore suggest that the beamed radio emission of these AGN is aligned away from us, increasing their likelihood of being heavily obscured.

#### 2.6.4 Intrinsic X-ray vs. Radio Emission

We plot in Figure 9 the intrinsic X-ray to radio emission ratios,  $q'_{\text{corr}}$ , for the X-ray weakly-detected and X-ray detected samples. We calculate  $q'_{\text{corr}}$  by correcting the observed 0.5-8 keV X-ray flux for the estimated column densities. We assume a photon index of  $\Gamma = 2$  when applying this correction. Because the radio spectral slopes are known for the majority of the sources for which we have column density estimates, we apply a radio K-correction, such that  $q'_{\text{corr}} = \log(f_{1.4 \text{ GHz}}/f_{4 \text{ keV,corr}}) + (\alpha_{\text{radio}} - 1)\log(1 + z)$ . We list the values of  $q'_{\text{corr}}$  in Tables 2 and 4. For sources without known radio spectral indices, we assume  $\alpha = 0.7$ .

The X-ray detected sample has, on average, a lower  $q'_{\text{corr}}$  than the X-ray non-detected sample, although there is a significant amount of overlap between the 2 samples and many of the sources have only lower limits on  $q'_{\text{corr}}$ . This suggests, however, that some fraction of the X-ray detected sample may have intrinsically higher X-ray luminosities (with respect to their radio luminosities) than do sources that were not detected in the X-ray. Such a conclusion is in agreement with the absorption-corrected X-ray luminosities, which are generally higher for the X-ray-detected AGN. A sample of intrinsically X-ray weak AGN with hard

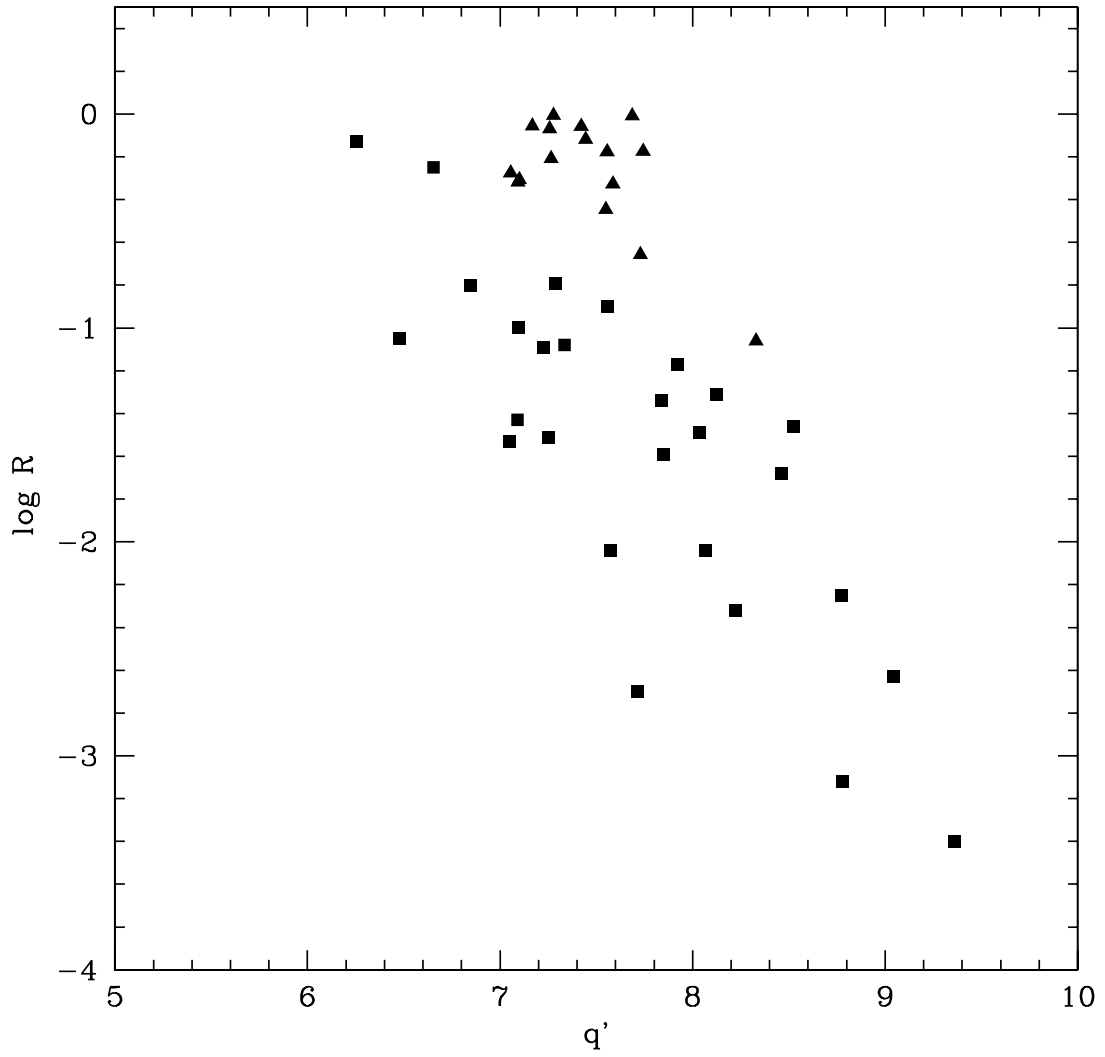


Figure 2.8 Relationship between  $\log R$ , the ratio of compact to total radio emission, and  $q'$  for the local AGN samples of Sambruna et al. (1999; squares) and Gambill et al. (2003; triangles).

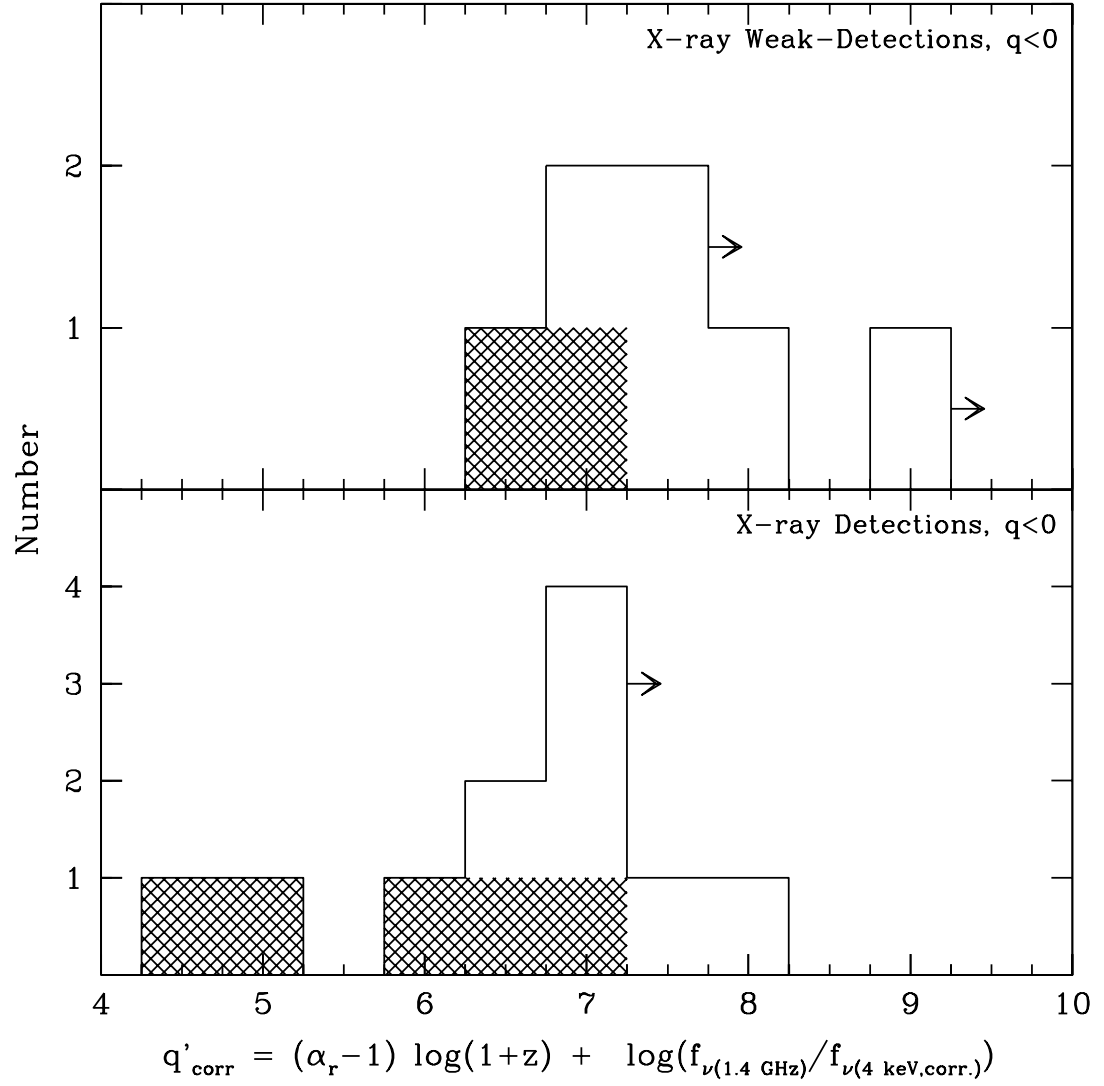


Figure 2.9 Histogram of the absorption- and K-corrected  $q'$ . The clear histograms represent all sources, including those for which we have only lower limits on  $q'_{\text{corr}}$ . The cross-hatched histograms represent only those sources with known  $q'_{\text{corr}}$ .

X-ray spectra was studied by Risaliti et al. (2003), who suggest that such objects could contribute significantly to the hard component of the X-ray background. Unfortunately, because we do not have column density estimates for the X-ray non-detected sources, it is unclear whether this trend will hold for the entire sample.

It is also possible that a selection effect is responsible for the apparently lower intrinsic X-ray luminosities of the X-ray weakly-detected sample. Because the X-ray detected and X-ray weakly-detected samples span similar ranges of column densities, it is likely that the AGN that were previously X-ray detected are those that are intrinsically the most luminous.

#### 2.6.5 X-ray vs. Optical Emission

The optical to X-ray emission ratio is a powerful diagnostic for distinguishing AGN from star-forming galaxies (e.g. Maccacaro et al. 1988). AGN typically lie within  $\log f_X/f_R = \pm 1$ ; at the highest fluxes probed by the CDFN, the mean AGN flux ratio is consistent with  $\log f_X/f_R = 0$ , whereas at lower fluxes, the mean ratio rises slightly due to increased optical obscuration (Barger et al. 2003). Starbursts and lower-luminosity AGN populate the transition region ( $-2 < \log f_X/f_R < -1$ ), whereas normal star-forming galaxies, starbursts, and LLAGN typically have X-ray to optical flux ratios of  $\log f_X/f_R < -2$  (see Barger et al. 2003, Hornschemeier et al. 2003)

Figure 10 shows the observed R-band magnitudes and hard (2-8 keV) X-ray fluxes of our radio-excess AGN sample. We place a lower limit of  $R=25.0$  mag on sources with no R-band counterpart. For sources with multiple GOODS counterparts, but only a single ground-based R-band counterpart, we treat the R-band magnitude as a lower limit.

Of the 11 hard X-ray-detected radio-excess AGN, all but 1 lie within the AGN

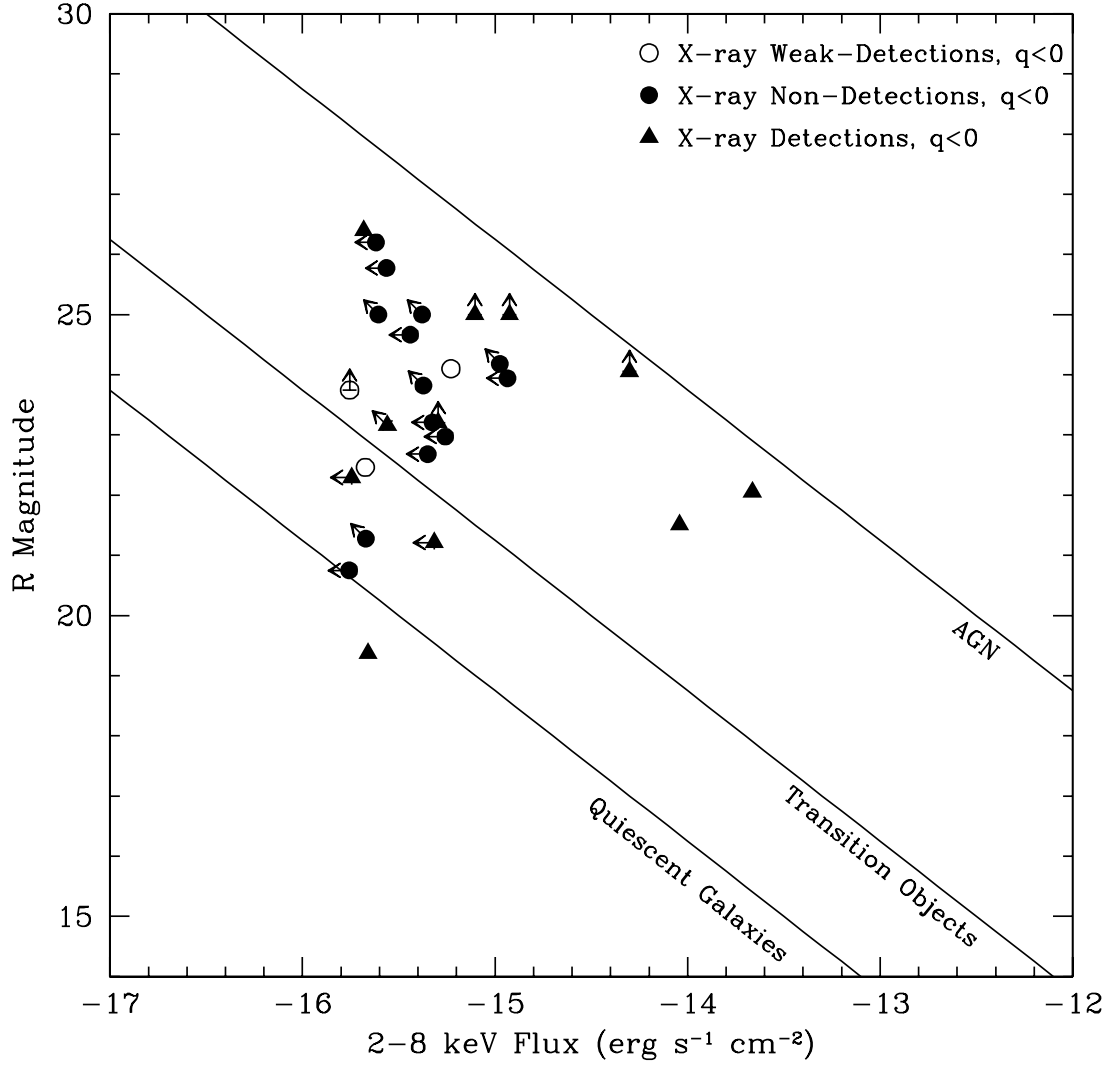


Figure 2.10 Relationship between the observed R magnitude and 2-8 keV (hard band) X-ray flux. X-ray detected sources are given by triangles, and X-ray weakly- and non-detected sources by circles. The lines represent the regions populated by AGN ( $f_X/f_R < |1|$ ), AGN and starbursts ( $-2 < \log f_X/f_R < -1$ ), and quiescent galaxies, starbursts, and LLAGN ( $\log f_X/f_R < -2$ ) (see Barger et al. 2003, Hornschmeier et al. 2003).



or transition regions, as expected. The source that lies in the quiescent galaxy region is the LLAGN, VLA J123652+621444, discussed in §6.2. The current X-ray and optical limits also place the X-ray weakly- and non-detected AGN primarily in the AGN region, with 3 extending into the transition region. Higher sensitivity X-ray observations are needed to determine the true locations of the sample. Given the current limits, however, all 16 sources are consistent with the predictions for normal AGN.

## 2.7 Conclusions

We define a sample of 27 radio-excess AGN in the CDFN by selecting galaxies that do not obey the radio/infrared relation for star-forming galaxies and radio-quiet AGN. Sixteen (60%) of these AGN are previously undetected at X-ray exposures of  $> 1$  Ms, although we have subsequently detected X-ray signals from 7 more at significance levels of 2.5 to  $5.2 \sigma$ . In this paper, we examine the characteristics of these 16 X-ray weak AGN, and their relationship to the 11 AGN previously detected in the X-ray. We find:

- The values and limits we place on  $N_H$  for the X-ray weak AGN are all consistent with their being obscured, but not Compton-thick (i.e.,  $10^{22} \text{ cm}^{-2} < N_H < 10^{24} \text{ cm}^{-2}$ ). Of the 9 AGN that are either X-ray non-detected or are too close to a known X-ray source to search for weak X-ray emission, we estimate that 6 could be Compton thick. This corresponds to 22% of our sample and is consistent with predictions from the X-ray background.
- The column densities to the X-ray-detected members of our sample are similar to those of the X-ray weak AGN, although they extend to lower absorbing column. All but 1 (or 2 if a Compton reflection component is considered) fall in the range of obscured but not Compton-thick AGN. This corresponds

to 80% of the sample, and is consistent with predictions that X-ray obscured AGN outnumber non-obscured AGN by a factor of 4:1. If we assume that all of the X-ray non-detected AGN are obscured, however, the overall fraction of obscured AGN rises to 93%.

- The ratio of radio to X-ray emission indicates that orientation of the circumnuclear torus, and therefore obscuration, is at least partly responsible for attenuating the X-ray fluxes, as we would expect. To support this scenario, we show that a local sample of radio AGN has a ratio of radio to X-ray emission that shows a dependence on viewing angle consistent with the effects of X-ray absorption by a circumnuclear torus.
- Indicators such as the ratio of optical to X-ray emission, the intrinsic absorption corrected X-ray luminosities, and the radio luminosities all support the argument that the weak X-ray sources are similar in intrinsic properties to the AGN selected in a similar way but with stronger X-ray fluxes. This similarity would be strengthened by the usual tendency that any sample selected in a given spectral band (e.g., X-ray or radio) will tend to include preferentially the sources of a given population that are relatively brighter in that band.

In summary,  $\sim 60\%$  of radio-excess AGN have been missed in the CDFN survey at X-ray exposures  $> 1$  Ms. At least  $1/2$  of the radio-excess AGN have high, but not extreme column densities ( $10^{22} \text{ cm}^{-2} < N_H < 10^{24} \text{ cm}^{-2}$ ), and X-ray, radio, and infrared luminosities similar to those of normal radio-excess X-ray detected AGN. Six (22%) of the sample may be Compton thick ( $N_H > 10^{24} \text{ cm}^{-2}$ ). These results are consistent with proposals that obscured AGN outnumber unobscured ones by  $\sim 4:1$ , although the proportion of potentially Compton-thick

objects is at the low end of the predictions.

## CHAPTER 3

POWER-LAW AGN CANDIDATES IN THE *Chandra* DEEP FIELD-NORTH

We define a sample of 62 galaxies in the *Chandra* Deep Field-North whose *Spitzer* IRAC SEDs exhibit the characteristic power-law emission expected of luminous AGN. We study the multiwavelength properties of this sample, and compare the AGN selected in this way to those selected via other *Spitzer* color-color criteria. Only 55% of the power-law galaxies are detected in the X-ray catalog at exposures of  $> 0.5$  Ms, although a search for faint emission results in the detection of 85% of the power-law galaxies at the  $\geq 2.5\sigma$  detection level. Most of the remaining galaxies are likely to host AGN that are heavily obscured in the X-ray. Because the power-law selection requires the AGN to be energetically dominant in the near- and mid-infrared, the power-law galaxies comprise a significant fraction of the *Spitzer*-detected AGN population at high luminosities and redshifts. The high  $24\ \mu\text{m}$  detection fraction also points to a luminous population. The power-law galaxies comprise a subset of color-selected AGN candidates. A comparison with various mid-infrared color selection criteria demonstrates that while the color-selected samples contain a larger fraction of the X-ray luminous AGN, there is evidence that these selection techniques also suffer from a higher degree of contamination by star-forming galaxies in the deepest exposures. Considering only those power-law galaxies detected in the X-ray catalog, we derive an obscured fraction of 68% (2:1). Including all of the power-law galaxies suggests an obscured fraction of  $< 81\%$  (4:1).

### 3.1 Introduction

Detecting complete samples of AGN, both locally and in the deep cosmological fields, has been a major ongoing goal. Hard X-ray selection is a powerful way to detect both relatively uncontaminated and complete samples of AGN. Deep X-ray surveys with *Chandra* and *XMM-Newton* have now resolved 70-90% of the cosmic X-ray background (CXRB) at 2-8 keV into discrete sources (Mushotzky et al. 2000; Giacconi et al. 2002; Alexander et al. 2003; Bauer et al. 2004; Worsley et al. 2004, 2005), detecting the majority of the X-ray unobscured AGN population in the deep X-ray fields. At high column densities, however, the dust and gas surrounding the central engine (in combination with that located in the host galaxy) are capable of hiding virtually all accessible AGN tracers. Therefore, while the overall resolved fraction of the CXRB is high, it drops with increasing energy to 60% at 6-8 keV and to 50% at  $> 8$  keV (Worsley et al. 2004, 2005).

Population synthesis models of the CXRB and of X-ray luminosity functions therefore predict a significant population of heavily obscured AGN not detected in the deepest X-ray fields (i.e., the 1 Ms *Chandra* Deep Field–South (CDF-S) and the 2 Ms *Chandra* Deep Field–North (CDF-N)). Predictions of their properties are in rough, but not complete, agreement. Treister et al. (2004) predict an X-ray incompleteness of 25% at  $N_{\text{H}} = 10^{23} \text{ cm}^{-2}$  and of 70% at  $N_{\text{H}} = 10^{24} \text{ cm}^{-2}$ . Ballantyne et al. (2006) estimate that the deep X-ray surveys miss  $\sim 50\%$  of obscured AGN with  $\log L_{\text{x}}(\text{ergs s}^{-1}) > 44$  at all  $z$ , and that most of the missing objects are Compton-thick ( $\log N_{\text{H}}(\text{cm}^{-2}) > 24$ ). Worsley et al. (2005) find that the unresolved sources are likely to lie at redshifts of  $z = 0.5 - 1.5$ , have column densities in excess of  $10^{23} \text{ cm}^{-2}$ , and have intrinsic X-ray luminosities of  $< 5 \times 10^{43} \text{ ergs s}^{-1}$ .

Numerous attempts have been made to detect this population of heavily obscured AGN, many of which have focused on the mid-infrared (MIR) emission

where the obscured radiation is re-emitted (Ivison et al. 2004; Lacy et al. 2004; Hatziminaoglou et al. 2005; Stern et al. 2005; Alonso-Herrero et al. 2006; Polletta et al. 2006) or on combinations of MIR and multi-wavelength data (Johansson et al. 2004; Yan et al. 2004, 2005; Donley et al. 2005; Franceschini et al. 2005; Houck et al. 2005; Leipski et al. 2005; Martínez-Sansigre et al. 2005, 2006; Richards et al. 2006; Weedman et al. 2006). In the MIR, luminous AGN can often be distinguished by their characteristic power-law emission, which extends from the infrared to the ultraviolet (e.g. Neugebauer 1979; Elvis et al. 1994). This emission is not necessarily due to a single source, but can arise from the combination of non-thermal nuclear emission and thermal emission from various nuclear dust components (e.g. Rieke & Lebofsky 1981). In contrast, star-forming galaxies are characterized by dust and stellar emission features redward and blueward of a local minimum at  $\sim 5 \mu\text{m}$ .

We focus here on AGN with red power-law SEDs in the *Spitzer* 3.6-8.0  $\mu\text{m}$  bands. Alonso-Herrero et al. (2006) selected a sample of 92 such sources in the CDF-S, 70% of which are hyper-luminous infrared galaxies (HyperLIRGS,  $\log L_{\text{IR}}(L_{\odot}) > 13$ ) or ultra-luminous infrared galaxies (ULIRGS,  $\log L_{\text{IR}}(L_{\odot}) > 12$ ). Nearly half (47%) of their power-law sample were not detected in X-rays at exposures of up to 1 Ms. We use a selection similar to that of Alonso-Herrero et al. (2006) to identify power-law galaxies in the 2 Ms CDF-N. Because the central regions of the *Chandra* Deep Fields are photon-limited, not background-limited, the 2 Ms CDF-N is twice as sensitive as the 1 Ms CDF-S at the *Chandra* aimpoint (e.g. Alexander et al. 2003).

We use a combination of spectroscopic and photometric redshifts to estimate distances and luminosities for this class of AGN, placing them in the context of the overall AGN population. The observations and data reduction are outlined in

§2 and the selection criteria are discussed in §3. The photometric redshift code is discussed in §4. Making use of the deepest available (2 Ms) X-ray data, we search for faint X-ray emission from sources missed in the X-ray catalogs. The X-ray, MIR, radio, and optical properties of the sample, including detection fractions, X-ray luminosities, radio classifications, and optical–MIR SEDs, are discussed in §5. In §6, we compare the power-law selection to other MIR color selection techniques, and discuss the completeness and reliability of the power-law and color-selection criteria. Finally, in §7, we use the X-ray data to calculate the obscuring columns of the power-law galaxies and to estimate the obscured fraction of the power-law sample. Throughout the paper, we assume a cosmology of  $(\Omega_m, \Omega_\Lambda, H_0) = (0.3, 0.7, 72 \text{ km s}^{-1} \text{ Mpc}^{-1})$ .

### 3.2 Observations and Data Reduction

*Spitzer* was used to obtain MIPS and IRAC MIR observations of the CDF-N, with 1400 s and 500 s exposures, respectively. We use these MIPS GTO images in place of the GOODS *Spitzer* data because the former cover the full CDF-N, whereas the latter cover a field approximately two times smaller. The MIPS image was processed using the MIPS GTO data analysis tool (Gordon et al. 2004b, 2005); the IRAC data analysis is described in Huang et al. (2004). We used the IRAF task *allstar* to select sources at  $24 \mu\text{m}$ , and SExtractor (Bertin & Arnouts 1996) to select sources in the IRAC bands. The 80% completeness limit for the  $24 \mu\text{m}$  data is  $83 \mu\text{Jy}$  (Papovich et al. 2004). The IRAC detection limits of our survey (see §3) are 1.8, 2.8, 14.5, and  $18.0 \mu\text{Jy}$ , at 3.6, 4.5, 5.8, and  $8.0 \mu\text{m}$ , respectively. Optical and NIR photometry were measured from the GOODS dataset (*bviz*, Giavalisco et al. 2004), as well as from the data of Capak et al. (2004) (*UBVRIZ'HK'*). The ground-based photometry was aperture-matched for consistency, using the aperture of

the most sensitive band in which the source was detected. For cases in which multiple ground-based sources in a  $1.5''$  radius caused the aperture-matched flux density to differ from that of the nearest source by a factor of  $\geq 1.5$ , we replaced the aperture-matched flux densities with the cataloged flux densities of the nearest source in all bands. In addition, if the ground-based photometry of sources with multiple GOODS counterparts (in a  $1.5''$  radius) differed from the GOODS photometry by a factor of 2 or more in any of the bands, we treated the ground-based photometry as upper limits. For further details, see Pérez-González et al. (2005).

### 3.3 Sample selection

We selected as power-law galaxies sources that were detected with  $S/N \geq 6$  in each of the four IRAC bands and whose IRAC spectra are well-fit by a line of spectral index  $\alpha \leq -0.5$ , where  $f_\nu \propto \nu^\alpha$ . In a similar study, Alonso-Herrero et al. (2006) chose a limit of  $\alpha \leq -0.5$  based on the mean spectral slope of optically-selected quasars ( $\alpha \sim -1$ , Elvis et al. 1994; Neugebauer et al. 1979) and the optical spectral indices of Sloan Digital Sky Survey (SDSS) QSOs ( $\alpha = 0.5$  to  $-2$ , Ivezić et al. 2002). For comparison, broad-line AGN (BLAGN) from the AGN and Galaxy Evolution Survey (AGES, C. S. Kochanek et al., in prep) have  $3.6\text{--}8\text{ }\mu\text{m}$  slopes of  $\alpha = -1.07 \pm 0.53$  (Stern et al. 2005), indicating that our cut lies within  $\sim 1\sigma$  of the mean. To ensure a good linear fit, we applied a cut in the chi-squared probability of  $P_\chi \geq 0.1$ .  $P_\chi$  is the probability that a fit to a power-law distribution would yield a value greater than or equal to the observed chi-squared; a probability of 0.5 corresponds to a reduced chi-squared of 1.  $P_\chi$  tends to either lie close to 0.5, or is very small (see Bevington & Robinson 2003). Because we are primarily interested in the X-ray and radio properties of the power-law galaxies, we also restricted



the sample to those galaxies with X-ray exposures of  $\geq 0.5$  Ms (Alexander et al. 2003); this selection also ensures deep 1.4 GHz radio coverage (Richards 2000) and results in a total survey area of 350 arcmin<sup>2</sup>. In addition, we required the IRAC SED to rise monotonically in  $f_\nu$  to prevent contamination from star-forming galaxies with possible stellar features in the IRAC bands (resulting in the rejection of 10 sources). Using these criteria, we identified 79 power-law galaxies in the CDF-N.

We removed 10 of the selected galaxies due to blended or problematic IRAC photometry and we removed 1 galaxy (CDFN 22363) because of its stellar dominated spectrum. CDFN 22363 has a shallow slope of only  $-0.56 \pm 0.20$  and hence might have been scattered into the power-law sample by noise (it has the second flattest slope in the sample). It is the only source in the power-law sample with a spectroscopic redshift that is not detected in X-rays, and it lacks a 24  $\mu\text{m}$  counterpart (see §5.2). Six additional sources were removed because their optical-MIR SEDs exhibited possible stellar bumps. The final sample of 62 power-law galaxies is listed in Table 1; radio through X-ray SEDs are shown in Figure 1. We indicate in Figure 1 the 27 sources that lie in the GOODS ACS region. In addition, we flag all sources for which we have either replaced the ground-based aperture-matched flux densities with the cataloged flux densities of the nearest source or for which we treat the ground-based photometry as upper limits (see §2).

The  $S/N$  cut of 6 in each of the IRAC bands imposes the following detection limits on the IRAC 3.6, 4.5, 5.8, and 8.0  $\mu\text{m}$  bands: 1.8, 2.8, 14.5, and 18.0  $\mu\text{Jy}$ . This large range of flux limits imposes complicated selection effects on the power-law sample. At  $\alpha < -0.67$ , the sample is flux-limited by the 5.8  $\mu\text{m}$  band. That is, all sources whose 5.8  $\mu\text{m}$  flux density exceeds the detection limit of 14.5  $\mu\text{Jy}$  are detectable in all of the IRAC channels. At  $\alpha > -0.67$ , however, the limiting flux

shifts to the  $8.0\ \mu\text{m}$  band. Because there is little change in the  $5.8\ \mu\text{m}$  detection limit for red power-law sources with  $-0.67 < \alpha < -0.5$  ( $f_{\text{lim}}$  increases from  $14.5\ \mu\text{Jy}$  at  $-3 < \alpha < -0.67$  to  $15.3\ \mu\text{Jy}$  at  $\alpha = -0.5$ ), the power-law sample is essentially flux-limited in the  $5.8\ \mu\text{m}$  band. Comparisons between the number of red ( $\alpha \leq -0.5$ ) and blue ( $\alpha > -0.5$ ) sources in the full IRAC sample, however, will be complicated by these effects, as the  $5.8\ \mu\text{m}$  limiting flux increases with increasing spectral slope, reducing the number of blue sources that meet the requirements of the power-law sample.

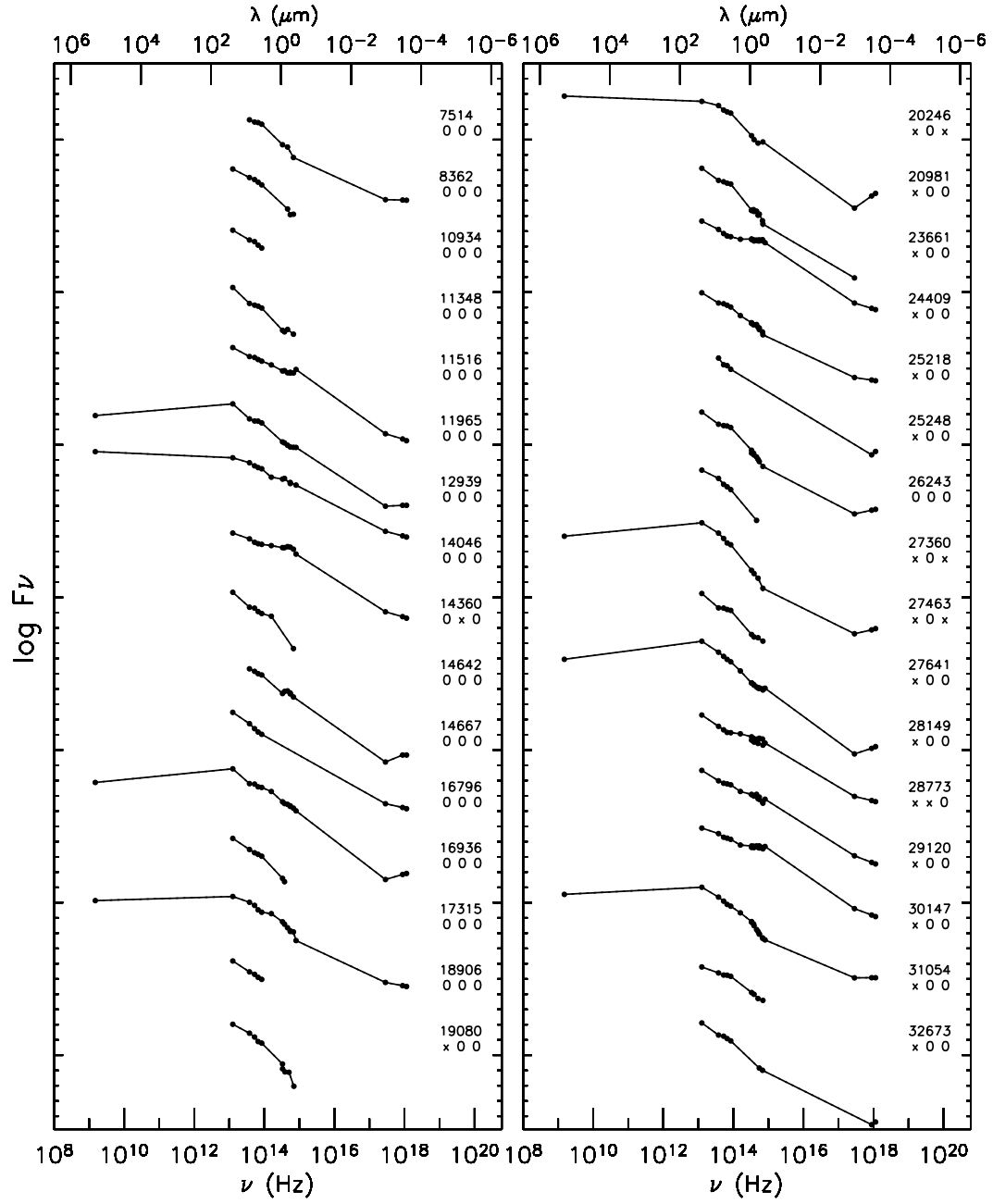


Figure 3.1 X-ray through radio observed-frame SEDs of the power-law galaxies. The flags printed under the source ID indicate by x whether (1) the source lies in the GOODS ACS field, (2) the aperture-matched flux densities have been replaced by the cataloged flux densities of the nearest source and (3) the ground-based photometry have been treated as upper limits (see §2).

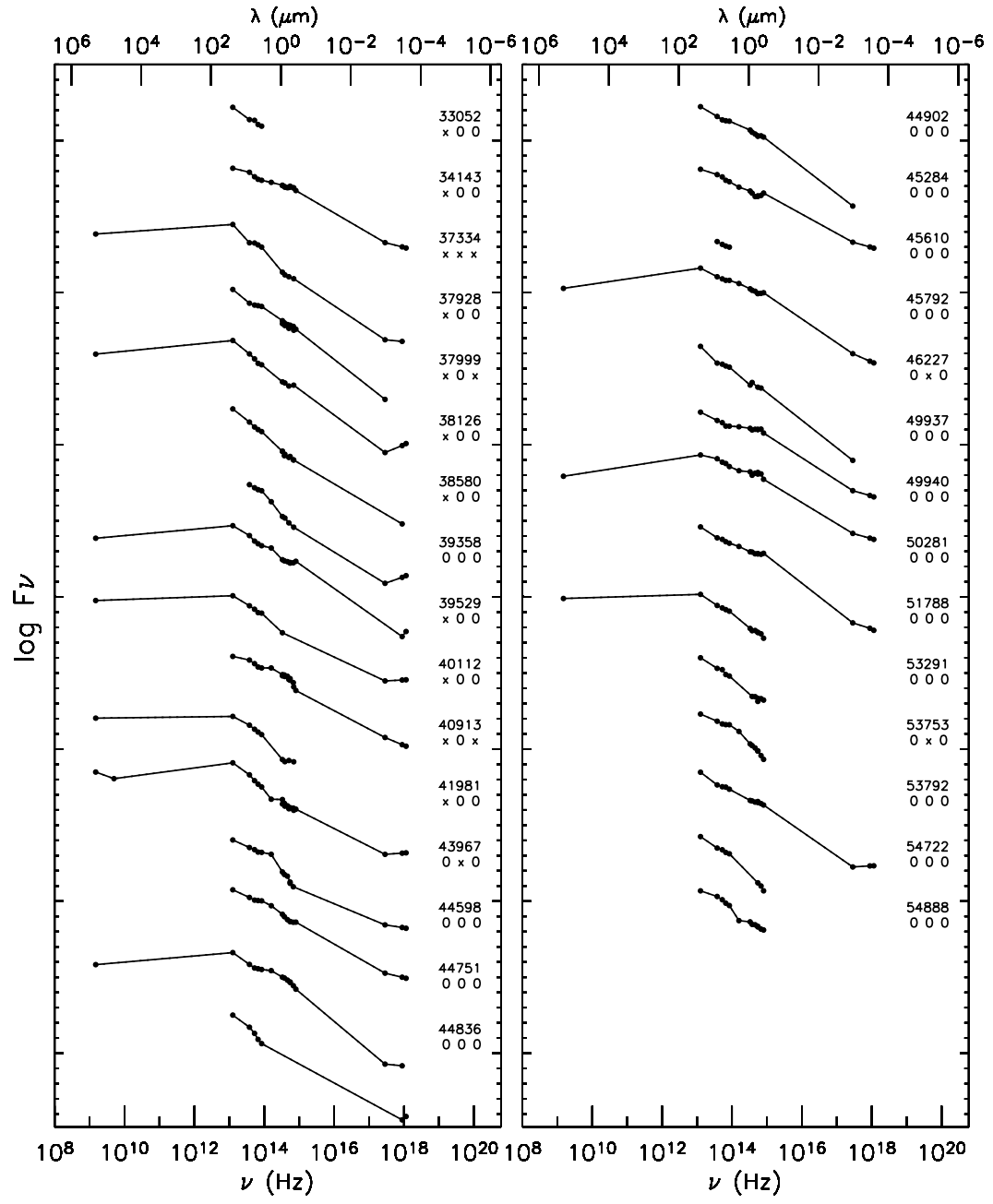


Fig. 1. — Continued.

To minimize the chances of selecting non-active galaxies via the power-law selection, we compared the spiral galaxy templates from Devriendt et al. (1999) to the optical–MIR SEDs of the sources. None of the sources in the final sample are well-fit by a spiral template. In addition to contamination from local spiral galaxies, Alonso-Herrero et al. (2006) found that cool ULIRGS at  $z > 2$  and with  $\alpha > -1$  could appear as power-law galaxies. Of the 62 power-law galaxies in the sample, nine have  $\alpha > -1$  and potentially lie at  $z > 2$ . Seven of these sources, however, have X-ray counterparts, and all but one (a source with no redshift estimate) have X-ray luminosities of  $\log L_x(\text{ergs s}^{-1}) > 43$ , and are therefore unlikely to be starburst-powered ULIRGS. We further explore the possibility of contamination due to star-forming galaxies in §6.2.2, using several updated SEDs, described in detail in Appendix A.

We have also considered whether the contributions of  $3.3 \mu\text{m}$  ( $z > 0.5$ ) and  $6.2 \mu\text{m}$  ( $z < 0.5$ ) aromatic emission features to the flux in the IRAC  $8.0 \mu\text{m}$  band could create the appearance of a red power-law continuum. Observations of starbursts detect these aromatic features to equivalent widths of  $\sim 0.1 \mu\text{m}$  and  $\sim 0.7 \mu\text{m}$ , respectively (Risaliti et al. 2006; Brandl et al. 2006). Due to the large bandpass of the  $8.0 \mu\text{m}$  IRAC channel, however, the  $3.3$  and  $6.2 \mu\text{m}$  emission features should have at most a 3% or 20% effect, respectively, on the total flux. (The models of Devriendt et al. (1999) predict a slightly larger (20%) effect due to the  $3.3 \mu\text{m}$  feature (Stern et al. 2005)). Given the small impact of these features and the small number of power-law galaxies with  $z < 0.5$  for which the  $8 \mu\text{m}$  feature could have an effect, we expect little contamination in the sample.

As a final check on the selection criteria, we plot in Figure 2 the ratio of X-ray to optical emission, a well-known AGN diagnostic (e.g. Maccacaro et al. 1988; Barger et al. 2003; Hornschemeier et al. 2003). Sources not detected in R-band

are assigned a lower limit of 26 mag, the approximate completeness limit of the R-band catalog of Capak et al. (2004). As was found by Alonso-Herrero et al. (2006), all of the power-law galaxies lie within the region typically populated by AGN or transition objects, given the current X-ray and optical limits. Four of the X-ray sources appear to be optically-faint with respect to their X-ray fluxes (e.g. Rigby et al. 2005).

### 3.4 Redshifts

Twenty one of the power-law galaxies have secure spectroscopic redshifts (Barger et al. 2001, 2002, 2003; Hornschemeier et al. 2001; Dawson et al. 2003; Cowie et al. 2004; Swinbank et al. 2004; Wirth et al. 2004 [Team Keck Redshift Survey]; Chapman et al. 2005; the Sloan Digital Sky Survey [SDSS]) and 2 additional sources have photometric redshifts from Barger et al. (2003). The spectroscopic redshifts range from  $z = 0.29$  to  $2.92$ , with a mean of  $z = 1.77$  and a median of  $z = 2.02$ . Of these 21 sources, 15 are classified as broad-line AGN, 4 have low  $S/N$  narrow emission lines, and 2 are AGN whose line width is not classified in the available literature.

We supplement the available spectroscopic redshifts with photometric redshifts. Photometric redshifts were estimated with an improved version of the method described in Pérez-González et al. (2005). Our technique is based on the construction of a complete set of SED templates composed from the galaxies with highly reliable spectroscopic redshifts (about 1500 sources selected in the CDF-N and CDF-S), which are later used to fit the SEDs of all the sample and estimate a photometric redshift. The technique described in Pérez-González et al. (2005) has been improved by significantly increasing the resolution of the templates. This is achieved by fitting the SEDs from the UV to the FIR to stel-

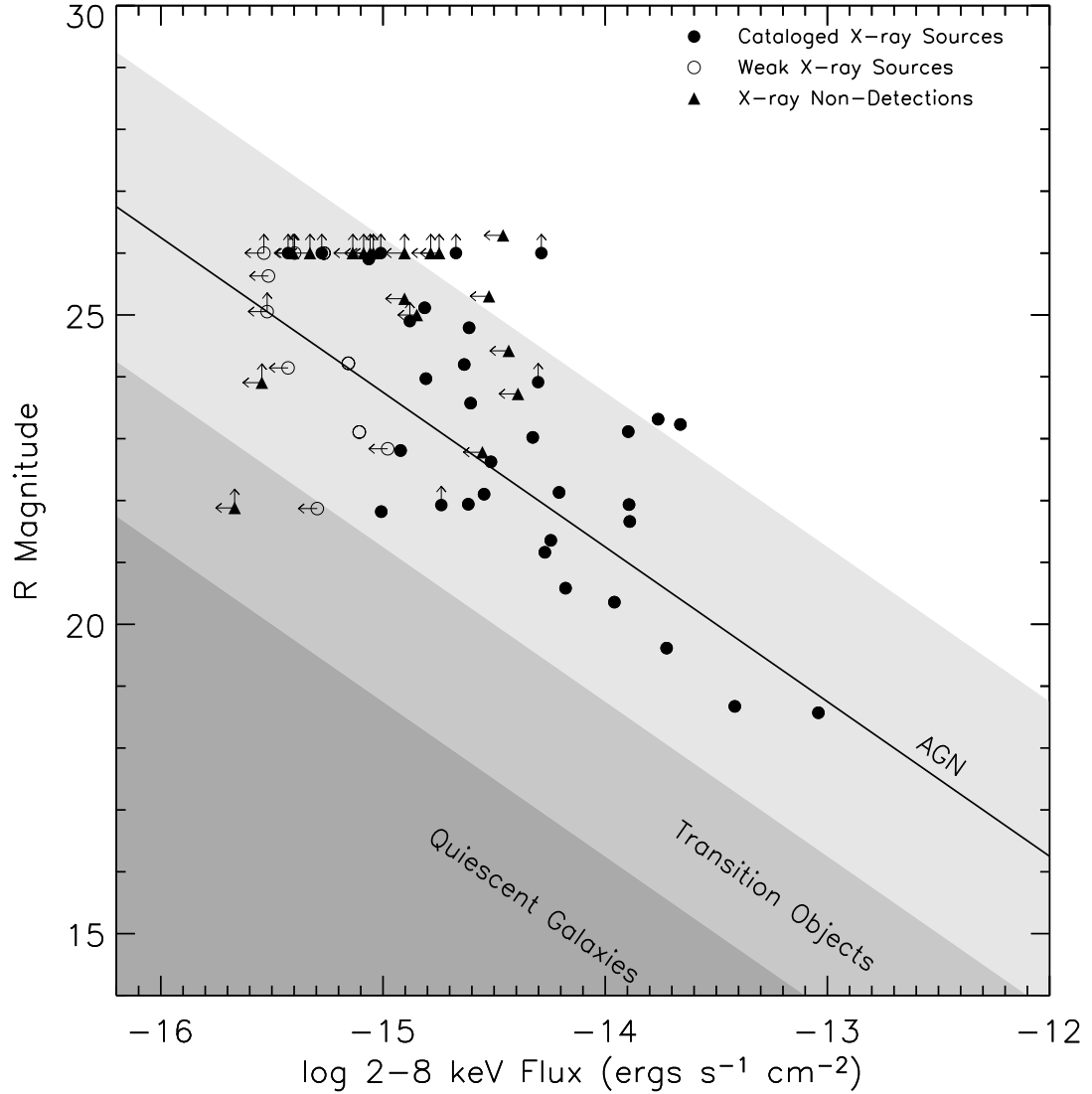


Figure 3.2 Relationship between the observed R-band magnitude and hard (2–8 keV) hard X-ray fluxes of power-law galaxies detected in the X-ray (filled circles), weakly-detected in the X-ray (open circles), and non-detected in the X-ray (triangles). For non-detected sources, we plot the  $5\sigma$  upper limits calculated as described in §5.1. The lines and shading represent the regions populated by AGN ( $f_X/f_R < |1|$ ), AGN and starbursts ( $-2 < \log f_X/f_R < -1$ ), and quiescent galaxies, starbursts, and LLAGN ( $\log f_X/f_R < -2$ ) (see Barger et al. 2003; Hornschemeier et al. 2003).

lar population synthesis and dust emission models. With this improvement, by comparing with all the available spectroscopic redshifts, our photometric redshifts have a value of  $\Delta(z)/(1+z) < 0.1$  for 88% of the galaxies in the CDF-N and CDF-S, and  $\Delta(z)/(1+z) < 0.2$  for 96% of these sources. The average (median) value of  $\Delta(z)/(1+z)$  is 0.05 (0.03). Further details about the photometric redshift technique can be found in P. G. Pérez-González et al. (2007, in preparation).

Using this technique, we estimated redshifts for an additional 20 sources, bringing the total number of power-law galaxies with redshifts or redshift estimates to 43 (69%). We plot in Figure 3 a comparison between the photometric and spectroscopic redshifts of what we will refer to as the ‘comparison sample’. This sample consists of the 1420 IRAC sources that meet the detection cut of  $S/N > 6$  in each of the IRAC bands and that have X-ray exposures  $\geq 0.5$  Ms; the 11 sources in the original power-law sample removed due to bad or blended photometry were excluded. The mean (median) spectroscopic redshift of the comparison sample is  $z = 0.74$  (0.64). Nearly half of the sources in the comparison sample have IRAC SEDs that cannot be fit by a power-law. Of the remaining galaxies, 6% and 40% can be fit by red ( $\alpha \leq -0.5$ ) or blue ( $\alpha \geq -0.5$ ) power-laws, respectively. Only 50% of the X-ray sources in the main CDF-N catalog (Alexander et al. 2003) meet the exposure time and IRAC  $S/N$  cuts used to define the comparison sample.

We also plot in Figure 3 the redshift comparison for those galaxies that meet the power-law criterion. While the power-law galaxies tend to be the farthest outliers, the agreement between the spectroscopic and photometric redshifts is reasonable, given the difficulty in assigning redshifts to sources with power-law dominated SEDs. Notably, several power-law galaxies at low spectroscopic redshifts have been assigned high redshifts by our photometric code. We take this



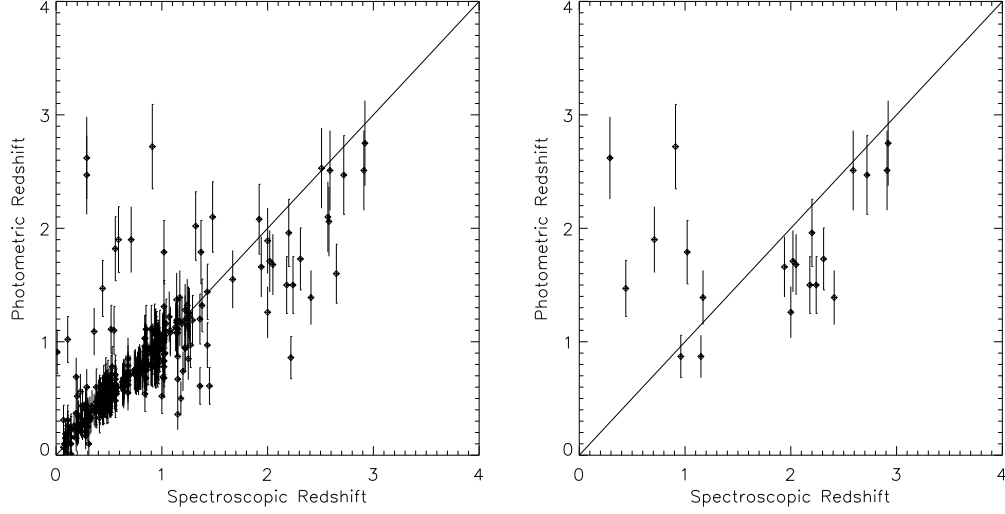


Figure 3.3 Comparison between secure spectroscopic redshifts and photometric redshifts for the comparison sample (left) and the power-law galaxy sample (right). We overplot on each panel a line of slope 1.

into consideration during the analysis, and rely on spectroscopic redshifts alone wherever possible. Nonetheless, the success rate in the photometric redshifts (defined by agreement to 2 standard deviations) implies that our total suite of redshifts is  $\geq 80\%$  correct.

As shown in Figure 4, the power-law galaxies tend to lie at significantly higher redshift than both the average source from the comparison sample and X-ray-detected members of the comparison sample, a trend that will be investigated further in §5.1.2. The power-law galaxies are comparable in number to the X-ray-detected AGN in the comparison sample at  $z > 2$ , although as will be discussed in §5.1, only half of the power-law galaxies are cataloged X-ray sources. Alonso-Herrero et al. (2006) similarly found that the power-law galaxies have a relatively flat redshift distribution (with the exception of a spike at  $z = 1.4$ ), with most sources lying at  $z > 1$ .

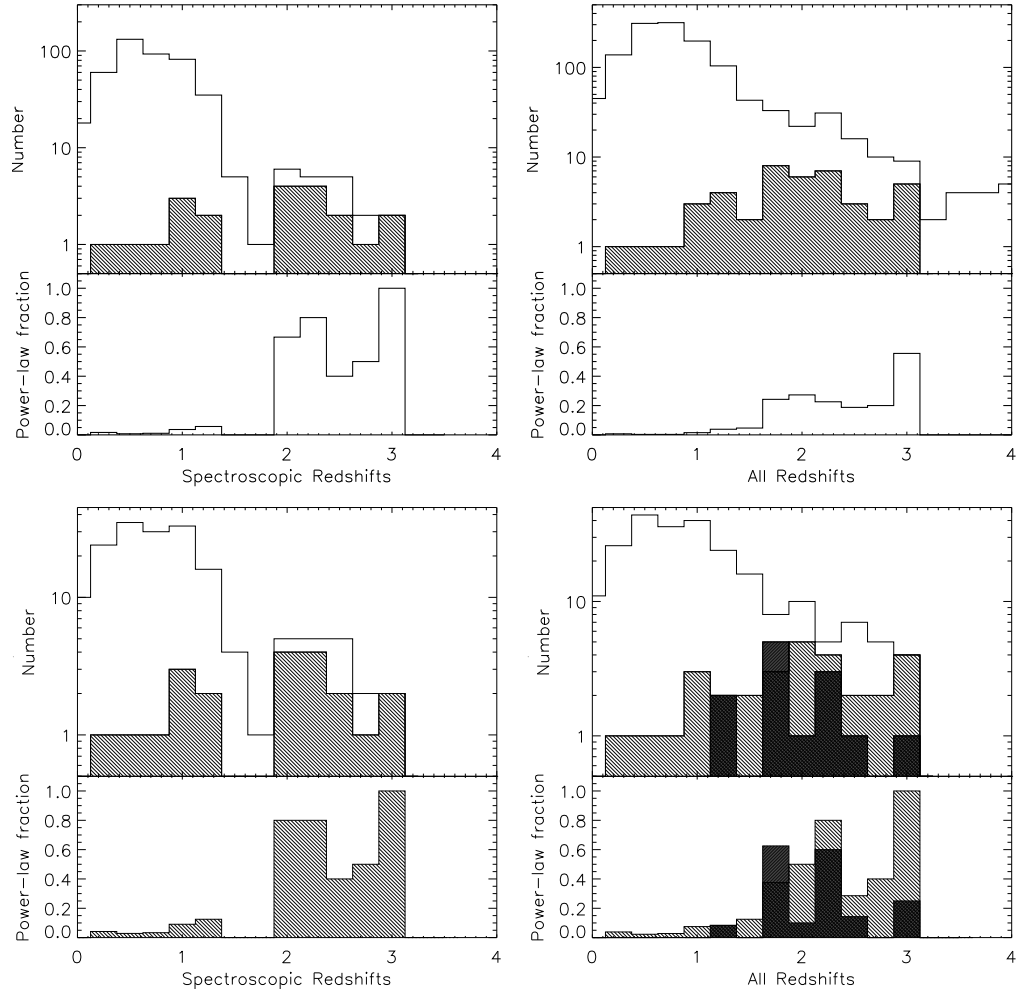


Figure 3.4 Top: Redshift distributions of the comparison sample (unshaded) and the power-law galaxy sample (shaded). Bottom: Redshift distributions of the X-ray-detected members of the comparison sample (unshaded) and the X-ray-detected (lightly shaded) and non-detected (heavily shaded) members of the power-law galaxy sample. The distributions based only on spectroscopic redshifts are shown on the left; those based on both photometric and spectroscopic redshifts are shown on the right. The lower panels give the power-law fraction, as a function of redshift.

### 3.5 Multiwavelength Properties

In the following sections, we discuss the X-ray, infrared, radio, and optical properties of the power-law galaxies. We show that while only 55% of them have cataloged X-ray counterparts, as many as 85% show evidence for faint X-ray emission. These X-ray-detected power-law galaxies make up a significant fraction of the X-ray luminous AGN in the comparison sample. As such, they are detectable to large distances, explaining the high redshifts of the sample.

The power-law galaxies also have a 24  $\mu\text{m}$  detection fraction of nearly unity, which we show to be indicative of an intrinsically luminous X-ray population. While only 29% of the sources have radio counterparts, and all but 2 are radio-quiet, nearly all of the power-law galaxies also have radio luminosities or upper limits consistent with that of AGN-dominated sources. It is therefore likely that the power-law galaxies not detected in the X-ray are intrinsically luminous AGN hidden behind high columns of obscuring gas and dust. The optical-MIR SEDs of the sample, which are flatter than the typical radio-quiet (star-formation subtracted) AGN SED (Elvis et al. 1994), also suggest increasing obscuration in the sources not detected in the X-ray. The optical detection fraction in the GOODS field is high (85%), with approximately 50% of the X-ray sources having compact optical counterparts.

#### 3.5.1 X-ray Emission

Of the 62 power-law galaxies, only 34 (55%) have cataloged X-ray counterparts in the Alexander et al. (2003) catalog of the 2 Ms CDF-N X-ray field<sup>1</sup>. Sources in the Alexander et al. (2003) catalog were chosen using WAVDETECT (Free-

---

<sup>1</sup>Throughout the paper, we use only the main source catalog from Alexander et al. (2003), and do not include the lower-significance X-ray sources detected in the supplemental optically bright X-ray catalog. No power-law galaxies and only 2 of the color-selected sources discussed in §6.2 are detected in the optically bright catalog.

man et al. 2002) with a false-positive probability threshold of  $1 \times 10^{-7}$ . For those power-law galaxies without X-ray counterparts, we searched for faint X-ray emission following the procedure outlined in Donley et al. (2005). We restricted this search to sources with off-axis angles of  $\theta < 10'$ , as sources that lie outside this radius fall in regions of rapidly changing exposure, and often have sky backgrounds that cannot be well-fit by Poisson distributions; 84% (52) of the power-law galaxies met this criterion. Of these, 58% (30) are detected in the Alexander et al. catalog, 19% (10) have at least a  $2.5\sigma$  detection in one X-ray band and at one encircled-energy radius (EER)<sup>2</sup>, and 13% (7) remain non-detected. Coadding the 7 non-detected power-law galaxies does not lead to a detection. Four additional sources lie too close to a cataloged X-ray source to search for faint emission, and 1 source (CDFN 8362) has an irregular sky background, preventing us from accurately testing for detection. If we assume that, like those sources for which we could test for emission, 85% of the 5 sources with nearby counterparts or irregular sky backgrounds would be detected (either strongly or weakly), then 85% of the power-law galaxies show evidence for X-ray emission, while 15% do not. Changing the detection threshold to 3, 4, and 5  $\sigma$  changes the detected fraction to 77%, 71%, and 65%, respectively.

We list the X-ray properties of the weakly-detected power-law galaxies in Table 2. If a source was not detected to  $> 2.5\sigma$  in one or more of the three bands, we list in Table 2 a conservative  $2.5\sigma$  upper limit, measured by adding any positive source flux to a  $2.5\sigma$  limit on the local sky background. The 70% EER was used to calculate both the source counts and sky background; no aperture correction was applied. For those power-law galaxies without a cataloged or weak X-ray counterpart, we list in Table 1  $5\sigma$  upper limits, calculated as described above.

---

<sup>2</sup>The 80% EER refers to the radius within which 80% of the energy is found.

Table 1. Power-law Galaxy Sample

ID	$\alpha_{2000}$	$\delta_{2000}$	$P_{\chi}^a$	$\alpha^b$	$z$	24 $\mu\text{m}$ Flux Density ( $\mu\text{Jy}$ )	1.4 GHz Flux Density ( $\mu\text{Jy}$ )	0.5-8 keV X-ray Flux ( $\text{ergs s}^{-1} \text{ cm}^{-2}$ )	$\log L_x^c$ ( $\text{ergs s}^{-1}$ )	X-ray Exposure (s)	$\theta^d$ (')	$q^e$
CDFN 11348	12 35 25.58	62 16 09.41	0.86	-0.86	...	204.0	< 80.0	< 8.10E-16	...	9.59E+05	9.6	> 0.41
CDFN 17315	12 35 29.37	62 12 56.53	0.22	-1.94	2.41	251.9	135.0	7.02E-15	44.5	7.43E+05	8.9	0.27
CDFN 11516	12 35 37.11	62 17 23.40	0.49	-0.89	2.05	234.9	< 80.0	5.27E-15	44.2	9.00E+05	8.7	> 0.47
CDFN 07514	12 35 38.08	62 19 40.56	0.86	-0.79	$2.97 \pm 0.40$	< 157.2	< 80.0	2.00E-15	44.2	9.86E+05	9.7	...
CDFN 12939	12 35 38.52	62 16 42.91	0.69	-1.15	0.71	1413.8	3550.0	2.23E-13	44.7	9.60E+05	8.3	-0.40
CDFN 14642	12 35 43.35	62 16 17.15	0.84	-1.17	$2.36 \pm 0.34$	< 117.6	< 80.0	9.19E-16	43.6	1.25E+06	7.6	...
CDFN 08362	12 35 46.64	62 20 13.23	0.57	-1.39	...	118.5	< 80.0	< 7.85E-16	...	9.66E+05	9.3	> 0.17
CDFN 10934	12 35 48.89	62 19 04.46	0.26	-1.58	...	115.4	< 80.0	< 4.92E-16	...	9.84E+05	8.4	> 0.16
CDFN 16796	12 35 49.43	62 15 36.52	0.22	-0.79	2.20	585.6	74.6	1.34E-15	43.7	1.58E+06	6.8	0.89
CDFN 25218	12 35 50.36	62 10 41.70	0.11	-2.04	...	< 108.5	< 80.0	4.21E-16	...	7.04E+05	7.2	...
CDFN 20981	12 35 54.30	62 13 43.37	0.95	-0.69	...	131.7	< 80.0	< 2.04E-16	...	1.74E+06	6.0	> 0.22
CDFN 25248	12 36 06.37	62 12 32.41	0.81	-0.60	$2.89 \pm 0.39$	139.2	< 80.0	9.64E-16	43.8	1.81E+06	4.8	> 0.24
CDFN 33052	12 36 08.87	62 08 03.56	0.10	-1.37	...	151.8	< 80.0	< 4.67E-16	...	5.43E+05	7.3	> 0.28
CDFN 27463	12 36 11.95	62 11 47.18	0.77	-0.53	$2.92 \pm 0.39$	180.3	< 80.0	< 1.23E-16	< 42.9	1.68E+06	4.5	> 0.35
CDFN 31054	12 36 14.04	62 09 47.93	0.78	-0.59	$1.65 \pm 0.27$	60.8	< 80.0	< 2.46E-16	< 42.6	1.79E+06	5.6	> -0.12
CDFN 23661	12 36 22.98	62 15 26.28	0.16	-1.40	2.59	454.5	< 80.0	1.88E-14	45.0	1.85E+06	3.0	> 0.75
CDFN 39358	12 36 23.37	62 06 05.23	0.21	-1.92	$1.86 \pm 0.29$	479.5	71.7	4.71E-16	43.0	5.42E+05	8.3	0.83
CDFN 37928	12 36 29.21	62 07 37.61	0.91	-0.59	$1.35 \pm 0.23$	161.6	< 80.0	< 2.15E-16	< 42.3	1.77E+06	6.6	> 0.31
CDFN 37999	12 36 32.59	62 07 58.95	0.11	-2.14	2.00	711.8	90.6	1.83E-15	43.7	1.78E+06	6.2	0.90
CDFN 27641	12 36 35.60	62 14 23.51	0.86	-1.82	2.02	1345.2	87.8	2.52E-15	43.8	1.92E+06	1.2	1.19
CDFN 28773	12 36 36.66	62 13 46.46	0.63	-0.74	0.96	459.6	< 80.0	1.01E-14	43.7	1.91E+06	1.1	> 0.76
CDFN 14667	12 36 36.90	62 22 27.27	0.57	-2.03	...	292.9	< 80.0	3.45E-15	...	1.06E+06	8.6	> 0.56
CDFN 37334	12 36 37.08	62 08 51.90	0.32	-0.90	$1.71 \pm 0.27$	301.7	71.1	1.19E-16	42.3	1.78E+06	5.2	0.63
CDFN 44902	12 36 40.59	62 04 51.34	0.27	-0.87	$1.16 \pm 0.22$	166.6	< 80.0	< 8.28E-16	< 42.8	6.96E+05	9.1	> 0.32
CDFN 24409	12 36 42.22	62 17 10.89	0.65	-0.80	2.72	91.7	< 80.0	3.35E-15	44.3	1.65E+06	3.2	> 0.06
CDFN 11965	12 36 42.23	62 24 39.01	0.59	-0.71	$1.90 \pm 0.29$	480.4	82.1	1.95E-15	43.7	9.62E+05	10.7	0.77
CDFN 14360	12 36 47.27	62 23 49.06	0.29	-1.28	...	216.0	< 80.0	< 7.05E-16	...	9.75E+05	9.9	> 0.43
CDFN 18906	12 36 48.30	62 21 06.89	0.76	-1.45	...	149.4	< 80.0	< 2.94E-16	...	1.68E+06	7.2	> 0.27
CDFN 41981	12 36 49.66	62 07 37.84	0.50	-2.30	$1.54 \pm 0.25$	1239.3	307.0	2.59E-14	44.6	1.74E+06	6.3	0.61

Table 1—Continued

ID	$\alpha_{2000}$	$\delta_{2000}$	$P_X^a$	$\alpha^b$	$z$	24 $\mu\text{m}$ Flux Density ( $\mu\text{Jy}$ )	1.4 GHz Flux Density ( $\mu\text{Jy}$ )	0.5-8 keV X-ray Flux ( $\text{ergs s}^{-1} \text{ cm}^{-2}$ )	$\log L_X^c$ ( $\text{ergs s}^{-1}$ )	X-ray Exposure (s)	$\theta^d$ (')	$q^e$
CDFN 49937	12 36 58.76	62 04 01.80	0.12	-1.17	0.29	138.7	< 80.0	9.75E-15	42.4	7.33E+05	10.1	> 0.24
CDFN 19080	12 36 58.96	62 22 14.89	0.28	-1.94	...	106.6	< 80.0	< 4.41E-16	...	1.62E+06	8.4	> 0.12
CDFN 14046	12 36 59.07	62 25 21.81	0.31	-1.04	$2.82 \pm 0.38$	164.3	< 80.0	1.16E-14	44.9	8.68E+05	11.5	> 0.31
CDFN 44836	12 37 01.69	62 07 20.21	0.56	-3.15	...	323.6	< 80.0	8.56E-16	...	1.74E+06	6.9	> 0.61
CDFN 53291	12 37 01.70	62 02 22.05	0.10	-1.59	$2.17 \pm 0.32$	99.6	< 80.0	< 1.89E-15	< 43.8	6.41E+05	11.8	> 0.10
CDFN 45610	12 37 06.59	62 07 26.83	0.79	-1.05	...	-1.0	< 80.0	< 7.08E-16	...	1.76E+06	7.0	...
CDFN 29120	12 37 06.90	62 17 02.37	0.29	-1.06	1.02	766.3	< 80.0	3.54E-14	44.3	1.87E+06	3.9	> 0.98
CDFN 16936	12 37 07.01	62 24 27.81	0.92	-1.25	...	161.3	< 80.0	< 1.00E-15	...	1.08E+06	10.8	> 0.30
CDFN 45284	12 37 09.85	62 08 00.82	0.39	-1.40	2.18	128.6	< 80.0	2.11E-14	44.9	1.71E+06	6.6	> 0.21
CDFN 20246	12 37 10.00	62 22 58.92	0.20	-1.42	$1.41 \pm 0.24$	318.6	708.0	5.21E-15	43.8	1.60E+06	9.4	-0.35
CDFN 38580	12 37 12.07	62 12 11.61	0.70	-1.14	2.91	< 80.0	< 80.0	3.84E-16	43.4	1.72E+06	3.5	...
CDFN 32673	12 37 13.72	62 15 45.14	0.52	-1.14	...	129.8	< 80.0	4.46E-16	...	1.90E+06	3.7	> 0.21
CDFN 43967	12 37 14.06	62 09 16.80	0.38	-0.96	$1.84 \pm 0.28$	105.3	< 80.0	3.57E-15	43.9	1.83E+06	5.7	> 0.12
CDFN 30147	12 37 16.69	62 17 33.18	0.56	-1.75	1.15	1015.7	346.0	2.17E-14	44.2	1.84E+06	5.1	0.47
CDFN 50281	12 37 16.99	62 05 53.05	0.59	-1.05	1.94	398.5	< 80.0	1.94E-15	43.7	7.26E+05	8.9	> 0.70
CDFN 28149	12 37 17.90	62 18 55.56	0.17	-1.24	2.24	195.2	< 80.0	9.95E-15	44.6	1.78E+06	6.2	> 0.39
CDFN 46227	12 37 21.72	62 08 50.41	0.84	-0.80	$2.56 \pm 0.36$	292.1	< 80.0	< 2.43E-16	< 43.1	1.77E+06	6.6	> 0.56
CDFN 51788	12 37 23.03	62 05 39.45	0.99	-1.08	$2.28 \pm 0.33$	146.6	78.5	< 2.65E-15	< 44.0	7.43E+05	9.4	0.27
CDFN 27360	12 37 26.58	62 20 26.46	0.14	-2.26	$1.86 \pm 0.29$	777.7	102.0	1.40E-15	43.5	1.40E+06	8.0	0.88
CDFN 38126	12 37 28.65	62 14 22.56	0.58	-1.80	...	226.1	< 80.0	1.20E-16	...	1.82E+06	5.0	> 0.45
CDFN 40913	12 37 30.77	62 12 58.50	0.97	-1.78	...	139.3	107.0	< 2.08E-16	...	1.79E+06	5.3	0.11
CDFN 39529	12 37 36.83	62 14 28.72	0.20	-1.44	...	118.9	57.8	6.21E-15	...	1.74E+06	6.0	0.31
CDFN 26243	12 37 39.78	62 22 39.67	0.38	-2.08	...	218.2	< 80.0	< 3.33E-15	...	6.12E+05	10.7	> 0.44
CDFN 44598	12 37 41.00	62 12 00.29	0.26	-0.63	1.17	558.2	< 80.0	2.02E-14	44.2	1.76E+06	6.7	> 0.84
CDFN 34143	12 37 42.58	62 18 11.67	0.16	-1.55	2.31	149.6	< 80.0	2.08E-14	44.9	1.69E+06	7.8	> 0.27
CDFN 44751	12 37 44.67	62 12 18.71	0.21	-0.94	$1.69 \pm 0.27$	416.1	67.3	2.88E-16	42.7	1.76E+06	7.1	0.79
CDFN 40112	12 37 57.32	62 16 27.57	0.28	-1.55	2.92	122.3	< 80.0	4.68E-15	44.5	1.70E+06	8.7	> 0.18
CDFN 54722	12 37 57.55	62 08 00.51	0.65	-1.13	...	174.9	< 80.0	< 1.01E-15	...	6.41E+05	10.3	> 0.34
CDFN 49940	12 37 59.62	62 11 02.09	0.58	-1.42	0.91	2132.0	85.0	1.52E-13	44.8	7.33E+05	9.1	1.40

While Alonso-Herrero et al. (2006) found that their sample of power-law galaxies included about 1/3 of the hard X-ray sources with  $24\ \mu\text{m}$  detections, our more conservative selection detects only 14% of the X-ray sources in the Alexander et al. (2003) catalog that meet our exposure time cut of 0.5 Ms and that have  $24\ \mu\text{m}$  flux densities of  $S_{24} > 80\ \mu\text{Jy}$ . (Further restricting the comparison to those X-ray sources that also meet our IRAC significance cut of  $S/N > 6$  only increases the selection fraction to 17%). If we consider only those X-ray and MIR sources in the CDF-N catalog with  $\log L_x(\text{erg s}^{-1}) > 42$  (to rule out sources dominated by star-formation), the X-ray-detected power-law galaxies comprise  $\sim 20\%$  of the X-ray sources (with exposures of  $> 0.5$  Ms) detected at  $24\ \mu\text{m}$  (to  $S_{24} > 80\ \mu\text{Jy}$ ). Because our selection criteria were designed to be quite robust, we exclude a number of IRAC color-selected AGN candidates with power-law like emission (see §6). Determining the intrinsic proportion of “power-law” AGN will therefore require a more careful analysis. As mentioned in §4 and shown in Figure 4, the power-law galaxies comprise a significantly higher fraction of the high-redshift X-ray sources.

#### 3.5.1.1 Dependence on Sample Properties

We plot in Figure 5 the X-ray detection fraction for the power-law galaxies as a function of redshift, X-ray exposure time, power-law slope, and power-law fit probability, where we consider as ‘detected’ only those sources with cataloged X-ray counterparts. For the sources with redshift estimates, X-ray detection appears to be relatively insensitive to redshift. The X-ray detection fraction, however, is higher for those sources with redshift estimates (70%) than for the full power-law sample (55%). The detection fraction as a function of X-ray exposure time is lower than average at the lowest exposures, as expected, but does not increase substantially at the highest exposures. We note that in our analysis of the X-ray

Table 1—Continued

ID	$\alpha_{2000}$	$\delta_{2000}$	$P_{\chi}$ <sup>a</sup>	$\alpha$ <sup>b</sup>	$z$	24 $\mu\text{m}$ Flux Density ( $\mu\text{Jy}$ )	1.4 GHz Flux Density ( $\mu\text{Jy}$ )	0.5-8 keV X-ray Flux ( $\text{ergs s}^{-1} \text{ cm}^{-2}$ )	$\log L_{\text{x}}$ <sup>c</sup> ( $\text{ergs s}^{-1}$ )	X-ray Exposure (s)	$\theta$ <sup>d</sup> ( $'$ )	$q$ <sup>e</sup>
CDFN 45792	12 38 00.94	62 13 35.90	0.43	-0.72	0.44	4092.5	190.0	7.78E-14	43.7	1.44E+06	8.8	1.33
CDFN 53792	12 38 31.18	62 12 21.98	0.59	-0.77	$1.63 \pm 0.26$	297.0	< 80.0	3.76E-15	43.8	6.62E+05	12.4	> 0.57
CDFN 53753	12 38 32.19	62 12 30.60	0.25	-0.66	$1.63 \pm 0.26$	198.4	< 80.0	< 2.79E-15	< 43.7	6.15E+05	12.5	> 0.39
CDFN 54888	12 38 34.09	62 12 05.88	0.67	-1.75	$1.96 \pm 0.30$	476.4	< 80.0	< 1.59E-15	< 43.6	5.57E+05	12.8	> 0.77

<sup>a</sup>Chi-squared probability (see §3)<sup>b</sup>IRAC spectra index;  $f_{\nu} \propto \nu^{\alpha}$ <sup>c</sup>0.5-8 keV<sup>d</sup>X-ray off-axis angle<sup>e</sup> $q = \log (f_{24 \mu\text{m}} / f_{1.4 \text{ GHz}})$



Table 2. X-ray Properties of X-ray Weakly-Detected Power-law Galaxies

Source	z	X-ray Band <sup>a</sup>	EER (%)	Detection $\sigma$	Aperture Corrected Count Rate ( $s^{-1}$ )	$\Gamma$	Flux ( $erg\ s^{-1}\ cm^{-2}$ )	H/S <sup>b</sup>	log $N_H$ ( $cm^{-2}$ )
CDFN14642	2.36	Full	80	4.6	4.44E-05	0.28	9.19E-16	11.17	$23.7^{+0.1}_{-0.1}$
		Hard	70	3.3	2.33E-05		6.98E-16		
		Soft	60	3.3	1.27E-05		6.08E-17		
CDFN20981	...	Full	80	$\leq 2.5$	$\leq 1.44E-05$	$\geq 0.41$	$\leq 1.68E-16$	$\leq 6.96$	$\leq 22.5^{+0.1}_{-0.1} - \leq 23.7^{+0.1}_{-0.1}$
		Hard	80	$\leq 2.5$	$\leq 1.00E-05$		$\leq 2.31E-16$		
		Soft	60	3.3	6.35E-06		3.18E-17		
CDFN25218	...	Full	80	3.5	3.61E-05	$\leq 0.61$	4.21E-16	$\geq 5.58$	$\geq 22.4^{+0.1}_{-0.1} - \geq 23.6^{+0.1}_{-0.1}$
		Hard	70	2.8	2.35E-05		5.42E-16		
		Soft	80	$\leq 2.5$	$\leq 1.86E-05$		$\leq 9.33E-17$		
CDFN37334	1.71	Full	80	2.6	1.02E-05	$\geq 0.20$	1.19E-16	$\leq 8.83$	$\leq 23.3^{+0.1}_{-0.1}$
		Hard	80	$\leq 2.5$	$\leq 1.17E-05$		$\leq 2.70E-16$		
		Soft	70	3.2	5.85E-06		2.93E-17		
CDFN37928	1.35	Full	70	$\leq 2.5$	$\leq 9.22E-06$	$\geq 0.69$	$\leq 1.07E-16$	$\leq 5.09$	$\leq 22.9^{+0.1}_{-0.1}$
		Hard	70	$\leq 2.5$	$\leq 8.10E-06$		$\leq 1.87E-16$		
		Soft	60	2.8	7.03E-06		3.52E-17		
CDFN38126	...	Full	80	2.7	1.03E-05	...	1.20E-16	...	...
		Hard	80	$\leq 2.5$	$\leq 1.03E-05$		$\leq 2.38E-16$		
		Soft	80	$\leq 2.5$	$\leq 6.97E-06$		$\leq 3.49E-17$		
CDFN39358	1.86	Full	80	2.8	4.04E-05	$\leq 0.14$	4.71E-16	$\geq 9.42$	$\geq 23.4^{+0.1}_{-0.1}$
		Hard	80	2.6	3.39E-05		7.82E-16		
		Soft	70	$\leq 2.5$	$\leq 1.59E-05$		$\leq 7.97E-17$		
CDFN44751	1.69	Full	80	3.7	2.47E-05	$\geq 0.52$	2.88E-16	$\leq 6.21$	$\leq 23.2^{+0.1}_{-0.1}$
		Hard	80	$\leq 2.5$	$\leq 2.01E-05$		$\leq 4.64E-16$		
		Soft	80	4.2	1.43E-05		7.17E-17		
CDFN44902	1.16	Full	70	$\leq 2.5$	$\leq 4.54E-05$	$\geq 1.05$	$\leq 5.29E-16$	$\leq 3.41$	$\leq 22.5^{+0.1}_{-0.2}$
		Hard	80	$\leq 2.5$	$\leq 2.78E-05$		$\leq 6.41E-16$		
		Soft	60	5.0	3.60E-05		1.80E-16		
CDFN46227	2.56	Full	60	$\leq 2.5$	$\leq 1.04E-05$	$\geq 0.83$	$\leq 1.21E-16$	$\leq 4.37$	$\leq 23.3^{+0.1}_{-0.2}$
		Hard	60	$\leq 2.5$	$\leq 6.83E-06$		$\leq 1.58E-16$		
		Soft	60	2.7	6.91E-06		3.46E-17		

<sup>a</sup>Full band = 0.5-8 keV; Hard band = 2-8 keV; Soft band = 0.5-2 keV<sup>b</sup>Flux ratio corrected for Galactic absorption

detection fraction in §5.1, we considered only those power-law galaxies with off-axis angles of  $\theta < 10'$ , and therefore excluded 6 of the 10 sources in the lowest two exposure bins. There is significant variation in the detection fraction as a function of power-law index, with an increase at the steepest indices and a possible decrease at the flattest indices. The power-law fit probability, however, appears to have a minimal effect on the X-ray detection fraction, with only a slight drop towards the highest values of  $P_x$  (recall that  $P_x = 0.5$ , not  $P_x = 1$ , is ideal). These results suggest that the X-ray detection fraction of the power-law sample is relatively insensitive to variations in redshift, X-ray exposure time, and power-law properties, to the limits imposed by our selection criteria.

### 3.5.1.2 X-ray Luminosity

We plot in Figure 6 the observed 0.5-8 keV X-ray luminosities of the power-law galaxies and the members of the comparison sample detected in the X-ray catalog. The luminosities of sources selected via the Lacy et al. selection criteria (see §6.2) are also plotted. As was discussed by Alonso-Herrero et al. (2006), power-law galaxies have X-ray luminosities typical of AGN ( $\log L_x(\text{ergs s}^{-1}) \geq 42$ ), and significantly higher than those of star-forming galaxies ( $\log L_x(\text{ergs s}^{-1}) < 41$ ).

The power-law galaxies comprise a significant fraction of the high luminosity sample. This is not surprising, as the power-law selection requires the AGN to be energetically dominant, and therefore preferentially selects the most luminous AGN. To illustrate the effect of X-ray luminosity on the AGN contribution to the optical through MIR continuum, we plot in Figure 7 the median rest- and observed-frame optical-MIR SEDs of the X-ray-detected members of the comparison sample, as a function of X-ray luminosity. We normalize the SEDs to the  $12 \mu\text{m}$  monochromatic power, which, for the rest-frame comparison, is representative of bolometric luminosity and independent of galaxy or AGN type (Spinoglio

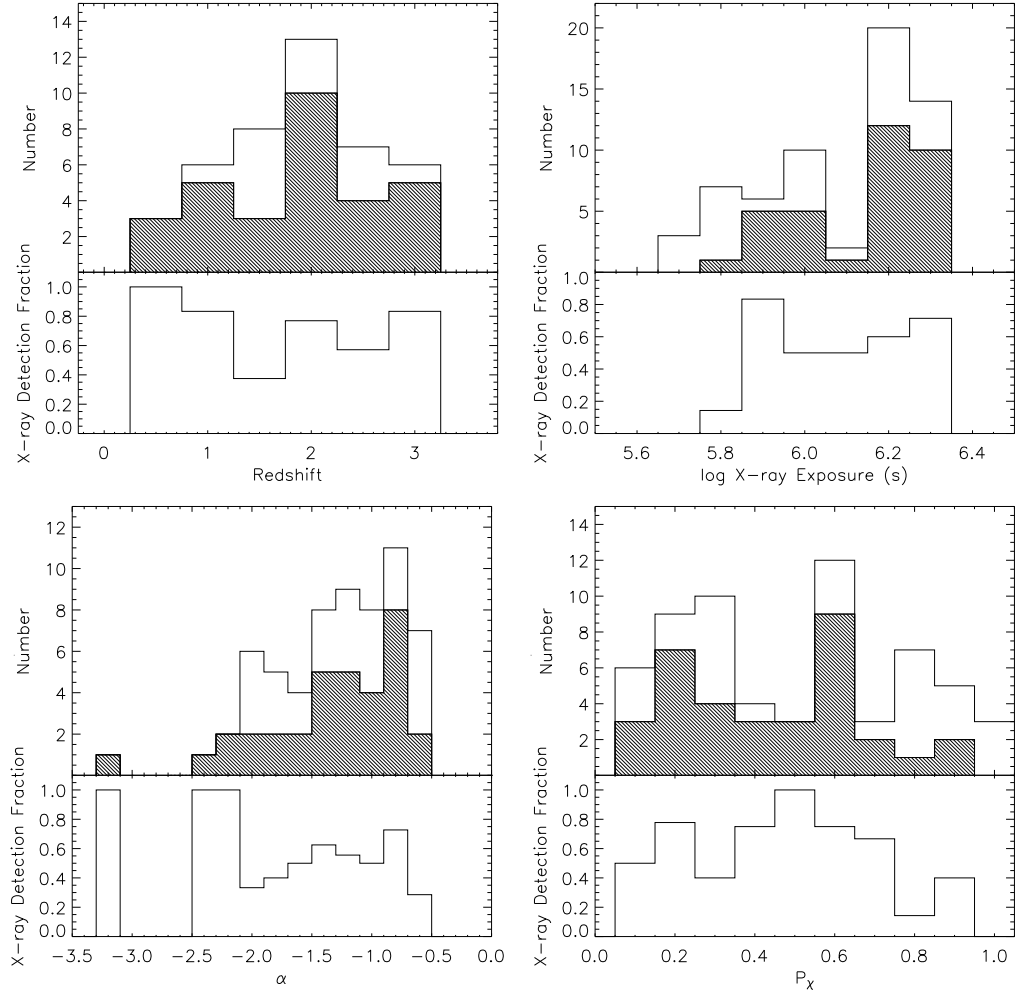


Figure 3.5 X-ray detection fraction as a function of redshift (top left), X-ray exposure time (top right), power-law spectral index  $\alpha$  (bottom left), and power-law fit probability  $P_\chi$  (bottom right). Shaded histograms represent the X-ray-cataloged power-law galaxies; clear histograms represent the full power-law sample.

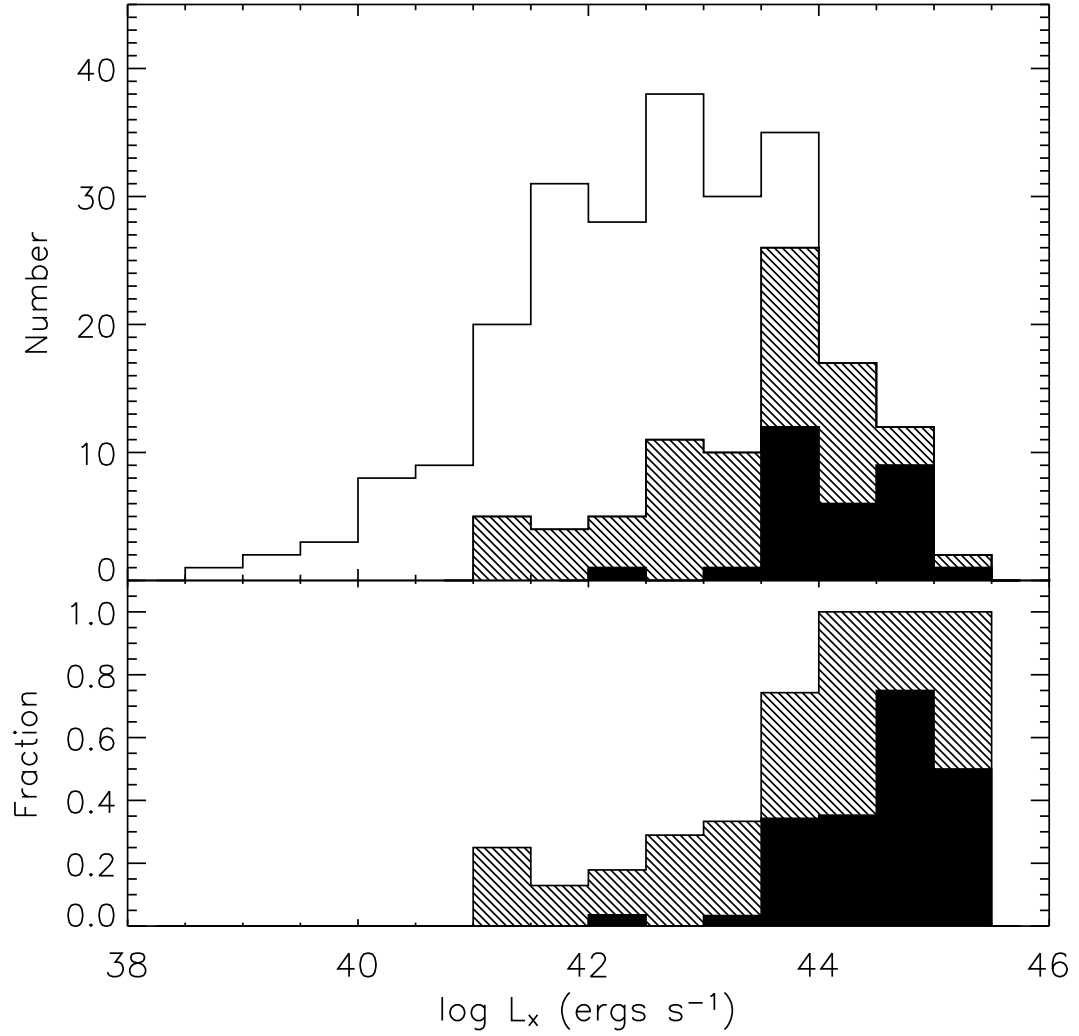


Figure 3.6 Comparison between the observed 0.5-8 keV X-ray luminosity ( $L_x$ ) distributions of the cataloged X-ray sources in the comparison sample (unshaded histogram), the power-law sample (filled histogram), and the Lacy et al. sample (lightly shaded histogram; see §6.2). The lower panel gives the fraction of the X-ray sources that meet the power-law or Lacy et al. criteria.

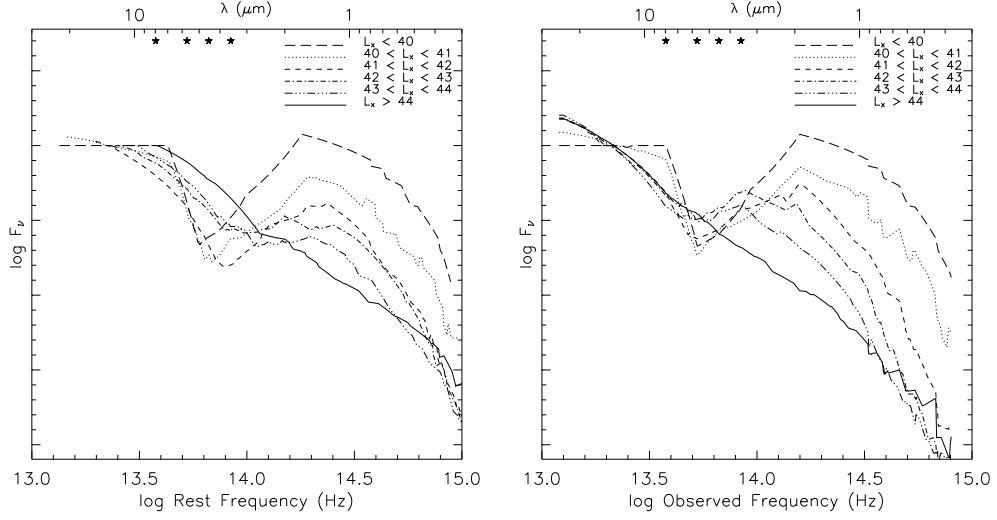


Figure 3.7 Median rest-frame (left) and observed-frame (right) SEDs of the X-ray-detected members of the comparison sample, as a function of observed 0.5-8 keV luminosity (in units of  $\text{ergs s}^{-1}$ ). Stars indicate the wavelengths of the four IRAC bands.

& Malkan 1989). As can be seen, low-luminosity X-ray sources are dominated by the  $1.6 \mu\text{m}$  stellar bump in the optical-NIR bands (e.g. Alonso-Herrero et al. 2004). The relative strength of this feature decreases with increasing X-ray luminosity, and disappears almost entirely at luminosities of  $L_x > 44.0$ , taking on the characteristic power-law shape required by the selection used here. The fraction of X-ray sources in the comparison sample that can be fit by red, AGN-dominated power-laws ( $\alpha \leq -0.5$ ) is therefore a strong function of X-ray luminosity, increasing from 0% at  $\log L_x(\text{ergs s}^{-1}) = 41 - 42$  to 3%, 24%, and 59% at luminosity limits of  $\log L_x(\text{ergs s}^{-1}) = 42 - 43$ ,  $43 - 44$ , and  $44 - 45$ . Blue power-laws ( $\alpha > -0.5$ ) in the IRAC bands are indicative of stellar-photosphere-dominated SEDs in the rest-frame near-infrared (for  $z \leq 1.5$ ). The corresponding percentages of X-ray sources fit by blue power-laws are 39%, 46%, 41%, and 14%, showing the reduced proportion of stellar-dominated objects in the highest luminosity bin.

A similar trend is seen as a function of redshift. In a flux limited sample

such as this, low-luminosity AGN are detected primarily at low redshift, whereas high-luminosity AGN are detectable over a range of redshifts (see Figure 8). To first order, the high redshifts of the power-law sample can therefore be explained by their preferentially high luminosities. In addition, AGN with high X-ray luminosities have comoving space densities that peak at higher redshifts than low-luminosity AGN, amplifying the selection effect discussed above (e.g. Ueda et al. 2003). The color-redshift relation for AGN may also play a minor role in this trend. Richards et al. (2006) show that the  $3.6\ \mu\text{m}$  to  $5.8\ \mu\text{m}$  color ( $\log(S_{5.8}/S_{3.6})$ ) of an AGN with the median radio-quiet SED (Elvis et al. 1994) shifts from 0.2 at  $z = 0$  to 0.44 at  $z = 1.5$  before falling to 0.08 at  $z = 4$ . As will be shown in §5.4, however, the power-law galaxies tend to have flatter SEDs than the Elvis et al. (1994) AGN template and as such, they should have colors less sensitive to changes in redshift.

### 3.5.2 $24\ \mu\text{m}$ Emission

Unlike Alonso-Herrero et al. (2006), we do not require a  $24\ \mu\text{m}$  detection for source selection. However, all but 5 of the power-law galaxies have a cataloged  $24\ \mu\text{m}$  counterpart within a  $2''$  radius. The  $24\ \mu\text{m}$  flux densities are listed in Table 1. Of the remaining 5 sources, 3 (CDFN 7514, CDFN 14642, and CDFN 25218) have a cataloged counterpart within  $2\text{--}3''$ . For these power-law galaxies, we use the flux density of the nearby source as an upper limit if it exceeds our nominal limit of  $80\ \mu\text{Jy}$ . One additional power-law galaxy, CDFN 45610, lies within the PSF of a bright  $24\ \mu\text{m}$  source, preventing a detailed analysis of its properties. Only one source, CDFN 38580, an X-ray-detected power-law galaxy at  $z = 2.91$  (Chapman et al. 2005), shows no evidence for  $24\ \mu\text{m}$  emission. As was found for the power-law X-ray sources in the EGS (Barmby et al. 2006), there is only weak agreement between the  $24\ \mu\text{m}$  flux densities and those predicted by extending the

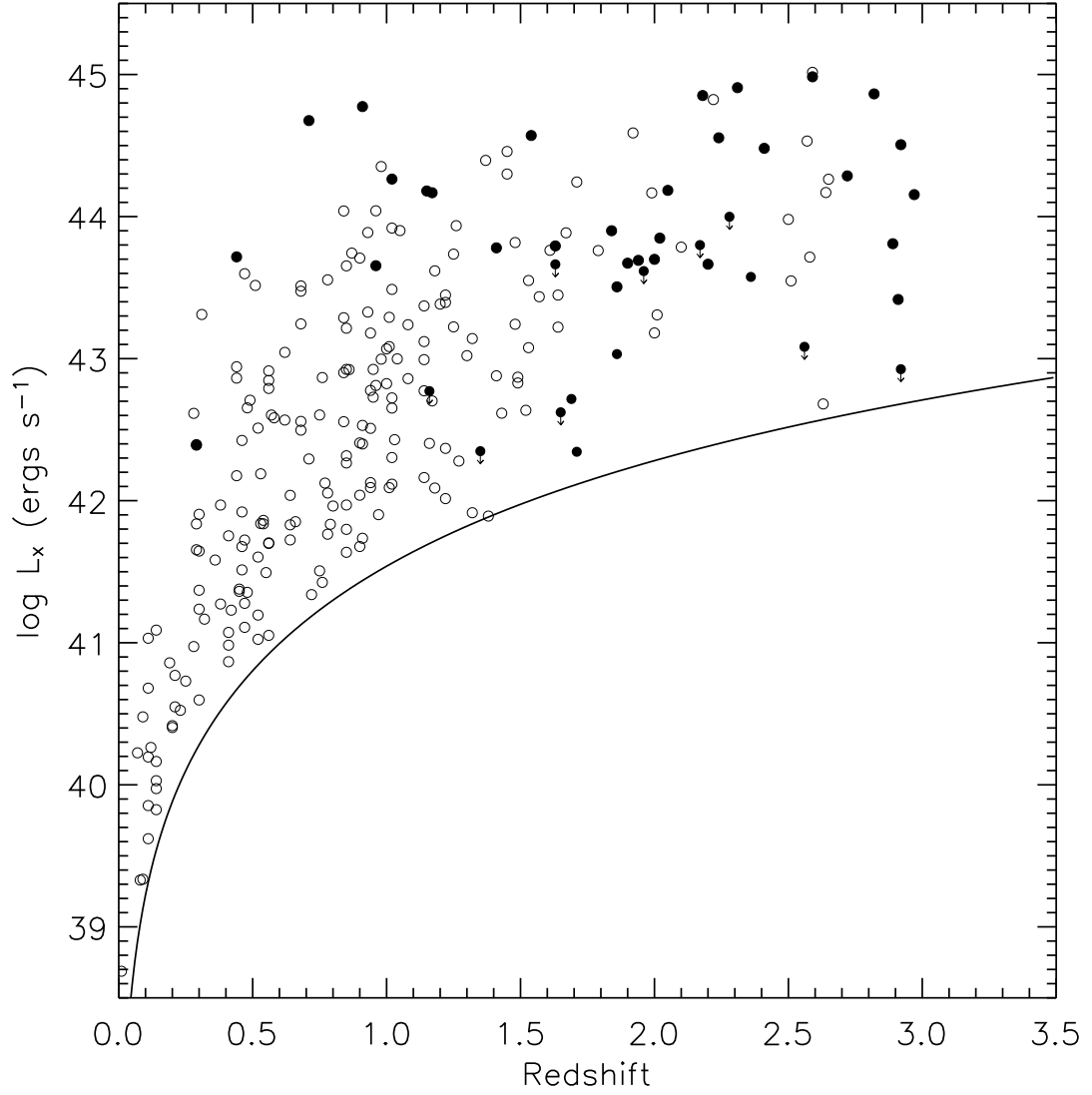


Figure 3.8 X-ray luminosity vs. redshift for the X-ray sources in the comparison sample (open circles) and the power-law galaxies with available redshift estimates (filled circles). The on-axis X-ray flux limit of  $7 \times 10^{-17} \text{ erg s}^{-1} \text{ cm}^{-2}$  (Alexander et al. 2003) is plotted for reference.

IRAC power-law fit, with the X-ray-detected and X-ray non-detected power-law galaxies having observed  $24\ \mu\text{m}$  flux densities that tend to lie within only 53% and 60% of the predicted values, respectively.

The fraction of AGN in MIR samples has been shown to increase with increasing  $24\ \mu\text{m}$  flux density (Treister et al. 2005; Brand et al. 2006) in general agreement with the models of Pearson (2005). We would therefore expect luminous AGN in a flux-limited sample to have a high  $24\ \mu\text{m}$  detection fraction, such as that seen for the power-law sample. To test this, we plot in Figure 9 the  $24\ \mu\text{m}$  detection fraction for the members of the comparison sample as a function of X-ray luminosity. The detection fraction is relatively high ( $\sim 90\%$ ) at X-ray luminosities typical of starburst galaxies ( $\log L_x(\text{ergs s}^{-1}) < 41$ , see Alexander et al. 2002a). This is not surprising, as rapidly star-forming galaxies with large numbers of X-ray binaries will also be luminous infrared sources. The detection fraction then drops to  $\sim 65\%$  at luminosities typical of starbursts and low-luminosity AGN ( $41 < \log L_x(\text{ergs s}^{-1}) < 42$ ) before rising to 100% at  $\log L_x(\text{ergs s}^{-1}) > 44 - 45$ . Because the comparison sample is composed of objects with high significance IRAC MIR detections, the  $24\ \mu\text{m}$  detection fraction is higher than that of an unbiased sample. For comparison, Rigby et al. (2004) find an overall  $24\ \mu\text{m}$  detection fraction of only 60% for hard X-ray sources in the CDF-S. Nevertheless, for AGN-dominated sources, a high  $24\ \mu\text{m}$  detection fraction like that of the power-law galaxies accompanies an X-ray-luminous AGN population. We note that of the 18 power-law galaxies not detected in X-rays, all but one are detected at  $24\ \mu\text{m}$ , with the exception being CDFN 45610, the power-law galaxy that lies in the PSF of a bright  $24\ \mu\text{m}$  source. Therefore, if these sources are AGN-dominated as expected, it is likely that they, along with the rest of the power-law sample (§5.1.2 and Figure 6), are intrinsically X-ray luminous but heavily obscured.



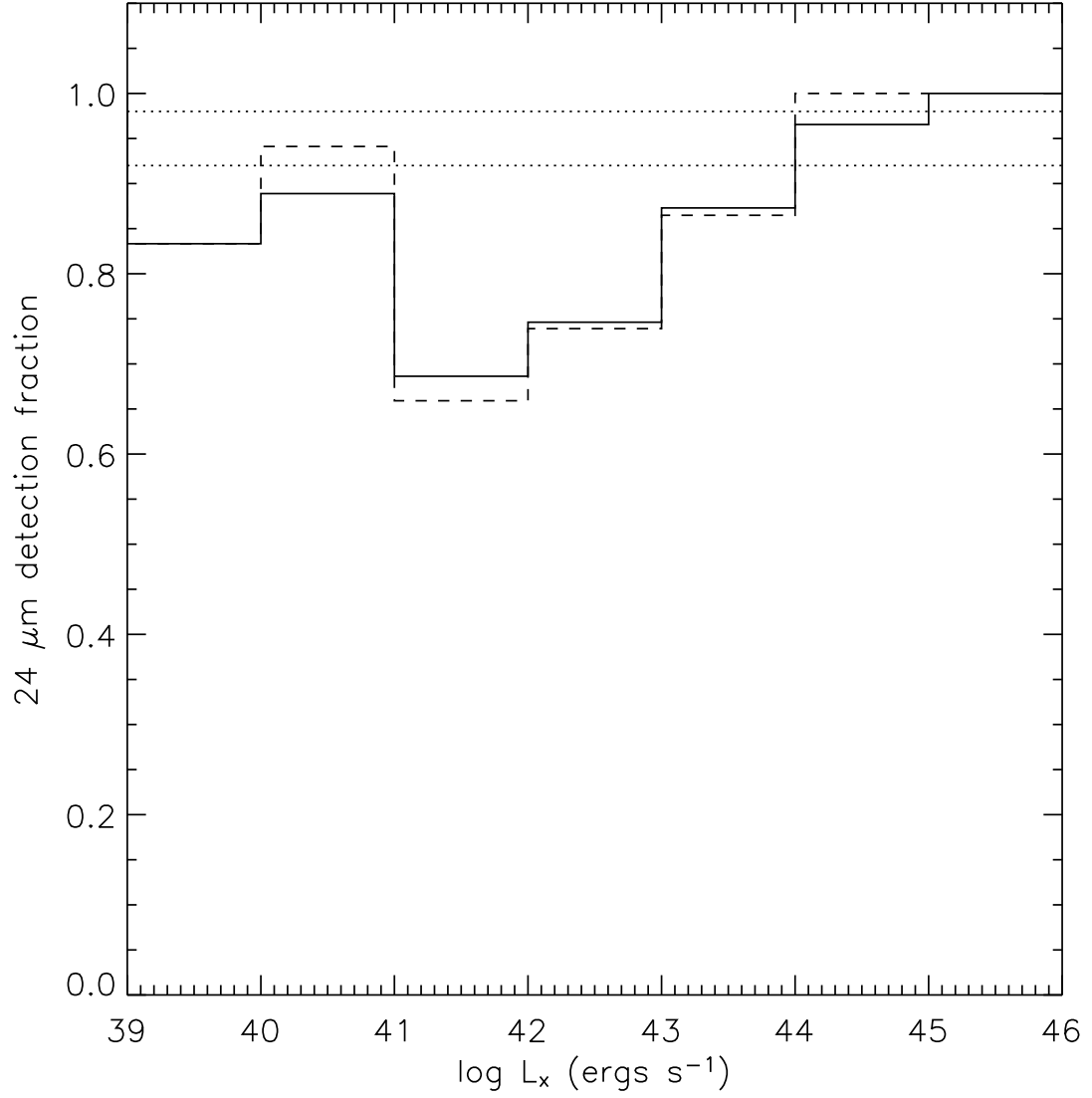


Figure 3.9 24  $\mu\text{m}$  detection fraction as a function of X-ray luminosity for the members of the comparison sample detected in the X-ray. The solid and dashed lines give the detection fraction for all sources with redshift estimates and for those with spectroscopic redshifts, respectively. Dotted lines give the upper and lower limit on the 24  $\mu\text{m}$  detection fraction of the power-law galaxies.

### 3.5.3 Radio Loudness

Eighteen of the 62 power-law galaxies (29%) have cataloged radio counterparts from the Richards (2000) 1.4 GHz VLA survey of the CDF-N. This survey has a detection limit of  $40 \mu\text{Jy}$  and is 95% complete at  $80 \mu\text{Jy}$ . In addition, 3 of these power-law galaxies (CDFN 16796, CDFN 27641, and CDFN 37999) are members of the radio-selected sub-millimeter SCUBA sample of Chapman et al. (2005), as is one radio source that fell below the Richards (2000) detection limit (CDFN 38580). For comparison, Polletta et al. (2006) found that half of their obscured AGN sample were radio-detected, although their radio limits were deeper and their IRAC coverage more shallow.

Since all of the radio-detected power-law galaxies are also detected at  $24 \mu\text{m}$ , we can test for radio-loudness via the parameter  $q$ , where  $q = \log (f_{24 \mu\text{m}}/f_{1.4 \text{ GHz}})$  (see Appleton et al. 2004). Sources with  $q < 0$  have far more radio emission (with respect to MIR emission) than is expected from the radio/infrared correlation of radio-quiet AGN and star-forming galaxies, and are referred to as radio-excess AGN (e.g. Yun, Reddy, & Condon 2001, Donley et al. 2005). Kuraszkiewicz et al. (2007) show that  $q$  is less sensitive to reddening and host galaxy dilution than measures of radio loudness based on radio and optical flux densities. Only 2 of the 18 radio-detected power-law galaxies are radio-excess AGN; the remaining galaxies are consistent with the radio/infrared correlation<sup>3</sup>. Kuraszkiewicz et al. (2007) find that  $\lesssim 15\%$  of AGN are radio-intermediate or radio-loud based on a cut of  $q < 0$ , consistent with the radio-loud fractions of Kellermann et al. (1989) and Stern et al. (2000). The fraction of radio-excess AGN in the power-law sample ( $\sim 3\%$ ) may therefore be lower than average.

---

<sup>3</sup>We note that the radio-excess AGN CDFN 12939 was not included in the sample of Donley et al. (2005) because its X-ray exposure time fell slightly below the more stringent cut of 1 Ms. The source CDFN 20246 corresponds to VLA 123709+622258 in Donley et al. (2005).

Both sources classified as radio-excess AGN have a cataloged X-ray counterpart; 11 of the remaining 16 radio sources are also bright X-ray sources, while 3 are weakly-detected. Only two radio sources (CDFN 40913 and CDFN 51788) are not detected in the X-ray. As such, selection criteria that include a radio flux density cut may be more likely to select X-ray bright AGN than selection via MIR properties alone. If such a cut were based on the current sensitivity of the CDF-N radio and X-ray surveys, however, only 13 of the 34 power-law galaxies detected in the X-ray catalog (38%) would be selected; the remaining 62% would be missed.

While the majority of the power-law galaxies with radio counterparts appear to be radio-quiet as defined by the radio/infrared correlation, their radio luminosities are consistent with those of AGN-powered sources. In the local universe, galaxies with  $\log L_{\text{radio}} (\text{W Hz}^{-1}) > 23$  tend to be AGN-dominated (Condon et al. 2002; Yun et al. 2001). In the GOODS-North (GOODS-N) field, Morrison et al. (2006) show that galaxies with  $\log L_{\text{radio}} (\text{W Hz}^{-1}) > 24$  and  $z > 1$  have up to an 80% X-ray detection rate. While a source of this luminosity could be a star-formation powered ULIRG (from the radio/infrared correlation, a radio luminosity of  $\log L_{\text{radio}} (\text{W Hz}^{-1}) = 24$  corresponds to a total infrared (TIR, 8-1000  $\mu\text{m}$ ) luminosity of  $4 \times 10^{12} L_{\odot}$  (Bell 2003)), the high X-ray detection rate suggests that the population is dominated by AGN.

All 16 of the 18 radio-detected power-law galaxies with redshifts have observed 1.4 GHz luminosities in excess of  $\log L_{1.4\text{GHz}} (\text{W Hz}^{-1}) > 23$ , and 14 (88%) have  $\log L_{1.4\text{GHz}} (\text{W Hz}^{-1}) > 24$ . In addition, 26 of the 27 radio non-detected power-law galaxies with redshifts have upper limits greater than  $\log L_{1.4\text{GHz}} (\text{W Hz}^{-1}) = 23$  (the exception being CDFN 49937, a low-luminosity X-ray source), and 21 (78%) have limits greater than  $\log L_{1.4\text{GHz}} (\text{W Hz}^{-1}) = 24$ . Using a cut of

$\log L_{1.4\text{GHz}} (\text{W Hz}^{-1}) > 24$ , Morrison et al. (2006) found that 60% of luminous radio galaxies in the GOODS-N field have power-law dominant SEDs. Using the same cut, we find that as many as 81% of power-law selected AGN are radio luminous, though not necessarily radio-loud.

### 3.5.4 Optical Morphology and Detection Fraction

While it is difficult to determine optical morphologies for faint sources, particularly those with only ground-based optical data, at least 20 of the power-law galaxies have point-like optical/NIR counterparts (8 of which were detected in the GOODS *Hubble Space Telescope* (HST) field, and 12 of which have only ground-based data). Of these, 18 are detected in the X-ray, one is weakly-detected, and one is non-detected. As such, at least 50% of the X-ray-detected sources have optical counterparts dominated by the central engine. Of the 15 sources with BLAGN spectra, 13 are point-like, compared to 2 of the 4 sources with NLAGN spectra. Of the power-law galaxies with available GOODS HST data,  $\sim 30\%$  of the sources with optical counterparts are point-like.

Worsley et al. (2006) stacked the X-ray emission from optical sources in the GOODS Fields to test whether these galaxies could account for the remaining unresolved fraction of the CXRB. While the stacked emission of galaxies not individually detected in the X-ray accounts for the unresolved portion of the CXRB at 0.5-6 keV, the reduced sensitivity of *Chandra* at higher energies makes a determination of the resolved fraction more difficult. They estimate that GOODS optical sources account for at most 40% of the unresolved emission from 6-8 keV, suggesting that some of the missing CXRB sources may also be missed in the GOODS images. Of the 27 power-law galaxies that lie in the GOODS region, 23 (85%) have cataloged GOODS optical counterparts. Two of the sources missed in the catalog (CDFN 32673 and CDFN 39529) are obscured X-ray sources sim-

ilar to the extreme X-ray/optical sources (EXOs, e.g. Koekemoer et al. 2004), one (CDFN 33052) is not detected in the X-ray, and one (CDFN 25218) is an obscured, weakly-detected X-ray source that may have a faint B-band counterpart. Therefore, at most 7% (2/27) of the power-law galaxies in the GOODS region are obscured AGN not detected in either the GOODS optical or the X-ray catalogs.

### 3.5.5 Optical–MIR SEDs

We plot in Figure 10 the median optical through MIR rest-frame SEDs of the cataloged, weakly-detected, and X-ray non-detected power-law galaxies, normalized by their  $1.25\ \mu\text{m}$  monochromatic flux densities. For comparison, we plot the median radio-quiet, starlight-subtracted AGN SED of Elvis et al. (1994). The median SEDs of the power-law galaxies are generally flatter than the Elvis et al. SED, and show no evidence of a UV bump. The median SED of the power-law galaxies with X-ray detections resembles that of the BLAGN SED class of Alonso-Herrero et al. (2006); that of the non-detected power-law galaxies drops much more rapidly in the optical, presumably due to increasing optical obscuration, and resembles that of the the NLAGN SED class of Alonso-Herrero et al. (2006). The weakly-detected sources have optical SEDs that fall between those of the detected and non-detected sources, suggesting an intermediate level of obscuration. The steepest IRAC spectral index found in our sample is  $\alpha = -3.15$ , only slightly steeper than that found by Alonso-Herrero et al. (2006) ( $\alpha = -2.8$ ) and Rigby et al. (2005) ( $\alpha = -2.9$ ).

Brand et al. (2006) show that X-ray detected AGN in the 5 ks XBoötes field and MIR-detected sources with clear signs of AGN activity in their optical spectra tend to have flat MIR spectral slopes ( $\log \nu f_\nu(24)/\nu f_\nu(8) = 0$ , e.g. Elvis et al. 1994), whereas star-forming galaxies typically have higher values of  $\log \nu f_\nu(24)/\nu f_\nu(8) \sim 0.5$ . Power-law galaxies have  $\log \nu f_\nu(24)/\nu f_\nu(8) = -0.24$  to  $0.73$ , with a mean

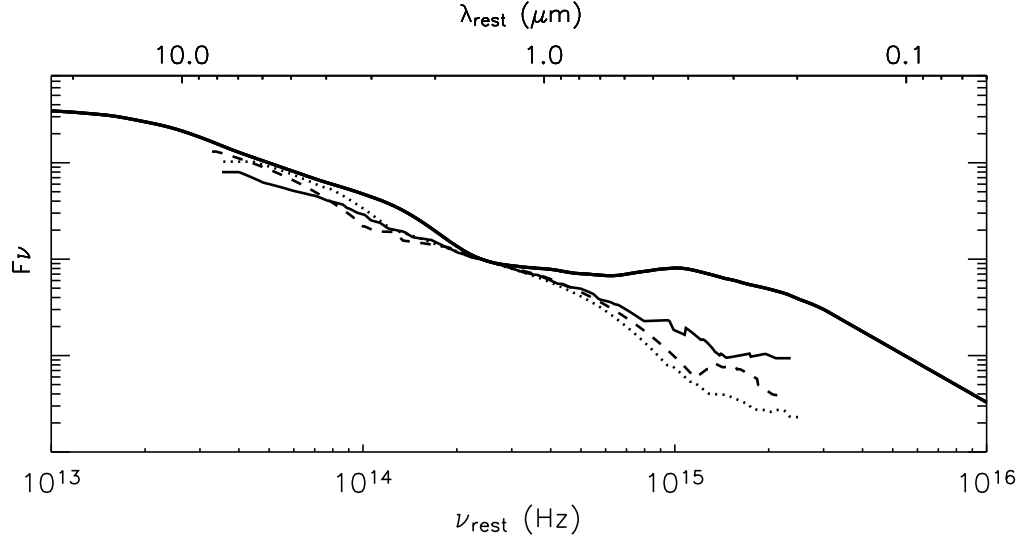


Figure 3.10 Median optical through MIR rest-frame SEDs of the X-ray-detected (solid line), weakly-detected (dashed line), and non-detected (dotted line) power-law galaxies. The median radio-quiet SED of Elvis et al. (1994) is shown by a solid line that spans the frequency range of the plot. The SEDs have been normalized to their  $1.25 \mu\text{m}$  flux densities.

slope in  $\nu f_\nu$  of  $0.18 \pm 0.22$ , suggesting that, when compared to unobscured AGN flat in  $\log \nu f_\nu$ , either relatively more flux is observed at  $24 \mu\text{m}$  or relatively less flux is observed at  $8 \mu\text{m}$ . The power-law galaxies in the X-ray catalog tend to have slightly flatter slopes ( $0.12 \pm 0.21$ ) than those not strongly detected in X-rays ( $0.26 \pm 0.21$ ). This trend can be seen in Figure 10, where the power-law galaxies not detected in the X-ray rise more prominently in  $\log \nu f_\nu$  with increasing wavelength than do those galaxies detected in X-rays, suggesting that the X-ray non-detected power-law galaxies are more heavily obscured in the optical.

### 3.6 Comparison with other MIR selection techniques

In the following section, we compare the power-law selection technique to a number of other MIR-based AGN selection criteria. While the power-law galaxies display a large range of infrared-to-optical ratios, and cannot be selected on

this basis, they comprise a significant fraction of the sources with high infrared-to-optical ratios, suggesting that many heavily optically-reddened sources have power-law continua in the NIR/MIR. The power-law selection more closely matches the *Spitzer* color-color selection criteria of Lacy et al. (2004) and Stern et al. (2005). We compare the X-ray completeness of these techniques, and show that, like the power-law selection, these color criteria tend to select high-redshift X-ray luminous AGN in the deep X-ray fields. We also discuss the X-ray detection fractions of the color-selected samples, which are lower than that of the power-law sample. We argue that this is due, at least in part, to a larger contamination by star-forming galaxies.

### 3.6.1 Optical vs 24 $\mu\text{m}$ Emission

The selection of infrared-bright, optically-faint sources has been suggested as a means of identifying obscured AGN (Houck et al. 2005; Weedman et al. 2006; Yan et al. 2004, 2005). Approximately 40 such sources have been observed with the *Spitzer* IRS; the majority (75%) are dominated by silicate absorption, indicative of heavy obscuration, or are featureless. Although no deep X-ray information is available for those sources observed thus far, their spectral characteristics suggest that many are likely to be obscured AGN.

Only one member of the power-law sample, CDFN 27360 (an X-ray-detected AGN with a column density of  $N_{\text{H}} = 2.5 \times 10^{23} \text{ cm}^{-2}$  (see Table 3)), meets the strict criterion used by Houck et al. (2004) and Weedman et al. (2006) to select infrared-bright, optically-faint sources:  $f_{24} > 0.75 \text{ mJy}$  and  $R > 24.5$  (Houck et al. 2004), or  $f_{24} > 1.0 \text{ mJy}$  and  $R > 23.9$  (Weedman et al. 2006). These selection criteria, however, have been set to ensure that sources can be followed-up effectively with IRS. We plot in Figure 11 the positions of the comparison sample (discussed in §4) on the color-color plot of Yan et al. (2004); with the exception of the 7 sources that

are X-ray non-detected at the  $2.5\sigma$  level (see §5.1), 6 of which have no R-band counterpart, only sources detected at  $8\mu\text{m}$ ,  $24\mu\text{m}$ , and R-band are shown.

Following Yan et al. (2004, 2005) we define the following quantities:

$$R(24, 0.7) = \log(\nu f_\nu(24\mu\text{m})/\nu f_\nu(R)) \quad (3.1)$$

$$R(24, 8) = \log(\nu f_\nu(24\mu\text{m})/\nu f_\nu(8\mu\text{m})) \quad (3.2)$$

According to Yan et al. (2004), sources with  $R(24, 0.7) > 1.5$  and  $R(24, 8) \sim 0.5$  are likely to be dust-reddened AGN, although 75% of the luminous starburst candidates with  $R(24, 0.7) > 1$  and  $R(24, 8) > 0.3$  followed-up with IRS by Yan et al. (2005) appear to be either unobscured AGN or galaxies with both a buried AGN and a starburst component. While the power-law galaxies (and X-ray-detected members of the comparison sample) cover a large range of  $R(24, 0.7)$  and  $R(24, 8)$ , as is expected for a sample of AGN with a variety of redshifts and obscurations, the power-law galaxies comprise an increasingly significant fraction of the highly optically-reddened members of the comparison sample with  $R(24, 0.7) \geq 1.2$ . This suggests that power-law selection is capable of detecting both optically obscured and unobscured AGN, as expected, and that a significant fraction (20-40%) of the infrared-bright/optically-faint sources in the comparison sample have power-law SEDs in the NIR/MIR. In addition, those power-law galaxies shown to be X-ray undetected to the  $2.5\sigma$  level all have upper limits of  $R(24, 0.7) \geq 1$ , consistent with the expectations for obscured AGN. In the following section, we compare the power-law selection to selection criteria that more closely match those used here.

### 3.6.2 *Spitzer* Color-Color Selection

MIR AGN color selection criteria have been defined by Ivison et al. (2004), Lacy et al. (2004), Stern et al. (2005), and Hatziminaoglou et al. (2005). The complete-



Table 3. X-ray Properties of X-ray-Detected Power-law AGN

Source	z	0.5-8 keV Flux <sup>a</sup> (erg s <sup>-1</sup> cm <sup>-2</sup> )	2-8 keV Flux <sup>a</sup> (erg s <sup>-1</sup> cm <sup>-2</sup> )	0.5-2 keV Flux <sup>a</sup> (erg s <sup>-1</sup> cm <sup>-2</sup> )	$\Gamma^a$	H/S <sup>b</sup>	log N <sub>H</sub> <sup>c</sup> (cm <sup>-2</sup> )
CDFN07514	2.97	2.00E-15	1.54E-15	4.19E-16	1.1	3.54	23.3 <sup>+0.1</sup> <sub>-0.2</sub>
CDFN11516	2.05	5.27E-15	2.85E-15	2.04E-15	1.8	1.33	21.2 <sup>+1.0</sup> <sub>...</sub>
CDFN11965	1.90	1.95E-15	1.56E-15	3.44E-16	0.9	4.38	23.1 <sup>+0.1</sup> <sub>-0.2</sub>
CDFN12939	0.71	2.23E-13	1.36E-13	8.05E-14	1.6	1.62	21.4 <sup>+0.4</sup> <sub>...</sub>
CDFN14046	2.82	1.16E-14	6.63E-15	4.32E-15	1.7	1.47	22.0 <sup>+0.6</sup> <sub>...</sub>
CDFN14667	...	3.45E-15	2.13E-15	1.13E-15	1.6	1.81	21.5 <sup>+0.3</sup> <sub>-1.3</sub> - 22.6 <sup>+0.3</sup> <sub>-0.9</sub>
CDFN16796	2.20	1.34E-15	1.20E-15	1.20E-16	0.4	9.72	23.6 <sup>+0.1</sup> <sub>-0.1</sub>
CDFN17315	2.41	7.02E-15	4.72E-15	2.18E-15	1.5	2.08	22.6 <sup>+0.3</sup> <sub>-0.4</sub>
CDFN20246	1.41	5.21E-15	4.99E-15	1.35E-16	-0.6	36.19	23.6 <sup>+0.0</sup> <sub>-0.0</sub>
CDFN23661	2.59	1.88E-14	1.10E-14	7.43E-15	1.8	1.41	21.8 <sup>+0.7</sup> <sub>...</sub>
CDFN24409	2.72	3.35E-15	2.32E-15	9.48E-16	1.4	2.35	22.8 <sup>+0.2</sup> <sub>-0.3</sub>
CDFN25248	2.89	9.64E-16	8.63E-16	1.08E-16	0.5	7.75	23.7 <sup>+0.1</sup> <sub>-0.1</sub>
CDFN27360	1.86	1.40E-15	1.32E-15	1.52E-16	0.5	8.43	23.4 <sup>+0.1</sup> <sub>-0.1</sub>
CDFN27641	2.02	2.52E-15	2.48E-15	2.07E-16	0.2	11.66	23.6 <sup>+0.1</sup> <sub>-0.1</sub>
CDFN28149	2.24	9.95E-15	6.20E-15	3.43E-15	1.6	1.73	22.3 <sup>+0.3</sup> <sub>-1.2</sub>
CDFN28773	0.96	1.01E-14	5.35E-15	4.57E-15	1.9	1.12	≤ 21.2
CDFN29120	1.02	3.54E-14	1.89E-14	1.57E-14	1.9	1.15	≤ 21.4
CDFN30147	1.15	2.17E-14	1.73E-14	4.26E-15	1.0	3.92	22.6 <sup>+0.1</sup> <sub>-0.2</sub>
CDFN32673	...	4.46E-16	5.30E-16	≤ 2.55E-17	≤ 1.4	≥ 19.96	≥ 22.9 <sup>+0.0</sup> <sub>-0.1</sub> - ≥ 24.0 <sup>+0.0</sup> <sub>-0.1</sub>
CDFN34143	2.31	2.08E-14	1.29E-14	7.30E-15	1.6	1.69	22.2 <sup>+0.4</sup> <sub>...</sub>
CDFN37999	2.00	1.83E-15	1.83E-15	1.17E-16	0.1	15.24	23.7 <sup>+0.1</sup> <sub>-0.1</sub>
CDFN38580	2.91	3.84E-16	3.74E-16	2.93E-17	0.2	12.42	23.9 <sup>+0.1</sup> <sub>-0.1</sub>
CDFN39529	...	6.21E-15	5.16E-15	1.09E-15	0.9	4.57	22.3 <sup>+0.1</sup> <sub>-0.1</sub> - 23.5 <sup>+0.1</sup> <sub>-0.1</sub>
CDFN40112	2.92	4.68E-15	2.42E-15	2.27E-15	2.0	1.02	≤ 20.7
CDFN41981	1.54	2.59E-14	2.18E-14	4.34E-15	0.9	4.85	23.0 <sup>+0.1</sup> <sub>-0.1</sub>
CDFN43967	1.84	3.57E-15	2.44E-15	1.02E-15	1.4	2.30	22.5 <sup>+0.2</sup> <sub>-0.3</sub>
CDFN44598	1.17	2.02E-14	1.28E-14	6.96E-15	1.6	1.76	21.8 <sup>+0.3</sup> <sub>-2.2</sub>
CDFN44836	...	8.56E-16	9.77E-16	≤ 5.71E-17	≤ 1.4	≥ 16.43	≥ 22.8 <sup>+0.1</sup> <sub>-0.1</sub> - ≥ 24.0 <sup>+0.1</sup> <sub>-0.1</sub>
CDFN45284	2.18	2.11E-14	1.27E-14	7.82E-15	1.7	1.55	22.1 <sup>+0.4</sup> <sub>...</sub>
CDFN45792	0.44	7.78E-14	3.83E-14	3.87E-14	2.0	0.94	...
CDFN49937	0.29	9.75E-15	5.69E-15	3.65E-15	1.7	1.49	21.0 <sup>+0.4</sup> <sub>...</sub>
CDFN49940	0.91	1.52E-13	9.11E-14	5.64E-14	1.7	1.54	21.4 <sup>+0.5</sup> <sub>...</sub>
CDFN50281	1.94	1.94E-15	9.82E-16	7.57E-16	1.8	1.24	≤ 22.0
CDFN53792	1.63	3.76E-15	3.06E-15	6.42E-16	0.9	4.60	23.0 <sup>+0.1</sup> <sub>-0.1</sub>

<sup>a</sup>Alexander et al. (2003)<sup>b</sup>Flux ratio corrected for Galactic absorption<sup>c</sup>Sources with no lower error have an immeasurably low lower limit.

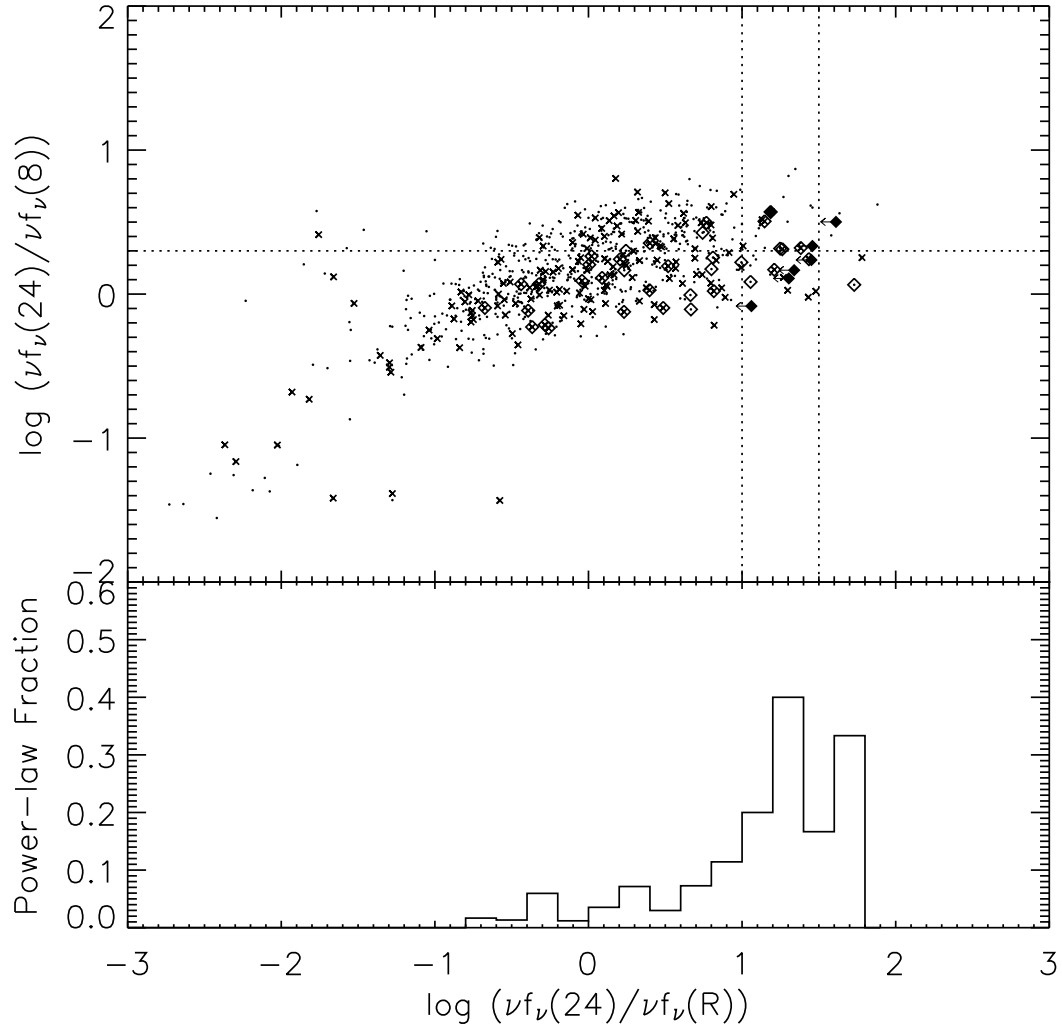


Figure 3.11 Location of the comparison sample on the color-color diagram of Yan et al. (2004). All members of the comparison sample are shown (dots), as are the power-law galaxies (diamonds) and the X-ray-detected members of the comparison sample (crosses). The 7 power-law galaxies that are X-ray non-detected to the  $2.5\sigma$  level are indicated by filled diamonds. Dotted lines show the selection criteria of Yan et al. (2004), as discussed in §6.1. The lower panel shows the power-law fraction of the comparison sample as a function of  $R(24,0.7)$ .

ness and reliability of the latter three criteria in selecting X-ray-detected AGN in the Extended Groth Strip (EGS) is discussed by Barmby et al. (2005). We plot in Figures 12 and 13 the position of the power-law galaxies with respect to the IRAC color-color cuts of Lacy et al. (2004) and Stern et al. (2005), both of which have been designed for relatively shallow surveys. In addition, we overplot the redshifted IRAC colors of the Dale & Helou (2002) star-forming template (which is degenerate with their parameter  $\alpha$  for the wavelengths of interest), the median radio-quiet AGN SED of Elvis et al. (1994), and the SEDs of the ULIRGs Mrk 273, IRAS 17208-0014, and Arp 220, described in Appendix A.

The selection criteria of Lacy et al. are based on SDSS quasars, and therefore are not designed to select AGN in which the host galaxy dominates the MIR energy, as well as AGN that are obscured in the MIR. As discussed in Alonso-Herrero et al. (2006) and as shown in Figure 12, IRAC power-law galaxies fall along a line well within the Lacy et al. selection region, although these galaxies fill only a small fraction of the available color space within the defined cut. Only 16% of the objects from the comparison sample that satisfy the Lacy et al. color cuts also meet the power-law criteria.

The Stern et al. (2005) selection criteria provide a slightly closer match to the power-law selection technique. Stern et al. define their color cut using  $\sim 9400$  sources from AGES<sup>4</sup>, 800 of which are spectroscopically confirmed AGN. Their color criterion identifies 91% of the BLAGN and 40% of the NLAGN in the AGES sample. 17% of the sources that met their AGN criteria were not classified as AGN based on their optical spectra, but may be optically normal (optically dull) AGN. All of the power-law galaxies meet the Stern et al. criteria, and 29% of the sources from the sample that meet the Stern et al. criteria also meet the power-law

---

<sup>4</sup>the AGN and Galaxy Evolution Survey, C. S. Kochanek et al., in prep

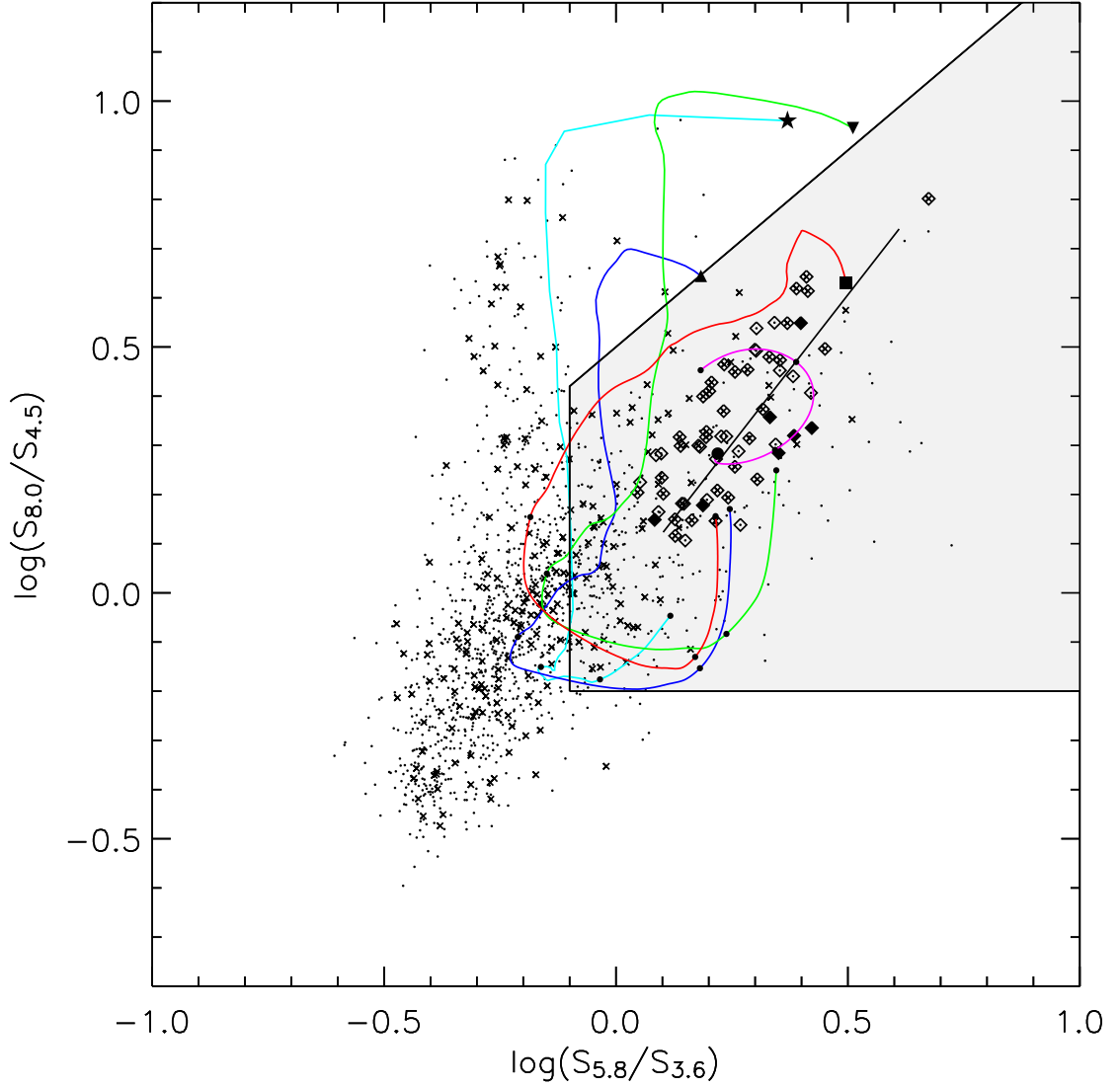


Figure 3.12 Location of the comparison sample on the color-color diagram of Lacy et al. (2004). Symbols are as described in Figure 11. Overplotted are the power-law locus from  $\alpha = -0.5$  to  $\alpha = -3$  (thin black line) and the redshifted IRAC colors of a typical star-forming galaxy (Dale & Helou 2002, cyan, star), the cold (starburst dominated) ULIRGs Arp 220 (blue, triangle) and IRAS 17208-0014 (green, upside down triangle), the ULIRG/Sey 2 Mrk 273 (red, square) and the radio-quiet AGN SED from Elvis et al. (1994, magenta, circle), where the indicated point represents the colors at  $z = 0$ , and small circles mark the colors at  $z = 1, 2$ , and 3.

criteria. The power-law galaxies show a larger scatter about the power-law locus in the Stern et al. diagram (Figure 13) than they do in the Lacy et al. diagram (Figure 12); this is likely to be due, at least in part, to the smaller wavelength baseline probed by the Stern et al. colors.

### 3.6.2.1 X-ray completeness of color-selected samples

In the EGS, with an X-ray exposure time of  $\leq 200$  ks, the Lacy et al. and Stern et al. color criteria selected 73% and 51% of the X-ray AGN, respectively (Barmby et al. 2005). In the deeper CDF-N field, these criteria select only 21% and 17% of the Alexander et al. (2003) X-ray sample. However, only 50% of the X-ray sources in the CDF-N meet the exposure time and IRAC  $S/N$  cuts used to define the comparison and color-selected samples. When we consider only those X-ray sources in the comparison sample, the Lacy et al. and Stern et al. criteria select 39% and 33% of the X-ray sources, respectively. Further restricting the comparison to sources in the comparison sample with X-ray luminosities indicative of AGN activity,  $\log L_x \text{ (erg s}^{-1}\text{)} \geq 42$ , increases the selection fractions to 52% and 47%, respectively. For comparison, our strict power-law criteria recover  $\sim 20\%$  of the X-ray luminous AGN in the comparison sample.

Power-law galaxies, a subsample of both the Lacy et al. and Stern et al. criteria, tend to preferentially lie at both high luminosity and high redshift. The same is true for the full color-selected samples, as shown in Figures 14 and 15, in which we plot only sources with spectroscopic redshifts and only the Lacy et al. color criteria. Including photometric redshifts does not change the results, and the same trends are seen for both the Lacy et al. and Stern et al. selection techniques.

At low redshift, only a small fraction of the comparison sample lies inside the Lacy et al. selection region (see Figure 14). At redshifts of  $z > 1$ , however,

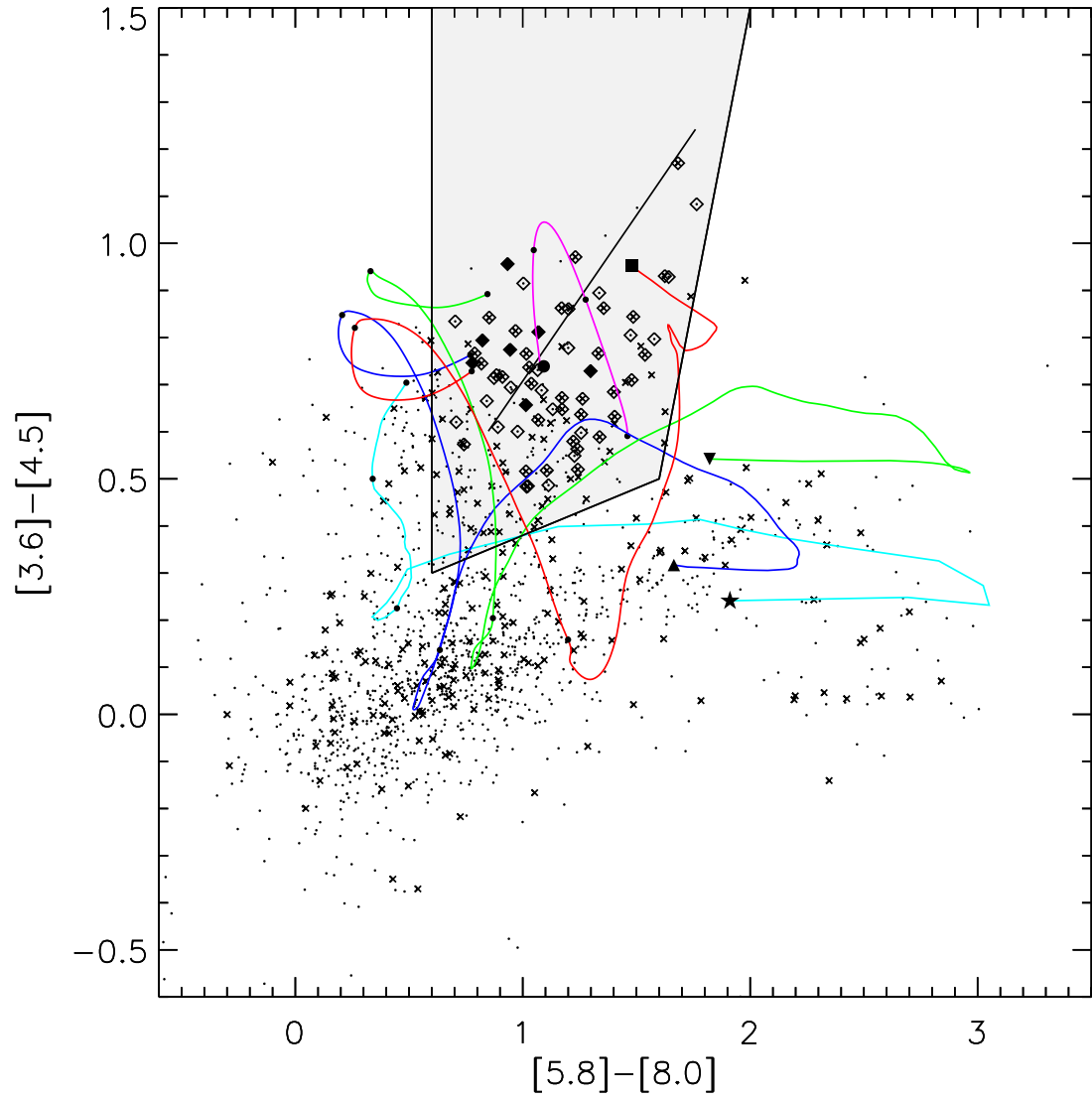


Figure 3.13 Location of the comparison sample on the color-color diagram of Stern et al. (2005). Symbols are as described in Figure 11 and templates are as described in Figure 12.

the vertical branch in color-space populated by low-redshift ( $z < 0.3$ ) aromatic-dominated sources (Sajina, Lacy, & Scott 2005) disappears, and at  $z > 2$ , all of the remaining IRAC sources meet the Lacy et al. criteria. Similarly, at  $\log L_x \text{ (erg s}^{-1}\text{)} < 42$ , only a small fraction of the sources in the comparison sample fall in the selection region (see Figure 15). In contrast, 72% of the X-ray sources in the comparison sample with  $\log L_x \text{ (erg s}^{-1}\text{)} > 43$  and 100% of those sources with  $\log L_x \text{ (erg s}^{-1}\text{)} > 44$  meet the Lacy et al. selection criteria. These high luminosity sources lie in the same region of color space as the power-law selected AGN (see Figure 12), although as is apparent from Figure 6, the Lacy et al. criteria (and the Stern et al. criteria) select a more complete sample of AGN with high X-ray luminosities than does the power-law selection. As is also shown in Figure 6, however, the X-ray luminosities of the color-selected sources extend below the traditional AGN limit of  $\log L_x \text{ (erg s}^{-1}\text{)} > 42$ , suggesting either heavy obscuration of highly-luminous AGN, or possible contamination by star-forming galaxies.

### 3.6.2.2 AGN Reliability

Of the sources selected via the power-law criteria, 55% were detected in the X-ray catalog of Alexander et al. (2003). The X-ray detection fractions of the sources selected via the Lacy et al. and Stern et al. criteria are lower: 25% and 38%, respectively. We searched for faint X-ray emission from the color-selected sources using the method described in §5.1; 65% of the Lacy et al. sources and 70% of the Stern et al. sources show evidence for X-ray emission (at the  $2.5\sigma$  level or higher), compared to 85% for the power-law galaxies. Do these techniques select a larger fraction of AGN not detected in X-rays, or do they suffer from greater contamination from star-forming galaxies?

A spectroscopic follow-up of candidate obscured AGN selected via the Lacy

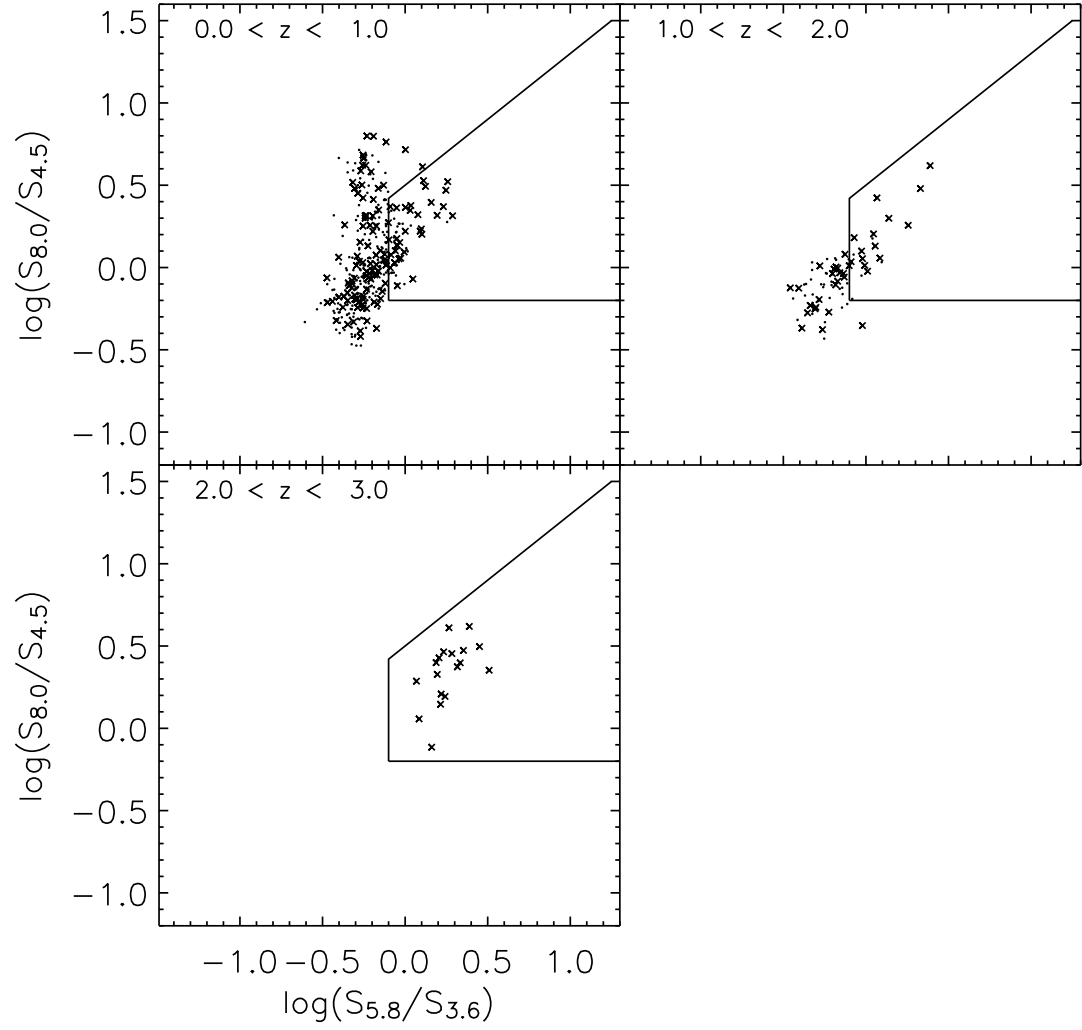


Figure 3.14 Location in the Lacy et al. (2004) color space of the comparison sample as a function of redshift. Only sources with spectroscopic redshifts are shown. X-ray sources in the comparison sample are indicated by crosses.



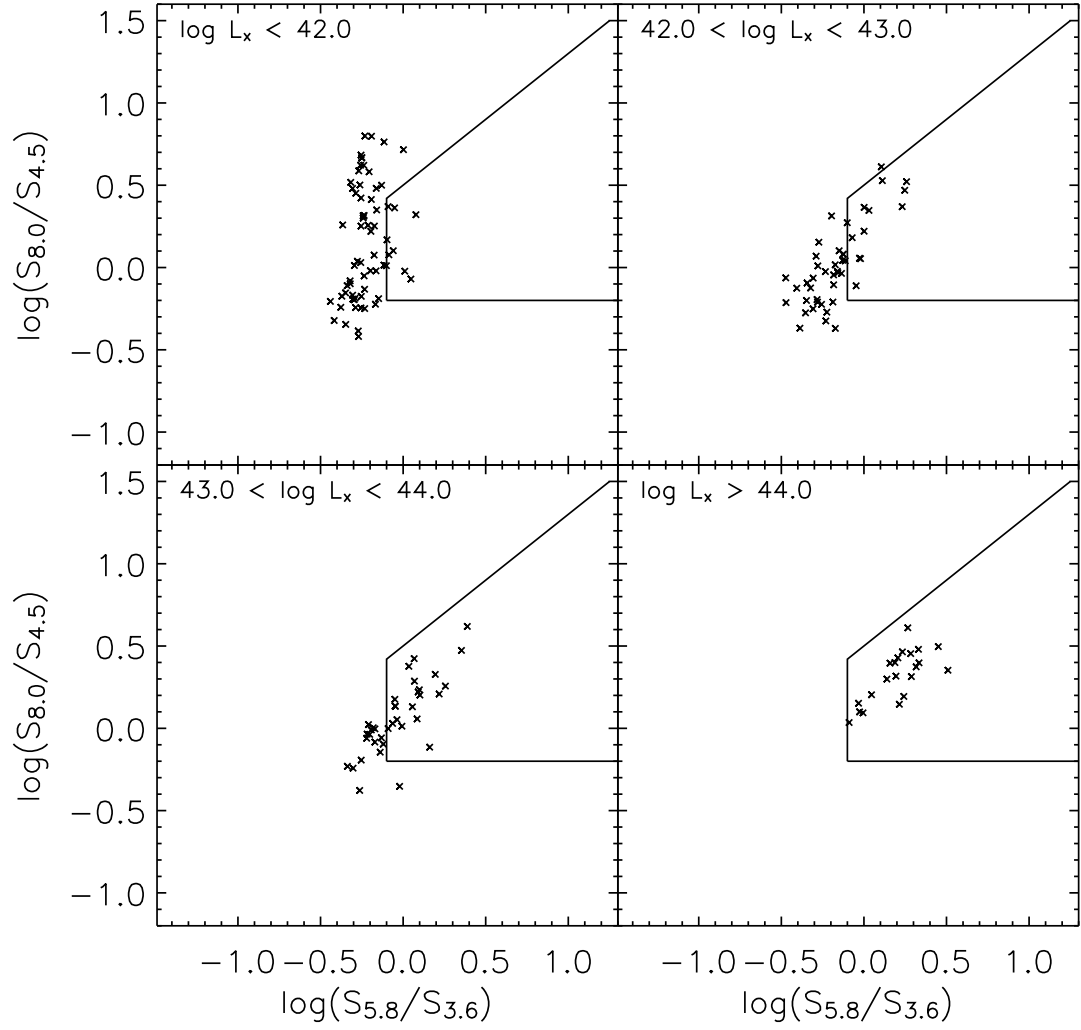


Figure 3.15 Location in the Lacy et al. (2004) color space of the comparison sample as a function of X-ray luminosity (in units of  $\text{ergs s}^{-1}$ ). Only sources with spectroscopic redshifts are shown.

et al. criteria reveals that most ( $\sim 80\%$ ) have spectral signatures typical of type-2 AGN (Lacy et al. 2005a). However, the 12 candidate sources for which spectra were taken were chosen to have  $8\ \mu\text{m}$  flux densities  $> 1\ \text{mJy}$ , and all lie at  $z < 1.34$ . As shown in Figure 12, the SEDs of the star-formation dominated ULIRG Arp 220 enters the Lacy et al. selection region at low ( $z = 0.23$  to  $0.67$ ) and moderately high ( $z > 1.43$ ) redshift, as does that of IRAS 17208-0014 ( $z = 0.36$  to  $0.89$  and  $z > 1.35$ ). The Dale & Helou (2002) star-forming template shows similar behavior, falling just inside the AGN selection region at low redshift ( $z = 0.48$  to  $0.58$ ) and re-entering the region at high redshift ( $z > 1.66$ ), suggesting that pure color-selection is capable of selecting both normal and highly-luminous star-forming galaxies at low and moderately high redshift. The simulations of Sajina et al. (2005) also show a significant number of aromatic feature-dominated sources near the outskirts of the Lacy et al. AGN selection region, and suggest that while the IRAC colors provide an effective means of identifying obscured AGN up to  $z = 2$ , such criteria are less effective at higher redshift, where the IRAC bands sample the NIR light from the galaxy (see also Alonso-Herrero et al. 2006). As expected, the AGN template (Elvis et al. 1994) lies in the same region of color space as the power-law galaxies, as does the low-redshift template of Mrk 273, a ULIRG with AGN signatures in the optical and NIR (Veilleux et al. 1999; Risaliti et al. 2006). Mrk 273 meets the Lacy et al. criteria at all redshifts except  $z = 0.83$  to  $1.40$ .

The Stern et al. criteria also suffer from potential contamination from cold ULIRGs and star-forming galaxies, although the star-forming templates tend to fall in the selection region for smaller redshift intervals than in the Lacy et al. color-space. The star-forming template of Dale & Helou (2002) lies along the edge of the selection region at low redshift ( $z = 0.51$  to  $0.56$ ) but it does not re-enter the selection region at the redshifts plotted here ( $z < 3$ ). Arp 220 falls in the

selection region twice (from redshifts of  $z = 0.28$  to  $0.55$  and  $z = 1.17$  to  $1.44$ ), as does IRAS 17208-0014 ( $z = 0.49$  to  $0.58$  and  $z = 1.15$  to  $1.60$ ). Once again, both the AGN template (Elvis et al. 1994) and the low-redshift Mrk 273 template have colors similar to those of the power-law galaxies. The Mrk 273 template meets the Stern et al. criteria in three redshift intervals ( $z = 0$  to  $0.06$ ,  $z = 0.19$  to  $0.39$ , and  $z = 1.22$  to  $1.59$ ), whereas the AGN template falls in the selection region at all redshifts plotted here.

The Mrk 273, Arp 220, and IRAS 17208-0014 templates all lie near regions of color-space populated by power-law galaxies. The template of Mrk 273, a ULIRG with AGN signatures, meets our power-law criteria ( $\alpha \leq -0.5$ ,  $P > 0.1$ , monotonically rising) at redshifts of  $z = 0$  to  $0.08$ ,  $z = 0.18$  to  $0.39$  and at  $z > 2.88$  (assuming 10% flux errors in the  $3.6$  and  $4.5 \mu\text{m}$  bands, and 15% flux errors in the  $5.8$  and  $8.0 \mu\text{m}$  bands). The Arp 220 template, however, does not meet these criteria at redshifts less than  $z \sim 2.9$ , as expected. With the exception of a narrow redshift window of  $z = 0.51$  to  $0.53$  in which IRAS 17208-0014 appears as a power-law galaxy, the same is true for this star-forming template, which meets our criteria at  $z \gtrsim 2.8$ . Only five of the sources in our sample with redshift estimates lie at  $z < 1$ ; none of these lie between  $z = 0.51$  and  $0.53$ , and all are detected in the X-ray. We therefore expect little contamination from low-redshift ULIRGS, although the presence of such sources cannot be ruled out. As for contamination from high redshift star-forming galaxies, a ULIRG with an SED like that of Arp 220 that lies at  $z = 2.8$  must have a total infrared luminosity (TIR,  $8\text{-}1000 \mu\text{m}$ ) of  $\log L_{\text{TIR}}(L_{\odot}) > 13.3$  to have a  $24 \mu\text{m}$  flux density  $> 80 \mu\text{Jy}$  (see Figure 16). The fraction of ULIRGS dominated by AGN increases with infrared luminosity, with 50% of ULIRGS showing Seyfert-like properties at  $\log L_{\text{TIR}}(L_{\odot}) > 12.3$  (Veilleux et al. 1999). It is therefore unlikely that HyperLIRGS with  $\log L_{\text{TIR}}(L_{\odot}) > 13$  have

NIR luminosities dominated by star-formation. As such, we also expect little contamination in the power-law sample from high-redshift star-forming galaxies, so long as the power-law objects are also detected at  $24\ \mu\text{m}$  (as is the case both for the sample of Alonso-Herrero et al. (2006) and for the majority of our sample).

As a final check, we plot in Figures 12 and 13 the seven power-law galaxies in our sample that are not detected in the X-ray at the  $2.5\ \sigma$  level. With one or two exceptions, they are well removed from the colors of Arp 220 and IRAS 17208-0014 for any value of  $z < 2.8$  (particularly in Figure 12). We therefore believe they contain AGN that are heavily obscured in the X-ray. This test illustrates the utility of the color-color plots in identifying regions of color space within the color selection regions and near the power-law locus in which contamination by star-forming galaxies is possible. The current templates suggest that pure color selection is likely to select star-forming galaxies and ULIRGs at both low and high redshifts. Several other lines of evidence also point towards a higher fraction of star-forming galaxies in the color-selected samples. While  $\geq 92\%$  of the power-law galaxies are detected at  $24\ \mu\text{m}$ , the  $24\ \mu\text{m}$  detection fractions of the Lacy et al. and Stern et al. samples are lower: 72% and 83%, respectively. In addition, while 88% of the radio-detected power-law galaxies with redshift estimates have radio luminosities of  $L(1.4\text{GHz}) > 24\ \text{W Hz}^{-1}$ , the value typical of AGN-powered radio galaxies in GOODS-N (Morrison et al. 2006), only 49% and 54% of the Lacy et al. and Stern et al. radio sources (with redshift estimates) have luminosities that exceed this value. Finally, we plot in Figure 17 the position of the color-selected sources on the X-ray to optical diagnostic diagram. While the current detections and upper limits place only two power-law galaxies within the transition region and none near the region populated by quiescent galaxies (see Figure 2), 15% and 10% of the Lacy et al. and Stern et al. sources fall in these regions, and more have

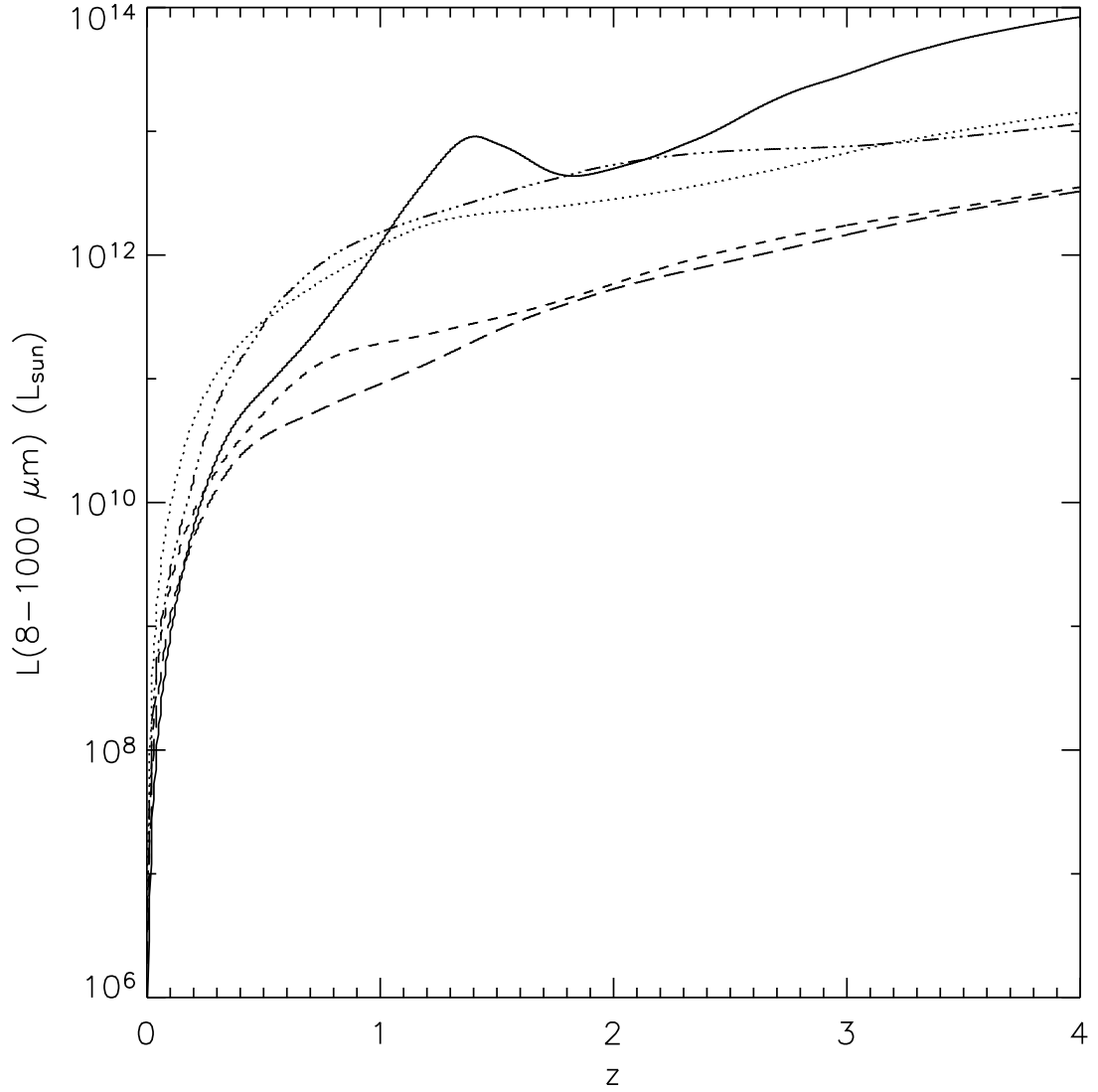


Figure 3.16 Total infrared luminosity (8-1000  $\mu\text{m}$ ) required for Arp 220 to meet the detection limits of our survey (see §3). The lines represent the luminosity required for detection in the MIPS 24  $\mu\text{m}$  (solid) and IRAC 3.6  $\mu\text{m}$  (long-dashed), 4.5  $\mu\text{m}$  (short-dashed), 5.8  $\mu\text{m}$  (dotted), and 8.0  $\mu\text{m}$  (dot-dashed) bands.

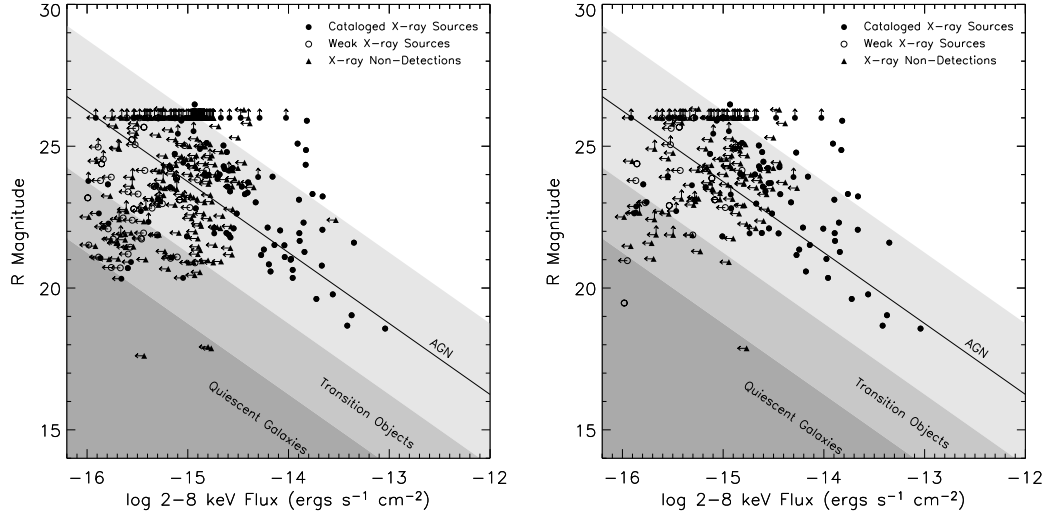


Figure 3.17 Relationship between the observed R-band magnitude and hard (2–8 keV) X-ray fluxes for the Lacy et al. (2004) sources (left) and the Stern et al. (2005) sources (right). Symbols, lines, and shading are as described in Figure 2.

upper limits that place them just outside.

### 3.6.2.3 SEDs of color-selected sources

How do the MIR SEDs of the Lacy et al. and Stern et al. selected sources compare to those of the power-law galaxies? Of the Lacy et al. sources, 20% can be fit by red, AGN-dominated power-laws ( $\alpha < -0.5$ ) and 30% can be fit by blue, stellar-dominated power-laws ( $\alpha > -0.5$ ). A higher fraction of the Stern et al. sources have good power-law fits: 37% are red power-laws and 34% are blue power-laws<sup>5</sup>. The comparison sample (see Section 4) shows the behavior of objects selected without regard to the presence of an AGN; 6% and 39% of the full comparison sample can be fit by red and blue power-laws, as can 16% and 35% of the cataloged X-ray sources in the comparison sample.

<sup>5</sup>We note we have applied only a power-law fit probability to derive the above numbers, and have excluded the other criteria discussed in §3 (i.e. no turnovers in flux density, no apparent stellar bump). The number of galaxies identified with red power-laws using just these two criteria is therefore 79, not 62.

### 3.7 Obscuration

In the local universe, Seyfert 2's are four times more numerous than Seyfert 1's (Maiolino & Rieke 1995) and at least half of all Seyfert 2's are Compton-thick (Maiolino et al. 1998; Risaliti et al. 1999). In the more distant universe, X-ray background and luminosity function synthesis models predict global obscured ( $\log N_{\text{H}}(\text{cm}^{-2}) \geq 22$ ) ratios of 3:1 to 4:1 (Comastri et al. 2001; Ueda et al. 2003; Gilli 2004; Treister et al. 2005; Tozzi et al. 2006), significantly higher than the observed type 2 to type 1 ratio of spectroscopically identified X-ray sources in the deep fields, 2:1 (e.g., Barger et al. 2003; Szokoly et al. 2004; Treister et al. 2005), but slightly lower than the 6:1 ratio observed for high-redshift X-ray-detected SCUBA galaxies (Alexander et al. 2005).

In the following discussion, we estimate the X-ray column densities of the power-law sample and compare the resulting obscured fraction to predictions from the XRB. If we consider only those power-law galaxies detected in the X-ray, we find an obscured ratio of 2:1. Including the power-law galaxies both weakly- and non-detected in the X-ray results in an obscured ratio of  $\lesssim 4 : 1$ . We use a Monte Carlo code to measure the dispersion in this ratio, and investigate the change in the obscured fraction with X-ray luminosity and redshift. By comparing the space density of obscured AGN in the power-law sample to the predictions of Treister et al. (2006), we estimate that at most 20-30% of obscured, MIR-detected AGN have SEDs that meet our robust power-law criteria. We also discuss the effect of large obscuring columns on the NIR/MIR continuum, and show that while heavily obscured AGN can have NIR emission dominated by the AGN, the power-law criteria may be biased against the most heavily obscured (Compton-thick) AGN.

### 3.7.1 Column Densities

We estimated the intrinsic column density,  $N_{\text{H}}$ , of each X-ray–detected power-law and color-selected galaxy by comparing the observed hard to soft-band X-ray flux ratio to that expected for a typical AGN at a given redshift, after correcting the flux ratios for a Galactic column density of  $N_{\text{H}} = 1.6 \times 10^{20} \text{ cm}^{-2}$ . When no redshift was available, we estimated the column densities at redshifts of  $z = 0.5$  and  $z = 3.0$ , the approximate limits of the power-law sample. We assumed an intrinsic photon index of  $\Gamma = 1.81$  (Tozzi et al. 2006), and did not include a Compton reflection component, which tends to decrease the necessary column by  $\sim 20\%$  (see Donley et al. 2005). The estimated column densities of the power-law galaxies are given in Tables 2 and 3 and plotted in Figure 18.

#### 3.7.1.1 Obscured fraction

A comparison between the X-ray-cataloged and weakly-detected power-law galaxies is complicated, because only one of the latter has both a hard and soft-band detection. We can therefore place only upper limits on the columns of 6 of the weakly-detected AGN, lower limits on two, and no limit on the remaining one. However, all weakly-detected power-law galaxies for which we can estimate  $N_{\text{H}}$  are consistent with being obscured ( $N_{\text{H}} > 10^{22} \text{ cm}^{-2}$ ), but not Compton-thick ( $N_{\text{H}} > 10^{24} \text{ cm}^{-2}$ ). Of the X-ray–detected power-law galaxies,  $\sim 68\%$  are obscured, in agreement with obscured fractions found by Ueda et al. (2003) for AGN at similar redshifts. If we consider only those power-law galaxies in the X-ray catalog, we therefore derive an obscured to unobscured ratio of  $\sim 2:1$ .

Several lines of evidence point towards high obscuration in the sources not detected in X-rays. First, the power-law selection criteria (§5.1.2) and high  $24 \mu\text{m}$  detection fraction (§5.2) appear to be indicative of a population of intrinsically X-ray luminous sources (see Fig. 10), sources that, if unobscured, should



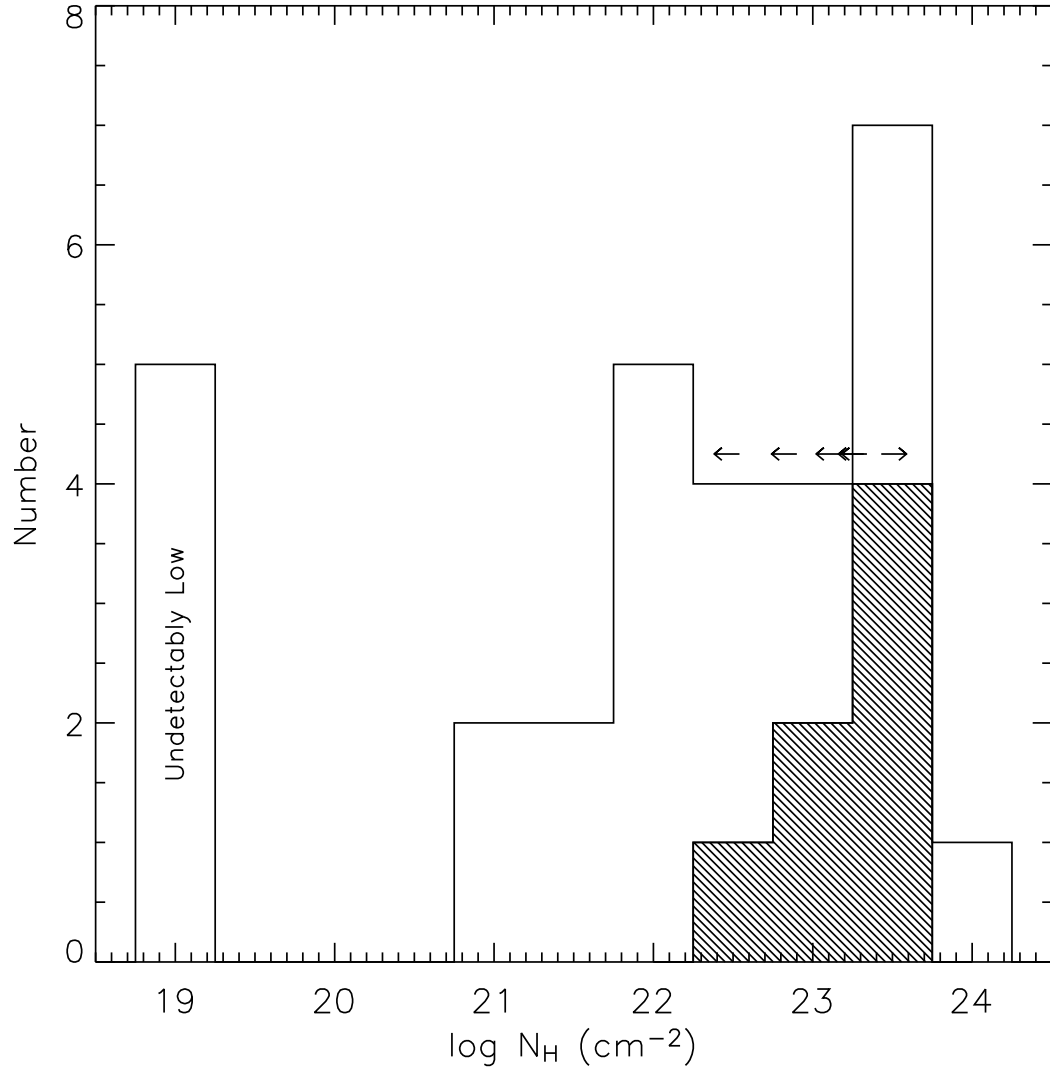


Figure 3.18 Distribution of X-ray column densities  $N_H(\text{cm}^{-2})$  for the power-law galaxies in the X-ray catalog (unshaded) and those only weakly-detected (shaded). We place only upper or lower limits on the column densities of all but one of the weakly-detected sources; the limits of sources with redshift estimates are shown by small arrows. Sources with undetectably low column densities were assigned columns of  $\log N_H(\text{cm}^{-2})=19$  for plotting.

be detectable out to high redshift (see Fig. 9). Secondly, the median optical–MIR SED of the sources not detected in X-rays falls below that of the weakly-detected sources at optical wavelengths, which in turn falls below that of the strongly-detected sources, suggesting a continuously increasing optical obscuration for a given  $1.25\ \mu\text{m}$  flux density (see Fig. 11). Adding the 10 weakly-detected power-law galaxies, all of which are likely to be obscured (see Table 2), we calculate an obscured fraction of  $\sim 75\%$ . If we further include the power-law galaxies not detected in X-rays, assuming that all are obscured, the maximum obscured fraction of power-law galaxies rises to  $82\%$  (4:1-5:1). (Considering only those power-law galaxies with  $\theta < 10'$  gives an obscured fraction of  $81\%$ ). This upper limit on the obscured fraction is consistent with the fraction of NLAGN SEDs found by Alonso-Herrero et al. (2006) for power-law sources in the CDF-S ( $\sim 75\%$ ).

To place a lower limit on the obscured fraction, we consider two additional scenarios. If we assume that all of the X-ray non-detected power-law galaxies are obscured, as before, but assume instead that the 6 weakly-detected power-law galaxies with upper limits on their column densities are *unobscured*, the obscured fraction drops to  $\sim 71\%$ . If we further consider only those power-law galaxies with column density estimates (i.e. those sources strongly or weakly detected in the X-ray) and assume again that all of the weakly-detected power-law galaxies with upper limits on their column densities are unobscured, the minimum obscured fraction drops to  $\sim 60\%$ . This lower limit, however, falls below the obscured fraction of the X-ray–detected power-law galaxies ( $68\%$ ). As it is unlikely that the power-law galaxies not detected in the X-ray are significantly less obscured than those detected in the X-ray, the obscured fraction of the X-ray–detected power-law galaxies can be taken as the lower limit on the obscured fraction.

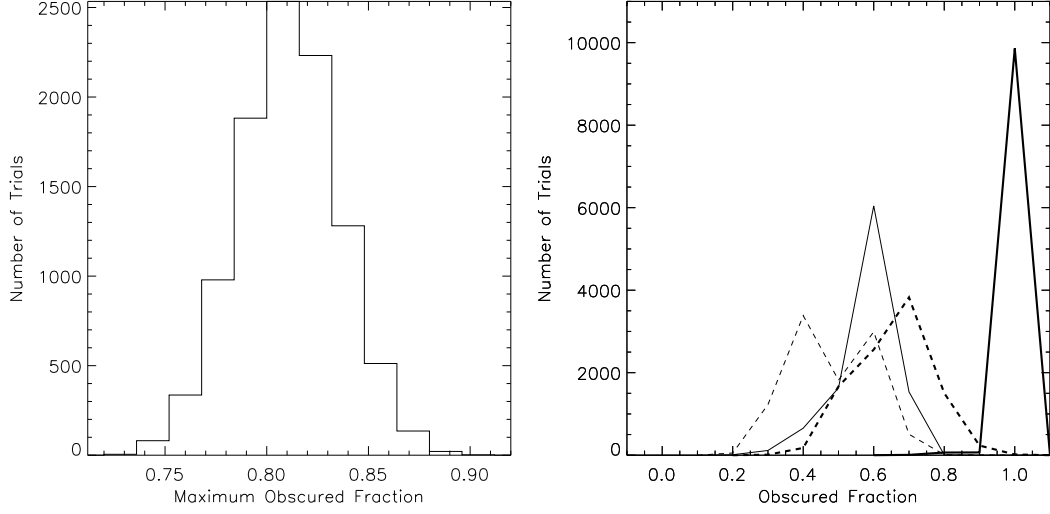


Figure 3.19 Left: Upper limit on the fraction of obscured ( $\log N_{\text{H}}(\text{cm}^{-2}) \geq 22$ ) power-law galaxies. All power-law galaxies not strongly or weakly detected in X-rays were assumed to be obscured. Right: Upper limit on the obscured fraction as a function of redshift and X-ray luminosity. Sources with absorption-corrected  $\log L_{\text{x}} (\text{erg s}^{-1}) < 44$  are shown by solid lines; dotted lines represent sources with  $\log L_{\text{x}} (\text{erg s}^{-1}) > 44$ . Thin and thick lines represent sources with redshifts of  $z < 2$  and  $z > 2$ , respectively. For viewing clarity, we do not plot the histograms, but instead connect their points.

To investigate the dispersion in the observed ratio of obscured to unobscured AGN, we ran a Monte Carlo simulation in which we varied both the assumed intrinsic photon index,  $\Gamma$ , and the photometric redshifts, and then recalculated the column densities of the power-law galaxies. The intrinsic photon index was drawn from the distribution of Tozzi et al (2006), as measured for the brightest 30 sources in their sample:  $\Gamma = 1.81 \pm 0.20$ . We allowed the photometric redshifts of the power-law galaxies to vary about their mean by  $\Delta(z) = 0.1(1 + z)$  (see §4). For the simulation, we assigned the 6 cataloged and weakly-detected sources with hard-to-soft flux ratios but no redshift estimate the median redshift of our sample,  $z = 1.9$ . The results are shown in Figure 19. The maximum obscured fraction varies from  $\sim 75\%$  to  $85\%$  (3:1-6:1), with a mean of  $81\%$  (4:1).

### 3.7.1.2 Redshift and luminosity dependence of obscured fraction

We plot in the right panel of Figure 19 the obscured fraction as a function of redshift and observed X-ray luminosity. Solid and dotted lines represent power-law galaxies with low ( $\log L_x (\text{erg s}^{-1}) < 44$ ) and high ( $\log L_x (\text{erg s}^{-1}) > 44$ ) absorption-corrected X-ray luminosities, and thin and thick lines represent power-law galaxies with low ( $z < 2$ ) and high ( $z > 2$ ) redshifts, respectively. We include all X-ray sources with redshifts for which column densities are available, and exclude those sources with only upper limits on the X-ray luminosity. In addition to having a relatively high obscured to unobscured ratio, power-law galaxies appear to be more heavily obscured at low X-ray luminosities and at high redshifts. The upper limit on the obscured fraction varies from 0.5, for low-redshift, high-luminosity power-law galaxies, to 1, for high-redshift, low-luminosity sources. As we can plot only those power-law galaxies detected in the X-ray for which redshift estimates are available (37/63), systematic effects are likely to be present (e.g. Treister et al. 2005).

The trends we find are consistent with previous results. A number of authors have predicted an increase in the obscured fraction of AGN with increasing redshift (e.g., Gilli et al. 2001, 2003; La Franca et al. 2005; Ballantyne et al. 2006; Tozzi et al. 2006), although a constant obscured fraction also appears to be consistent with the current data (Ueda et al. 2003; Gilli 2004; Treister et al. 2004; Treister & Urry 2005). Akylas et al. (2006) suggest that the observed increase in the obscured fraction with redshift may be due to statistical fluctuations in the small number of counts in the low energy bands, which can cause the column densities of high redshift sources to be overestimated. Stronger evidence exists for a decrease in the obscured fraction with increasing X-ray luminosity (Ueda et al. 2003; Steffen et al. 2003; Hasinger 2004; Szokoly et al. 2004; Barger

et al. 2005; Treister et al. 2005; Ballantyne et al. 2006), as expected from the receding torus model (Lawrence 1991). For instance, Szoloky et al. (2004) find X-ray Type 2 fractions of 75%, 44%, and 33% for AGN with X-ray luminosities of  $\log L_x \text{ (erg s}^{-1}\text{)} = 42 - 43$ ,  $43 - 44$ , and  $44 - 45$ , respectively, and Ballantyne et al. (2006) find that the model that simultaneously best describes local AGN data, the CXRB spectrum, and X-ray number counts requires an obscured ratio of 4:1 for low luminosity AGN and 1:1 to 2:1 for AGN with  $\log L_x \text{ (erg s}^{-1}\text{)} > 44$ .

### 3.7.1.3 Obscured fraction of color-selected samples

If we assume that all of the color-selected sources are AGN, and that all X-ray-non-detected sources are obscured, the Lacy et al. and Stern et al. selection criteria give upper limits on the obscured fraction of 92% (12:1) and 88% (7:1). As discussed in §6.2.2, however, it is likely that these samples contain star-forming galaxies as well as AGN; these estimates of the obscured fractions are therefore almost certainly high. By comparing the numbers of IR color-selected and optically-selected AGN, Stern et al. (2004) estimated an obscured AGN fraction of 76%, similar to that found for the power-law galaxies, although Richards et al. (2006) use a different infrared-to-optical flux ratio to revise this estimate to  $\geq 41\%$ . Lacy et al. (2004) similarly found an obscured ratio of 46% for the brightest members of their sample. It is important to note, however, that both the color- and power-law criteria select luminous AGN whose NIR/MIR emission is dominated by the central engine. Low-luminosity and heavily-obscured AGN whose NIR/MIR emission is dominated by the host galaxy will tend to fall outside of the color-selection and power-law regions, increasing the total obscured fraction of AGN.

### 3.7.2 Space Densities of Obscured AGN

If we assume that all of the power-law galaxies not detected in X-rays are obscured, the power-law sample contains at most  $\sim 51$  obscured AGN and at least  $\sim 11$  unobscured AGN (assuming that CDFN 50281, with a column density of  $N_{\text{H}} \leq 10^{22} \text{ cm}^{-2}$  is unobscured). How do these numbers compare to the predicted space densities of Type 1 and Type 2 AGN?

Treister et al. (2006, private comm.) predict 199 AGN in a  $350 \text{ arcmin}^2$  area (the area of our survey) down to a  $24 \mu\text{m}$  limiting flux density of  $80 \mu\text{Jy}$ ,  $\sim 105 - 110$  of which should be detected in the hard X-ray band and  $\sim 174$  of which are obscured (Type II). For comparison, the X-ray catalog of Alexander et al. (2003) contains 147-149 hard X-ray sources that meet our exposure cut (and therefore lie in the survey area) and which have  $S_{24} > 80 \mu\text{Jy}$  and AGN-like X-ray luminosities of  $\log L_{\text{x}}(\text{ergs s}^{-1}) > 42$ . At a flux density of  $80 \mu\text{Jy}$ , the predicted number counts (for X-ray detected AGN) therefore lie within a factor of  $\sim 1.4$  of the observed values.

As discussed in §5.2, all but 5 of the power-law galaxies have  $24 \mu\text{m}$  counterparts and all but one of the MIPS-detected sources have a  $24 \mu\text{m}$  flux density  $> 80 \mu\text{Jy}$ . Of the 5 sources without  $24 \mu\text{m}$  counterparts, however, only one source is a clear non-detection. The power-law sample therefore contains 56-60 galaxies with  $24 \mu\text{m}$  fluxes  $> 80 \mu\text{Jy}$ . Based on the Treister et al. (2006) predictions, these sources should account for  $\sim 28 - 30\%$  of the MIR-detected AGN (or  $\sim 20 - 22\%$  if we boost the Treister et al. counts by a factor of 1.4). Likewise, the 45-49 obscured power-law galaxies with  $24 \mu\text{m}$  fluxes  $> 80 \mu\text{Jy}$  should account for at most  $\sim 26 - 28\%$  ( $\sim 18 - 20\%$ ) of the obscured, Type II, MIR-detected AGN.

Our results therefore suggest that at most  $\sim 20 - 30\%$  of the MIPS-detected AGN and MIPS-detected obscured AGN have high  $S/N$  power-law IRAC continua; the remainder could have SEDs dominated by or strongly affected by the

host galaxy, red power-law SEDs that fall below our IRAC detection limit, or have been rejected due to noise that caused them to fail our relatively stringent signal-to-noise criteria. It is not surprising that we find a fairly small portion of power-law AGN, as our selection criteria require the AGN to be both of high luminosity and energetically dominant over the other source components in the near- to mid-IR. Franceschini et al. (2005) find that of a sample of *Chandra*-detected AGN in the SWIRE survey, only 62% have optical-IR SEDs typical of Type 1 or Type 2 AGN, and 40-60% of X-ray-selected AGN are known to be optically-dull (Hornschemeier et al. 2001; Barger et al. 2001; Giacconi et al. 2001). The fraction of AGN with optical-IR SEDs dominated by star-formation is likely to be even higher for heavily obscured AGN samples, such as that identified here. Polletta et al. (2006) select obscured AGN candidates on the basis of red non-stellar SEDs, similar to the power-law criterion used here; only 40% of their obscured AGN candidates show AGN signatures in the optical/NIR SEDs.

### 3.7.3 Effect of Reddening on Obscured AGN

Is it reasonable to assume that heavily obscured AGN at high redshift could have NIR/MIR SEDs still dominated by the central engine? Observations of QSOs indicate that AGN can be up to 2–3 magnitudes brighter than their host galaxies in the NIR (e.g. McLeod & Rieke 1994; Percival et al. 2001; Marble et al. 2003), although the contribution of the non-stellar continuum varies from source to source and as a function of wavelength. The total H-band contribution of luminous AGN, for example, ranges from  $\sim 35$  to 90% (McLeod & Rieke 1994), and while the non-stellar continuum of NGC 1068 accounts for  $>80\%$  of the flux at  $2.3\ \mu\text{m}$  in the inner  $4''4$ , the contribution drops to 30% at  $1.6\ \mu\text{m}$  (Origlia et al. 1993).

In the Milky Way, a column density of  $\log N_{\text{H}}(\text{cm}^{-2}) = 23$  corresponds to an  $A_{\text{V}}$  of  $\sim 50$  mag (Bohlin, Savage, & Drake 1978). The  $A_{\text{V}}$  to  $N_{\text{H}}$  ratio of AGN,

however, appears to be an order of magnitude lower than that of the Milky Way (e.g. Maccacaro, Perola, & Elvis 1982; Reichert et al. 1985; Granato et al. 1997; Maiolino et al. 2001a), due either to a higher gas-to-dust ratio, or to the formation of large grains in the dense AGN environment (Maiolino et al. 2001a, 2001b). Following Martínez-Sansigre (2006), we therefore adopt an AGN  $N_{\text{H}}$  to  $A_{\text{V}}$  conversion of  $2.0 \times 10^{-23}$ , for which column densities of  $\log N_{\text{H}}(\text{cm}^{-2}) = 22, 23$ , and  $24$  correspond to  $A_{\text{V}} = 0.2, 2$ , and  $20$  mag, respectively.

Assuming the IR extinction law of Rieke & Lebofsky (1985), we estimate the observed IRAC extinctions for an obscured AGN at  $z = 2$ , where IRAC samples the  $1 - 3 \mu\text{m}$  rest-frame emission. At a column density of  $\log N_{\text{H}}(\text{cm}^{-2}) = 22$ , the extinctions at the center of the IRAC channels are negligible (0.02-0.06 mag), but they rise with column density to 0.2-0.6 mag for  $\log N_{\text{H}}(\text{cm}^{-2}) = 23$  and 1.8-6.2 mag for  $\log N_{\text{H}}(\text{cm}^{-2}) = 24$ . It is therefore reasonable to assume that luminous obscured AGN could dominate the emission of their host galaxies at all but the highest column densities.

If the interstellar extinction law is applicable to AGN, differential extinction across the IRAC bands will redden the observed spectral slope, potentially increasing the number of heavily obscured luminous AGN in the power-law sample. At  $z = 2$ , a column density of  $\log N_{\text{H}}(\text{cm}^{-2}) = 22$  has only a minor effect on the measured slope: an observed spectral index of  $\alpha = -0.5$  corresponds to an unreddened intrinsic slope of  $\alpha = -0.45$ . At higher column densities of  $\log N_{\text{H}}(\text{cm}^{-2}) = 23$  and  $\log N_{\text{H}}(\text{cm}^{-2}) = 24$ , however, the best-fit intrinsic slopes at  $z = 2$  increase to  $\alpha = 0.0$  and  $\alpha = 4.5$ . The unrealistic predicted intrinsic slope of the high-redshift Compton-thick model suggests that highly obscured AGN at high redshift are likely to have steep observed spectral slopes, if their IR and X-ray emission are subject to the same obscuring material. For example, the spec-



tral slope of CDFN 44836,  $\alpha = -3.2$ , could be caused by the extinction of an  $\alpha = 0$  source by a column density of  $\log N_{\text{H}}(\text{cm}^{-2}) = 23.8$  at  $z = 2$ . At such high column densities, however, the de-reddened source begins to steepen at the bluest bands, no longer resembling a power-law source.

While the above results therefore suggest that power-law selection may be biased against Compton-thick AGN, there exist a population of AGN whose X-rays are more heavily obscured than their optical/NIR emission (e.g. Akiyama et al. 2003; Brusa et al. 2003; Page et al. 2003; Wilkes et al. 2005). For instance, 10% of the BLAGN sample of Perola et al. (2004) have X-ray columns of  $\log N_{\text{H}}(\text{cm}^{-2}) \geq 22$ . Shi et al. (2006) also find several Compton-thick AGN that do not follow an observed correlation between X-ray column density and the strength of the silicate emission or absorption feature. Instead, their silicate absorption is weaker than expected, suggesting a Compton-thick absorber that obscures the X-ray emission, but not the IR emission. These outliers could also be explained, however, by a Compton-thick absorber that obscures the mid-IR so strongly that the output in this range is dominated by star formation in the host galaxies.

### 3.8 Conclusions

We define a sample of 62 power-law galaxies in the CDF-N. Sources were required to be detected to  $S/N > 6$  in each of the IRAC bands, have IRAC slopes of  $\alpha < -0.5$  (where  $f_{\nu} \propto \nu^{\alpha}$ ), and to lie in regions with both deep X-ray ( $> 0.5$  Ms) and radio coverage. We studied the multiwavelength properties of the power-law galaxies and compared the power-law selection technique to other MIR-based AGN selection criteria. We then measured the intrinsic obscuring column densities of the power-law galaxies to estimate the obscured fraction of the sam-

ple, which should be less affected by obscuration than optical and/or X-ray selected samples. The main results of this paper are as follows:

- Power-law selection requires the AGN to be energetically-dominant in the near/mid infrared. On average, AGN with X-ray luminosities of  $\log L_x$  ( $\text{erg s}^{-1}$ )  $< 44$  have SEDs dominated by or strongly affected by the stellar continuum. Therefore, power-law galaxies tend to have high X-ray luminosities, and make up a significant fraction of the X-ray luminous AGN population.
- Power-law galaxies lie at significantly higher redshifts than the typical IRAC or X-ray-detected source, primarily due to their high luminosities. While the power-law sample defined here accounts for only  $\sim 20\%$  of the X-ray and MIR-detected AGN in the comparison sample, approximately 50% of the high-redshift X-ray sample are power-law galaxies.
- 45% of the power-law galaxies are not detected in the X-ray catalog of Alexander et al. (2003) at exposures of  $> 0.5$  Ms. A search for faint emission reveals that 15% remain undetected at the  $2.5\sigma$  detection level. X-ray detection is not a strong function of redshift, X-ray exposure time (at  $> 1$  Ms), power-law slope, or power-law fit probability.
- Almost all (93-98%) of the IRAC-selected power-law galaxies are detected at  $24 \mu\text{m}$ . The  $24 \mu\text{m}$  detection fraction of AGN in the comparison sample increases with X-ray luminosity. Because we require all power-law galaxies to be detected in each of the four IRAC bands, the  $24 \mu\text{m}$  detection fraction is almost certainly higher than would be expected for an unbiased sample of AGN. Nevertheless, comparison with a sample suffering from the same

bias (the comparison sample) shows that the high detection fraction is representative of an intrinsically X-ray luminous AGN population.

- 30% of the power-law galaxies have radio counterparts from the Richards et al. (2000) VLA survey of the CDF-N. Only two of the 18 radio-detected sources (11%) have radio emission in excess of that predicted by the radio-infrared correlation, suggesting an overall radio-loud fraction of only 3%. In comparison, almost all of the radio-excess AGN of Donley et al. (2005) have optical/MIR SEDs dominated by the stellar bump. Further exploration of a possible systematic difference in the radio properties of the two samples would be interesting. While there is very little overlap between the radio-excess and power-law samples, both have similarly low X-ray detection fractions, suggesting that this may be a common feature of AGN selected independently of their X-ray and optical properties, regardless of redshift or luminosity.
- The optical–MIR SEDs of the power-law galaxies are flatter than the median radio-quiet SED of Elvis et al. (1994). Sources not detected in X-rays have SEDs that drop off more rapidly in the optical than those of the power-law galaxies detected in X-rays, as discussed in Alonso-Herrero et al. (2006), presumably due to increasing optical obscuration. Weakly-detected power-law galaxies have intermediate optical SEDs.
- At least half of the power-law galaxies detected in the X-ray catalog have compact optical counterparts, suggesting that the optical light is dominated by the AGN, as expected. Only 2 non- or weakly-detected sources have compact optical counterparts. 15% of the power-law galaxies in the GOODS field do not have optical counterparts brighter than the GOODS limiting

magnitudes.

- Power-law galaxies comprise a subset of the MIR sources selected via color criteria (e.g. Lacy et al. 2004; Stern et al. 2005). While color-selected AGN samples include a higher fraction of high-luminosity AGN than does the power-law selected sample, the color criteria select larger fractions of sources not detected in X-rays, due at least in part to a higher degree of contamination by star-forming galaxies. Combining color-selection with additional tests designed to rule out emission from star-forming galaxies is likely to produce more reliable samples of AGN.
- 68% (2:1) of the X-ray-detected power-law galaxies are obscured ( $\log N_{\text{H}}(\text{cm}^{-2}) > 22$ ), and all of the weakly-detected power-law galaxies are consistent with being obscured, but not Compton-thick ( $\log N_{\text{H}}(\text{cm}^{-2}) > 24$ ). If we assume that all of the X-ray non-detected power-law galaxies are obscured, we derive a maximum obscured fraction of 81% (4:1). Power-law galaxies also appear to be more heavily obscured at low X-ray luminosities and at high redshift.
- Power-law galaxies detected to high  $S/N$  in the IRAC bands account for  $\sim 20 - 30\%$  of both the MIR-detected AGN and the MIR-detected obscured AGN predicted by the X-ray luminosity function synthesis models of Treister et al. (2006) down to  $24 \mu\text{m}$  flux densities of  $80 \mu\text{Jy}$ . This percentage is best interpreted as a lower limit since our conservative selection criteria may exclude some power-law objects.
- At all but the highest column densities, NIR/MIR extinction should have only a minor effect on the power-law emission of luminous AGN. IRAC power-law selection, however, is likely to be biased against high-redshift

Compton-thick AGN if the covering fractions of the X-ray and NIR-emitting regions are the same.

## CHAPTER 4

*Spitzer's* CONTRIBUTION TO THE AGN POPULATION

Infrared selection is a potentially powerful way to identify heavily obscured AGN missed in even the deepest X-ray surveys. Using a  $24\ \mu\text{m}$ -selected sample in GOODS-S, we test the reliability and completeness of three infrared AGN selection methods: (1) IRAC color-color selection, (2) IRAC power-law selection, and (3) IR-excess selection; we also evaluate a number of infrared excess approaches. We find that the vast majority of non-power-law IRAC color-selected AGN candidates in GOODS-S have colors consistent with those of star-forming galaxies. Contamination by star-forming galaxies is most prevalent at low  $24\ \mu\text{m}$  flux densities ( $\sim 100\ \mu\text{Jy}$ ) and high redshifts ( $z \sim 2$ ), but the fraction of potential contaminants is still high ( $\sim 50\%$ ) at  $500\ \mu\text{Jy}$ , the highest flux density probed reliably by our survey. AGN candidates selected via a simple, physically-motivated power-law criterion (PLGs), however, appear to be reliable. We confirm that the infrared excess methods successfully identify a number of AGN, but we also find that such samples may be significantly contaminated by star-forming galaxies. Adding only the secure *Spitzer*-selected PLG, color-selected, IR-excess, and radio/IR-selected AGN candidates to the deepest X-ray-selected AGN samples directly increases the number of known X-ray AGN (84) by  $54 - 77\%$ , and implies an increase to the number of  $24\ \mu\text{m}$ -detected AGN of  $71 - 94\%$ . Finally, we show that the fraction of MIR sources dominated by an AGN decreases with decreasing MIR flux density, but only down to  $f_{24\ \mu\text{m}} = 300\ \mu\text{Jy}$ . Below this limit, the AGN fraction levels out, indicating that a non-negligible fraction ( $\sim 10\%$ ) of faint  $24\ \mu\text{m}$  sources (the majority of which are missed in the X-ray) are powered not by star formation, but by the central engine. The fraction of all AGN (regardless

of their MIR properties) exceeds 15% at all 24  $\mu\text{m}$  flux densities.

#### 4.1 Introduction

Identifying complete and reliable samples of AGN has become a necessity for extragalactic surveys, whether the goal be the selection of AGN candidates or the removal of AGN “contaminants”. Only when armed with complete samples of AGN will we be able to determine the role of obscured accretion in the build-up of the present day black hole mass function, or accurately characterize the star-formation history of the universe. Complete AGN samples are also required to test proposed evolutionary theories in which black hole formation and star-formation are intimately linked by merger and feedback processes (e.g. Hopkins et al. 2006), ultimately producing the correlation between black hole mass and bulge velocity dispersion (Ferrarese & Merritt 2000; Gebhardt et al. 2000). Unfortunately, the varied luminosities, accretion rates, orientations, and intrinsic obscurations of AGN prevent any one selection technique from reliably identifying all of them. For instance, while current UV, optical, and X-ray surveys are capable of detecting unobscured AGN, they miss many of the obscured AGN and nearly all of the Compton-thick AGN thought to dominate AGN number counts at both low and high redshift (e.g. Gilli et al. 2007; Daddi et al. 2007a,b). Likewise, only 10-15% of AGN are radio-loud, making radio surveys relatively incomplete.

The Multiband Imaging Photometer (MIPS; Rieke et al. 2004) and Infrared Array Camera (IRAC; Fazio et al. 2004) instruments aboard *Spitzer* have provided sensitive surveys in multiple mid-IR bands. Infrared selection with MIPS and IRAC data is being used widely to select AGN candidates independently of their optical and/or X-ray properties. In addition to identifying AGN in fields with little or no X-ray data, infrared selection criteria are capable of identifying heavily

obscured AGN missed in even the deepest X-ray fields (e.g. Donley et al. 2007). As such, IR selection has the potential to complement traditional AGN selection methods and to yield a more complete census of AGN activity.

In this paper, we critically review the following infrared selection criteria: (1) IRAC color-color selection, (2) IRAC power-law selection, and (3) IR-excess selection. The first selection method employs color cuts in two representations of IRAC 4-band mid-infrared (MIR) color-color space (Lacy et al. 2004; Stern et al. 2005), the second identifies AGN whose IRAC SEDs are well-fit by a power-law (Alonso-Herrero et al. 2006, Donley et al. 2007), and the third selects red galaxies with large infrared to UV/optical flux ratios (Daddi et al. 2007a, Dey et al. 2008, Fiore et al. 2008, Polletta et al. 2008). The first two criteria are based on the same principle: the hot dust near an AGN's central engine reprocesses absorbed UV, optical, and X-ray emission into short-wavelength MIR emission, filling in the gap between the stellar emission that peaks near  $1.5 \mu\text{m}$  and the long-wavelength dust emission features that dominate the SEDs of star-forming galaxies. The color-color and power-law selection criteria, however, differ in the range of mid-IR characteristics they include as possible AGN indicators. The third selection method identifies sources in which heavy obscuration with re-emission in the infrared diminishes the optical emission and/or enhances the infrared emission.

This paper utilizes improved spectral templates with a sample of infrared color-selected, power-law galaxies (PLGs), and IR-excess galaxies in the ultra-deep GOODS-S field to test the reliability and completeness of these selection techniques over a wide range of sample properties. From this analysis, we then quantify the contribution of these approaches plus *Spitzer* identification of radio-intermediate and radio-loud AGN to the X-ray-selected AGN population. The



paper is organized as follows. In §2, we describe the selection of the color-selected, PLG, and IR-excess samples. The construction of high-reliability photometric redshifts is described in §3, as are the overall redshift properties of the sample. In §4, we briefly discuss the X-ray properties of our MIPS-selected sample. The infrared color selection criteria of Lacy et al. (2004) and Stern et al. (2005) are discussed in §5, where we compare and contrast the two selection criteria, investigate the behavior in color space of the star-forming templates, determine the redshift and flux dependencies of the color selection techniques, and investigate the properties of the most secure color-selected AGN candidates. In §6, we discuss the PLG selection criteria, and in §7 we investigate the IR-excess sources. Finally, in §8, we discuss the overall statistics of AGN revealed by IR-based methods compared with X-ray-selected samples. A summary is given in §9. Throughout the paper, we assume the following cosmology:  $(\Omega_m, \Omega_\Lambda, H_0) = (0.3, 0.7, 72 \text{ km s}^{-1} \text{ Mpc}^{-1})$ .

## 4.2 Sample Selection

### 4.2.1 Multi-wavelength Data

We take as our initial GOODS-S sample all MIPS sources detected at  $24 \mu\text{m}$  to a flux density of  $f_{24 \mu\text{m}} > 80.0 \mu\text{Jy}$ . At this flux limit, 99% of the MIPS sample are detected to  $> 10\sigma$ . There are several advantages to choosing a flux-limited MIPS sample. First, AGN (and LIRGS/ULIRGS) tend to be bright at  $24 \mu\text{m}$  (e.g. Rigby et al. 2004). Selecting only those galaxies with  $f_{24 \mu\text{m}} > 80.0 \mu\text{Jy}$  therefore retains all but the faintest AGN while excluding 50-60% of IRAC-selected IR-normal star-forming galaxies at all flux densities. Second, a MIPS flux-limited sample is not subject to the complicated slope-dependent selection bias present in IRAC selected samples due to the significant variation in the sensitivity of the

4 IRAC bands (see Donley et al. 2007). Third, this selection gives a complete and well-defined sample of objects with extreme red  $R - [24]$  colors.

The MIPS 24  $\mu\text{m}$  catalog of the GOODS Legacy team (Dickinson et al., in prep.) is comprised of 948 sources in the MIPS CDF-S Legacy field with  $f_\nu > 80.0 \mu\text{Jy}$ . While this MIPS depth can be obtained over the full CDF-S, we chose to limit this study to the GOODS region to take advantage of the super-deep IRAC imaging. The relative depths of the limiting MIPS flux and the super-deep IRAC photometry ensure that essentially all MIPS sources have high S/N IRAC SEDs, allowing us to study in an unbiased way the IRAC properties of this flux-limited MIPS sample. To ensure that all AGN candidates have sufficient X-ray coverage, we also required X-ray coverage of  $T_X > 250$  ks from the deep 1  $M_s$  CDF-S X-ray dataset (see Giacconi et al. (2002) and Alexander et al. (2003)). Despite this relatively low cut, 96% of the final MIPS sample have  $T_X > 0.5$  Ms and 80% have  $T_X > 0.75$  Ms. The resulting sample was drawn from an area of 195.3 sq. arcmin and contains 846 MIPS sources.

The CDF-S is one of the best-imaged fields in the UV, optical, NIR, and X-ray. We took advantage of this extensive multiwavelength dataset by creating an aperture-matched catalog using the UV-NIR photometry of Marzke et al. (1999,  $RIZ$ ), Vandame et al. (2001,  $JK$ ), Arnouts et al. (2002,  $UU_pBVRI$ ), COMBO17 (Wolf et al. 2004), Giavalisco et al. (2004,  $bviziJHK$ ), Le Fèvre et al. (2004,  $I$ ), and GALEX ( $FUV$ ,  $NUV$ ) (see Pérez-González et al. 2005 and the UCM Extragalactic Database<sup>1</sup> for more details). We then removed from our sample the 89 MIPS sources that had multiple optical counterparts that were (1) within a  $2.5''$  search radius of the MIPS source and (2) separated by more than  $0.5''$ . (At  $r < 0.5''$ , it is difficult to distinguish between multiple counterparts and an extended/irregular

---

<sup>1</sup><http://t-rex.fis.ucm.es/pgperez/Proyectos/databaseuse.en.html>

source with multiple components.) While we do not restrict our sample to regions covered by GOODS ACS imaging, 83% of the MIPS sources in our sample have deep ACS coverage.

SExtractor-selected IRAC sources were similarly matched to the MIPS sample after combining the super-deep IRAC data with data from the deep, wide-area, *Spitzer* Legacy Program (PI: van Dokkum) and the MIPS-GTO IRAC program (see Pérez-González et al. 2008 for further details). To ensure accurate MIR SEDs, we removed from the IR PLG and color-selected samples 32 sources with blended IRAC or MIPS photometry. Of the remaining 725 MIPS sources that meet our criteria, 713 (98%) have unique IRAC counterparts within a  $2''$  search radius, and 699 (96%) have  $> 5\sigma$  IRAC detections in all 4 IRAC bands, allowing us to determine accurately the MIR colors of essentially all members of the MIPS-selected sample. Of the 12 sources without IRAC counterparts, 6 were not detected due to blending with a nearby source, 4 had badly centered MIPS positions, and 2 had faint IRAC counterparts that fall below our catalog limit.

#### 4.2.2 Power-law, color-selected, and IR-normal samples

After assigning IRAC counterparts, we separated the MIPS sample into three subsets: IR PLGs, IR color-selected galaxies, and IR-normal galaxies. We defined as PLGs sources whose 4-band IRAC photometry is well-fit by a line of slope  $\alpha \leq -0.5$ , where  $f_\nu \propto \nu^\alpha$  (Alonso-Herrero et al. 2006; Donley et al. 2007). The effect of different cuts in  $\alpha$  will be discussed in §6. To ensure a good fit, we required the chi-squared probability  $P_\chi$  (the probability that the fit would yield a chi-squared greater than or equal to the observed chi-squared) to exceed 0.1.  $P_\chi$  tends either to lie close to 0.5 (the probability that corresponds to a reduced chi-squared of 1) or is very small (see Bevington & Robinson 2003). This selection, which identified 55 PLGs, was done using the LINFIT task in IDL. This task takes

the following 4-band input from IRAC:

$$x = \log(\nu) \quad (4.1)$$

$$y = \log(f_\nu) \quad (4.2)$$

$$\Delta y = [1/\ln(10)] * \Delta f_\nu / f_\nu \quad (4.3)$$

and returns the best fit slope,  $\alpha$ , and the chi-squared probability,  $P_\chi$ . While sources selected via this method are dominated by the AGN in the mid-IR, we do not require that the power-law extend into the optical. Consequently, many infrared-selected PLGs are dominated by stellar emission at wavelengths short of  $\sim 2 \mu\text{m}$ , where the reprocessed emission from hot dust is suppressed because of dust sublimation.

Color-selected galaxies were defined as sources that meet the AGN IRAC color-cuts of Lacy et al. (2004) or Stern et al. (2005), but that **do not meet the PLG criterion**. As discussed in Alonso-Herrero et al. (2006) and Donley et al. (2007), both the PLG and IRAC color cuts attempt to select luminous AGN that outshine their host galaxies in the infrared, filling in the dip in a galaxy's SED between the short-wavelength stellar emission feature and the long-wavelength dust emission features. As such, the IRAC AGN color selection regions contain, but also extend beyond, the power-law locus in color space. While nearly all PLGs meet the IRAC AGN color selection criteria, not all color-selected galaxies meet the PLG criteria. We therefore separate color-selected sources that can be identified via a power-law fit (PLGs) from those that can not (color-selected galaxies). The color-selected sample consists of 210 sources, 188 of which meet the Lacy et al. criteria, 72 of which meet the Stern et al. criteria, and 50 of which meet both criteria.

Finally, we define IR-normal galaxies as sources that meet neither the IRAC PLG nor the color selection criteria; these sources comprise the remaining 448 galaxies in the MIPS sample. As they are not the focus of this study, we have not checked their IRAC and MIPS photometry by eye. Instead, we estimate that the fraction of IR-normal galaxies with blended IRAC or MIPS photometry is similar to that found for the PLG and color-selected samples, 11%, or  $\sim 50$  galaxies. We caution that IR-normal does *not* mean purely star-forming. Instead, 'IR-normal' only indicates that any mid-IR emission from an AGN is overwhelmed by emission from the host-galaxy. In fact, many Type 2 and Seyfert-luminosity AGN meet the IR-normal criteria (Stern et al. 2005, Donley et al. 2007, Cardamone et al. 2008).

#### 4.2.3 IR-Excess Galaxies

In addition to dividing the MIPS-selected sample into the 3 sub-samples discussed above, we identified IR-excess galaxies using the criteria of Daddi et al. (2007a), Dey et al. (2008), Fiore et al. (2008), and Polletta et al. (2008). (We also searched for bright ULIRGS that met the IR-excess criteria of Yan et al. (2007), but found none in our faint sample.) Daddi et al. (2007a) selected galaxies in GOODS (with a  $3\sigma$   $24\ \mu\text{m}$  flux limit of 15-30  $\mu\text{Jy}$ ) whose total MIR+UV star-formation rate (SFR) exceeds the dust-corrected UV SFR by a factor of  $> 3$ , and estimate that at least  $\sim 50\%$  of their sample are Compton-thick AGN. Dey et al. (2008) select sources with  $R - [24] \geq 14$  ( $f_{24\ \mu\text{m}}/f_R \gtrsim 1000$ ) and  $f_{24\ \mu\text{m}} > 300\ \mu\text{Jy}$ , criteria which yield a sample of both heavily obscured AGN and star-forming galaxies. Fiore et al. similarly require that  $f_{24\ \mu\text{m}}/f_R \geq 1000$ , but also include an optical/NIR criterion of  $R - K > 4.5$  and extend their selection to fainter  $24\ \mu\text{m}$  fluxes of  $f_{24\ \mu\text{m}} \geq 40\ \mu\text{Jy}$ . They estimate from simulations that 80% of the sources selected via these criteria are obscured AGN. Polletta et al. (2008) focus only on

the most luminous AGN ( $f_{24} \mu\text{m} \gtrsim 1 \text{ mJy}$ ) with large infrared to optical flux ratios, whose IRAC and MIPS colors can be described by the following criteria:  $f_{5.8}/f_{3.6} > 2$ ,  $f_{8.0}/f_{4.5} > 2$ , and  $\log[f_{8.0}/f_{3.6}] + \log[f_{24}/f_{3.6}] > 2$ .

Because IR-excess sources tend to be optically-faint, we use the approach of Fiore et al. (2008, private communication) and estimate the R-band magnitudes by interpolating the ACS v- and i-band data from the MUSIC catalog (Grazian et al. 2006). Despite the inherent uncertainties associated with this relatively simple method, the interpolated R-band magnitudes are in excellent agreement with ground-based R-band measurements for bright sources, and they greatly improve upon the uncertain R-band estimations at faint flux densities. Because the MUSIC catalog is based on identifications at  $z$  and  $K$  (the latter of which is universally bright for the IR-excess sources), the use of the MUSIC catalog for these sources also ensures that the correct optical counterpart is chosen, as verified by a visual inspection of the sources selected via the Fiore et al. criteria. The only disadvantage of this method is that, of the 195.3 sq. arcmin of our survey, only 132.7 sq. arcmin (68%) are covered by the deep ISAAC K-band data, which was also used in the selection of the Daddi et al. sources. Our identification of the Dey et al., Daddi et al., and Fiore et al. IR-excess samples is therefore limited to this region.

Of the 465/713 sources in our MIPS-selected sample that lie in the ISAAC field, 10 meet the Dey et al. criteria, 52 meet the Fiore et al. criteria, and 42 lie in the Daddi et al. IR-excess sample (the list of which was kindly provided by D. Alexander, private communication 2008). In addition, 71 MIPS sources have red IR/optical colors of  $f_{24} \mu\text{m}/f_R \geq 1000$ ; we will refer to this sample as 'IR-bright/optically-faint'. Of the full sample of 713 sources, 5 meet the Polletta et al. criteria. The properties of these IR-excess galaxies, nearly all of which also

meet the power-law or color-selection criteria outlined above, will be discussed in more detail in §7.

### 4.3 Redshifts

While the redshift coverage in the CDF-S is amongst the highest in all cosmological fields, only 34% of the sources in our faint sample have spectroscopic redshifts. As one of our main goals is to investigate the redshift-dependency of infrared color selection, we require both accurate and complete redshift information. However, the mean magnitude of the sources without spectroscopic redshifts,  $V \sim 24.1$ , is very faint, making further spectroscopic follow-up challenging. We therefore supplement the spectroscopic redshifts with photometric ones. The sources that are the focus of this study generally have SEDs with weak stellar features and require extra care to fit accurate photometric redshifts. To insure this accuracy, we have used two complementary photo- $z$  approaches and have incorporated two stages of independent visual inspection by two reviewers, as described in Appendix B. The final results, shown in Figure 1, support the high accuracy and completeness of the adopted redshifts for this faint sample.

Of the 713 MIPS-selected sources in our sample, 249 have secure spectroscopic redshifts from the VVDS (Le Fèvre et al. 2004), VLT/FORS2 (Vanzella et al. 2006), K20 (Mignoli et al. 2005), and Szokoly et al. (2004) redshift surveys. For our photometric redshifts, the mean offset is  $\overline{\Delta(z)} = 0.012$ , where  $\Delta(z) = (z_p - z_s)/(1 + z_s)$ , and the dispersion is  $\sigma_z = 0.15$ , where  $\sigma_z^2 = (1/N) \sum \Delta(z)^2$ . Eighty-nine percent of the sample have  $\Delta(z) < 0.1$ , and 95% have  $\Delta(z) < 0.2$ . As shown in Table 1, while the redshift completeness and accuracy are high for the IR-normal and color-selected samples, they drop significantly for the PLG sample. A comparison of their spectroscopic and photometric redshifts illustrates some of the issues. Three

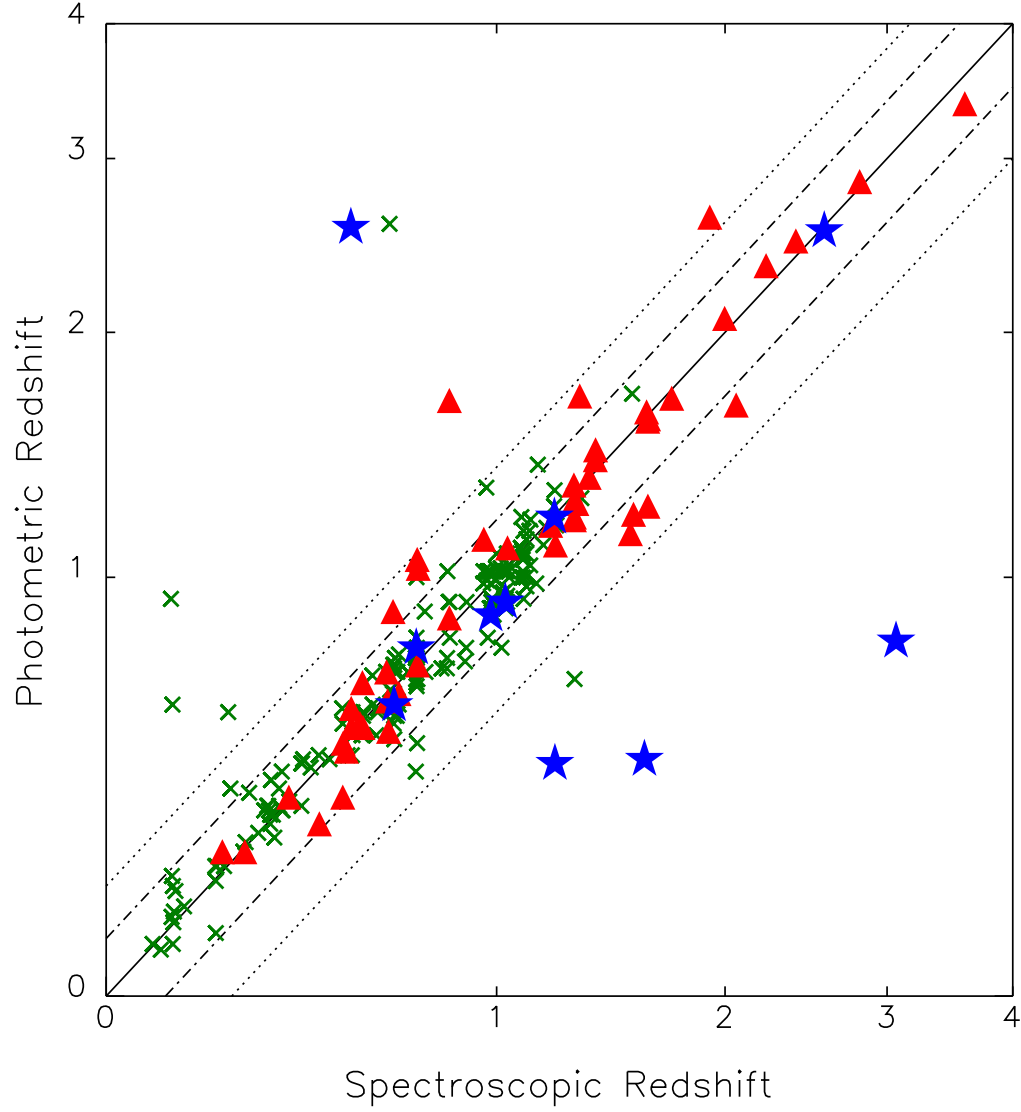


Figure 4.1 Photometric vs. secure spectroscopic redshifts for PLGs (navy stars), color-selected galaxies (red triangles), and IR-normal galaxies (green crosses). Values are plotted in  $\log(1 + z)$ . Dot-dashed and dotted lines give 10% and 20% errors on  $\Delta z$ , respectively. 89% of the sample have  $\Delta(z) < 0.1$ , and 95% have  $\Delta(z) < 0.2$ .



Table 4.1. Photometric Redshifts

Sample	$N_{\text{srcs}}$	$N_z$	$N_{\text{spec}}$	$\Delta z$	$\sigma_z$	% with $\Delta z > 0.10$	% with $\Delta z > 0.20$
All	713	649	249	0.012	0.15	11.3%	4.6%
IR-Normal	448	424	187	0.012	0.12	7.2%	2.8%
Color-Selected	210	196	51	0.015	0.10	20.4%	4.1%
Power-law	55	29	11	-0.013	0.48	40.0%	40.0%

of the four PLG outliers are best fit by a Type 1 QSO template, whose redshift is particularly difficult to constrain. However, of the 18 PLGs for which only photometric redshifts are available, only 2 (11%) are fit by a Type 1 QSO template. The remainder show optical features/breaks that make their redshift determination more secure. As such, we expect the overall accuracy of the PLG redshifts to be higher than one would assume given the limited comparison with spectroscopic redshifts.

With the addition of 400 photometric redshifts, computed as described above, our redshift completeness is 91%. The redshift distribution is shown in Figure 2. Also plotted in Figure 2 is a redshift histogram that incorporates typical errors in the photometric redshifts. To produce this distribution, we simulated 10,000 redshift distributions in which the photometric redshifts were randomly varied according to the appropriate  $\sigma$  given in Table 1. We plot in Figure 2 the mean of the resulting distributions. Both redshift distributions show a strong peak at  $z = 1$ , and while the first shows a potential peak at  $z \sim 2$ , we cannot confirm its presence due to the errors on the photometric redshifts.

We separate the sample in Figure 2 into the PLG, color-selected (Lacy et al.

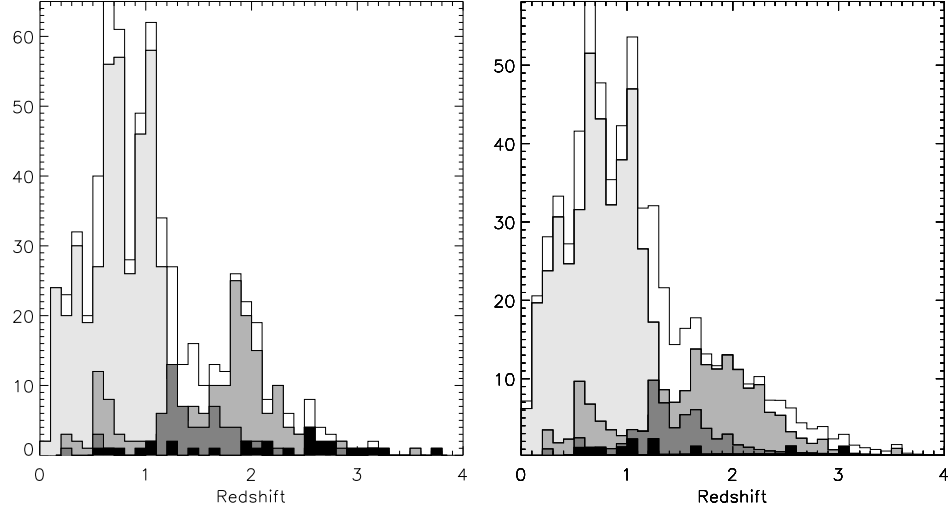


Figure 4.2 Redshift distribution of the MIPS-selected sample. The plot on the left gives the observed distribution, while the plot on the right incorporates the typical errors on the photometric redshifts. From lightest to darkest shading, the histograms represent all MIPS sources in our sample, IR-normal galaxies, color-selected sources that meet the Lacy et al. (2004) criteria, color-selected sources that meet the Stern et al. (2005) criteria, and PLGs.

and Stern et al.), and IR-normal subsamples. As expected, the number of IR-normal galaxies peaks at  $z = 0.7$  (a well-known redshift peak in the CDF-S) and at  $z = 1.1$  (another known redshift peak). We also detect a peak at  $z = 0.3$  similar to that found by Desai et al. (2008), whose strength increases if we apply their cut of  $f_{24\ \mu\text{m}} \geq 300\ \mu\text{Jy}$ . In the CDF-S, however, this peak is dwarfed by the stronger peak at  $z = 0.7$ , even at large flux densities. The redshift distribution of the IR-normal galaxies decreases rapidly at redshifts of  $z > 1.2$ , where only highly luminous star-forming galaxies are detectable. In contrast, the PLGs with redshift estimates have a relatively flat distribution in redshift space, as was found for the PLGs in the CDF-N (Donley et al. 2007).

The redshift distributions of the (non-power-law) Lacy et al. and Stern et al. selected samples differ significantly, both from the IR-normal and PLG samples, as well as from one another. The Stern-selected galaxies peak at  $z \sim 1.25$  whereas

the Lacy-selected galaxies show significant peaks at  $z \sim 0.5$  and  $z \sim 2$ , with very few galaxies falling in the  $z < 1$  regime originally probed by these selection methods (see §5). In addition, at  $z \geq 1.75$ , nearly all (94%) MIPS-selected sources meet the Lacy AGN selection criteria, regardless of their nature. A large concentration of galaxies at  $z \sim 2$  was previously observed in this field by Caputi et al. (2006), and in a brighter sample of MIPS sources by Desai et al. (2008), and is most probably due to the  $7.7 \mu\text{m}$  aromatic feature passing through the  $24 \mu\text{m}$  band. This behavior suggests that the mid-IR continua of the Lacy color-selected galaxies contain substantial contributions from star-formation (e.g. Genzel et al. 1998).

Finally, the mean redshifts of the IR-excess samples are as follows:  $z = 1.92 \pm 0.36$  for the Daddi et al. sources,  $z = 2.19 \pm 0.61$  for the dust obscured galaxies (DOGs, Dey et al. 2008),  $z = 2.09 \pm 0.48$  for the Fiore-selected sources,  $z = 2.11$  for the one Polletta source with a known redshift, and  $z = 2.05 \pm 0.49$  for the IR-bright/optically-faint sources. As discussed above, this concentration about a redshift of 2 (when not a design of the selection as in Daddi et al. (2007)) is likely to be due at least in part to the passage of the  $7.7 \mu\text{m}$  aromatic feature through the MIPS  $24 \mu\text{m}$  band, suggesting a significant contribution from star-formation.

#### 4.4 X-ray Properties

Of the 713 MIPS sources, 109 (15%) have X-ray counterparts in the Alexander et al. (2003) or Giacconi et al. (2002) catalogs. Of these, 25 are PLGs, 35 are color-selected galaxies (33 from the Lacy criteria, and 12 from the Stern criteria), and 49 are IR-normal. While the IR-normal galaxies therefore dominate the X-ray counts, the fraction of such sources is low: only 11% of the IR-normal galaxies have X-ray counterparts, as compared to 17% of the color-selected galaxies and 45% of the PLGs.

We test for faint ( $\geq 2\sigma$ ) X-ray emission from the MIPS sources using the procedure outlined in Donley et al. (2005). The resulting detection fractions for the PLG, color-selected, IR-normal, and IR-excess samples are given in Table 2. With the inclusion of the weakly-detected X-ray sources, the detection fractions of the IR-normal, color-selected, and PLG samples increase to 40%, 42%, and 64%, respectively. As indicated in Table 2, however, while all strongly and weakly-detected PLGs have AGN X-ray luminosities of  $\log L_x(\text{ergs s}^{-1}) \geq 42$ , the same is true for only 74% of the color-selected galaxies, and 34% of the IR-normal galaxies. Given the infrared luminosities implied by our  $24\ \mu\text{m}$  selection criterion, the portion of the sample with  $\log L_x(\text{ergs s}^{-1}) < 42$  will be heavily contaminated with star-forming galaxies (Ranalli et al. 2003).

While the X-ray detection fraction of PLGs is relatively low (though significantly higher than that of the color-selected galaxies), it is comparable to that of previously-selected samples (Alonso-Herrero et al. 2006, Donley et al. 2007). Of the PLGs in the 2 Ms CDF-N, 55% had high-significance X-ray counterparts. However, only 15% remained undetected down to the  $2.5\sigma$  detection level, suggesting that many PLGs are likely to be heavily obscured X-ray sources whose fluxes fall below the current detection limits (Donley et al. 2007). In the CDF-S, only 45% of the PLGs have cataloged X-ray counterparts and 36% remain undetected down to  $2\sigma$ . This slightly lower detection fraction is due at least in part to the lower X-ray exposure of the 1 Ms CDF-S, and will be discussed further in §6.

The X-ray detection fraction of the luminous IR-excess sources selected via the Polletta et al. (2008) sample is high (80%). However, the same can not be said for the remaining IR-excess samples: only 30% of the DOGs, 19% of the Fiore et al. sources, and 15% of the sources with high  $24\ \mu\text{m}$  to optical flux ratios have cataloged X-ray counterparts. By definition, none of the Daddi et al. sources

Table 4.2. X-ray Detection Statistics

	MIPS <sup>a</sup> Sample	MIPS/ISAAC Sample	Daddi et al. (2007)	Dey et al. (2008)	Fiore et al. (2008)	Polletta et al. (2008)	$f_{24\ \mu\text{m}}/f_{\text{R}}$ > 1000	All IR-Excess
Total	713	465	42	10	52	5	71	101
X-rays	109	76	3	3	10	4	11	15
Power	25 (100%)	14	0	3	4	4	4	7
Color	35 (79%)	28	3	0	5	0	6	7
Normal	49 (65%)	34	0	0	1	0	1	1
Weak X-rays	157	125	13	2	10	1	16	26
Power	7 (100%)	5	1	1	3	1	4	4
Color	44 (70%)	35	11	1	7	0	11	20
Normal	106 (19%)	85	1	0	0	0	1	2
No X-rays	361	226	21	3	26	0	38	51
Power	18	12	3	0	7	0	9	11
Color	109	72	15	3	19	0	28	36
Normal	234	142	3	0	0	0	1	4

<sup>a</sup>The fraction of X-ray sources with AGN X-ray luminosities of  $\log L_{\text{x}}(\text{ergs s}^{-1}) > 42$  is given in parentheses.

Note. — The sum of the weakly and non-detected sources does not equal the full number of X-ray non-cataloged sources. The difference represents the number of sources that lie too close to a known X-ray counterpart to test for faint X-ray emission.

have cataloged hard X-ray counterparts, although 3 have soft-band counterparts. When the weakly-detected X-ray counterparts are included, these numbers rise to 100% for the Polletta sources, 63% for the DOGs, 44% for the Daddi et al. sources, 43% for the Fiore et al. sources, and 42% for the IR-bright/optically-faint sources.

#### 4.5 IRAC color-color selection

There are several reasons why a re-examination of the color-color selection criteria is needed before applying these techniques to our sample. First, thanks to the availability of high quality NIR and *Spitzer* MIR spectra and photometry, we can now construct more accurate MIR templates for both AGN and star-forming galaxies than were available when the Lacy et al. and Stern et al. AGN selection criteria were initially defined. Second, the AGN selection criteria of Lacy and Stern were initially designed for use with shallow surveys, and have not yet been properly tested over a range of both redshift and flux density (but see Cardamone et al. 2008). Third, photometric redshift techniques for *Spitzer*-detected galaxies have advanced sufficiently to allow nearly complete redshift estimation.

The positions of the MIPS-selected sample in IRAC color space are shown in Figure 3, where stars represent the PLGs and circles represent the remaining MIPS sources. As expected, all PLGs meet the Lacy criteria and all but 3 meet the Stern criteria. The relatively large scatter of the PLGs on the Stern plot probably arises in part from the use of adjacent color bands, whereas the power-law fitting tends to smooth over noise.

##### 4.5.1 Comparison of the IRAC color-color selection criteria

To illuminate the strengths and weaknesses of the two color-color selection criteria in Figure 3, we separate the sources that meet both the Lacy et al. (2004) and Stern et al. (2005) AGN selection criteria from those that meet only one of the

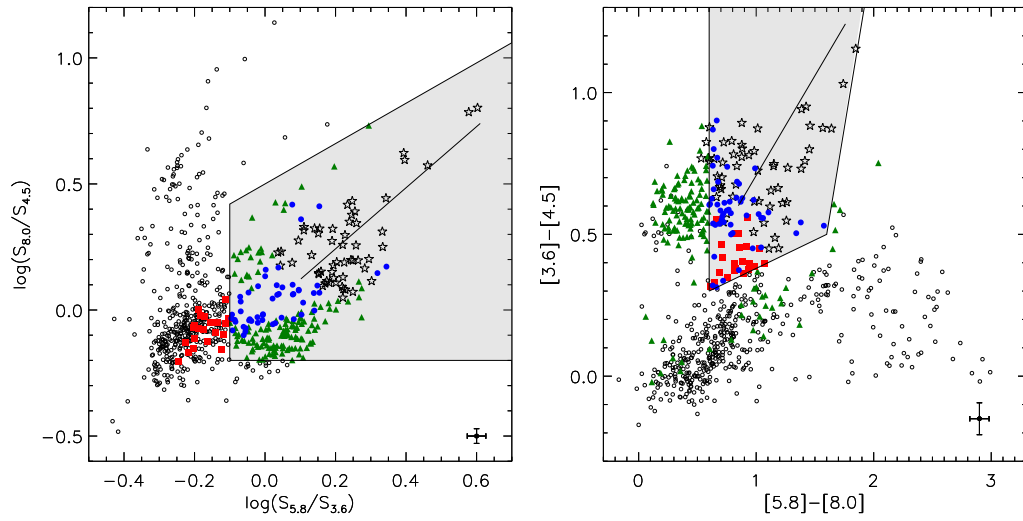


Figure 4.3 Position in Lacy et al. (2004; left) and Stern et al. (2005; right) color-space of the MIPS-selected sample, where PLGs are given as stars. Blue filled circles represent color-selected galaxies that meet both the Lacy et al. and Stern et al. criteria. Green triangles and red squares represent sources that meet only the Lacy et al. or Stern et al. criteria, respectively. The small open circles are IR-normal galaxies. The shaded regions represent the AGN selection regions, and the diagonal lines within are the loci of perfect power laws with  $\alpha = -0.5$  to  $-3.0$ .

two criteria. The color-selected sources that meet both criteria primarily define an extension of the power-law locus to a blue slope of  $\alpha = +0.5$  (recall that our definition of PLGs includes only those sources with red slopes of  $\alpha < -0.5$ ). We will discuss in detail the effects of different power-law slope criteria in §6.

The Lacy-only sources occupy two regions in color-space. The first, located in the lower portion of the Lacy diagram, corresponds to the concentration in the upper-left corner of the Stern et al. selection region. These sources were intentionally excluded from the Stern selection region to minimize contamination from high-redshift ( $z \sim 2$ ) star-forming galaxies. The second concentration of Lacy-only galaxies is scattered throughout the star-forming locus of the Stern diagram. Are these normal, low- $z$  star-forming galaxies, or obscured AGN not selected by the Stern criteria?

The Stern-only sources fall almost exclusively in the lower left portion of the Stern wedge, and occupy the region dominated by low-redshift IR-normal galaxies in the Lacy et al. color diagram, suggesting that, like the Lacy criteria, the Stern et al. criteria are likely to suffer from low-redshift star-forming galaxy contamination. Because of the exclusion of  $z \sim 2$  star-forming galaxies, however, the Stern et al. criteria should perform better at high  $z$ . To test this hypothesis, we next consider the evolution in IRAC color-space of a number of high-quality star-forming and AGN templates.

#### 4.5.2 Star-forming Templates

As discussed above, the availability of high-quality near- and mid-infrared data has allowed the construction of high-quality star-forming SEDs, particularly for luminous and ultra-luminous infrared galaxies (LIRGS and ULIRGS). In Figure 4, we plot the redshift evolution of these templates in IRAC color-color space over  $z = 0 - 4$ , where purple and blue tracks represent the *purely star-forming* ULIRG



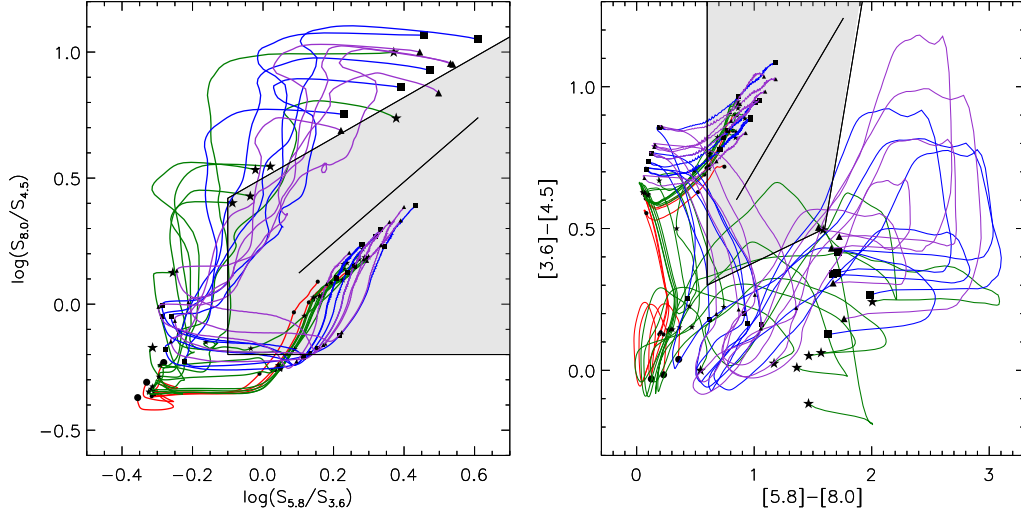


Figure 4.4 Tracks in color-space of the *purely star-forming* SEDs of ULIRGS (purple, triangles), LIRGS (blue, squares), spirals and starbursts (green, stars), and elliptical galaxies (red, circles), from redshifts of  $z = 0$  (large symbols) to  $z = 4$ . Small symbols mark redshift intervals of 1. The power-law locus with  $\alpha = -0.5$  to  $-3.0$  is shown as a line inside the shaded AGN selection regions. The star-forming SEDs enter the AGN selection regions at both low and high redshift.

and LIRG templates of Rieke et al. (2008, see Table A1), green tracks represent the spiral and starburst templates of Polletta et al. (2007) and Dale & Helou (2002), and red tracks represent the elliptical templates of Silva et al. (1998). Large circles mark the tracks at  $z = 0$ , and small circles mark each integer redshift from  $z = 1$  to 4.

While the star-forming templates generally avoid the power-law locus itself, they enter the Lacy and Stern selection regions at both low and high redshifts, tracing out the same regions in color space occupied by many of the color-selected AGN, particularly those selected via only one of the two criteria. The templates therefore suggest potential star-forming galaxy contamination of color-selected AGN, as previously predicted by Barmby et al. (2006), Donley et al. (2007), and Cardamone et al. (2008), and indicate that the current AGN selection regions may inadequately separate AGN and star-forming galaxies.

Our results can be compared with the simulations of Sajina, Lacy, & Scott (2005), who calculated mathematical models of galaxies from three spectral components: stars, aromatic features, and a continuum. For  $0 < z < 1$ , we agree with their Figure 8 (upper left) that starburst luminosity galaxies do not significantly ‘invade’ the Lacy AGN color wedge (see our Figure 4). However, we find that more luminous galaxies can invade this wedge much more seriously (again see Figure 4). The difference may arise because the inputs to their models included few star-forming LIRGs and only one ULIRG (Arp 220, an atypical case). Therefore, it is likely that the behavior of the most luminous star forming galaxies is not captured as accurately in their models as is that of lower luminosity ones. By  $z = 1$ , the typical *Spitzer* 24  $\mu\text{m}$  survey sensitivity limit reaches only to the bottom of the LIRG range, so the Lacy AGN color wedge is more susceptible to contamination than was concluded by Sajina et al. (2005).

#### 4.5.3 Redshift-dependent color selection

While the star-forming templates appear to trace quite well the positions of many of the color-selected galaxies in color-color space, Figure 4 covers a wide range of redshifts ( $z = 0 - 4$ ). To understand better the overlap between the star-forming templates and the color-selected galaxies (and PLGs), we must take the redshift information into account. We therefore break the sample down into smaller redshift bins, as shown in Figures 5 and 6. We overplot on the color-color diagrams the redshift-appropriate colors of purely star-forming galaxies. To simplify the plots, we do not plot each galaxy track separately, as was done in Figure 3, but instead draw  $1\sigma$  contours around the tracks, where  $\sigma$  is taken to be the median IRAC measurement error of the full MIPS sample. We find that, unlike the PLGs, the majority of the color-selected AGN candidates fall within or very close to the contours for star-forming galaxies of similar redshifts. Thus, it is likely that their

mid-IR SEDs are dominated by star formation. This result suggests that simple mid-IR color-color cuts cannot identify reliable AGN samples without also including redshift-based or additional SED (e.g. power-law) criteria. We discuss in Appendix C the individual redshift intervals.

The summary of our findings can be found in Table 3, where we present the overall fraction of color selected galaxies and PLGs that lie outside the  $1\sigma$ ,  $2\sigma$ , and  $3\sigma$  star-forming contours. The top half of the table gives the fractions assuming no errors on the photometric redshifts; the lower half incorporates 10% errors which for clarity are imposed on the templates rather than on the individual galaxy measurements. For the PLGs, we give two percentages: the fraction of sources that lie outside the star-forming contours in Lacy and Stern color-space, respectively.

As is clear from Table 3, the fraction of color-selected galaxies that lie outside the star-forming contours is lower than that of the PLGs by a factor of 2-10 at all three levels of significance. For instance, while 57% - 71% of PLGs lie more than  $3\sigma$  from the star-forming contours in Lacy color space, the same can be said for only 5%-10% of the color-selected galaxies. In addition, increasing the significance from  $1\sigma$  to  $3\sigma$  has a far greater effect on the reliability of the color-selected galaxies than on that of the PLGs, especially in Lacy color-space, indicating that the color-selected galaxies lie noticeably closer to the star-forming templates than do the PLGs, as expected. We note that this analysis depends on the templates being used, as the addition or removal of any one star-forming template will result in changes in the numerical results presented above and in the table. The overall trends discussed above, however, will remain the same.

#### 4.5.4 Properties of Color-selected AGN candidates

While the majority of color-selected AGN candidates lie inside the star-forming contours (see Table 3), a number of non-power-law color-selected galaxies meet

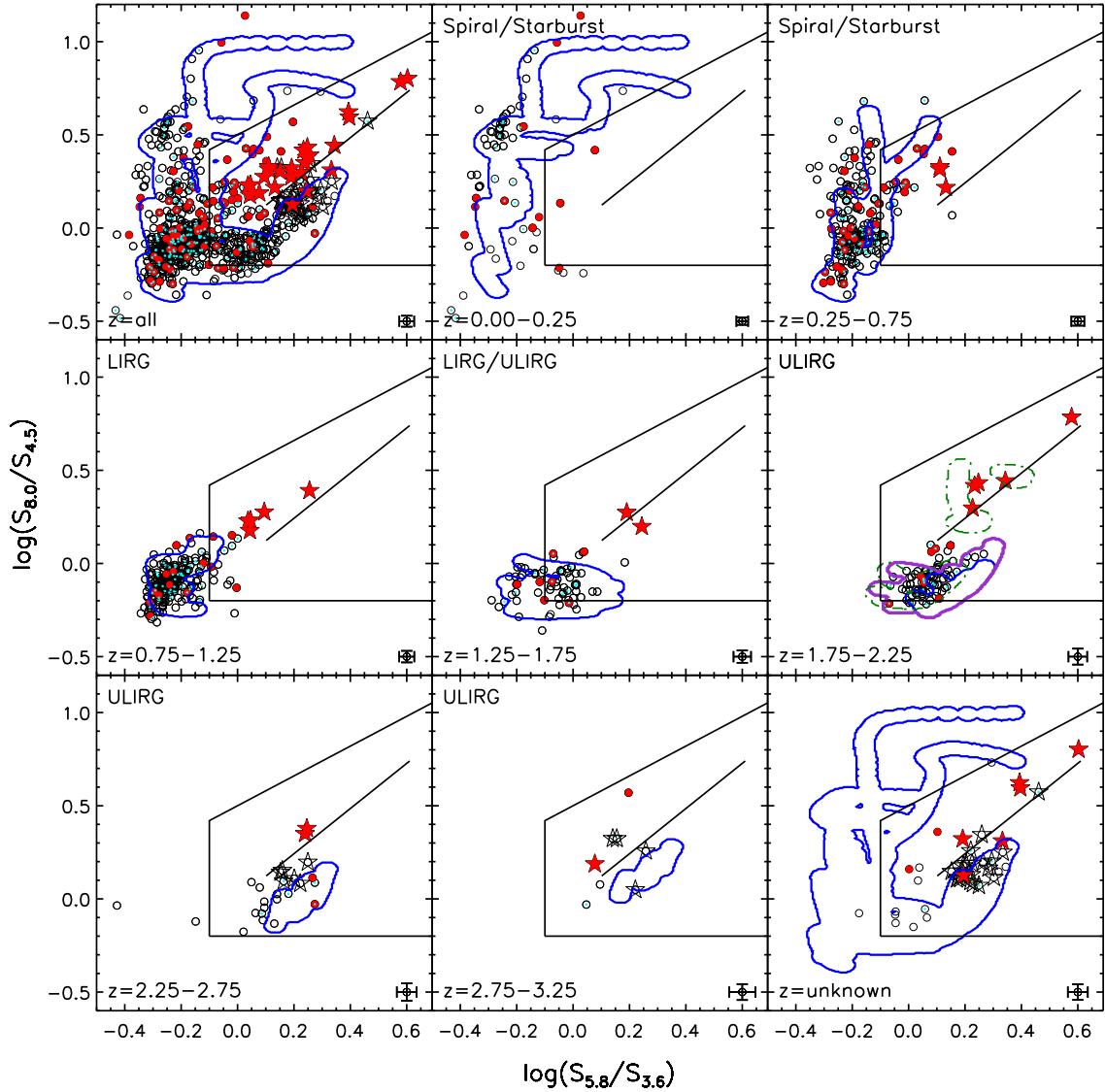


Figure 4.5 Position in Lacy et al. (2004) color-space of the MIPS-selected sample, as a function of redshift, where PLGs are shown as stars, X-ray-cataloged sources are given by filled (red) symbols, and X-ray weakly-detected sources are given as small cyan symbols. Overplotted are the redshift-appropriate contours representing the IRAC colors of purely star-forming templates, assuming no errors on the photometric redshifts. The thick (purple) contours and dot-dashed (green) contours in the  $z = 1.75 - 2.25$  redshift bin represent star-forming galaxy templates for which 10% errors were incorporated into the redshift range, and AGN templates, respectively.

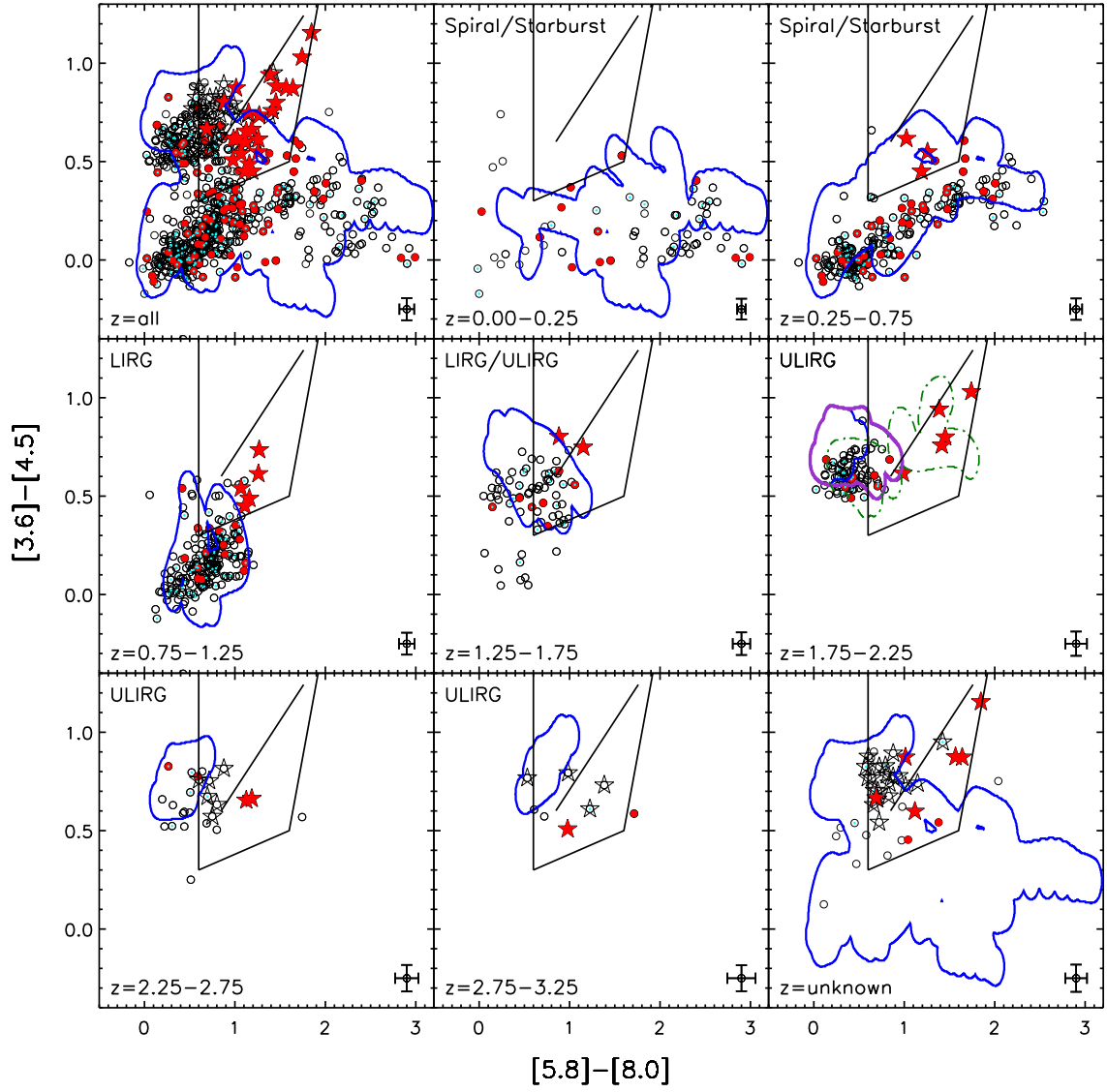


Figure 4.6 Position in Stern et al. (2005) color-space of the MIPS-selected sample, as a function of redshift. Symbols and contours are as described in Figure 5.

Table 4.3. Fraction of sources that lie outside the star-forming contours

Selection	$1\sigma$	$2\sigma$	$3\sigma$
Lacy	52%	21%	10%
Stern	40%	18%	8%
Power-law	93%,82%	79%,61%	71%,43%
Lacy	29%	12%	5%
Stern	22%	5%	0%
Power-law	71%,68%	61%,46%	57%,39%

Note. — The upper portion of the table assumes no errors on the photometric redshifts. The lower portion assumes 10% errors. The two values given for the PLGs represent the fraction of sources that lie outside the star-forming contours in Lacy and Stern color-space, respectively.

the AGN selection criteria and have colors inconsistent with those of our star-forming templates. Are these AGN, as predicted? How do their redshift distributions, X-ray detection fractions, and numbers compare to those of the PLGs? In the following discussion, we define as ‘secure’ color-selected galaxies (and PLGs) those AGN candidates that lie  $> 1\sigma$  away from the redshift-appropriate star-forming templates.

As discussed above, and as shown in Figure 2, the redshift distributions of the color-selected sources show a strong peak at  $z = 2.0$ , attributed to the  $7.7\ \mu\text{m}$  aromatic feature, a star-formation indicator. In contrast, the PLGs have a relatively flat redshift distribution, indicating little or no contribution from aromatic features. If we do not account for errors in the photometric redshifts, the resulting sample of ‘secure’ color-selected galaxies retains the large  $z = 2$  peak, suggesting a large star-formation contribution. If we incorporate 10% errors on the redshifts of the star-forming templates when selecting our secure candidates, however, the redshift distributions of the remaining color-selected galaxies become relatively flat, with mean redshifts of  $z = 1.59 \pm 0.83$  and  $z = 1.62 \pm 0.84$  for the Lacy and Stern-selected sources, respectively, suggesting that a significant fraction of the high-redshift star-forming contaminants have been removed. For comparison, the mean redshifts and rms ranges of the secure PLGs selected in Lacy and Stern color-space are  $1.98 \pm 0.87$  and  $2.09 \pm 0.78$ .

While the redshift distribution therefore suggests that many of the star-forming contaminants have been rejected from the secure sample, the X-ray detection fractions, shown in Table 4, suggest otherwise. At distances of 1 and  $2\ \sigma$  from the star-forming templates, the X-ray detection fraction of the PLGs exceeds that of the color-selected galaxies by factors of  $> 2 - 3$ . This factor, however, should be taken with reservations; X-ray sources are far more likely to have spectroscopic

Table 4.4. X-ray detection fraction (and total number) of sources that lie outside the star-forming contours

Selection	$1\sigma$		$2\sigma$		$3\sigma$	
Lacy	21%	(19)	26%	(10)	42%	(8)
Power-law (Lacy)	70%	(19)	83%	(19)	90%	(19)
Stern	19%	(5)	25%	(3)	40%	(2)
Power-law (Stern)	67%	(16)	72%	(13)	85%	(11)
Lacy	29%	(15)	36%	(8)	67%	(6)
Power-law (Lacy)	81%	(17)	89%	(16)	88%	(15)
Stern	14%	(2)	0%	(0)	0%	(0)
Power-law (Stern)	80%	(16)	86%	(12)	82%	(9)

Note. — The upper portion of the table assumes no errors on the photometric redshifts. The lower portion assumes 10% errors.

redshift estimates, and are therefore far more likely to be included in our secure sample, which requires redshift information. While this has a minimal effect on the color-selected galaxies, for which the redshift completeness is high, it has a large effect on the PLGs, boosting their probable X-ray detection fraction.

A better comparison is therefore with the IR-normal galaxy population, 11% of which are detected in the X-ray. The X-ray detection fractions of the secure color-selected AGN candidates (14-29%), exceed this value, but only by a factor



of  $\sim 1 - 3$ . In comparison, the full sample of PLGs has an X-ray detection fraction of 45%, which exceeds that of the IR-normal galaxies by a factor of 4. Only at the highest significance,  $3\sigma$  from the star-forming contours, does the X-ray detection fraction of the secure color-selected galaxies approach that of the full PLG sample.

This significant offset in X-ray detection fraction could be due either to a difference in intrinsic luminosity or to lingering contamination of the color-selected sample by star-forming galaxies. While the average X-ray luminosity of the secure PLGs,  $\log L_x(\text{ergs s}^{-1}) = 44.1$ , exceeds that of the secure Lacy and Stern-selected sources detected in the X-ray,  $\log L_x(\text{ergs s}^{-1}) = 43.8$  and  $43.9$ , respectively, the offset is relatively small, suggesting that the large discrepancy in the X-ray detection fractions is not driven primarily by a systematic offset in X-ray luminosity of the relevant AGN. Instead, it likely arises from the inclusion of star-forming galaxies, even in the  $1\sigma$  ‘secure’ color-selected population, suggesting that a larger cut in  $\sigma$  (e.g.  $3\sigma$ ) is required to define a reasonably secure sample.

Also shown in Table 4 are the total number of X-ray selected galaxies in both the secure color-selected and PLG samples. After applying completeness corrections for the fraction of Lacy, Stern, and PLG X-ray sources that have redshifts and that can therefore be included in the secure sample (94%, 83%, and 76%, respectively), the number of secure X-ray selected PLGs exceeds that of the secure X-ray-detected color-selected galaxies, regardless of whether we define the secure sample as those sources that lie 1, 2, or  $3\sigma$  from the star-forming contours. This indicates that *the PLG selection criterion identifies the overwhelming majority of secure AGN candidates in IRAC color-space.*

#### 4.5.5 Flux dependency of color selection

While the Lacy and Stern AGN selection criteria were defined using relatively shallow surveys, these selection techniques are now being applied to samples

with a range of flux densities (e.g. Cardamone et al. 2008). How does the limiting flux affect the completeness and reliability of AGN color selection? Are the problems discussed above present in shallow as well as deep surveys?

There are several reasons why we might expect to see a shift in reliability with flux. First, the AGN fraction of MIPS sources depends quite strongly on the  $24\ \mu\text{m}$  flux density (e.g. Treister et al. 2006, Brand et al. 2006). For instance, while only  $\sim 4\%$  of MIPS sources at our flux limit of  $80\ \mu\text{Jy}$  are expected to be AGN (Treister et al. 2006), the fraction at  $5\ \text{mJy}$  is more than an order of magnitude greater ( $\sim 45\%$ ). Therefore, MIPS-selected shallow surveys should contain fewer star-forming galaxies, although those that remain are likely to be LIRGs/ULIRGs that enter the AGN selection region in greater numbers than spirals and starbursts (see Figure 4).

Second, many of the ‘problem’ sources that lie inside the AGN color selection region but that also fall inside the star-forming contours have moderately high-redshifts ( $z > 1.25$ ), and are therefore likely to drop out of shallow surveys. While shallow samples may therefore contain high-luminosity ULIRGs, the exclusion of lower-luminosity high-redshift galaxies reduces the risk of contamination. Other flux cuts, such as the  $R$  magnitude  $< 21.5$  requirement of Stern et al. (2005), also prevent contamination at high- $z$ , as normal galaxies at this magnitude are detected only to  $z \sim 0.6$ .

To investigate the effect of intermediate flux density cuts on the AGN color selection, we show in Table 5 the fraction of ‘secure’ color-selected and PLGs (those that lie outside the  $1\sigma$  star-forming contours) as a function of flux density. If we do not incorporate errors in the photometric redshifts into our definition of the secure sources, we find that the fraction of secure sources is relatively constant at  $\sim 50\%$  regardless of flux density. If we allow errors on the photometric redshifts

when constructing our ‘secure’ sample, the reliability of Lacy-selected sources at  $f \geq 80 \mu\text{Jy}$  drops to 29%, and that of Stern-selected sources drops to 21%. At  $f \geq 500 \mu\text{Jy}$ , the fraction of secure sources amongst both samples rises, but only to 50%. Regardless of our assumptions, therefore, the fraction of potential contaminants is still high ( $\sim 50\%$ ), even at the highest fluxes probed by our survey. Because of the pencil-beam nature of the CDF-S survey, 95% of the sources in our sample have  $f_{24 \mu\text{m}} \leq 600 \mu\text{Jy}$ , so our ability to comment on brighter samples is limited.

It is also worth noting that the brightest MIPS sources tend to lie above the power-law locus in Lacy color-space and to the right of the power-law locus in Stern space, regions where we expect minimal contamination from star-forming galaxies. Not surprisingly, these sources are also almost always detected in the X-ray, suggesting that these regions of IRAC color-space are the most secure.

#### 4.5.6 Comparison with previous work

In a study of 77 AGN candidates selected from the *Spitzer* First-Look (Lacy et al. 2005b) and SWIRE surveys (Lonsdale et al. 2003) via the Lacy et al. (2004) criteria, Lacy et al. (2007) found that 33% are unobscured type 1 quasars, 44% are type 2 AGN, and 14% are dust-reddened type 1 quasars. Only 9% have star-forming or LINER spectra. Is this relatively low contamination by star-forming galaxies consistent with our findings?

There are three main factors that lead to the high reliability of the Lacy et al. (2007) sample. First, the sample members are very bright, with a typical  $24 \mu\text{m}$  flux density of 5 mJy. As discussed above, Treister et al. (2006) predict that 45% of sources at this flux density should be AGN, regardless of their MIR SEDs, compared to only 4% of sources at our flux limit of  $80 \mu\text{Jy}$ . Indeed, of the brightest 50 sources in the XFLS (whose median  $24 \mu\text{m}$  flux density is 9.4 mJy), 58% are

Table 4.5. Percent of secure color-selected galaxies vs.  $24\ \mu\text{m}$  flux

$24\ \mu\text{m}$ flux cut ( $\mu\text{Jy}$ )	Lacy	Stern	Power-law
80	52%	40%	93%, 82%
100	54%	44%	96%, 84%
150	53%	43%	94%, 78%
200	60%	63%	100%, 76%
300	53%	25%	100%, 72%
400	52%	50%	100%, 66%
500	56%	50%	100%, 71%
80	29%	21%	72%, 68%
100	29%	24%	76%, 72%
150	25%	21%	73%, 63%
200	32%	27%	92%, 76%
300	31%	25%	90%, 72%
400	39%	50%	88%, 66%
500	50%	50%	85%, 71%

Note. — The upper portion of the table assumes no errors on the photometric redshifts. The lower portion assumes 10% errors. The two values given for the PLGs represent the fraction of sources that lie outside the star-forming contours in Lacy and Stern color-space, respectively.

optically classified as AGN (Lacy et al. 2007). Thus, the sample from which these color-selected AGN was drawn contains far fewer star-forming galaxies than the deeper GOODS sample.

Second, while the sources in the Lacy et al. (2007) sample have redshifts ranging from  $z = 0.053$  to 4.27, the median redshift of the sample is low:  $z = 0.6$ . Only 5 color-selected sources have redshifts in excess of  $z = 1.75$ , the redshift above which nearly all sources in our sample (AGN or star-forming) meet the Lacy et al. criteria. We would therefore expect little or no contamination by *high-redshift* star-forming galaxies, the predominant source of contamination in our faint sample.

The third and most important reason for the high reliability of this sample, however, is the high PLG fraction of the Lacy-selected AGN candidates. Of the 77 sources in the Lacy et al. (2007) sample, 59 are PLGs as defined in §2. The 18 sources that are excluded by the PLG criteria include the only two starburst galaxies detected in this subsample, one starburst/LINER, an unclassified high-redshift galaxy with narrow UV emission lines, two composite galaxies, 8 Type 2 AGN (the identification of 4 of which were based on a BPT analysis), 3 reddened Type 1 AGN, and 1 Type 1 AGN. If we relax the probability constraint of the PLG criterion to  $P_\chi > 0.01$ , as was done in Alonso-Herrero et al. (2006), we recover 69 of the 77 Lacy et al. (2007) sources selected for optical follow-up. Excluded are the two starburst galaxies, one high- $z$  unidentified galaxy, three Type 2 AGN, one reddened Type 1 AGN, and 1 Type 1 AGN whose slope of  $\alpha = -0.41$  falls just short of our cut of  $\alpha \leq -0.5$ . The high reliability of this luminous color-selected sample is therefore consistent with our findings in §6 that while non-PLG color-selected AGN are subject to contamination by star-forming galaxies, sources selected via a power-law criterion are reliable.

#### 4.6 IRAC Power-law selection

Thus far, we have focused primarily on the reliability of the AGN color selection criteria of Lacy et al. (2004) and Stern et al. (2005). In doing so, we have separated out the subset of sources that meet the power-law criteria of Alonso-Herrero et al. (2006) and Donley et al. (2007). Here, we discuss the PLG selection itself, in particular the consequences of various choices of limiting power-law slope,  $\alpha$ .

Our default cut of  $\alpha < -0.5$  was chosen to match the spectral indices of typical AGN (e.g. Alonso-Herrero et al. 2006, Donley et al. 2007). In the optical, AGN have spectral slopes of  $\alpha = 0.5$  to  $-2$  (SDSS, Ivezić et al. 2002), with a mean value of  $\alpha \sim -1$  (Neugebauer et al. 1979, Elvis et al. 1994). In the IRAC bands, broad-line AGN exhibit similar slopes, with a mean value of  $\alpha = -1.07 \pm 0.53$  (Stern et al. 2005).

In Figures 7 and 8, we plot PLGs selected via cuts in  $\alpha$  ranging from  $+0.5$  to  $-1.5$ . At high redshift ( $z \sim 1.5 - 2$ ) the IRAC bands trace the blue side of the stellar bump. It is therefore not surprising that at the bluest slopes ( $\alpha = +0.5$ ), the PLG sample is dominated by the population of high redshift X-ray–non-detected star-forming galaxies discussed above. As the required slope reddens towards our cut of  $\alpha < -0.5$ , the high-redshift star-forming galaxies gradually drop out of the sample, and the X-ray detection fractions rise from 21% at  $\alpha = +0.5$  to 30%, 45%, 67%, 88%, and 80% at  $\alpha = 0.0, -0.5, -1.0, -1.5$ , and  $-2.0$ . While choosing a redder cut in  $\alpha$  therefore increases the apparent reliability of the PLG selection, it also decreases the number of galaxies selected, and may exclude interesting heavily obscured, X-ray–non-detected AGN like those seen in the CDF-N (e.g. Donley et al. 2007).

The X-ray–non-detected PLGs in the current sample tend to be the faintest sources both in the IRAC bands and at  $24 \mu\text{m}$ , where their mean flux density,

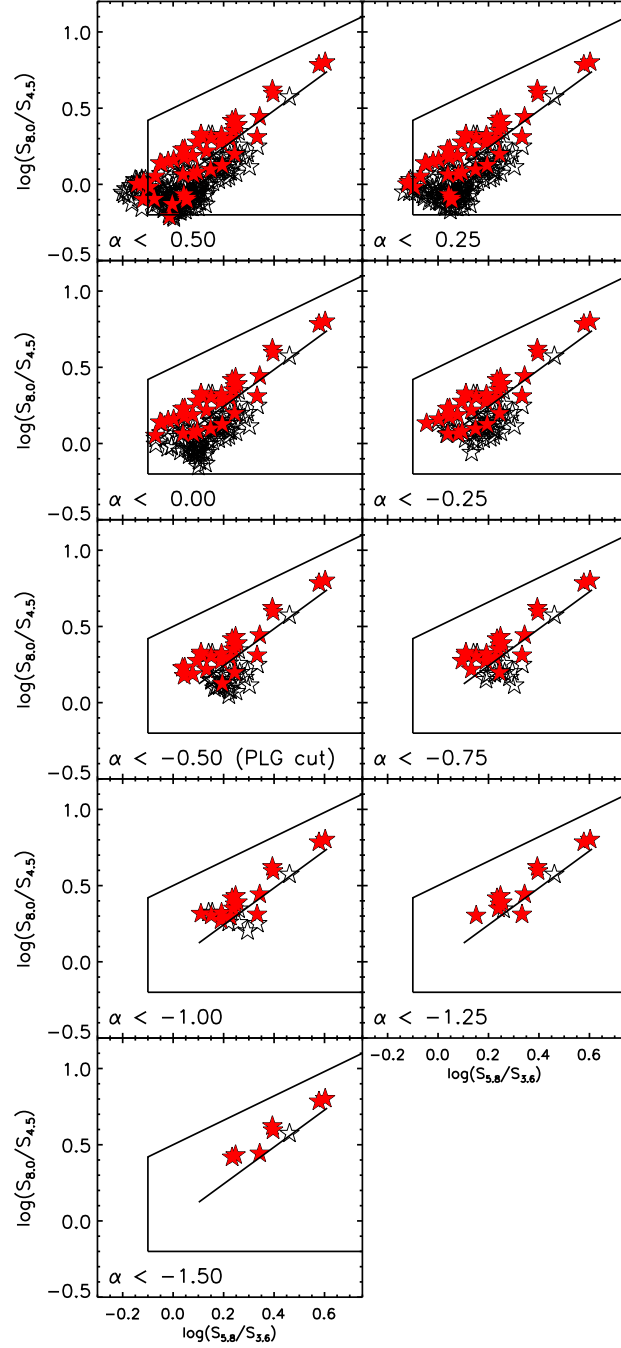


Figure 4.7 Position in Lacy et al. (2004) color space of PLGs as a function of the power-law slope cut,  $\alpha$ . X-ray-detected sources are shown as filled (red) symbols.

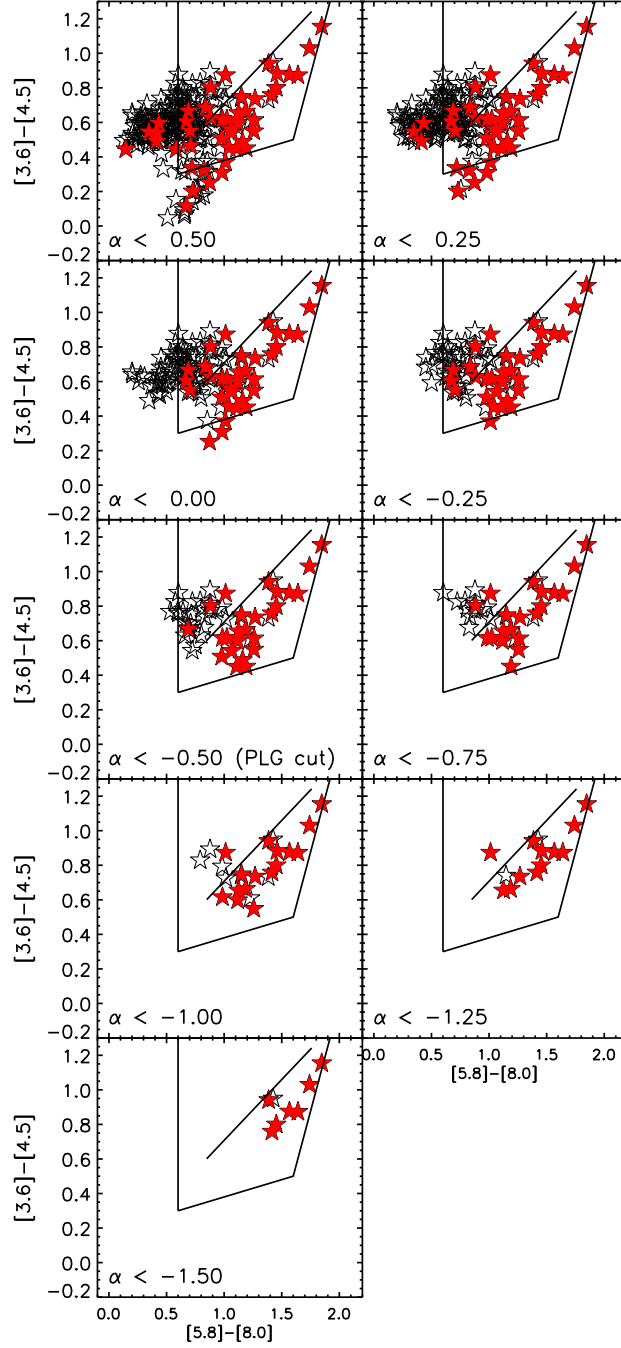


Figure 4.8 Position in Stern et al. (2004) color space of PLGs as a function of the power-law slope cut,  $\alpha$ . X-ray-detected sources are shown as filled (red) symbols.



146  $\mu\text{Jy}$ , is over a factor of 2 lower than that of the X-ray-detected sample, 334  $\mu\text{Jy}$ . The low X-ray detection fraction of these faint sources may therefore be due simply to their systematically lower fluxes. At  $z > 2.6 - 2.9$ , however, the star-forming ULIRG templates have IRAC SEDs that meet the PLG criteria, although dropping the power-law slope criterion to  $\alpha \leq -1.0$  and  $\alpha \leq -1.5$  raises this redshift range to  $z > 2.74 - 3.92$  (depending on the template) and to  $z > 3.4 - 4.2$ , respectively (with the IRAS 22491-1808 template never reaching an  $\alpha$  of -1.5). It is therefore possible that the X-ray non-detected PLGs (which tend not to have redshift estimates, to be faint, and to lie at relatively high  $\alpha$ ) are high-redshift star-forming galaxies. To test this hypothesis, we plot in Figure 9 the ratio of the MIPS 24  $\mu\text{m}$  flux density to that of the 3.6  $\mu\text{m}$  IRAC band. At the redshifts of interest ( $z > 2.6$ ), this flux ratio allows a direct comparison of the hot dust emission at 5-7  $\mu\text{m}$  to the stellar emission at  $\sim 1 \mu\text{m}$ . Overplotted on the colors of our MIPS-selected sample are the redshifted colors of the AGN templates of Polletta et al. (2007, see Table 1) and the purely star-forming LIRG and ULIRG templates of Rieke et al. (2008). The mean colors of PLGs without redshift estimates are given by large symbols placed at  $z = 2.6$ , the redshift above which contamination by star-forming galaxies is possible. The circle, square, and triangle represent all PLGs without redshifts, those that are detected in the X-ray, and those that are not, respectively.

As can be seen in Figure 9, the X-ray-detected and X-ray-non-detected PLGs lacking redshifts have consistent 24  $\mu\text{m}$  to 3.6  $\mu\text{m}$  colors, suggesting that there is no significant difference between these two sub-samples. In addition, while the colors of these sources are consistent with those of AGN, they lie well above those of star-forming galaxies, not only at high redshift, but at all redshifts greater than  $z \sim 0.6$ . In other words, the PLGs that are undetected in the X-ray and that lack

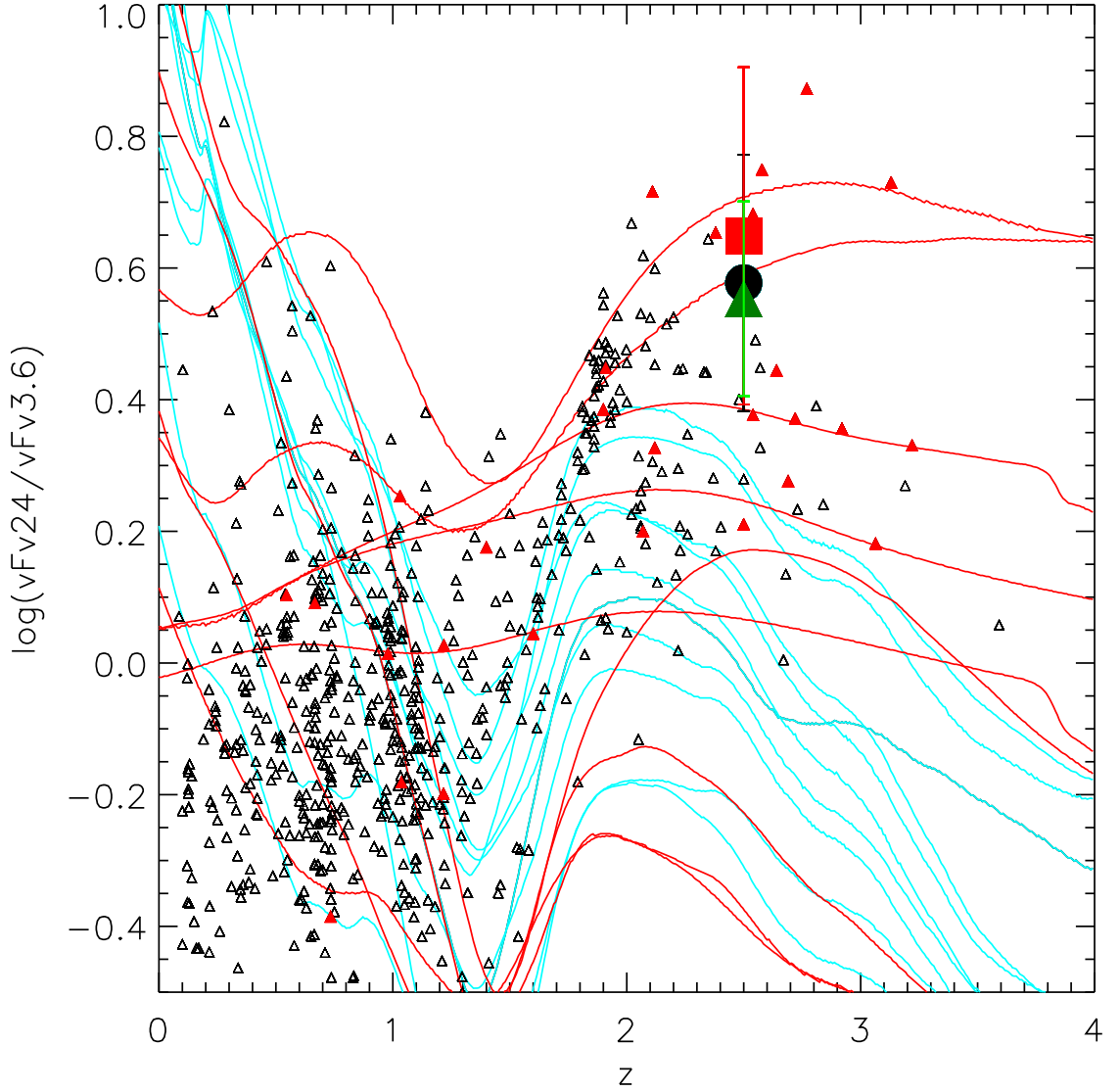


Figure 4.9 Observed 24  $\mu\text{m}$  to 3.6  $\mu\text{m}$  color as a function of redshift. The tracks represent the AGN templates of Polletta et al. (2007, red) (see Table A1), and the purely star-forming LIRG and ULIRG templates of Rieke et al. (2008, cyan). Triangles represent all sources in our sample with redshift estimates, and filled (red) triangles indicate a PLG source. The mean colors of PLGs without redshift estimates are given by a large circle (all PLGs), a large square (X-ray-detected PLGs), and a large triangle (X-ray-non-detected PLGs). We arbitrarily placed these mean colors at a redshift of  $z = 2.6$ , above which contamination of the PLG sample by star-forming galaxies is possible. The colors of these sources, however, are consistent with AGN, not star-forming galaxies.

redshifts (preventing us from testing their reliability as in §5.3) appear to have more hot dust emission than can be explained by purely star-forming templates, especially at high- $z$  where star-forming contamination of the PLG sample is most likely. This result suggests that these sources are more likely to be AGN than star-forming galaxies. Other lines of evidence, e.g. variability (Klesman & Sarajedini 2007), and X-ray properties (Steffen et al. 2007), tend to support this conclusion. In addition, we note from Figure 9 that a number of the other galaxies at  $z \sim 2$  have colors slightly redder than those predicted by star-forming galaxies at this redshift. This behavior may be due to a minor issue with the templates, a small AGN contribution to the MIR flux density, or to reddening that exceeds that seen in our local LIRG/ULIRG templates.

Finally, the segregation of the X-ray-detected and X-ray-non-detected sources about the power-law locus, seen in Figures 7 and 8, warrants discussion, as this was not seen in the CDF-N (Donley et al. 2007). This behavior appears to be due largely to the different selection methods and limiting fluxes of the two samples. While the CDF-N PLG sample was selected on the basis of IRAC fluxes, the current sample was selected from a flux-limited MIPS sample with far deeper IRAC data. If we require the CDF-S sample to meet the IRAC detection limits of the CDF-N study, the PLG sample size decreases by a factor of 2 and the X-ray detection fraction rises to 78%. The segregation in the PLG sample is also greatly reduced, due largely to the loss of many of the X-ray-non-detected sources. This high X-ray detection fraction of 78%, however, is surprising as it is significantly higher than the 55% found for the CDF-N PLG sample. To test whether this change is a result of the much improved IRAC data, we recalculated the spectral properties of the galaxies in the CDF-N using the most current IRAC data, which now includes the super-deep GOODS-N coverage not previously avail-

able. Drawing PLGs from the same initial sample used in Donley et al. (2007), we find an updated X-ray detection fraction of 57%, a value nearly identical to that found previously. For consistency with the current sample, we further restricted the PLG sample to those sources detected in the super-deep GOODS field, where the X-ray exposure is generally higher. Doing so raises the X-ray detection fraction to 65%. The remaining offset in the X-ray detection fractions of the IRAC flux-limited PLGs in the GOODS-N and GOODS-S fields, 13%, therefore appears to be due primarily to cosmic variance and small number statistics.

#### 4.7 IR-Excess Selection

Both high-redshift star-forming galaxies and AGN can exhibit extremely red infrared to optical colors when heavily dust-obscured (e.g. Dey et al. 2008). While the relative fractions of AGN and star-forming galaxies among IR-excess samples is still a matter of debate, the fraction of dust-obscured galaxies (DOGs) with AGN-like power-law SEDs has been shown to decrease with decreasing flux from  $\sim 70\%$  at  $f = 1$  mJy to  $\sim 20-25\%$  at  $f \leq 300$   $\mu$ Jy (Dey et al. 2008). We might therefore expect a relatively small AGN fraction amongst the faint IR-excess sources in the GOODS fields, whose mean 24  $\mu$ m flux is 215  $\mu$ Jy. Fiore et al. (2008), however, estimate that 80% of their red, IR-excess galaxies are heavily obscured, Compton-thick AGN. Here, we probe the nature of the IR-excess sources and examine the overlap between the IR-excess galaxies and the X-ray, color-selected, and power-law samples discussed above.

The positions of the IR-excess galaxies in Lacy and Stern IRAC color-space are shown in Figure 10, and their overlap with the X-ray, PLG, and color-selected samples is given in Table 2. Of the 101 IR-excess sources, 24 (24%) are PLGs and all but 7 meet either the Lacy, Stern, or power-law criteria. At least 1/4 of the IR-

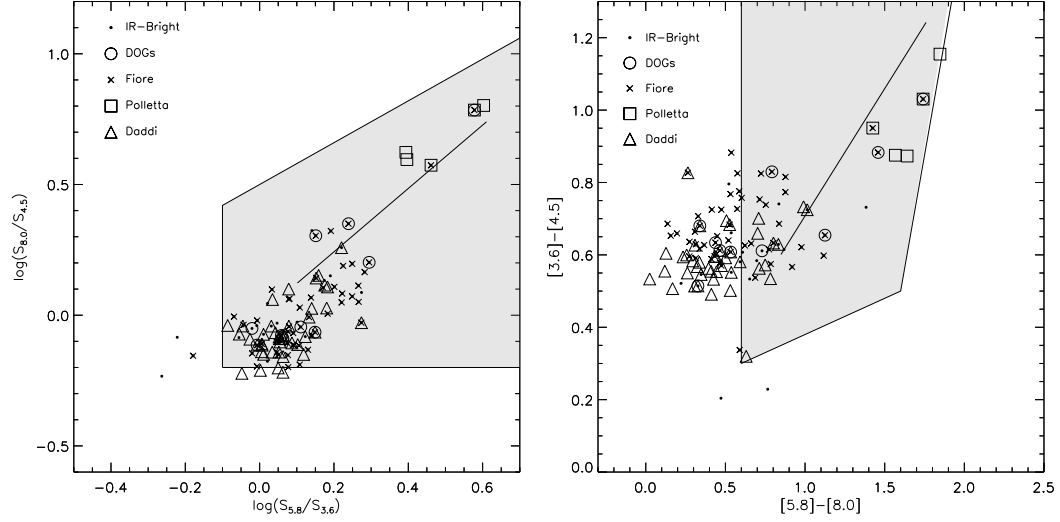


Figure 4.10 Position in Lacy et al. (left) and Stern et al. (right) color-space of the IR-excess sources.

excess galaxies therefore show evidence for AGN-heated dust (with the fraction rising to 100% for the luminous AGN selected via the Polletta et al. (2008) criteria, as expected). Not all PLGs, however, have IR-excess colors. Of the 55 PLGs, only 44% meet one or more of the IR-excess criteria. The same can be said for 33% of the IRAC color-selected galaxies, but for only 2% of the IR-normal galaxies.

Of the IR-excess sources, only 15% have cataloged X-ray counterparts, with the fraction rising to 45% when weak ( $\geq 2\sigma$ ) X-ray detections are considered (see Table 2). Of the X-ray-cataloged sources, 47% are PLGs, 47% are color-selected galaxies, and 1 (6%) is IR-normal. The statistics are quite different for those sources with no cataloged X-ray emission, where the power-law fraction drops to 19% and the color-selected fraction rises to 73%.

While a strong argument can be made for the AGN nature of the 32 IR-excess sources with cataloged X-ray counterparts and/or PLG SEDs, what can be said about the remaining IR-excess sources? As discussed in §3, the concentration of the redshifts of these sources about  $z = 2$  may be due to the passage of the  $7.7 \mu\text{m}$

aromatic feature through the  $24\ \mu\text{m}$  band, suggesting a significant contribution from star-formation. In addition, the vast majority of color-selected sources at  $z = 2$  (of which these are a subset) have IRAC colors consistent with those of star-forming galaxies or low-luminosity AGN whose IRAC SEDs are dominated by the host galaxy. In combination with the lack of significant X-ray emission, these facts suggest that the remaining 68% of the IR-excess sample could be either star-forming galaxies, or extremely obscured AGN. To distinguish between these two possibilities, we consider in more detail the sources selected via the Daddi et al. and Fiore et al. criteria.

#### 4.7.1 Daddi et al. (2007) Compton-thick AGN candidates

Of the 88 IR-excess AGN candidates selected in the ISAAC region of GOODS-S by Daddi et al. (2007a), the list of which was kindly provided by D. Alexander (private communication, 2008), 42 fall in our MIPS-selected sample. Twenty-three of the remaining 46 galaxies have MIPS fluxes that fall below our cut of  $f_{24\ \mu\text{m}} \geq 80\ \mu\text{Jy}$ , and 6 galaxies lack MIPS and/or IRAC counterparts in our catalogs, indicating that they too are faint. Seven galaxies were excluded because of observable blending in the MIPS or IRAC bands, and an additional 10 were removed from our sample because of multiple optical counterparts.

The positions of the Daddi et al. sources in IRAC color-space are shown in Figure 10. Thirty-eight of the 42 Daddi et al. sources in our sample meet the Lacy et al. IRAC color-selection criteria. Only 10 meet the Stern et al. AGN selection criterion, and only 5 are PLGs (4 of which have relatively shallow slopes of only  $\alpha \sim -0.6$ ). In addition, only 15 (36%) meet any of the other IR-excess criteria. This is not surprising, as the MIR emission from the Daddi et al. IR-excess sources exceeds that of a typical star-forming galaxy by a factor of only  $\gtrsim 3$  (Daddi et al. 2007b). Of the 42 IR-excess galaxies, 18 have IRAC colors that

lie  $> 1\sigma$  from the redshift-appropriate star-forming contours in either Lacy or Stern color-space. Only 3 and 1, however, have colors that lie outside the  $2\sigma$  and  $3\sigma$  contours, respectively. As discussed above, however, this indicates only that any AGN activity can not be identified on the basis of the MIR IRAC colors alone.

To determine the nature of the Daddi et al. (2007) sources in our sample, we therefore turn to the X-ray data. While none of the IR-excess galaxies are individually detected in the hard X-ray band (by definition), 3 have soft X-ray detections and 13 have faint ( $> 2\sigma$ ) X-ray counterparts. Twenty remain X-ray-undetected, and 6 sources have a nearby X-ray counterpart that prevents an accurate test for low- $\sigma$  X-ray flux. Using the procedure outlined in Steffen et al. (2007), with the only change being our slightly different choice of source aperture radius,  $2''$ , we coadded the three sources detected in the soft band, whose soft-band luminosities of  $L_x > 10^{42}$  ergs s $^{-1}$  indicate that they are AGN. We verify that our stacking method reproduces the results of Daddi et al. (2007b) for the same sample of 59 IR-excess galaxies used in that work. While the coaddition of the 3 soft X-ray detected sources did not lead to a hard band detection, we place a  $3\sigma$  limit on the hard-band flux that constrains their column density to  $N_H \lesssim 2 \times 10^{22}$  cm $^{-2}$ , assuming an intrinsic photon index of  $\Gamma = 1.8$ .

A coaddition of the 13 weakly-detected sources leads to a  $3.3\sigma$  hard-band detection, a  $9.7\sigma$  soft-band detection, a hardness ratio of  $HR = -0.31$ , and a photon index of  $\Gamma = 1.4$ . If we assume that these sources are AGN at their mean redshift of  $z = 1.81$ , the hard to soft flux ratio corresponds to an obscured column density of  $N_H = 3.6 \times 10^{22}$  cm $^{-2}$ . At this modest obscured yet Compton-thin column density, the observed soft band flux is only attenuated by a factor of 2, implying that the sources must have relatively low luminosities. Indeed, the rest-frame 2-10 keV absorption-corrected luminosity derived from the observed soft-band flux is

only  $L_x = 1.6 \times 10^{42} \text{ ergs s}^{-1}$ .

However, Daddi et al. (2007b) argue that the coadded soft X-ray flux of their full IR-excess sample can be attributed to star-formation. When they subtract this component from the detected fluxes, the hardness of the remaining X-ray emission implies a significantly larger (e.g. Compton-thick) column density as well as a larger absorption-corrected luminosity.

To test the origin of the X-ray emission, we plot in Figure 11 the 2-10 keV luminosity and 25  $\mu\text{m}$  power ( $\nu L\nu$ ) of a sample of starburst and AGN-dominated galaxies and ULIRGs drawn from Franceschini et al. (2003), Ranalli et al. (2003), and Persic et al. (2004). The 25  $\mu\text{m}$  luminosities were extracted from the IRAS Revised Bright Galaxy Sample (RBGS, Sanders et al. 2003) when available, and from ISO (Klaas et al. 2001) or the IRAS Faint Source Catalog otherwise. As both the hard X-ray and MIR flux densities of star-forming galaxies trace the current star-formation rate (e.g. Ranalli et al. 2003, Franceschini et al. 2003), these two luminosities are well correlated for starbursts and starburst-dominated ULIRGS (though there is a hint of a turnover to lower X-ray luminosities amongst the ULIRG sample). AGN, however, show an increased X-ray output for their observed 25  $\mu\text{m}$  flux density.

To compare the Daddi et al. sample to these local starburst and ULIRG samples, we convert the observed soft-band (rest frame  $\sim 1.5 - 6 \text{ keV}$ ) luminosity to a rest-frame 2-10 keV luminosity, and the observed 70  $\mu\text{m}$  (rest-frame  $\sim 23 \mu\text{m}$ ) flux density given by Daddi et al. (2007b) to a rest-frame 25  $\mu\text{m}$  power. The mean luminosities of the full Daddi et al. (2007b) IR-normal and IR-excess samples fall on the best-fit correlation for star-forming galaxies, confirming that their observed soft X-ray flux can be attributed to star-formation. The X-ray luminosity of the X-ray weakly-detected IR-excess galaxies in our MIPS sample, however,



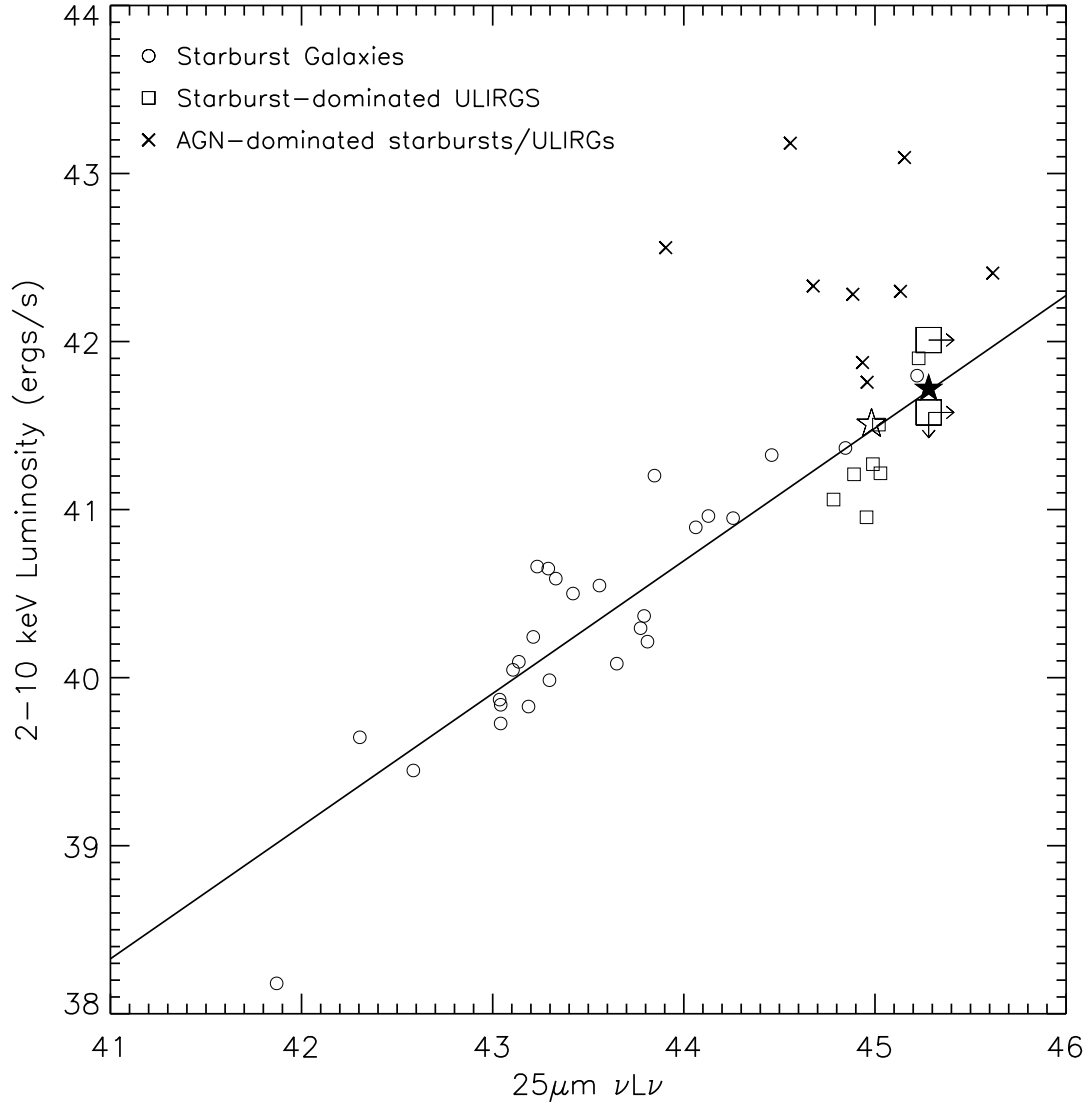


Figure 4.11 Rest-frame 2-10 keV luminosity vs. rest-frame  $25\ \mu\text{m}$  power. The small symbols represent the starburst and ULIRG samples of Franceschini et al. (2003), Ranalli et al. (2003), and Persic et al. (2004), where starburst dominated sources are given as squares and circles, and AGN-dominated sources are given by crosses. The solid line gives the best-fit linear relationship between the X-ray and  $25\ \mu\text{m}$  luminosities of the star-formation-dominated sources. The large filled and open stars represent the full IR-excess and IR-normal samples from Daddi et al. (2007b), respectively, and the large squares represent the X-ray weakly- and non-detected members of the Daddi et al. sources in our sample. Because these sources comprise the brighter subset of the full Daddi et al. sample, we treat the full  $25\ \mu\text{m}$  flux density (derived from the coadded  $70\ \mu\text{m}$  flux density given by Daddi et al. (2007b)) as a lower-limit.

is somewhat higher than predicted. The AGN origin of the soft X-ray emission is supported by the 2-10 keV luminosity implied by the soft X-ray flux,  $L_x = 1.6 \times 10^{42}$  ergs s<sup>-1</sup>. If the soft X-ray flux has a significant contribution from the AGN, then it cannot be fully subtracted from the AGN spectrum, resulting in column densities lower than estimated by Daddi et al. (2007b).

However, the indicated AGN contribution is modest, and is based on an average. Therefore, it is likely that there will be a significant range of star-formation-corrected absorbing columns, including some that are Compton thick. Indeed, Alexander et al. (2008) show that a sample of 6 spectroscopically-confirmed Compton-thick AGN would be selected via the Daddi et al. (2007) method, although 4 of the 6 have infrared excesses of a factor of  $> 100$ , and thus represent the most extreme IR-excess sources.

A coaddition of the 20 X-ray non-detected Daddi et al. sources in our sample leads only to a marginal  $2.0\sigma$  detection in the full band (0.5-8 keV), and  $1.8\sigma$  and  $1.0\sigma$  detections in the hard and soft bands, respectively. A  $3\sigma$  limit on the soft flux gives a 2-10 keV luminosity of  $L_x \leq 3.8 \times 10^{41}$  ergs s<sup>-1</sup>, fully consistent with a star-forming origin (see Figure 11). (The 2-10 keV luminosity derived from the marginal full-band detection is even lower:  $L_x \leq 2.2 \times 10^{41}$  ergs s<sup>-1</sup>). The near-detection in the hard-band, however, suggests that these sources may have relatively hard X-ray spectra. By coadding the weakly and non-detected sources, the photon index drops to  $\Gamma = 1.04^{+0.16}_{-0.14}$ , from a value of  $\Gamma = 1.39^{+0.21}_{-0.17}$  measured for the weakly-detected sources. There is therefore marginal ( $1\sigma$ ) evidence that the X-ray non-detected sources have spectra harder than those of their weakly-detected counterparts. Does this hard spectrum confirm that these sources are AGN, or might there be another explanation?

#### 4.7.1.1 A Star-formation Origin?

While it is well-known that heavily obscured AGN exhibit hard X-ray spectra, star-forming galaxies can also produce such spectra. As discussed in Persic & Rephaeli (2002) and Persic et al. (2004), the hard ( $> 2 - 10$  keV) X-ray emission of star-forming galaxies is dominated by low and high-mass X-ray binaries (LMXBs, HMXBs), with the HMXB fraction increasing from  $\sim 20\%$  at starburst luminosities to  $\sim 100\%$  at ULIRG luminosities. As shown by White, Swank, & Holt (1983), HMXBs have X-ray spectra with  $\Gamma = 1.2 \pm 0.2$ , a cutoff energy of 20 keV, and an  $e$ -folding energy of  $\sim 12$  keV (see e.g. Persic & Rephaeli 2002). At  $z = 2$ , the 0.5-2 keV and 2-8 keV X-ray bands sample the rest-frame 1.5-6 keV and 6-24 keV X-ray bands, and therefore should be minimally affected by the power-law cutoff. A luminous star-forming galaxy undergoing an isolated burst of star-formation is therefore expected to display a hard X-ray spectrum of  $\Gamma = 1.0 - 1.4$  over the energies observed in our sample. X-ray binary emission has been proposed as an explanation for the hard ( $\Gamma \sim 1.0$ ) spectrum of Arp 220 (Iwasawa et al. 2001), the spectra of the apparently starburst-dominated ULIRGS of Ptak et al. (2003) and Teng et al. (2004), whose photon indices tend to lie at  $\Gamma = 1.0 - 1.5$ , and the starburst-dominated ULIRGS of Franceschini et al. (2003). The IR-excess sources are the most luminous galaxies in the Daddi et al. sample (see Figure 2 in Daddi et al. 2007b) and are therefore most likely to exhibit this X-ray behavior.

While the hard X-ray properties of the IR-excess sources do not therefore require an AGN origin, can the same be said of their MIR properties? To test the nature of these sources, we first plot in Figure 12 the median SEDs of the full GOODS-S IR-normal and IR-excess samples, as given in Figure 4 of Daddi et al. (2007b). Although these high-redshift sources appear to be highly luminous (see Figure 12), there are indications that local templates for lower-luminosity galaxies

are appropriate for them, at least in the optical–MIR (Rigby et al. 2008). It is therefore not surprising that the optical–MIR SED of the IR-normal galaxies is well-fit by the M82 SB template of Polletta et al. (2007). (The discrepancy between the observed SED and template at shorter wavelengths is likely due to a difference in the reddening and/or age of the stellar population.) The IR-excess SED is also very well fit by the *purely star-forming* template of the LIRG NGC 3256 (Rieke et al. 2008), to which we have applied an additional reddening of  $A_V \sim 0.8$ . While this does not rule out an AGN contribution to the Daddi et al. IR-excess sample, it does indicate that an AGN need not be present to produce the observed SEDs of the IR-excess sources, and that their IR-excesses may simply be due to strong aromatic emission associated with their systematically higher IR luminosities, as suggested by Daddi et al. (2007a).

If these IR-excess sources are dominated by star-formation, then it appears either that their IR SFRs have been overestimated or that their UV-derived SFRs have been underestimated. The former scenario could be partially attributed to the larger than unity slope between  $24\ \mu\text{m}$  luminosity and  $\text{Pa}\alpha$ -derived SFR (Alonso-Herrero et al. 2006, Calzetti et al. 2007), which indicates that as the SFR increases, an increasing fraction of the resulting light is emitted in the MIR. A simple proportional relationship between SFR and IR luminosity (e.g. that of Kennicutt 1998) will therefore increasingly overpredict the SFR for more luminous infrared galaxies.

An underestimate in the UV-derived star-formation rates could be due to the inherent difficulties in determining accurate UV SFRs for luminous, heavily obscured galaxies (e.g. Goldader et al. 2002, Buat et al. 2005). While UV extinction is known to correlate with luminosity (see Goldader et al. 2002; Vijn, Witt, & Gordon 2003; Buat et al. 2005), Daddi et al. (2007a) find no difference between

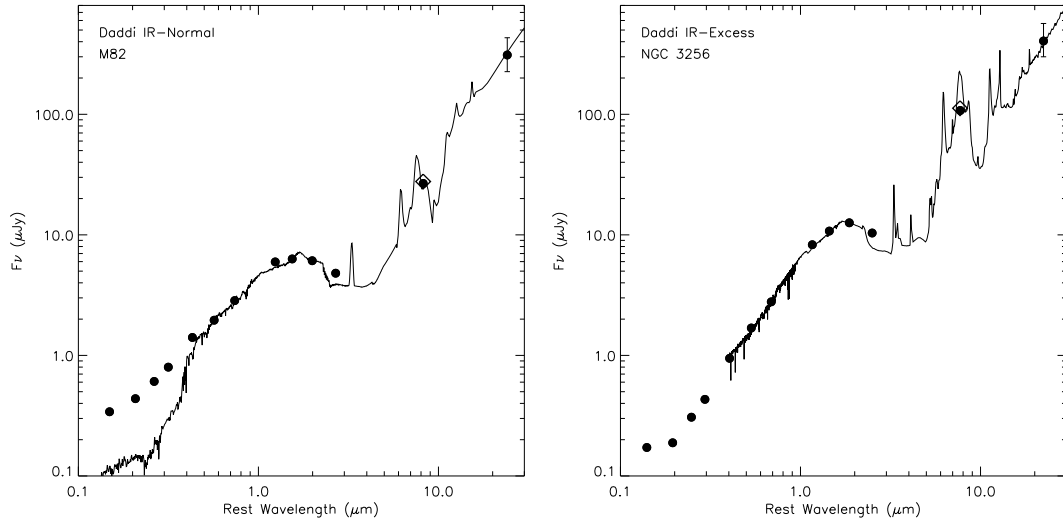


Figure 4.12 Median SEDs of the full Daddi et al. (2007a,b) IR-normal and IR-excess GOODS-S samples, as given in Figure 4 of Daddi et al. (2007b). Overplotted are the *purely star-forming* SEDs of the starburst galaxy M82 (left) and LIRG NGC 3256 (right) (The Rieke et al. (2008) templates only extend down to  $\sim 0.4 \mu\text{m}$ ). We have applied an additional reddening of  $A_V = 0.8$  to the NGC 3256 template. The open diamonds represents the flux that would be measured in the MIPS  $24 \mu\text{m}$  band when the bandpass is convolved with the SED. The optical-MIR SEDs of both the IR-normal and IR-excess sources are well-fit by star-forming SEDs.

the average derived  $A_{1500}$  values of the IR-normal and IR-excess samples, despite the systematically higher 8  $\mu\text{m}$  luminosities of the IR-excess sample (see Figure 2 of Daddi et al. 2007b). Under the assumption that the radio emission arises purely from star-formation, the radio luminosities of the 16 radio-detected IR-excess galaxies similarly indicate the UV SFRs have been underestimated by a mean factor of 6.4, and a median factor of 3.5 (see Figure 12 of Daddi et al. 2007a). A stack of all IR-excess galaxies, however, leads to radio SFRs that are consistent with those derived in the UV.

#### 4.7.1.2 Summary

We have divided the 42 Daddi et al. IR-excess galaxies in our MIPS-selected sample into three subsamples: those that are X-ray detected (3), those that are weakly-detected in the X-ray (13), and those that remain undetected in the X-ray down to  $2\sigma$  (20). (The remaining 6 sources lie too close to an X-ray source to test for faint emission.) The 3 X-ray detected sources are AGN with  $L_x > 10^{42} \text{ ergs s}^{-1}$ , but have relatively low obscuration ( $N_H \leq 2 \times 10^{22} \text{ cm}^{-2}$ ).

A coaddition of the weakly-detected sources leads to a hard ( $\Gamma = 1.4$ ) X-ray detection. If these sources are obscured AGN, the hardness ratio implies a column density of  $N_H = 3.6 \times 10^{22} \text{ cm}^{-2}$ . A hard detection, however, could be attributed either to obscured AGN activity or to star-formation via HMXBs, especially among the luminous IR-excess sources. Furthermore, the median SED of the full Daddi et al. (2007b) IR-excess sample is consistent with that of a local star-forming LIRG, suggesting that the MIR emission alone also cannot be used to rule out a star-forming origin. A comparison of the X-ray and MIR luminosities of these weakly-detected sources does not conclusively distinguish between a star-forming or AGN origin for the X-ray emission. There are therefore 3 possible explanations for the members of this sample of IR-excess galaxies: (1) the

sources are Compton-thick AGN whose soft X-ray emission can be attributed to star-formation and whose hard X-ray emission comes from the AGN, (2) they are relatively low-luminosity, Compton-thin AGN, whose soft X-ray emission can not be entirely attributed to star-formation, or (3) they are star-forming galaxies whose soft *and* hard X-ray emission arise from star-formation. While the derived 2-10 keV X-ray luminosity of  $\sim 10^{42}$  ergs s $^{-1}$  suggests explanation (2), it is not sufficiently high to definitively rule out the remaining scenarios. It is likely that no single possibility applies to all 13 galaxies, but that the possibilities define the range of their behavior.

The X-ray non-detected sources, when coadded alone and with the X-ray weakly-detected sample, also appear to have a relatively hard X-ray spectrum. Their X-ray luminosity, however, is significantly lower than that of the weakly-detected sources,  $L_x \leq 3.8 \times 10^{41}$  ergs s $^{-1}$ . If the hard spectrum arises from HMXBs, the properties of this sample would be consistent with a star-formation origin.

In summary, while we cannot rule out an obscured AGN origin for the Daddi et al. IR-excess sources in our MIPS-selected sample, their properties may also be consistent with a purely star-formation origin in the majority of cases. Further analysis, taking into account the additional 1 Ms of X-ray exposure in the CDF-S, is therefore required to establish their nature.

#### 4.7.2 Fiore et al. (2008) Compton-thick AGN candidates

Fiore et al. (2008) select IR-excess galaxies with the following properties:

$f_{24 \mu\text{m}}/f_R \geq 1000$  and  $R - K > 4.5$ . Using the MUSIC catalogs (see §2.3), we selected 64 sources that meet these criteria and that have 24  $\mu\text{m}$  flux densities  $> 80 \mu\text{Jy}$ . However, 9 of these sources were removed from our MIPS sample because of visible blending in the MIPS and/or IRAC bands (see §2), which may

have been responsible for their anomalously high IR to optical flux ratios (unlike Grazian et al. (2006), we do not attempt to de-blend such sources). A visual inspection of the remaining sources led to the removal of 3 additional sources with blended K-band fluxes, leaving 52 high-quality IR-excess sources.

The first Fiore criterion was designed to select obscured AGN with large X-ray to optical flux ratios (see their Figure 2) whose column densities tend to range from  $N_{\text{H}} = 10^{22}$  to  $10^{23} \text{ cm}^{-2}$  (see Fiore et al. 2008 and references therein). The  $R - K$  criterion ensures that only extremely red objects (EROs) fall in the sample. The AGN amongst ERO samples tend also to be X-ray obscured with  $N_{\text{H}} = 10^{22} - 10^{24} \text{ cm}^{-2}$  (Brusa et al. 2005). Obscured AGN are therefore likely to be targeted by these criteria. However, these two selection criteria are known to identify both AGN and star-forming galaxies (e.g. Alexander et al. 2002b, Doherty et al. 2005, Dey et al. 2008). We therefore examine whether these criteria are sufficiently stringent to exclude the possibility that the properties of these sources could arise from star formation.

The first of the three main arguments for the Compton-thick AGN nature of the Fiore et al. sources is the ability of the obscured AGN template of IRAS 09104+41091 (Pozzi et al. 2007) to reproduce the extreme colors of these sources, and the comparable inability of the M82 and Arp 220 star-forming templates to do the same (see their Figure 3). When fitting SEDs to the sources in their sample, Fiore et al. find that only 36% of their X-ray non-detected sources are best-fit by elliptical, spiral, M82, N6090, or Arp 220 star-forming templates. Of the sources in our MIPS-selected sample that meet the Fiore et al. criteria and have good redshift fits, we find an even lower fraction of sources best-fit by these templates: 20%. However, as shown in Figure 13, the purely star-forming IRAS 22491 template of Polletta et al. (2007) satisfies the Fiore et al. criteria when modest addi-



tional reddening ( $A_V \leq 1.2$ ) is allowed, indicating that the extreme colors of these sources can be reproduced not only by obscured AGN, but by highly reddened star-formation as well. Indeed, when we include this star-forming template, as well as the star-forming LIRG/ULIRG templates of Rieke et al. (2008), the fraction of Fiore sources in our sample best-fit by a star-forming template rises from 20% to 66%.

The second argument for the Compton-thick nature of the Fiore et al. sources is the high fraction of heavily obscured AGN ( $N_H = 10^{23} - 10^{26} \text{ cm}^{-2}$ ) required to reproduce the hardness ratios and counts of the stacked X-ray emission. Using a simulation, Fiore et al. (2007) estimate that 80% of their sources are obscured AGN. The prediction for the X-ray non-cataloged sources in our sample is somewhat lower:  $60\%_{-40\%}^{+20\%}$ , although this fraction rises for the weakly-detected IR-excess sources to  $80\%_{-20\%}^{+10\%}$  (F. Fiore, private communication, 2008).

To test this finding for the sources in our sample, we coadded the 36 X-ray non-cataloged Fiore et al. sources that lie far enough from known X-ray sources to allow an accurate test for faint X-ray emission. The coaddition gave a soft detection (0.5-2 keV,  $3.9\sigma$ ), but only a weak hard detection (2-8 keV,  $1.7\sigma$ ). The resulting hardness ratio,  $HR = (H - S)/(H + S) = -0.17$  is only slightly harder than that of the 10 X-ray cataloged Fiore et al. sources,  $HR = -0.21$ , whose column densities fall in the unobscured to highly obscured ( $\log N_H (\text{cm}^{-2}) = 23.9$ ) range (Tozzi et al. 2006), with a median value of  $\log N_H (\text{cm}^{-2}) = 22.6$ .

If we stack only the 10 sources with weak X-ray counterparts (that also lie sufficiently far from known X-ray sources), however, we find a  $5.3\sigma$  hard-band detection, a  $4.7\sigma$  soft-band detection, and a hardness ratio of  $HR = 0.33$ , significantly harder than that of the X-ray cataloged sample. At a redshift of  $z = 2$ , this  $HR$  corresponds to a column density of  $N_H = 2.7 \times 10^{23} \text{ cm}^{-2}$ . The observed

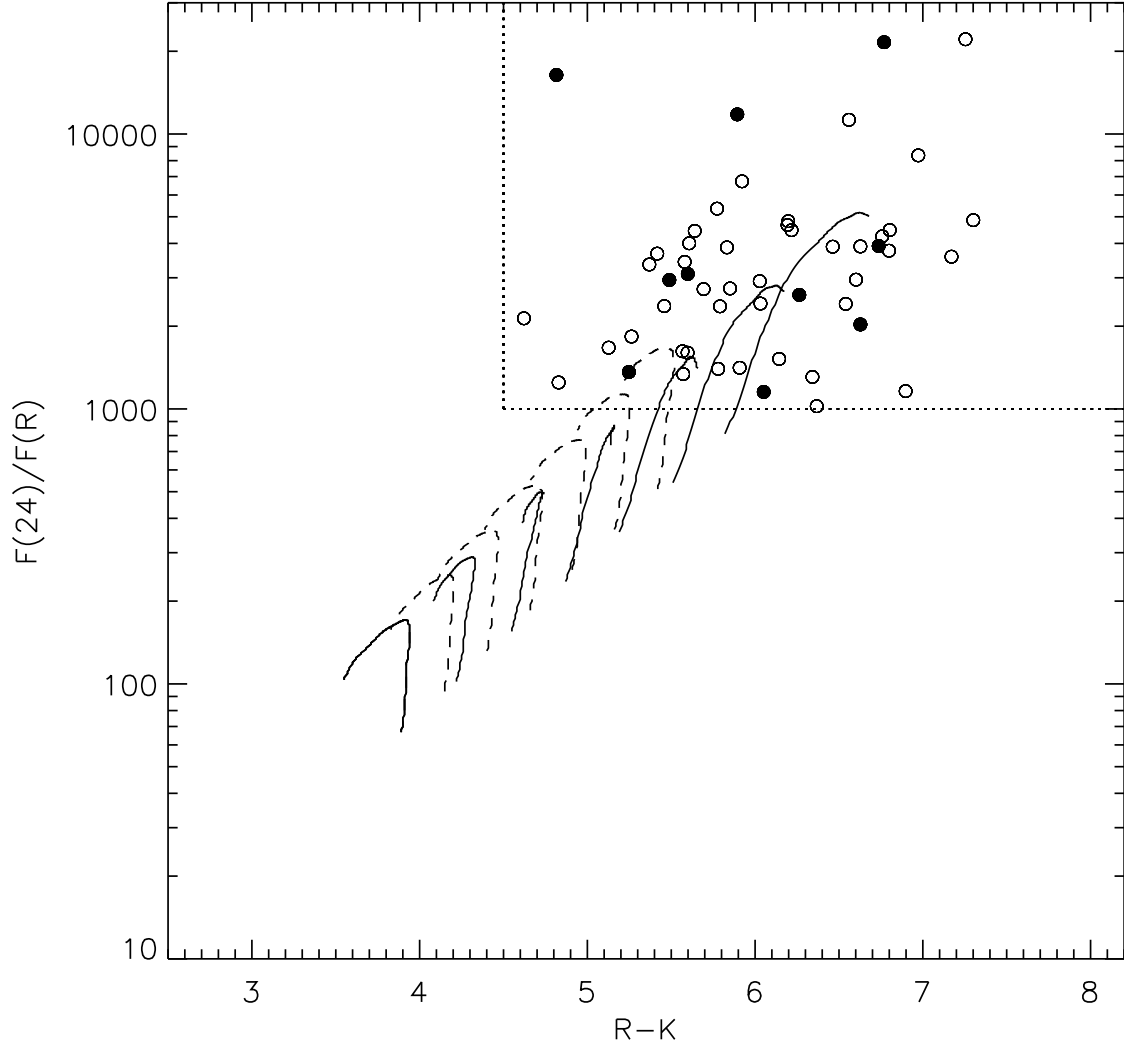


Figure 4.13 Redshifted ( $z = 1.5 - 2.5$ ) tracks of the star-forming template IRAS 22491-1808 in Fiore et al. color space. Additional extinctions of  $A_V = 0.0, 0.2, 0.4, 0.6, 0.8, 1.0$ , and  $1.2$  were applied via the SMC (solid, Prevot et al. 1984, Bouchet et al. 1985) or Calzetti (dashed, Calzetti et al. 2000) extinction laws. The dotted lines represent the Fiore et al. (2008) selection criteria, and circles represent the 52 sources in our sample that meet those criteria. The 10 X-ray-detected sources are given as filled circles. The star-forming template enters the selection region with only a modest ( $A_V \sim 1$ ) amount of additional extinction.

photon index,  $\Gamma = 0.33$ , indicates an obscured AGN origin, as it is inconsistent even with the moderately hard spectra of HMXB-dominated star-forming galaxies ( $\Gamma \sim 1.0 - 1.4$ ). Stacking the remaining 26 X-ray–non-detected Fiore sources does not lead to a detection in any band. It therefore appears plausible, at least in this bright subset of the Fiore et al. sample, that the hard X-ray flux can be attributed to a small number of obscured, yet mostly Compton-thin, AGN, as opposed to a large number of obscured, Compton-thick AGN.

The third argument for the AGN nature of the Fiore et al. sources is the significant (factor of 30) offset between the IR and UV-derived SFRs. However, the inherent difficulties in determining accurate UV SFRs for luminous, heavily obscured galaxies (e.g. Goldader et al. 2002, Buat et al. 2005), as well as the systematic uncertainties of factors of 10-30 in the TIR luminosity (Fiore et al. 2008), make this the weakest of the 3 arguments.

Of the 52 Fiore et al. sources in our MIPS sample, 10 (19%) are therefore X-ray–selected AGN, and 10 (19%) are weakly detected in the X-ray, with coadded properties consistent with their being obscured AGN. As for the remaining 26 sources for which we can test for faint X-ray emission, we cannot rule out the presence of Compton-thick AGN. However, the lack of coadded hard counts from this X-ray non-detected sample, the significant fraction of such sources that can be fit by star-forming templates, and the Compton-thin nature of the X-ray–detected Fiore et al. sources all suggest that many of these sources, which make up the remaining 56% of the sample, are instead star-forming galaxies.

#### 4.8 Implications for IR Selection of AGN

Our evaluation of the performance of the infrared selection methods allows a preliminary estimate of the overall role of *Spitzer*-discovered AGN in the total pop-

ulation. Of the 109 X-ray sources in the MIPS-selected sample, 95 have redshifts, and of these, 73 (77%) have AGN-like X-ray luminosities of  $(\log L_x(\text{ergs s}^{-1}) > 42)$ . We therefore assume a sample of 84 (77% of 109) X-ray-selected AGN in the MIPS-selected sample. We now consider how many IR-selected AGN can be added to this total.

#### 4.8.1 Infrared power-law and color-selected AGN

Of the 55 power-law AGN in our sample, 30 lack cataloged X-ray counterparts. If we assume that all of the X-ray weakly- and non-detected PLGs are AGN, the power-law selection criteria increases the number of known AGN (84) by 36%. Of the 25/30 X-ray non-cataloged sources for which we could test for faint emission, 7 (28%) show weak X-ray emission at the  $> 2\sigma$  confidence level, and 18 show no sign of X-ray emission. Correcting for the 5 sources with nearby X-ray counterparts therefore gives an estimate of 8.4 weakly-detected sources. To place a conservative lower-limit on the contribution of X-ray non-detected PLGs to the AGN population, we select as AGN those PLGs that are either weakly-detected in the X-ray (8.4) or that have extremely red slopes of  $\alpha < -1.0$  (8, see §6). Combining these two criteria results in a sample of 11.6 AGN candidates missed in the X-ray catalogs, for a contribution of 14%. We therefore conclude that PLG selection increases the number of known MIPS-detected AGN by  $\sim 14 - 36\%$ . Further adding the 3 color-selected galaxies that lie outside the  $3\sigma$  star-forming contours and that lack cataloged X-ray counterparts (after correcting for the fraction with redshifts and for which the distance from the star-forming contours could therefore be determined) increases the contribution of IRAC-selected AGN to  $\sim 18 - 40\%$ .

A search for weak X-ray emission from the full sample of color-selected galaxies results in the detection of 44 additional sources, 70% of which have X-ray lu-

minosities typical of AGN (see Table 2). Of these 30 AGN candidates, however, 19 (63%) lie at  $z > 1.75$ , the redshift above which nearly all (94%) MIPS sources meet the Lacy et al. criterion, regardless of their nature (AGN/star-forming). Their selection as AGN candidates is therefore not primarily a function of their IRAC colors, but of their X-ray properties. As such, we do not add these additional  $\sim 30$  AGN candidates to our *Spitzer*-selected total.

#### 4.8.2 Radio/Infrared-selected AGN

Radio/infrared selection, in which objects are selected for excess radio emission relative to that at  $24\ \mu\text{m}$ , provides an alternative way to identify AGN independently of their optical and X-ray characteristics. In Donley et al. (2005), radio-excess AGN are defined as those sources with  $\log f_{24\ \mu\text{m}}/f_{1.4\text{GHz}} < 0$ . Unlike PLGs, radio-excess AGN tend to lie at  $z \sim 1$ , have Seyfert-like X-ray luminosities of  $\log L_x(\text{ergs s}^{-1}) \sim 42 - 43$ , and have NIR SEDs dominated by the stellar bump (Donley et al. 2005). Of the PLGs detected in the CDF-N, only 3% meet the radio-excess criteria (Donley et al. 2007). While there is therefore almost no overlap between these two AGN populations, their X-ray detection statistics are very similar: only 40% of radio-excess AGN are cataloged in the 2 Ms CDF-N. If we consider only those radio-excess AGN with  $24\ \mu\text{m}$  flux densities in excess of  $80\ \mu\text{Jy}$ , the X-ray detection fraction rises to  $\sim 60\%$ . At this flux limit, the CDF-N sample is complete to radio-excess AGN as defined by Donley et al. (2005).

In the CDF-N, the X-ray and MIPS-detected radio-excess galaxies (with X-ray exposures greater than 1 Ms) account for 3% of the total number of such sources, and their X-ray non-detected counterparts increase the number of known AGN by 2%. Only 10-15% of AGN, however, are radio-intermediate or radio-loud. This small observed sample of radio-excess AGN is therefore indicative of an underlying population at least 7 times larger, which would increase the known

population of MIPS-detected AGN by  $\sim 15\%$  if a way could be found to identify them.

Martinez-Sansigre et al. (2006) also select high-redshift obscured AGN candidates via a  $24\ \mu\text{m}$  and radio flux cut, although of the 21 AGN candidates chosen by them, only 6 (29%) are sufficiently radio loud to meet the infrared-to-radio selection criteria used above to define radio-excess AGN. Their selection, however, also includes a  $3.6\ \mu\text{m}$  IRAC cut designed to select red galaxies. Because it is designed for use in shallow surveys, only three galaxies in the GOODS region of the CDF-N meet their MIPS and radio flux cuts (using the radio data of Richards 2000), and none are red enough to meet all three criteria. This selection method therefore does not contribute to the AGN sample in the deep CDF-S.

#### 4.8.3 IR-excess Galaxies

As discussed above, the IR-excess samples of Daddi et al. (2007a), Dey et al. (2008), Polletta et al. (2008), and Fiore et al. (2008) contain various fractions of AGN and star-forming galaxies, with only the Polletta et al. selection criteria unquestionably identifying AGN. Of the Polletta et al. sources, however, 80% are detected in the X-ray catalogs, and the remaining source is a weakly-detected PLG, whose contribution to the AGN population has already been considered.

Daddi et al. (2007a,b) conclude that at least 50% of their IR-excess galaxies are Compton-thick AGN. If this hypothesis holds for the sources in our sample, the Daddi et al. selection criteria would contribute  $\gtrsim 21$  AGN to the MIPS-selected sample in the ISAAC field, or  $\gtrsim 31$  AGN to the full MIPS sample (as the ISAAC region comprises only 68% of our full survey area). As discussed in §7.1, however, it appears plausible that the properties of many of these sources can be attributed to star-formation. We therefore add only the weakly-detected galaxies, whose mean X-ray luminosity suggests a likely AGN origin. Of the 13 weakly-

detected Daddi et al. IR-excess galaxies, 1 is a weakly-detected PLG and 1 is a color-selected galaxy that lies  $> 3\sigma$  from the star-forming contours, leaving 11 sources whose contribution is yet to be counted (or 12.6 when we correct for the sources for which we could not test for weak X-ray emission). Further scaling to the full sample region results in an additional contribution of 18.6 sources, or 22%.

F. Fiore (private communication, 2008) likewise concludes that  $\sim 60\%$  of the X-ray non-cataloged sources in our sample are obscured AGN. If so, our MIPS sample in the ISAAC field should contain 25 X-ray weakly or non-detected Fiore-selected AGN. Of the 36/42 X-ray non-cataloged Fiore sources in our sample (which do not lie too close to a known X-ray source to test for faint emission), however, only 10 (28%) are X-ray weakly-detected (with properties indicative of heavy obscuration). The remaining 26 sources show no evidence for X-ray emission, and have properties that may also be consistent with star-formation. We therefore only consider the contribution from the 10 weakly-detected sources. Of these 10 sources, 3 are weakly-detected power-law galaxies. Correcting for the ISAAC field of view (and the 6 sources for which we could not test for weak X-ray emission) results in an additional contribution of 12.0 AGN, or 14%.

#### 4.8.3.1 Combined Contribution

By combining the contribution of reliable power-law, color-selected, radio/ infrared, and IR-excess AGN candidates, we therefore estimate that *Spitzer*-selected samples increase the known X-ray-selected AGN population by  $\sim 54 - 77\%$ , down to a  $24 \mu\text{m}$  flux density of  $80 \mu\text{Jy}$ . In addition, the radio/infrared selection implies a  $\sim 17\%$  contribution from radio-excess and radio-quiet AGN yet to be identified. The number of AGN with  $24 \mu\text{m}$  flux densities  $> 80 \mu\text{Jy}$  is therefore  $71 - 94\%$  larger than that of current samples detected both in the X-ray and at

24  $\mu\text{m}$  in the deepest X-ray fields.

#### 4.9 AGN Fraction of the MIR Sample

We plot in Figure 14a the fraction of the MIPS sample comprised of MIR-dominated AGN as a function of 24  $\mu\text{m}$  flux density. We define as ‘MIR-dominated’ those AGN that (1) meet the PLG criteria, provided that they are also X-ray-weakly-detected or have extremely red slopes of  $\alpha < -1.0$  (these criteria were used above to place a conservative lower limit on the contribution from PLGs), (2) meet the IRAC color-color cuts of Lacy et al. (2004) or Stern et al. (2005) and lie outside the  $3\sigma$  star-forming contours, (3) meet the Polletta et al. (2008) criteria, (4) meet the Fiore et al. (2008) criteria and are X-ray cataloged or weakly-detected, or (5) meet the Daddi et al. (2007) criteria and are X-ray cataloged or weakly-detected. As above, we define as X-ray AGN those sources with cataloged X-ray counterparts whose total X-ray luminosities (when redshifts are available) exceed  $10^{42} \text{ ergs s}^{-1}$ . Because the PLG, Daddi et al. (2007), and Fiore et al. (2008) selection criteria all identify AGN candidates with mean redshifts of  $z \sim 2$ , the vast majority of the IR-selected AGN lie at high redshift regardless of their flux density.

As shown by Brand et al. (2006), the fraction of MIR sources dominated by an AGN drops with decreasing flux density. We verify this trend, showing excellent agreement with the Brand et al. results (see Figure 13a), and confirm that it continues down to  $\sim 300 \mu\text{Jy}$ . At lower flux densities, however, the fraction of MIR-dominated X-ray AGN begins to decrease at a much lower rate, and that of all MIR-dominated AGN plateaus at a value of  $\sim 10\%$ . This indicates that a non-negligible fraction of faint MIR sources are not powered primarily by star-formation, but by their central engines. The significant number of faint 24  $\mu\text{m}$



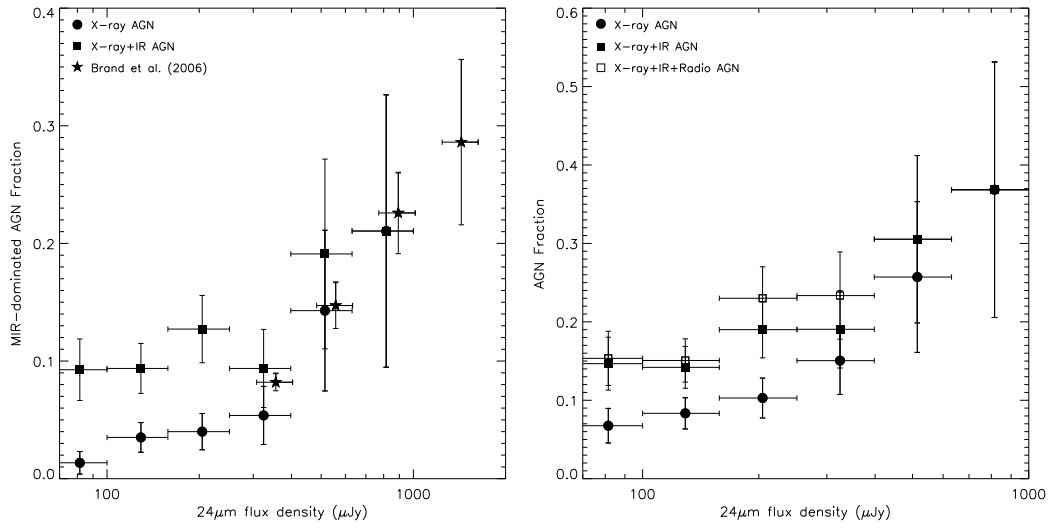


Figure 4.14 Fraction of MIR-dominated AGN, and all AGN (regardless of their contribution to the MIR light), as a function of 24  $\mu\text{m}$  flux density. The full definitions of 'MIR-dominated' and 'X-ray AGN' are given in §9. Error bars represent the  $1\sigma$  errors on the source number counts, and the width of the bins. The MIR-selected sources missed in the X-ray comprise the majority of the MIR-dominated AGN at low flux densities, where the trend towards lower AGN fractions plateaus.

sources that are AGN-dominated in the MIR is consistent with the finding of 6/19 such objects in the spectroscopy of faint  $24\ \mu\text{m}$  sources by Rigby et al. (2008). At these low flux densities, it is also evident from Figure 14a that the majority of the MIR-dominated AGN are not detected in the X-ray. For instance, at  $80\ \mu\text{Jy}$ , the total number of MIR-dominated AGN outnumbers that of MIR-dominated X-ray AGN by a factor of  $\sim 6$ . Using only the X-ray emission as a probe of AGN activity will therefore result in a serious underestimation of the AGN contribution to the MIR flux density.

Finally, we plot in Figure 14b the fraction of all AGN in the MIPS sample (not only those whose MIR flux is dominated by the AGN), as a function of MIPS  $24\ \mu\text{m}$  flux density. To account for the contribution of the AGN amongst the 14 X-ray sources lacking redshifts, we randomly add 11, or 77% (the AGN fraction of the X-ray sample), of these 14 X-ray sources to the X-ray AGN sample. We further supplement the AGN sample by including the assumed contribution from radio-excess and radio-quiet AGN, 17%, or 14 sources. Because these sources have not been individually identified in the CDF-S, we draw their flux densities randomly from the range of observed flux densities in the CDF-N ( $80 - 300\ \mu\text{Jy}$ ).

The X-ray non-detected AGN still comprise the majority of all AGN at the lowest  $24\ \mu\text{m}$  flux densities, and their contribution at larger flux densities is significant, raising the AGN fraction to  $> 15\%$  at all  $24\ \mu\text{m}$  flux densities. As was seen for the MIR-dominated AGN, the total fraction of AGN rises with increasing MIR flux density, reaching a value of 37% at  $f_{24\ \mu\text{m}} \sim 800\ \mu\text{Jy}$ , 15% higher than that of MIR-dominated AGN of the same flux density. The X-ray AGN fractions we find are somewhat higher than that of Treister et al. (2006). While the cause of this offset is not entirely clear, it is likely to be due at least in part to cosmic variance, as their  $24\ \mu\text{m}$  sample was drawn from GOODS-N, and ours from

GOODS-S. Once again, the vast majority of X-ray non-detected AGN at all flux densities lie at  $z \sim 2$ , the mean redshift of the sources selected via the PLG, Daddi et al. (2007), and Fiore et al. (2008) criteria. Only the radio-selected AGN samples lie at systematically lower redshifts of  $z \sim 1$ .

#### 4.10 Summary

Infrared selection of AGN is a powerful technique. Using new accurate star-forming and AGN templates along with a flux-limited MIPS-selected sample drawn from the GOODS-S field, we critically review three MIR selection criteria: (1) the IRAC color cuts of Lacy et al. (2004) and Stern et al. (2005), (2) the power-law galaxy (PLG) selection technique of Alonso-Herrero et al. (2006) and Donley et al. (2007), and (3) the IR-excess selection criteria of Daddi et al. (2007a,b), Dey et al. (2008), Fiore et al. (2008), and Polletta et al. (2008). From this analysis, we then quantify the contribution of *Spitzer*-selected AGN to the X-ray selected AGN population. The main conclusions of this paper are as follows:

- The majority of non-power-law IRAC color-selected AGN candidates have IR colors consistent with those of redshift-appropriate star-forming templates. In comparison, the majority of PLG AGN candidates lie outside of the star-forming contours. PLG selection recovers the majority of high-quality AGN candidates.
- The reliability of AGN IRAC color-color selection improves with increasing flux as high-redshift star-forming galaxies fall out of the sample. Nevertheless, the fraction of potential star-forming contaminants is still high ( $\sim 50\%$ ) at the highest fluxes probed by our survey ( $f_{24\ \mu\text{m}} \sim 500\ \mu\text{Jy}$ ).
- A comparison of the  $24\ \mu\text{m}$  to  $3.6\ \mu\text{m}$  colors of the X-ray non-detected PLGs

to those of AGN and star-forming templates suggests that the X-ray non-detected PLGs, like their X-ray-detected counterparts, have more hot dust emission than can be explained by star-formation alone.

- An analysis of the Daddi et al. (2007) IR-excess sources in our MIPS sample indicates that while these sources may be Compton-thick AGN, it is also possible that they are low-luminosity, Compton-thin AGN and/or luminous, highly-reddened star-forming galaxies.
- An X-ray stacking analysis of the sources selected via the Fiore et al. (2008) criteria indicate that  $\sim 42\%$  are consistent with being obscured AGN, and that the remaining 58% may be star-forming galaxies.
- Adding secure *Spitzer*-selected power-law, color-color, radio/IR, and IR-excess AGN candidates to the deepest X-ray samples directly increases the number of known AGN by  $\sim 54 - 77\%$ , and implies a total increase of  $71 - 94\%$ . This fraction excludes the full contributions from the Daddi et al. and Fiore et al. AGN candidates, whose nature is still uncertain.
- The fraction of MIR sources dominated by an AGN decreases with decreasing flux density, but only down to a  $24\ \mu\text{m}$  flux density of  $\sim 300\ \mu\text{Jy}$ . Below this limit, the AGN fraction levels out at  $\sim 10\%$ . This indicates that a non-negligible fraction of faint  $24\ \mu\text{m}$  sources are primarily powered not by star-formation, but by the central engine. In addition, the majority of AGN at low  $24\ \mu\text{m}$  flux densities are missed in the X-ray, indicating that X-ray emission alone cannot be used to identify AGN, especially amongst faint IR samples.

## CHAPTER 5

## CONCLUSIONS AND FUTURE DIRECTIONS

## 5.1 Radio-excess AGN

In Chapter 2, I selected AGN independently of their X-ray and optical properties using the radio-infrared correlation. Approximately 60% of the AGN selected in this way lacked counterparts in the 2 Ms X-ray catalog, and 25% lack even faint ( $\geq 2\sigma$ ) detections. This result therefore confirmed the prediction that even the deepest X-ray surveys are substantially incomplete to obscured AGN by detecting the first of this ‘missing population’. While the actual number of sources detected was relatively low (27 radio-excess AGN in total), radio-excess AGN comprise only  $\sim 15\%$  of the full AGN sample.

The radio-excess AGN have a mean redshift of  $z \sim 1$  and have X-ray luminosities characteristic of Seyfert galaxies ( $10^{42} < L_x(\text{ergs s}^{-1}) < 10^{44}$ ). While the X-ray-non-detected sources remain Compton-thick candidates, the X-ray column densities of the weakly-detected (e.g., non-cataloged) AGN indicate that they are obscured, yet Compton-thin. In the models of Worsley et al. (2005), the galaxies primarily responsible for the missing, unresolved CXRB radiation have properties generally consistent with those of the radio-excess AGN: they are predicted to lie at  $z = 0.5 - 1.5$ , have column densities of  $N_H > 10^{23} \text{ cm}^{-2}$  and have X-ray luminosities of  $< 5 \times 10^{43} \text{ ergs s}^{-1}$ . It therefore seems plausible that the radio-excess AGN comprise the radio-loud subset of this missing population.

Assuming that radio-excess AGN are not preferentially obscured compared to their radio-quiet counterparts, the radio-excess sample discussed above therefore implies a significant and still-hidden population of heavily obscured,  $z \sim 1$ , and Seyfert-luminosity radio-*quiet* AGN. How might such AGN be identified? As dis-

cussed in Chapter 3, the power-law selection technique preferentially identifies high-luminosity quasars. There is therefore little to no overlap between the radio-excess and power-law samples. While the infrared-excess selection techniques discussed in Chapter 4 may be less biased towards high AGN luminosities, they select samples at  $z \sim 2$  and appear to be subject to contamination by star-forming galaxies.

What options then remain? One possible approach comes from the *Herschel* far-infrared and submillimeter observatory, scheduled for launch in early 2009. At  $z = 1 - 2$ , the  $70 - 100 \mu\text{m}$  emission probes the predicted peak of the reprocessed radiation in heavily obscured, Compton-thick AGN. How well such radiation can be used to successfully separate Compton-thick AGN from star-forming galaxies, however, is yet to be determined. Alternatively, one could use the radio spectral slope. Seymour et al. (2008), for example, select as AGN all sources whose 1.4 GHz to 4.8 GHz spectral slope does not lie in the range  $-0.4 \lesssim \alpha \lesssim -1.1$ . To do so, however, we would need deeper radio surveys; in current surveys, only 30% of the luminous power-law AGN have radio counterparts. Likewise, high-resolution radio data from MERLIN or the future EVLA could be used to discriminate between AGN and star-formation powered sources via the radio morphology.

In the absence of extremely deep and/or high-resolution radio data, however, the best option lies in deeper X-ray surveys. Approximately 35% of the radio-excess AGN in the CDF-N lack high-significance cataloged X-ray counterparts, but show evidence for weak  $\geq 2\sigma$  X-ray emission. Because the *Chandra* deep fields are photon-limited, not background-limited, doubling the exposure results in twice the sensitivity, at least in the inner regions of the X-ray field where vignetting is minimal. Increasing the depths of the deep X-ray field(s) to 5 Ms, for

example, should therefore result in a  $5\sigma$  detection of  $\sim 75\%$  of the radio-excess (and radio-quiet) AGN samples, compared to the 40% detection rate in the currently available data.

Finally, it should be noted that the selection of AGN via their infrared and radio properties has thus-far been limited to regions of the sky with deep *Spitzer* coverage. This will soon change thanks to the Wide-field Infrared Survey Explorer (WISE), currently scheduled for launch in November, 2009. Over 500 times more sensitive than IRAS, WISE will provide an all-sky survey from 3-25  $\mu\text{m}$  down to a 23  $\mu\text{m}$  sensitivity limit of 2.6 mJy. This dataset will therefore be well-matched to the FIRST VLA survey, whose source detection threshold is  $\sim 1$  mJy, and will enable the identification and study of any radio-excess AGN with 20 cm flux densities in excess of  $\sim 3$  mJy.

## 5.2 Infrared power-law AGN

In Chapter 3, I used the unique power-law spectral shape of luminous AGN to select a sample of high-luminosity ( $L_x > 10^{44}$  ergs  $\text{s}^{-1}$ ) and high-redshift ( $z \sim 2$ ) AGN, again independently of their X-ray and optical properties. While there is almost no overlap between this sample of power-law galaxies (PLGs) and the Seyfert-luminosity,  $z \sim 1$ , radio-excess AGN discussed above, the X-ray detection statistics are similar: only  $\sim 50\%$  of the PLGs are detected in the X-ray. This result is in partial agreement with the predictions of Ballantyne et al. (2006), who estimate that deep X-ray surveys miss  $\sim 50\%$  of obscured AGN with  $L_x > 10^{44}$  ergs  $\text{s}^{-1}$ . Contrary to the Ballantyne et al. prediction that most of the missing objects are Compton-thick, however, all but 15% of the PLGs show evidence for faint X-ray emission that indicates an obscured, but Compton-thin, column density. This may be partially a function of the selection method. As

discussed in Chapter 3, the possibility of substantial NIR extinction in Compton-thick AGN may bias the power-law selection method against such sources. If this is the case, however, the fraction of luminous AGN missed in the deep X-ray fields will be even higher than observed.

Because of potential, though unlikely, contamination by high-redshift star-forming galaxies, it would be useful to obtain independent confirmation of the AGN nature of these sources. Such confirmation could come in the form of AGN lines in optical and/or NIR spectra, from the detection of hard X-ray emission, or from optical variability, which has already been observed for some X-ray non-detected power-law galaxies (Sarajedini et al. 2008). Follow-up studies of PLGs in the deep *Chandra* fields, however, are limited primarily by the faint optical and MIR magnitudes of this sample as well as their relatively small numbers. This limitation can be largely overcome by selecting a sample of PLGs in a larger field, such as COSMOS. For instance, GOODS-S contains only  $\sim 60$  power-law galaxies and only 7 with  $I < 24$ . In contrast, a quick analysis of the public COSMOS catalogs indicates that this field (which is 20 times the size of the combined GOODS fields) contains over 1000 power-law AGN, and over 100 with  $I < 24$ . While the multiwavelength coverage is not as deep, the large area allows for better selection of rare luminous sources such as PLGs. Optical spectroscopic follow-up of the bright PLGs in COSMOS would help to constrain their redshift distribution, and subsequent NIR observations could quantify the relative contributions from AGN and star-formation activity via measurement of the  $[\text{N II}]/\text{H}\alpha$  line ratio. Furthermore, X-ray coaddition of the large number of PLGs would provide far better constraints on the overall X-ray properties of this sample. Because the coolant on *Spitzer* will soon run out, a detailed study of the MIR spectral properties, however, will have to wait for JWST, whose MIRI instrument will provide



spectroscopic coverage from 5 to 27  $\mu\text{m}$ .

### 5.3 The Combined Contribution from *Spitzer*-selected AGN

In the 5+ years since the launch of *Spitzer*, a number of authors have developed IR-based AGN selection criteria. In Chapter 4, I critically reviewed all of the major selection methods defined to date, which include IRAC color-color and IR-excess selection methods in addition to the radio-excess and power-law techniques discussed above. As discussed in the introduction, the main difficulty in developing successful IR-based AGN selection methods lies in the separation of AGN- and star-formation-powered sources. Of course, these two processes often operate concurrently, further complicating the identification of AGN. We therefore set the following measure of success: the AGN selection criteria must not be reproducible by the template of a *purely star-forming* galaxy. When we consider only those AGN candidates that we believe to be secure, we confirm that a significant number of AGN have been missed in the deepest X-ray fields observed to date. Adding these secure *Spitzer*-detected AGN candidates to the X-ray-selected sample increases the known number of AGN by up to 94%.

*Spitzer*-selection therefore nearly doubles the number of known AGN in the distant Universe. Nevertheless, this number is likely a lower limit on the true number of obscured AGN missed in the deep X-ray fields. While the implied number of heavily obscured,  $z \sim 1$ , Seyfert-luminosity, radio-quiet AGN is included in the contribution above, only 60% of the most luminous AGN ( $10^{44} < L_{\text{x}}(\text{ergs s}^{-1}) < 10^{45}$ ) meet the power-law criterion, suggesting that a significant number of luminous, heavily obscured AGN are yet to be identified. Furthermore, the infrared-excess criteria discussed in Chapter 4 primarily select moder-

ate luminosity AGN that lie at  $z \sim 2$ , and are insensitive to lower-redshift obscured AGN. Future observatories such as *Herschel*, JWST, and ALMA are therefore likely to identify additional members of this missing population of obscured AGN.

The infrared detection of AGN would also benefit from a better understanding of the templates of high-redshift galaxies. In this work, we used the templates of a relatively small number of local LIRGs and ULIRGs. While our tests indicate that these templates trace quite well the general behavior of galaxies at high- $z$ , they do not encapsulate the full range of SED behavior at high-redshift. Similarly, a better understanding of the SEDs of heavily obscured AGN will aid their discovery and study in the distant universe. An effort to characterize the infrared properties of local Compton-thick AGN is already underway (J. Rigby et al., in preparation), and will likely guide future studies.

#### 5.4 The Role of Obscured AGN in Galaxy Formation and Evolution

In addition to constraining the accretion history of the universe, the detection and study of obscured AGN has direct implications for models of galaxy formation and evolution. Ever since the discovery of the  $M_{BH}/\sigma$  relationship (Ferrarese & Merritt 2000, Gebhardt et al. 2000), we have known that black hole and galaxy growth are fundamentally connected. While many scenarios have been suggested to explain this correlation, the currently favored explanation is one in which the formation of both the galaxy bulge and the SMBH are driven by a major merger (e.g., Sanders et al. 1988, Hopkins et al. 2008). As the galaxies collide, gas driven to the center triggers both ULIRG-level starburst activity and *heavily obscured yet rapid black hole accretion*. Eventually, the reservoir of gas is largely consumed, and feedback from the active galaxy and supernovae drives

the remaining gas outwards. Only after the gas has dispersed is an unobscured optically-bright quasar visible.

In this model, heavy obscuration is due not to the torus, but to large-scale gas inflows. While this major-merger scenario does not appear to dominate AGN growth in the local ( $z < 1$ ) universe (e.g., Kauffmann et al. 2003), or the growth of Seyfert-luminosity AGN at high redshift (Grogin et al. 2005), it may be the dominant means of evolution for luminous massive galaxies at high-redshift. In order to test this hypothesis, one must therefore define a sample of high-redshift ( $z \sim 2$ ), high-luminosity ( $L_x > 10^{44}$ ) ergs s<sup>-1</sup>, and heavily obscured AGN. Not only does the intrinsic obscuration serve as a coronagraph that blocks out the bright optical emission from the central engine, but it is predicted to be most prevalent during the final merger stages, when merger characteristics should be easily identifiable.

The luminous, high-redshift, and heavily obscured power-law galaxies discussed in Chapters 3 and 4 therefore provide the best possible sample with which to test the major-merger hypothesis. I therefore propose a morphological study of power-law AGN in the GOODS and COSMOS fields. While GOODS has the advantage of ultra-deep 2 Ms X-ray coverage, it covers only a small region of the sky ( $\sim 0.1$  sq. degrees). The AGN number counts are therefore dominated by low-luminosity sources. By supplementing the GOODS sample with power-law AGN from the 2 sq. degree COSMOS field, which has full XMM-Newton coverage and deep 200 ks *Chandra* coverage of 0.8 sq. degrees, I will be able to construct for the first time a statistically significant sample of high-luminosity, high-redshift, and heavily-obscured AGN.

Both GOODS and COSMOS have deep ( $I < 27.1$ ) ACS coverage, and it is from these data that I will calculate asymmetry and concentration indices. The

morphologies of the brighter sources will also be studied using the Gini and  $M_{20}$  indicators. In addition to testing for signs of merger activity in these luminous obscured AGN, I will compare the results to a control sample of inactive galaxies with similar redshifts and magnitudes, as well as the less luminous AGN that have been the focus of previous studies. Finally, I will use deconvolved images of nearby interacting galaxies to quantify the success of the asymmetry and concentration indices in identifying merger features in high-redshift galaxies. This program, which will expand on the work described in this thesis, will provide an important test of the proposed mechanism for the co-evolution of galaxies and their SMBHs.

## APPENDIX A

## STAR-FORMING TEMPLATES

To understand the performance of our power-law AGN selection at high redshift and high luminosity, it is necessary to test it with template spectral energy distributions of appropriately luminous infrared galaxies. It has recently become possible to construct accurate templates in the critical 0.8 to 10  $\mu\text{m}$  range using a combination of Spitzer data, 2MASS total galaxy measurements, and ground-based spectroscopy in the 3 - 4  $\mu\text{m}$  range. We used these data sources to build templates for 3 ultra-luminous infrared galaxies. Arp 220 and IRAS 17208-0014 are both strongly dominated by star formation, whereas Mrk 273 appears to be powered by a mixture of star formation and an obscured AGN (e.g., Ptak et al. 2003; Farrah et al. 2003).

The references in Table A1 provide total-galaxy flux densities in the optical, near infrared, and at 3.6 and 4.5  $\mu\text{m}$ . We derived the near infrared stellar continuum starting from the stellar spectra of Strecker et al. (1979). They have the advantage of being consistently calibrated, are not affected by terrestrial atmospheric absorption, and they extend to 5.5  $\mu\text{m}$ . Specifically, we used the spectrum of  $\beta$  And for the near infrared stellar continuum, since its CO absorption approximately matches that of actively star forming galaxies. At wavelengths shortward of 1.2  $\mu\text{m}$ , our starting point was the spectral energy distribution of Arp 220 from Silva et al. (1998). For each galaxy, we joined these two spectra at 1.2  $\mu\text{m}$  and then adjusted the normalization and reddening to give a good overall fit through the photometry (UBVR as available plus JHK). The resulting spectrum was taken as the stellar photospheric part of the template (since we need a template valid up to  $z = 3$  in the IRAC 3.6  $\mu\text{m}$  band, the behavior at wavelengths shortward of 0.8  $\mu\text{m}$

Table A1. Input Data for Templates

Galaxy	UBVR	JHK	3 – 4 $\mu\text{m}$ spectrum	3.6, 4.5 $\mu\text{m}$	6 – 15 $\mu\text{m}$ spectrum	Other
Arp 220	1	4	5	7; 54.2, 46.6 mJy	9	12, 13
IRAS 17208-0014	2	4	6	8; 17.9, 17.3 mJy	10	14
Mrk 273	3	4	5	7; 27.6, 38.2 mJy	11	15

References. — (1) Frueh et al. 1996; (2) Duc, Mirabel, & Maza 1997; (3) Surace, Sanders, & Evans 2000; (4) 2MASS via NED; (5) Imanishi, Dudley, & Maloney 2006; (6) Imanishi 2006; (7) Spitzer PID 32, extraction aperture diameter of 90'' for Arp 220 and 50'' for Mrk 273; (8) Spitzer PID 3672, extraction aperture 30'' in diameter; (9) Armus et al. 2007; (10) Rigopoulou et al. 1999; (11) Higdon et al. 2006; (12) Klaas et al. 1997; (13) Rieke et al. 1985; (14) Scoville et al. 2000; (15) Rieke 1978

is unimportant). From Goldader et al. (1995), all three galaxies have strong CO stellar absorption features (bandhead at rest 2.3  $\mu\text{m}$ ), so the photospheric spectrum is not significantly diluted by other sources at least to 2.4  $\mu\text{m}$ . Therefore, we use it to define the template from 0.8 to 2.4  $\mu\text{m}$ .

For wavelengths longer than about 6  $\mu\text{m}$ , the templates are based on the spectra listed in Table A1. Because the infrared activity is generally concentrated in the nuclei, and the beams used for these spectra are relatively large, we made no corrections for extended emission. To bridge from 2.4 to 6  $\mu\text{m}$ , we proceeded as follows. The IRAC photometry at 3.6 and 4.5  $\mu\text{m}$  matches the apertures for the 2MASS total galaxy measurements, so it defines the overall output across the bridge region. The spectrum of M82 (Stürm et al. 2000) indicates that we should expect no strong spectral features between 4 and 6  $\mu\text{m}$  (other than Br  $\alpha$ , which should have small equivalent width). To fold in the 3 - 4  $\mu\text{m}$  region, we used

Table A2. Templates

Arp 200		IRAS 17208-0014		Mrk 273	
$\lambda(\mu\text{m})$	$f_\nu(\text{Jy})$	$\lambda(\mu\text{m})$	$f_\nu(\text{Jy})$	$\lambda(\mu\text{m})$	$f_\nu(\text{Jy})$
1.6572E-02	1.2100E-07	1.6177E-02	1.8200E-09	1.6256E-02	4.7100E-08
1.8124E-02	1.7100E-07	1.7693E-02	2.7100E-09	1.7778E-02	6.6600E-08
1.9823E-02	2.4300E-07	1.9352E-02	4.0800E-09	1.9445E-02	9.4900E-08
2.1690E-02	3.3200E-07	2.1174E-02	5.8800E-09	2.1276E-02	1.3000E-07
2.3723E-02	4.4200E-07	2.3159E-02	8.2500E-09	2.3271E-02	1.7200E-07

Note. — The complete version of this table is in the electronic edition of the Journal.  
The printed edition contains only a sample.

the spectra indicated in Table A1. We estimated the photospheric contribution to these spectra by applying corrections to our stellar template from small aperture photometry in the JHK region, or from small aperture photometry at L, or from both. This contribution was subtracted from the spectrum (using the  $\beta$  And template) and the remainder, representing the excess emission, was added to the total stellar template. This excess spectrum was scaled until the total template matched the photometric point at  $3.6 \mu\text{m}$  (the scaling factors required were small, between 1 and 1.5, indicating that the excess emission was nearly all within the  $\sim 1''$  slits used for the spectroscopy). We joined the longest wavelength point from these spectra to the shortest wavelength point in the  $6 - 15 \mu\text{m}$  spectra with a scaled and adjusted spectrum from M82 (Sturm et al. 2000). We found that adjusting the slope as a power law in wavelength and then normalizing gave a smooth connection that also was compatible with the photometry at  $4.5 \mu\text{m}$ . The templates are shown in Figure 20 and are given in Table A2.

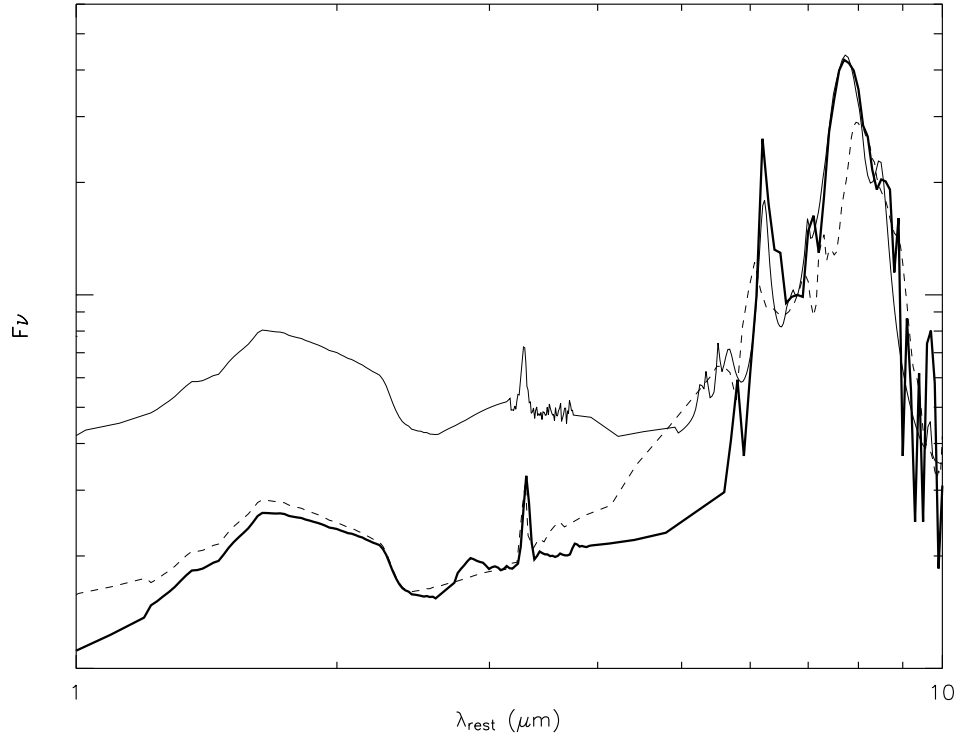


Figure A.1 SED templates for Arp 220 (light solid line), IRAS 17208-0014 (heavy solid line) and Mrk 273 (light dashed line) between 1 and 10  $\mu\text{m}$ . The templates have been normalized to the same value near 7  $\mu\text{m}$ . The influence of the AGN in Mrk 273 is apparent both in the reduced equivalent widths of the aromatic features and in the filling-in of the SED near 5  $\mu\text{m}$ .



## APPENDIX B

## PHOTOMETRIC REDSHIFT TECHNIQUE

We used two methods to determine photometric redshifts. The first utilizes the extensive high-resolution template set of Pérez-González et al. (2008), which was created by fitting stellar population synthesis and dust emission models to the  $\sim 1500$  galaxies in the CDF-N and CDF-S with secure spectroscopic redshifts. When applied to all spectroscopically-detected IRAC-selected galaxies in the GOODS-N and GOODS-S, this template library returns photometric redshifts with  $\Delta(z) < 0.1$  for 88% of the sources, and  $\Delta(z) < 0.2$  for 96%, where  $\Delta(z) = (z_p - z_s)/(1 + z_s)$  (Pérez-González et al. 2008). Because this method relies on star-forming templates, however, we do not expect it to provide equally reliable photometric redshifts for galaxies in which the stellar features are dominated by emission from an AGN.

Our second method is based on the chi-squared minimization routine HYPERZ (Bolzonella, Miralles, & Pelló 2000). With a suite of normal star-forming, LIRG/ULIRG, and AGN templates, we can better account for the range of sources expected in our  $24\ \mu\text{m}$  selected sample, albeit with a smaller template library. To create this library, we started with a sample of 10 star-forming templates and 8 AGN templates from Silva et al. (1998) and Polletta et al. (2007). The Polletta et al. AGN templates cover a range of intrinsic obscurations (Type 1 and Type 2) and luminosities (Sey/QSO). We then supplemented this sample with 10 empirical star-forming LIRG and ULIRG templates. The full template sample is listed in Table 1. The LIRG and ULIRG templates, described in detail in Rieke et al. (2008, in prep.), significantly improve upon previous semi-empirical templates by constraining the SEDs between 1 and  $6\ \mu\text{m}$  with 2MASS and IRAC photometry and

by basing the SEDs from 5 to 35  $\mu\text{m}$  on IRS spectra.

Using this template library, we ran HYPERZ on all robust optical–MIR data for the IR-normal and color-selected galaxies. For the PLGs, we removed all photometry longward of 3.6  $\mu\text{m}$  (IRAC channel 1). Including the full *Spitzer* photometry for PLGs provided little or no additional constraint on potential redshifts, and limited severely the SEDs for which a good fit could be found. We allowed  $z$  to vary from 0 to 4 and  $A_v$  to vary from 0 to 1.2. While its shape is still relatively unconstrained, a number of studies have suggested that the extinction curve of AGN most closely resembles that of the SMC (e.g. Richards et al. 2003). We therefore assumed by default the SMC extinction curve of Bouchet et al. (1985) for the PLGs and color-selected galaxies. For the IR-normal galaxies, we assume the Calzetti (2000) extinction curve, as this curve was modeled to represent the extinction properties of starburst galaxies. To prevent unrealistic redshift solutions, we applied the redshift- and model-dependent absolute magnitude cuts of Polletta et al. (2007). Finally, to increase the weight of the IRAC photometry, which solely defines the red slope of the stellar bump, we set the errors on the IRAC photometry to the measurement errors, as opposed to the total photometric errors. This procedure is acceptable because many types of photometric error will have similar effects on the four IRAC bands, so we are making use of the overall internal consistency expected for the data.

To improve the likelihood of obtaining a good fit for each source, we then varied a number of these assumptions, and examined by eye the resulting fits to choose the most convincing redshift solution. This visual inspection is an important characteristic of our work, and was made possible by the relatively small number of sources in our sample. First, each PLG and color-selected galaxy was fit by both the SMC and Calzetti extinction laws. In most cases, the resulting

redshift fits and solutions varied only slightly (in which case we chose the SMC-derived fit), but for some galaxies, one of the two extinction laws provided a clearly superior fit as determined by a visual inspection. Second, if the absolute magnitude of the resulting best-fit template did not meet the redshift-dependent absolute magnitude cut of Polletta et al. (2007), we allowed  $M_B$  to vary between -23.7 to -17 for star-forming templates and -28.8 to -19 for AGN templates (e.g. Polletta et al. 2007). Third, we allowed the IRAC errors to increase to their total estimated values by adding a 10% error to the flux; in only 4 cases did this lead to a better fit. Finally, for the PLGs, we explored fits that did not include the  $3.6\ \mu\text{m}$  IRAC channel; only 2 sources benefited from this change.

The final step in our redshift estimation was an independent review of the redshifts by two authors. By examining by eye the resulting redshift fits, we chose for each PLG and color-selected galaxy the best HYPERZ redshift. We then compared this to the redshift fit from the Pérez-González et al. (2008) technique, and replaced the former with the latter if it clearly provided a better fit. For the IR-normal galaxies, we use the Pérez-González et al. (2008) redshifts by default, as these are optimized for normal galaxies. We do, however, remove unconvincing redshift fits, and substitute a solid HYPERZ redshift if available. For all sources, we only assign a photometric redshift if a convincing fit exists. We rejected 76 sources with poor data or other problems that compromise our redshift determination. The photometric redshifts classified as being of high quality are summarized in Table 1 and shown in Figure 1.

Table B1. Photometric Redshift Templates

Template	Type	Ref
Ell2	2 Gyr old elliptical	(2)
Ell5	5 Gyr old elliptical	(2)
Ell13	13 Gyr old elliptical	(2)
S0	Spiral 0	(1)
Sa	Spiral a	(1)
Sb	Spiral b	(1)
Sc	Spiral c	(1)
Sd	Spiral d	(1)
Sdm	Spiral dm	(1)
M82	Starburst	(1)
NGC 6090	LIRG/Starburst	(1)
ESO320-G030	LIRG/Starburst	(3)
NGC 1614	LIRG/Starburst	(3)
NGC 2639	LIRG/Starburst	(3)
NGC 3256	LIRG/Starburst	(3)
NGC 4194	LIRG/Starburst	(3)
Arp 220	ULIRG/Starburst	(1)
Arp 220	ULIRG/Starburst	(3)
IRAS 12112+0305	ULIRG/Starburst	(3)
IRAS 14348-1447	ULIRG/Starburst	(3)
IRAS 17208-0014	ULIRG/Starburst	(3)
IRAS 22491-1808	ULIRG/Starburst	(3)
IRAS 22491-1808	ULIRG/Starburst	(1)
Mrk 231	ULIRG/Seyfert 1	(1)
Sey1.8	Seyfert 1.8	(1)

Table B1—Continued

Template	Type	Ref
TQSO1	Type 1 QSO	(1)
Sey2	Seyfert 2	(1)
NGC 6240	Starburst/Seyfert 2	(1)
IRAS 19254-7245	ULIRG/Seyfert 2	(1)
IRAS 20551-4250	ULIRG/Buried AGN	(1)
QSO2	Type 2 QSO	(1)

References. — (1) Polletta et al. (2007), (2) Silva et al. (1998), (3) Rieke et al. (2008)

## APPENDIX C

## REDSHIFT-DEPENDENT COLOR SELECTION

C.0.0.2  $z = 0 - 0.25$ 

The lowest redshift bin contains no PLGs and 2 color-selected galaxies, both of which are detected in the X-ray, but with low observed X-ray luminosities of  $\log L_x(\text{ergs s}^{-1}) = 41.3$  and  $\log L_x(\text{ergs s}^{-1}) = 40.9$ , indicative of powerful starbursts or very low-luminosity AGN.

C.0.0.3  $z = 0.25 - 0.75$ 

The second redshift bin contains 3 PLGs, 27 Lacy-selected galaxies, and 4 Stern-selected galaxies. Of the Lacy and Stern-selected sources, only 41% and 25% are detected in the X-ray, respectively, compared to 100% of the PLGs. The average observed 0.5-8 keV X-ray luminosity of the X-ray-detected color-selected galaxies,  $\log L_x(\text{ergs s}^{-1}) = 43.0$ , is consistent with AGN activity, but is an order of magnitude less than that of the PLGs in this redshift bin,  $\log L_x(\text{ergs s}^{-1}) = 44.1$ . This is not surprising, as power-law selection preferentially identifies the most luminous AGN where the emission from the central engine is able to overpower that of the host galaxy (Donley et al. 2007). The AGN that lie amongst the color-selected sample clearly represent a less luminous AGN population than those selected via the PLG criteria. Furthermore, of the 27 Lacy-selected (and 4 Stern-selected) galaxies, only 11 (2) lie outside the  $1\sigma$  star-forming contours in their respective color-space, with the number dropping to 3 and 1 (2 and 0) at  $2\sigma$  and  $3\sigma$ . This suggests that the majority of the color-selected sources in this redshift bin have infrared colors indicative of IR-normal galaxies. While all of the PLGs lie outside even the  $3\sigma$  contours in the Lacy color-space, they lie inside the contours

in Stern-space, due primarily to the Sdm template of Polletta et al. (2007), whose strong  $3.3 \mu\text{m}$  aromatic feature passes through the  $4.5 \mu\text{m}$  IRAC band at  $z \sim 0.4$ , causing the template to enter the Stern AGN selection region at  $z = 0.23 - 0.51$ . Of the 2 PLGs whose colors overlap with this template, both have spectroscopic redshifts of  $z > 0.67$ , and would therefore be ‘safe’ if we considered smaller redshift bins. Removing this template, however, would have no effect on the number of Lacy or Stern-selected sources that lie outside the  $1\sigma$  contours.

#### C.0.0.4 $z = 0.75 - 1.25$

We find a higher proportion of secure color-selected galaxies in the  $z = 0.75 - 1.25$  bin, with 10/12 of the Lacy-selected sources and 6/13 of the Stern-selected sources lying outside the  $1\sigma$  star-forming contours. This is not surprising, as it is at  $z \sim 1$  that the star-forming contours are best separated from the AGN selection region. If we extend our test to  $2\sigma$ , however, the numbers drop significantly, to 5/12 and 1/13. The majority of the Stern-selected galaxies in this redshift bin fill the lower-left corner of the AGN selection region, the region populated by the Stern-only sources whose Lacy colors place them in the star-forming locus of color-space. These star-forming galaxies are likely responsible for the fact that this is the only redshift bin in which the Stern-selected sources outnumber the Lacy-selected sources. Of the 5 PLGs in this redshift bin, all lie outside the  $1\sigma$  star-forming contours in both Lacy and Stern color-space, and while only 3 lie outside of the  $2\sigma$  contours in Stern color-space, all lie outside of the  $2\sigma$  and  $3\sigma$  colors in Lacy color-space.

#### C.0.0.5 $z = 1.25 - 1.75$

The number of color-selected galaxies rises significantly in the  $z = 1.25 - 1.75$  redshift bin. The fraction of potential IR-selected AGN, however, is by far the lowest

at these redshifts, with only 6/38 Lacy-selected sources and 3/31 Stern-selected sources falling outside the  $1\sigma$  star-forming contours. In addition, only 3/38 Lacy sources and 4/31 Stern sources have X-ray counterparts, further suggesting that nearly all of the color-selected sources at this redshift are star-forming galaxies, and not AGN. In contrast, the 2 PLGs found in this redshift bin fall outside of the  $1\sigma$  contours in both the Lacy and Stern plots, and both are detected in the X-ray.

#### C.0.0.6 $z = 1.75 - 2.25$

The largest number of Lacy-selected sources, 77, is found in the  $z = 1.75 - 2.25$  bin. In addition, an extraordinarily high fraction, 50/77, lie outside of the  $1\sigma$  star-forming contours, a surprising fact given the X-ray detection fraction of only 9%. Have we discovered a significant population of  $z \sim 2$  obscured AGN similar to those claimed by Daddi et al. (2007), or is there another explanation for this population?

The AGN contours (shown in green) provide a better match to the IR colors of these color-selected galaxies than do the star-forming templates (shown in blue). At this redshift, the primary difference between the IRAC regions of the star-forming and the low-luminosity AGN templates is the strength of the CO index, which is stronger in the star-forming galaxies than in the AGN. The MIPS-selected sources therefore may have smaller CO indices than those of our local templates. One explanation for this offset is that an underlying AGN continuum has diluted this feature. A lower CO index, however, could also be attributed to evolution in the metallicity of the LIRGS/ULIRGS. At 1/3 solar metallicity, the CO index drops by 4-6 percentage points (McGregor 1987), causing the contours to shift upwards in Lacy color space by  $\sim 0.08$ . While this lessens this offset between the colors of star-forming contours and the observed galaxies, it cannot fully account for the observed discrepancy. Thus, if a change in the CO index is



invoked for the offset, it is likely that AGN continua are also present.

However, other possible explanations exist. If we incorporate into the contours a 10% error in  $(1+z)$  (recall that the measured  $\sigma$  for our photometric redshift fits was 0.15 and that 11% of the sources in our spectroscopic redshift sample have photometric errors  $> 10\%$ ) the resulting contours are far-better matched to the IR-colors of the color-selected galaxies. Of the Lacy- and Stern-selected galaxies, only 17% and 9% now lie outside of the  $1\sigma$  contours, with the numbers dropping to 8% and 0% at  $2\sigma$  and 4% and 0% at  $3\sigma$ , respectively.

The templates with which the photometric redshifts were best fit can provide further insight into the sources in this redshift bin. Of the 90 non-PLGs in the  $z \sim 2$  bin, 75 (86%) are best fit by a star-forming ULIRG template, 9 (10%) are best fit by a ULIRG/hidden AGN template, 1 (1%) is best-fit by a type 2 AGN template, and 1 (1%) is best fit by a type 1 AGN template. In contrast, all of the PLGs in this redshift range are best-fit by a type 2 AGN template. Therefore, while we can not rule out the possibility that we have detected a sample of high-redshift, heavily obscured AGN, the extremely low X-ray detection fraction of 9%, the much improved fit of the contours for which 10% errors in the photometric redshifts were included, and the overwhelming fraction of sources for which a purely star-forming ULIRG provided the best fit to the SED suggest that it is more likely that the vast majority of color-selected galaxies in this redshift bin are star-forming galaxies, not AGN.

#### C.0.0.7 $z > 2.25$

The number of color-selected galaxies in the remaining two redshift bins is relatively low: 18 Lacy-selected sources and 5 Stern selected sources. Of these, a large fraction (61% and 80%, respectively) lie outside of the star-forming contours, which cover a comparatively small portion of the color-space. At  $2\sigma$  and

$3\sigma$ , the fractions drop to 39% and 11% (Lacy) and 20% and 0% (Stern). At these redshifts, the X-ray detection fractions of both the color-selected sources and the PLGs are low: 17% for the Lacy sources, 40% for the Stern sources, and 23% for the PLGs. At  $z = 2.5$ , an unobscured AGN with  $\Gamma = 2$  requires a rest-frame 0.5-8 keV luminosity of  $\log L_x(\text{ergs s}^{-1}) = 42.8$  to meet the flux limit within  $1'$  of the CDF-S aimpoint. At  $z = 3$ , the required value rises to  $\log L_x(\text{ergs s}^{-1}) = 43.0$ , suggesting that if these sources are AGN, they must have low luminosities, or high obscuring columns.

#### C.0.0.8 $z = \text{unknown}$

Not all sources in our sample have redshift estimates. The redshift completeness for the Lacy and Stern color-selected samples is high (93% and 90%, respectively), but we have high-quality redshifts for only 49% of the PLGs. The difficulty in fitting redshifts to these sources stems largely from their faint fluxes: the power-law (color-selected) galaxies without redshifts are significantly fainter,  $V = 26.2$  (25.3), than those with redshift estimates,  $V = 25.4$  ( $V = 24.9$ ), suggesting that these sources may preferentially lie at high redshift.

The last panels of Figures 5 and 6 show the IRAC colors of sources without redshift estimates. Overplotted are the star-forming contours for  $z = 0 - 4$ . Of the sources without redshifts, all but 1 lie inside the Lacy selection region and all but 9 lie inside the Stern selection region. This is not surprising, as sources with non-stellar continua are the hardest sources to fit. Of the 13 Lacy-selected sources, 5 lie outside the  $1\sigma$  star-forming contours, and 2 have X-ray counterparts. Of the 26 PLGs, 11 lie outside the  $1\sigma$  star-forming contours, and 6 are X-ray-detected. There is a noticeable concentration of X-ray non-detected PLGs towards the red end of the power-law locus. These sources are discussed in more detail in §6.

## REFERENCES

- Akiyama, M., Ueda, Y., Ohta, K., Takahashi, T., & Yamada, T. 2003, *ApJS*, 148, 275
- Akylas, A., Georgantopoulos, I., Georgakakis, A., Kitsionas, S., & Hatziminaoglou, E. 2006, *A&A*, 459, 693
- Alexander, D. M., Aussel, H., Bauer, F. E., Brandt, W. N., Hornschemeier, A. E., Vignali, C., Garmire, G. P., & Schneider, D. P. 2002a, *ApJL*, 568, L85
- Alexander, D. M., Vignali, C., Bauer, F. E., Brandt, W. N., Hornschemeier, A. E., Garmire, G. P., & Schneider, D. P. 2002b, *AJ*, 123, 1149
- Alexander, D. M., et al. 2003, *AJ*, 126, 539
- Alexander, D. M., Smail, I., Bauer, F. E., Chapman, S. C., Blain, A. W., Brandt, W. N., & Ivison, R. J. 2005, *Nature*, 434, 738
- Alexander, D. M., et al. 2008, *ArXiv e-prints*, 803, arXiv:0803.0636
- Alonso-Herrero, A., et al. 2004, *ApJS*, 154, 155
- Alonso-Herrero, A., et al. 2006, *ApJ*, 640, 167
- Appleton, P. N., et al. 2004, *ApJS*, 154, 147
- Armus, L., et al. 2007, *ApJ*, 656, 148
- Arnouts, S., Vandame, B., Benoist, C., Groenewegen, M. A. T., da Costa, L., Schirmer, M., Mignani, R. P., & Slijkhuis, R. 2002, *VizieR Online Data Catalog*, 337, 90740
- Ballantyne, D. R., Everett, J. E., & Murray, N. 2006, *ApJ*, 639, 740

- Barger, A. J., Cowie, L. L., & Richards, E. A. 2000, *AJ*, 119, 2092
- Barger, A. J., Cowie, L. L., Bautz, M. W., Brandt, W. N., Garmire, G. P., Hornschemeier, A. E., Ivison, R. J., & Owen, F. N. 2001, *AJ*, 122, 2177
- Barger, A. J., Cowie, L. L., Brandt, W. N., Capak, P., Garmire, G. P., Hornschemeier, A. E., Steffen, A. T., & Wehner, E. H. 2002, *AJ*, 124, 1839
- Barger, A. J., et al. 2003, *AJ*, 126, 632
- Barger, A. J., Cowie, L. L., Mushotzky, R. F., Yang, Y., Wang, W.-H., Steffen, A. T., & Capak, P. 2005, *AJ*, 129, 578
- Barmby, P., et al. 2006, *ApJ*, 642, 126
- Bauer, F. E., Alexander, D. M., Brandt, W. N., Schneider, D. P., Treister, E., Hornschemeier, A. E., & Garmire, G. P. 2004, *AJ*, 128, 2048
- Bell, E. F. 2003, *ApJ*, 586, 794
- Bertin, E., & Arnouts, S. 1996, *A&AS*, 117, 393
- Bevington, P. R., & Robinson, D. K. 2003, *Data reduction and error analysis for the physical sciences*, 3rd ed., by Philip R. Bevington, and Keith D. Robinson. Boston, MA: McGraw-Hill, ISBN 0-07-247227-8, 2003.
- Bohlin, R. C., Savage, B. D., & Drake, J. F. 1978, *ApJ*, 224, 132
- Bolzonella, M., Miralles, J.-M., & Pelló, R. 2000, *A&A*, 363, 476
- Bouchet, P., Lequeux, J., Maurice, E., Prevot, L., & Prevot-Burnichon, M. L. 1985, *A&A*, 149, 330
- Brand, K., et al. 2006, *ApJ*, 644, 143

- Brandl, B. R., et al. 2006, *ApJ*, 653, 1129
- Brandt, W. N., Hornschmeier, A. E., Schneider, D. P., Alexander, D. M., Bauer, F. E., Garmire, G. P., & Vignali, C. 2001, *ApJ*, 558, L5
- Brandt, W. N., & Hasinger, G. 2005, *ARA&A*, 43, 827
- Bressan, A., Silva, L., & Granato, G. L. 2002, *A&A*, 392, 377
- Brusa, M., et al. 2003, *A&A*, 409, 65
- Brusa, M., et al. 2005, *A&A*, 432, 69
- Buat, V., et al. 2005, *ApJL*, 619, L51
- Calzetti, D., Armus, L., Bohlin, R. C., Kinney, A. L., Koornneef, J., & Storchi-Bergmann, T. 2000, *ApJ*, 533, 682
- Calzetti, D., et al. 2007, *ApJ*, 666, 870
- Capak, P., et al. 2004, *AJ*, 127, 180
- Caputi, K. I., et al. 2006, *ApJ*, 637, 727
- Cardamone, C. N., et al. 2008, *ApJ*, 680, 130
- Chapman, S. C., Blain, A. W., Smail, I., & Ivison, R. J. 2005, *ApJ*, 622, 772
- Churazov, E., et al. 2007, *A&A*, 467, 529
- Comastri, A., Fiore, F., Vignali, C., Matt, G., Perola, G. C., & La Franca, F. 2001, *MNRAS*, 327, 781
- Condon, J. J., Cotton, W. D., & Broderick, J. J. 2002, *AJ*, 124, 675
- Cowie, L. L., Barger, A. J., Hu, E. M., Capak, P., & Songaila, A. 2004, *AJ*, 127, 3137

- Daddi, E., et al. 2007a, *ApJ*, 670, 156
- Daddi, E., et al. 2007b, *ApJ*, 670, 173
- Dale, D. A., & Helou, G. 2002, *ApJ*, 576, 159
- Dawson, S., McCrady, N., Stern, D., Eckart, M. E., Spinrad, H., Liu, M. C., & Graham, J. R. 2003, *AJ*, 125, 1236
- Desai, V., et al. 2008, *ApJ*, 679, 1204
- Devriendt, J. E. G., Guiderdoni, B., & Sadat, R. 1999, *A&A*, 350, 381
- Dey, A., et al. 2008, *ApJ*, 677, 943
- Doherty, M., Bunker, A. J., Ellis, R. S., & McCarthy, P. J. 2005, *MNRAS*, 361, 525
- Donley, J. L., Rieke, G. H., Rigby, J. R., & Pérez-González, P. G. 2005, *ApJ*, 634, 169
- Donley, J. L., Rieke, G. H., Pérez-González, P. G., Rigby, J. R., & Alonso-Herrero, A. 2007, *ApJ*, 660, 167
- Drake, C. L. McGregor, P. J., Dopita, M. A., & van Breugel, W. J. M. 2003, *AJ*, 126, 2237
- Duc, P.-A., Mirabel, I. F., and Maza, J. 1997, *A&AS*, 124, 533
- Engelbracht, C. W., Gordon, K. D., Rieke, G. H., Werner, M. W., Dale, D. A., & Latter, W. B. 2005, *ApJL*, 628, L29
- Elvis, M., et al. 1994, *ApJS*, 95, 1
- Farrah, D., Alfonso, J., Efstathiou, A., Rowan-Robinson, M., Fox, M., & Clements, D. 2003, *MNRAS*, 343, 585

- Fazio, G. G., et al. 2004, *ApJS*, 154, 10
- Ferrarese, L., & Merritt, D. 2000, *ApJL*, 539, L9
- Fiore, F., et al. 2008, *ApJ*, 672, 94
- Franceschini, A., et al. 2003, *MNRAS*, 343, 1181
- Franceschini, A., et al. 2005, *AJ*, 129, 2074
- Freeman, P. E., Kashyap, V., Rosner, R., & Lamb, D. Q. 2002, *ApJS*, 138, 185
- Frueh, M. L., Corwin, H. G. Jr., de Vaucouleurs, G., & Buta, R. 1996, *AJ*, 111, 722
- Gambill, J. K., Sambruna, R. M., Chartas, G., Cheung, C. C., Maraschi, L., Tavecchio, F., Urry, C. M., & Pesce, J. E. 2003, *A&A*, 401, 505
- Gebhardt, K., et al. 2000, *ApJL*, 539, L13
- Genzel, R., et al. 1998, *ApJ*, 498, 579
- George, I. M., Turner, T. J., Yaqoob, T., Netzer, H., Laor, A., Mushotzky, R. F., Nandra, K., & Takahashi, T. 2000, *ApJ*, 531, 52
- Georgakakis, A., et al. 2006, *MNRAS*, 371, 221
- Giacconi, R., et al. 2001, *ApJ*, 551, 624
- Giacconi, R., et al. 2002, *ApJS*, 139, 369
- Giavalisco, M., et al. 2004, *ApJL*, 600, L93
- Gilli, R., Salvati, M., & Hasinger, G. 2001, *A&A*, 366, 407
- Gilli, R., et al. 2003, *ApJ*, 592, 721

- Gilli, R. 2004, *Advances in Space Research*, 34, 2470
- Gilli, R., Comastri, A., & Hasinger, G. 2007, *A&A*, 463, 79
- Goldader, J. D., Joseph, R. D., Doyon, Rene, & Sanders, D. B. 1995, *ApJ*, 444, 97
- Goldader, J. D., Meurer, G., Heckman, T. M., Seibert, M., Sanders, D. B., Calzetti, D., & Steidel, C. C. 2002, *ApJ*, 568, 651
- Gordon, K. D. et al. 2004b, *ApJS*, 154, 215
- Gordon, K. D., et al. 2004a, *Proc. SPIE*, 5487, 177
- Gordon, K. D., et al. 2005, *PASP*, 117, 503
- Granato, G. L., Danese, L., & Franceschini, A. 1997, *ApJ*, 486, 147
- Grazian, A., et al. 2006, *A&A*, 449, 951
- Grogin, N. A., et al. 2005, *ApJL*, 627, L97
- Hao, L., et al. 2005, *ApJL*, 625, L75
- Hardcastle, M. J. & Worrall, D. M. 1999, *MNRAS*, 309, 969
- Hasinger, G. 2004, *Nuclear Physics B Proceedings Supplements*, 132, 86
- Hatziminaoglou, E., et al. 2005, *AJ*, 129, 1198
- Helou, G., Soifer, B. T., & Rowan-Robinson, M. 1985, *ApJL*, 298, L7
- Higdon, S. J. U., Armus, L., Higdon, J. L., Soifer, B. T., & Spoon, H. W. W., 2006, *ApJ*, in press, astro-ph/0605359
- Hopkins, P. F., Hernquist, L., Cox, T. J., Di Matteo, T., Robertson, B., & Springel, V. 2006, *ApJS*, 163, 1



- Hopkins, P. F., Hernquist, L., Cox, T. J., & Kereš, D. 2008, *ApJS*, 175, 356
- Hornschemeier, A. E., et al. 2001, *ApJ*, 554, 742
- Hornschemeier, A. E., et al. 2003, *AJ*, 126, 575
- Houck, J. R. et al. 2004, *ApJS*, 154, 211
- Houck, J. R., et al. 2005, *ApJL*, 622, L105
- Huang, J.-S., et al. 2004, *ApJS*, 154, 44
- Imanishi, M. 2006, *AJ*, 131, 2406
- Imanishi, M., Dudley, C. C., & Maloney, P. R. 2006, *ApJ*, 637, 114
- Ivezić, Ž., et al. 2002, *AJ*, 124, 2364
- Iverson, R. J., et al. 2004, *ApJS*, 154, 124
- Iwasawa, K., Matt, G., Guainazzi, M., & Fabian, A. C. 2001, *MNRAS*, 326, 894
- Johansson, P. H., Väisänen, P., & Vaccari, M. 2004, *A&A*, 427, 795
- Kauffmann, G., et al. 2003, *MNRAS*, 346, 1055
- Kellermann, K. I., Sramek, R., Schmidt, M., Shaffer, D. B., & Green, R. 1989, *AJ*, 98, 1195
- Kennicutt, R. C., Jr. 1998, *ApJ*, 498, 541
- Klaas, U., Haas, M., Heinrichsen, I., & Schulz, B. 1997, *å*, 325, L21
- Klaas, U., et al. 2001, *A&A*, 379, 823
- Klesman, A., & Sarajedini, V. 2007, *ApJ*, 665, 225

- Koekemoer, A. M., et al. 2004, *ApJL*, 600, L123
- Kron, R. G. 1980, *ApJS*, 43, 305
- Kuraszkiewicz, J. et al. 2007, *ApJ*, submitted
- La Franca, F., et al. 2005, *ApJ*, 635, 864
- Lacy, M., et al. 2004, *ApJS*, 154, 166
- Lacy, M., Canalizo, G., Rawlings, S., Sajina, A., Storrie-Lombardi, L., Armus, L., Marleau, F. R., & Muzzin, A. 2005a, *Memorie della Societa Astronomica Italiana*, 76, 154
- Lacy, M., et al. 2005b, *ApJS*, 161, 41
- Lacy, M., Petric, A. O., Sajina, A., Canalizo, G., Storrie-Lombardi, L. J., Armus, L., Fadda, D., & Marleau, F. R. 2007, *AJ*, 133, 186
- Lawrence, A. 1991, *MNRAS*, 252, 586
- Lawson, A. J. & Turner, M. J. L. 1997, *MNRAS*, 288, 920
- Le Fèvre, O., et al. 2004, *A&A*, 428, 1043
- Leipski, C., et al. 2005, *A&A*, 440, L5
- Lonsdale, C. J., et al. 2003, *PASP*, 115, 897
- Maccacaro, T., Perola, G. C., & Elvis, M. 1982, *ApJ*, 257, 47
- Maccacaro, T., Gioia, I. M., Wolter, A., Zamorani, G., & Stocke, J. T. 1988, *ApJ*, 326, 680
- Magdziarz, P. & Zdziarski, A. A. 1995, *MNRAS*, 273, 837

- Maiolino, R., & Rieke, G. H. 1995, *ApJ*, 454, 95
- Maiolino, R., Salvati, M., Bassani, L., Dadina, M., della Ceca, R., Matt, G., Risaliti, G., & Zamorani, G. 1998, *A&A*, 338, 781
- Maiolino, R., Marconi, A., Salvati, M., Risaliti, G., Severgnini, P., Oliva, E., La Franca, F., & Vanzi, L. 2001a, *A&A*, 365, 28
- Maiolino, R., Marconi, A., & Oliva, E. 2001b, *A&A*, 365, 37
- Marble, A. R., Hines, D. C., Schmidt, G. D., Smith, P. S., Surace, J. A., Armus, L., Cutri, R. M., & Nelson, B. O. 2003, *ApJ*, 590, 707
- Martínez-Sansigre, A., Rawlings, S., Lacy, M., Fadda, D., Marleau, F. R., Simpson, C., Willott, C. J., & Jarvis, M. J. 2005, *Nature*, 436, 666
- Martínez-Sansigre, A., Rawlings, S., Lacy, M., Fadda, D., Jarvis, M. J., Marleau, F. R., Simpson, C., & Willott, C. J. 2006, *MNRAS*, 370, 1479
- Marzke, R., et al. 1999, Photometric Redshifts and the Detection of High Redshift Galaxies, 191, 148
- McGregor, P. J. 1987, *ApJ*, 312, 195
- McLeod, K. K., & Rieke, G. H. 1994, *ApJ*, 431, 137
- Mignoli, M., et al. 2005, *A&A*, 437, 883
- Miller, N. A. & Owen, F. N. 2001, *AJ*, 121, 1903
- Morrison, G., et al. 2006, ArXiv Astrophysics e-prints, arXiv:astro-ph/0603412
- Mushotzky, R. F., Cowie, L. L., Barger, A. J., & Arnaud, K. A. 2000, *Nature*, 404, 459

- Neugebauer, G., Oke, J. B., Becklin, E. E., & Matthews, K. 1979, *ApJ*, 230, 79
- Origlia, L., Moorwood, A. F. M., & Oliva, E. 1993, *A&A*, 280, 536
- Page, M. J., et al. 2003, *Astronomische Nachrichten*, 324, 101
- Papovich, C., et al. 2004, *ApJS*, 154, 70
- Pearson, C. 2005, *MNRAS*, 358, 1417
- Percival, W. J., Miller, L., McLure, R. J., & Dunlop, J. S. 2001, *MNRAS*, 322, 843
- Pérez-González, P. G., et al. 2005, *ApJ*, 630, 82
- Pérez-González, P. G., et al. 2008, *ApJ*, 675, 234
- Perola, G. C., et al. 2004, *A&A*, 421, 491
- Persic, M., & Rephaeli, Y. 2002, *A&A*, 382, 843
- Persic, M., Rephaeli, Y., Braito, V., Cappi, M., Della Ceca, R., Franceschini, A., & Gruber, D. E. 2004, *A&A*, 419, 849
- Polletta, M. d. C., et al. 2006, *ApJ*, 642, 673
- Polletta, M., et al. 2007, *ApJ*, 663, 81
- Polletta, M., Weedman, D., Hönig, S., Lonsdale, C. J., Smith, H. E., & Houck, J. 2008, *ApJ*, 675, 960
- Pozzi, F., et al. 2007, *A&A*, 468, 603
- Prevot, M. L., Lequeux, J., Prevot, L., Maurice, E., & Rocca-Volmerange, B. 1984, *A&A*, 132, 389

- Ptak, A., Heckman, T., Levenson, N. A., Weaver, K., & Strickland, D. 2003, *ApJ*, 592, 782
- Ranalli, P., Comastri, A., & Setti, G. 2003, *A&A*, 399, 39
- Reeves, J. N. & Turner, M. J. L. 2000, *MNRAS*, 316, 234
- Reichert, G. A., Mushotzky, R. F., Holt, S. S., & Petre, R. 1985, *ApJ*, 296, 69
- Richards, E. A., Kellermann, K. I., Fomalont, E. B., Windhorst, R. A., & Partridge, R. B. 1998, *AJ*, 116, 1039
- Richards, E. A. 2000, *ApJ*, 533, 611
- Richards, G. T., et al. 2003, *AJ*, 126, 1131
- Richards, G. T., et al. 2006, *ArXiv Astrophysics e-prints*, arXiv:astro-ph/0601558
- Rieke, G. H. 1978, *ApJ*, 226, 550
- Rieke, G. H., & Lebofsky, M. J. 1981, *ApJ*, 250, 87
- Rieke, G. H., & Lebofsky, M. J. 1985, *ApJ*, 288, 618
- Rieke, G. H., Cutri, R. M., Black, J. H., Kailey, W. F., McAlary, C. W., Lebofsky, M. J., & Elston, R. 1985, *ApJ*, 290, 116
- Rieke, G. H., et al. 2004, *ApJS*, 154, 25
- Rieke, G. H., et al. 2008, *ApJ*, submitted
- Rigby, J. R., et al. 2004, *ApJS*, 154, 160
- Rigby, J. R., Rieke, G. H., Pérez-González, P. G., Donley, J. L., Alonso-Herrero, A., Huang, J.-S., Barmby, P., & Fazio, G. G. 2005, *ApJ*, 627, 134

- Rigby, J. R., et al. 2008, *ApJ*, 675, 262
- Rigopoulou, D., Spoon, H. W. W., Genzel, R., Lutz, D., Moorwood, A. F. M., & Tran, Q. D. 1999, *AJ*, 118, 2625
- Risaliti, G., Maiolino, R., & Salvati, M. 1999, *ApJ*, 522, 157
- Risaliti, G., Elvis, M., Gilli, R., & Salvati, M., 2003, *ApJ*, 587, L9
- Risaliti, G., et al. 2006, *MNRAS*, 365, 303
- Sajina, A., Lacy, M., & Scott, D. 2005, *ApJ*, 621, 256
- Sambruna, R. M., Eracleous, M., & Mushotzky, R. F., 1999, *ApJ*, 526, 60
- Sanders, D. B., Soifer, B. T., Elias, J. H., Neugebauer, G., & Matthews, K. 1988, *ApJL*, 328, L35
- Sanders, D. B., Mazzarella, J. M., Kim, D.-C., Surace, J. A., & Soifer, B. T. 2003, *AJ*, 126, 1607
- Sarajedini, V. L. 2008, *Revista Mexicana de Astronomia y Astrofisica Conference Series*, 32, 34
- Scoville, N. Z., Evans, A. S., Thompson, R., Rieke, M., Hines, D. C., Low, F. J., Dinshaw, N., Surace, J. A., and Armus, L. 2000, *AJ*, 119, 991
- Seymour, N., et al. 2008, *MNRAS*, 386, 1695
- Shi, Y., et al. 2006, *ApJ*, 653, 127
- Silva, L., Granato, G. L., Bressan, A., & Danese, L. 1998, *ApJ*, 509, 103
- Spinoglio, L., & Malkan, M. A. 1989, *ApJ*, 342, 83

- Stark, A. A., Gammie, C. F., Wilson, R. W., Bally, J., Linke, R. A., Heiles, C., & Hurwitz, M. 1992, *ApJS*, 79, 77
- Steffen, A. T., Barger, A. J., Cowie, L. L., Mushotzky, R. F., & Yang, Y. 2003, *ApJL*, 596, L23
- Steffen, A. T., Brandt, W. N., Alexander, D. M., Gallagher, S. C., & Lehmer, B. D. 2007, *ApJL*, 667, L25
- Stern, D., Djorgovski, S. G., Perley, R. A., de Carvalho, R. R., & Wall, J. V. 2000, *AJ*, 119, 1526
- Stern, D., et al. 2005, *ApJ*, 631, 163
- Strecker, D. W., Erickson, E. F., & Witteborn, F. C. 1979, *ApJS*, 41, 501
- Stürm, E., Lutz, D., Tran, D., Feuchtgruber, H., Genzel, R., Kunze, D., Moorwood, A. F. M., & Thornley, M. D. 2000, *A&A*, 358, 481
- Surace, J. A., Sanders, D. B., & Evans, A. E. 2000, *ApJ*, 529, 170
- Swinbank, A. M., Smail, I., Chapman, S. C., Blain, A. W., Ivison, R. J., & Keel, W. C. 2004, *ApJ*, 617, 64
- Szokoly, G. P., et al. 2004, *ApJS*, 155, 271
- Tozzi, P., et al. 2006, *A&A*, 451, 457
- Treister, E., et al. 2004, *ApJ*, 616, 123
- Treister, E., et al. 2005, *ApJ*, 621, 104
- Treister, E., & Urry, C. M. 2005, *ApJ*, 630, 115
- Treister, E., et al. 2006, *ApJ*, 640, 603

- Teng, S. H., Wilson, A. S., Veilleux, S., Young, A. J., Sanders, D. B., & Nagar, N. M. 2005, *ApJ*, 633, 664
- Ueda, Y., Akiyama, M., Ohta, K., & Miyaji, T. 2003a, *ApJ*, 598, 886
- Vandame, B., et al. 2001, *ArXiv Astrophysics e-prints*, arXiv:astro-ph/0102300
- Vanzella, E., et al. 2006, *A&A*, 454, 423
- Veilleux, S., Kim, D.-C., & Sanders, D. B. 1999, *ApJ*, 522, 113
- Vijh, U. P., Witt, A. N., & Gordon, K. D. 2003, *ApJ*, 587, 533
- Waddington, I., Windhorst, R. A., Cohen, S. H., Partridge, R. B., Spinrad, H., & Stern, D., 1999, *ApJ*, 526, L77
- Weedman, D. W., Le Floc'h, E., Higdon, S. J. U., Higdon, J. L., & Houck, J. R. 2006, *ApJ*, 638, 613
- White, N. E., Swank, J. H., & Holt, S. S. 1983, *ApJ*, 270, 711
- Wilkes, B. J., Pounds, K. A., Schmidt, G. D., Smith, P. S., Cutri, R. M., Ghosh, H., Nelson, B., & Hines, D. C. 2005, *ApJ*, 634, 183
- Wirth, G. D., et al. 2004, *AJ*, 127, 3121
- Wolf, C., et al. 2004, *A&A*, 421, 913
- Worsley, M. A., Fabian, A. C., Barcons, X., Mateos, S., Hasinger, G., & Brunner, H. 2004, *MNRAS*, 352, L28
- Worsley, M. A., et al. 2005, *MNRAS*, 357, 1281
- Worsley, M. A., Fabian, A. C., Bauer, F. E., Alexander, D. M., Brandt, W. N., & Lehmer, B. D. 2006, *MNRAS*, 368, 1735



Yan, L., et al. 2004, *ApJS*, 154, 60

Yan, L., et al. 2005, *ApJ*, 628, 604

Yan, L., et al. 2007, *ApJ*, 658, 778

Yun, M. S., Reddy, N. A., & Condon, J. J. 2001, *ApJ*, 554, 803

Zdziarski, A. A., Johnson, W. N., Done, C., Smith, D. & McNaron-Brown, K. 1995,  
*ApJ*, 438, L63

Zdziarski, A. A., Poutanen, J. & Johnson, W. N. 2000, *ApJ*, 542, 703